



# **NAVAL POSTGRADUATE SCHOOL**

**MONTEREY, CALIFORNIA**

## **DISSERTATION**

**OBSERVATIONS AND HIGH-RESOLUTION  
NUMERICAL SIMULATIONS OF A NON-DEVELOPING  
TROPICAL DISTURBANCE IN THE WESTERN NORTH  
PACIFIC**

by

Andrew B. Penny

September 2013

Dissertation Supervisor:

Patrick A. Harr

**Approved for public release; distribution is unlimited**

THIS PAGE INTENTIONALLY LEFT BLANK



<b>REPORT DOCUMENTATION PAGE</b>			<i>Form Approved OMB No. 0704-0188</i>	
Public reporting burden for this collection of information is estimated to average 1 hour per response, including the time for reviewing instruction, searching existing data sources, gathering and maintaining the data needed, and completing and reviewing the collection of information. Send comments regarding this burden estimate or any other aspect of this collection of information, including suggestions for reducing this burden, to Washington headquarters Services, Directorate for Information Operations and Reports, 1215 Jefferson Davis Highway, Suite 1204, Arlington, VA 22202-4302, and to the Office of Management and Budget, Paperwork Reduction Project (0704-0188) Washington DC 20503.				
<b>1. AGENCY USE ONLY (Leave blank)</b>		<b>2. REPORT DATE</b> September 2013	<b>3. REPORT TYPE AND DATES COVERED</b> Dissertation	
<b>4. TITLE AND SUBTITLE</b> OBSERVATIONS AND HIGH-RESOLUTION NUMERICAL SIMULATIONS OF A NON-DEVELOPING TROPICAL DISTURBANCE IN THE WESTERN NORTH PACIFIC			<b>5. FUNDING NUMBERS</b>	
<b>6. AUTHOR(S)</b> Andrew B. Penny				
<b>7. PERFORMING ORGANIZATION NAME(S) AND ADDRESS(ES)</b> Naval Postgraduate School Monterey, CA 93943-5000			<b>8. PERFORMING ORGANIZATION REPORT NUMBER</b>	
<b>9. SPONSORING /MONITORING AGENCY NAME(S) AND ADDRESS(ES)</b> N/A			<b>10. SPONSORING/MONITORING AGENCY REPORT NUMBER</b>	
<b>11. SUPPLEMENTARY NOTES</b> The views expressed in this thesis are those of the author and do not reflect the official policy or position of the Department of Defense or the U.S. Government. IRB Protocol number ____N/A____.				
<b>12a. DISTRIBUTION / AVAILABILITY STATEMENT</b> Approved for public release; distribution is unlimited			<b>12b. DISTRIBUTION CODE</b> A	
<b>13. ABSTRACT (maximum 200 words)</b> <p>Uncertainty still remains in determining whether a tropical cloud cluster will eventually develop into a tropical cyclone. During T-PARC/TCS-08, a tropical disturbance (TCS025) was closely observed for potential formation during five aircraft reconnaissance missions. However, similar to the outcome for the majority of such systems, TCS025 failed to intensify. This provided for an unprecedented dataset of a non-developing system, which included airborne ELDORA dual Doppler radar. An in-depth examination of observations revealed that TCS025 failed to develop due to vertical wind shear and misalignment of the circulation structure in the vertical. Poor vertical alignment kept the circulation exposed to negative environmental influences that impacted the inner-core thermodynamic structure. This weakened subsequent convection that might otherwise have improved alignment and contributed to development. A multi-physics ensemble using the WRF-ARW model was employed to expand upon the observational findings. Simulations that developed TCS025 exhibited exaggerated convective precipitation processes and improved circulation alignment. Data assimilation experiments that incorporated aircraft and radar data provided improved initial conditions to examine the impact of a weak, misaligned circulation. Although convective precipitation processes were still over-represented, development of TCS025 was delayed, which allowed environmental factors to more severely impact TCS025 and limit its development.</p>				
<b>14. SUBJECT TERMS</b> tropical storm formation, TCS-08, T-PARC, airborne dual-Doppler Radar, dropwindsonde, ELDORA, SAMURAI, WRF-ARW, DART ensemble data assimilation			<b>15. NUMBER OF PAGES</b> 323	
			<b>16. PRICE CODE</b>	
<b>17. SECURITY CLASSIFICATION OF REPORT</b> Unclassified	<b>18. SECURITY CLASSIFICATION OF THIS PAGE</b> Unclassified	<b>19. SECURITY CLASSIFICATION OF ABSTRACT</b> Unclassified	<b>20. LIMITATION OF ABSTRACT</b> UU	

THIS PAGE INTENTIONALLY LEFT BLANK

**Approved for public release; distribution is unlimited**

**OBSERVATIONS AND HIGH-RESOLUTION NUMERICAL SIMULATIONS OF  
A NON-DEVELOPING TROPICAL DISTURBANCE IN THE WESTERN  
NORTH PACIFIC**

Andrew B. Penny  
B.Sc., University of Alberta, 2007  
M.S., University of Arizona, 2009

Submitted in partial fulfillment of the  
requirements for the degree of

**DOCTOR OF PHILOSOPHY IN METEOROLOGY**

from the

**NAVAL POSTGRADUATE SCHOOL  
September 2013**

Author:

---

Andrew B. Penny

Approved by:

---

Patrick Harr  
Professor of Meteorology  
Dissertation Supervisor/  
Dissertation Committee Chair

---

Joshua Hacker  
Associate Professor of Meteorology

---

Russell Elsberry  
Distinguished Research Professor of  
Meteorology

---

Rebecca Stone  
Professor of Oceanography

---

Michael Montgomery  
Distinguished Professor of  
Meteorology

---

Michael Bell  
Assistant Professor of Meteorology  
University of Hawaii

Approved by:

---

Wendell Nuss, Chair, Department of Meteorology

Approved by:

---

Douglas Moses, Vice Provost for Academic Affairs

THIS PAGE INTENTIONALLY LEFT BLANK

## ABSTRACT

Uncertainty still remains in determining whether a tropical cloud cluster will eventually develop into a tropical cyclone. During T-PARC/TCS-08, a tropical disturbance (TCS025) was closely observed for potential formation during five aircraft reconnaissance missions. However, similar to the outcome for the majority of such systems, TCS025 failed to intensify. This provided for an unprecedented dataset of a non-developing system, which included airborne ELDORA dual Doppler radar. An in-depth examination of observations revealed that TCS025 failed to develop due to vertical wind shear and misalignment of the circulation structure in the vertical. Poor vertical alignment kept the circulation exposed to negative environmental influences that impacted the inner-core thermodynamic structure. This weakened subsequent convection that might otherwise have improved alignment and contributed to development. A multi-physics ensemble using the WRF-ARW model was employed to expand upon the observational findings. Simulations that developed TCS025 exhibited exaggerated convective precipitation processes and improved circulation alignment. Data assimilation experiments that incorporated aircraft and radar data provided improved initial conditions to examine the impact of a weak, misaligned circulation. Although convective precipitation processes were still over-represented, development of TCS025 was delayed, which allowed environmental factors to more severely impact TCS025 and limit its development.

THIS PAGE INTENTIONALLY LEFT BLANK

# TABLE OF CONTENTS

<b>I. INTRODUCTION .....</b>	<b>1</b>
<b>A. MOTIVATION.....</b>	<b>1</b>
<b>B. PREVIOUS TROPICAL CYCLOGENESIS STUDIES .....</b>	<b>2</b>
1. Precipitation Processes .....	4
a. <i>Stratiform Precipitation Processes: Mid-level Vortex Formation and Its Possible Role in Storm Formation .....</i>	<i>4</i>
b. <i>Convective Processes: Deep Vortical Convection.....</i>	<i>9</i>
c. <i>Cooperative Stratiform and Convective Processes: VHT Development in the Presence of a MCV .....</i>	<i>11</i>
d. <i>Subsidence-induced Warm-core Development .....</i>	<i>14</i>
2. Environmental Influences .....	15
a. <i>Vertical Wind Shear.....</i>	<i>15</i>
b. <i>Protective Environment of the Pouch .....</i>	<i>19</i>
<b>C. OBJECTIVES AND HYPOTHESES.....</b>	<b>22</b>
1. Hypothesis #1.....	23
2. Hypothesis #2.....	24
3. Hypothesis #3.....	25
<b>II. DATA AND METHODOLOGY .....</b>	<b>37</b>
<b>A. OBSERVATIONS COLLECTED DURING TCS025 IOPS .....</b>	<b>37</b>
1. GPS Dropwindsondes and AXBTs .....	37
2. MTSAT IR Brightness Temperature and TRMM Precipitation .....	39
3. NRL P-3 ELDORA Dual-Doppler Radar.....	40
4. USAF WC-130J and NRL P-3 Flight-level Data.....	43
<b>B. GLOBAL FORECAST ANALYSES.....</b>	<b>44</b>
1. ECMWF YOTC: Synoptic Evolution .....	44
2. NCEP CFSR: Environmental Vertical Wind Shear .....	45
<b>C. SAMURAI ANALYSES .....</b>	<b>46</b>
<b>D. MULTI-PHYSICS ENSEMBLE: WRF-ARW MODEL .....</b>	<b>48</b>
<b>E. DART-WRF ENSEMBLE DATA ASSIMILATION EXPERIMENTS.....</b>	<b>49</b>
1. Data Assimilation Cycle .....	50
2. Data Preparation.....	52
<b>III. OBSERVATIONAL ANALYSIS.....</b>	<b>69</b>
<b>A. SYNOPTIC BACKGROUND AND SYSTEM EVOLUTION .....</b>	<b>69</b>
<b>B. CONVECTION AND MCS DEVELOPMENT .....</b>	<b>70</b>
<b>C. MESOSCALE ANALYSIS .....</b>	<b>72</b>
1. First IOP (1930 UTC 26 August – 0257 UTC 27 August) .....	73
2. Second IOP (2103 UTC August 27 – 0520 UTC 28 August) .....	74
3. Third IOP (2234 UTC 28 August – 0510 UTC 29 August) .....	78
<b>D. THERMODYNAMIC EVOLUTION .....</b>	<b>80</b>
<b>E. OBSERVATIONAL COMPARISON WITH TY FANAPI (2010) .....</b>	<b>83</b>
<b>F. OBSERVATIONAL SUMMARY AND DISCUSSION.....</b>	<b>86</b>

<b>IV. MULTI-PHYSICS ENSEMBLE.....</b>	<b>133</b>
<b>A. SYNOPTIC EVOLUTION.....</b>	<b>134</b>
<b>B. CIRCULATION BUDGET ANALYSES.....</b>	<b>139</b>
1. Blue-boxed Region: 1800 UTC 27 August – 0600 UTC 28 August..	141
2. Red-boxed Region: 1800 UTC 27 August – 0600 UTC 28 August ..	144
3. Frictional Spin-down in Simulation 25 .....	147
<b>C. COMPARISON OF CONVECTIVE INTENSITY .....</b>	<b>148</b>
1. Differenced Quantities: Blue-boxed Region: 1200 UTC 27 August - 1200 UTC 28 August.....	149
2. Average Convective/non-convective Profiles: Blue-boxed Region: 1800 UTC 27 August – 0600 UTC 28 August .....	150
3. Additional Numerical Simulations Examining Sensitivities to Microphysical Precipitation Processes.....	153
<b>D. OBSERVATIONAL VERIFICATION: CONVECTIVE INTENSITY ....</b>	<b>157</b>
1. MTSAT IR/model-derived Cloud-top Temperature .....	157
2. ELDORA and Model-derived Reflectivity .....	158
3. Equivalent Potential Temperature Deficit.....	160
<b>E. IMPACTS OF DEEP CONVECTION.....</b>	<b>161</b>
1. Circulation Alignment and Thermodynamic Response .....	161
2. Vertical Wind Shear .....	168
<b>F. MULTI-PHYSICS ENSEMBLE DISCUSSION AND SUMMARY .....</b>	<b>171</b>
<b>V. DATA ASSIMILATION .....</b>	<b>213</b>
<b>A. ELDORA RADIAL VELOCITIES IMPACT ON CIRCULATION         STRUCTURE.....</b>	<b>214</b>
<b>B. DART-WRF ENSEMBLE MEAN FORECAST.....</b>	<b>215</b>
<b>C. VORTICITY EVOLUTION COMPARISON .....</b>	<b>217</b>
<b>D. CIRCULATION RE-ALIGNMENT IN THE DWEMF .....</b>	<b>218</b>
<b>E. CIRCULATION BUDGET: PURPLE-BOXED REGION: 1200 UTC 28         AUGUST – 1800 UTC 28 AUGUST.....</b>	<b>219</b>
<b>F. AVERAGE PROFILES: PURPLE-BOXED REGION: 1200 UTC 28         AUGUST – 1800 UTC 28 AUGUST.....</b>	<b>222</b>
<b>G. ENSEMBLE FORECASTS .....</b>	<b>224</b>
1. 0600 UTC 28 August – 1200 UTC 30 August .....	224
2. 0600 UTC 29 August – 1200 UTC 30 August .....	225
<b>H. DATA ASSIMILATION DISCUSSION AND SUMMARY.....</b>	<b>225</b>
<b>VI. SUMMARY AND CONCLUSIONS.....</b>	<b>247</b>
<b>A. HYPOTHESIS #1 EVALUATION – OBSERVATIONS.....</b>	<b>247</b>
<b>B. HYPOTHESIS #2 EVALUATION – MULTI-PHYSICS ENSEMBLE ....</b>	<b>249</b>
<b>C. HYPOTHESIS #3 EVALUATION – DATA ASSIMILATION .....</b>	<b>252</b>
<b>D. CONCLUSIONS .....</b>	<b>255</b>
<b>VII. FUTURE WORK AND RECOMMENDATIONS .....</b>	<b>257</b>
<b>APPENDIX A. BUDGET BOX SENSITIVITY ANALYSIS .....</b>	<b>259</b>
<b>A. MAGENTA: 1200 UTC 27 AUGUST – 1800 UTC 27 AUGUST .....</b>	<b>259</b>
<b>B. BROWN: 1800 UTC 27 AUGUST – 0000 UTC 28 AUGUST.....</b>	<b>260</b>



C. BLUE: 1800 UTC 27 AUGUST – 0600 UTC 28 AUGUST .....	261
APPENDIX B. ECMWF-DROPWINDSONDE THERMODYNAMIC COMPARISON.....	267
APPENDIX C. PV-WEIGHTED CENTER POSITIONS .....	273
LIST OF REFERENCES.....	277
INITIAL DISTRIBUTION LIST .....	287

THIS PAGE INTENTIONALLY LEFT BLANK

## LIST OF FIGURES

Figure 1	Operational forecasts of 850 hPa relative vorticity and streamlines valid at 1200 UTC 29 August from the ECMWF (left panels) and GFS (right panels). Model initialization times (UTC) and forecast lead times (hours) are listed to the left of each set of graphics. Red circles indicate the vorticity features associated with the model development of the TCS025 disturbance. Forecast graphics taken from the NCAR EOL online T-PARC/TCS-08 field catalog: <a href="http://catalog.eol.ucar.edu/tparc/">http://catalog.eol.ucar.edu/tparc/</a> . ....	26
Figure 2	Schematic illustration of the mesoscale convective system (MCS) lifecycle in the presence of a developing tropical cyclone from Houze et al. (2009). (a) Deep convection possessing increased relative vorticity or “vortical hot towers” (VHTs) is followed by (b) MCS and mesoscale convective vortex development in the trailing stratiform precipitation region. After deep convection dissipates, the (c) stratiform precipitation region of MCS and associated MCV remain. Panel (d) depicts MCS development at various stages within the context of a preexisting disturbance.....	27
Figure 3	(a) Idealized net heating and cooling profiles for stratiform (solid line) and convective (dashed line) precipitation regions of a MCS. (b) Idealized heating rate profiles for various fractions of stratiform precipitation (from Houze 2004). ....	27
Figure 4	Diagram illustrating the formation of a MCV with a leading convective line (dark shaded areas) and trailing stratiform precipitation region. Panel (a) depicts the initial stage, and the MCV (denoted by “V”) formation and intensification are shown in panels (b) and (c), respectively. Warm temperature anomalies are indicated by “W” and cold anomalies “C” (from Chen and Frank 1993). ....	28
Figure 5	Illustration from Bister and Emanuel (1997) depicting the three-stage process of how tropical cyclogenesis is hypothesized to occur from a pre-existing MCS. ....	29
Figure 6	Graphic depicting how the thermal structure of a MCV could contribute to new convection. The environmental wind profile is shown at the left of diagram. Potential temperature and PV are contoured with dashed and solid lines, respectively. Open arrows indicate where horizontal vorticity is generated at the base of the cold pool associated with the vertical wind shear profile. The cold pool acts to lift low-level, high-equivalent potential temperature air inflowing relative to the system and trigger deep convection (from Raymond and Jiang 1990 and adapted by Houze 2004). ...	30
Figure 7	(a) Schematic from Harr and Elsberry (1996) illustrating where deep convection occurred in relation to the near-surface cold pool and MCV during the formation of TY Robyn (1993). Bold dark arrows denote low-level inflow. (b) Idealized south to north vertical cross-section through the convective structure depicted in (a) demonstrating how horizontal vorticity could be generated at the leading edge of the cold pool. Ellipse near 650	

	hPa marks the positive PV anomaly. Dark continuous arrow corresponds to the main MCS updraft. Dashed curved arrows at the leading edge of the cold pool mark the region where horizontal vorticity generation is occurring. ....	30
Figure 8	Schematic from Chen and Frank (1993) of the response to diabatic heating when the characteristic length scale ( $L$ ) of the disturbance is (a) less than the deformation radius ( $L_R$ ) and (b) greater than the deformation radius. “W” corresponds to warm temperature anomalies and “C” denotes cold anomalies. ....	31
Figure 9	Schematic from Montgomery et al. (2006) showing horizontal vorticity filaments (purple lines) tilted into vertical plane by MCV updrafts. Panel (a) is an illustration of how vorticity in the radial plane ( $\hat{r}$ ) is generated from a vertical wind shear profile and panel (b) illustrates how updrafts tilt horizontal vorticity to create vertical vorticity dipoles. ....	31
Figure 10	Profiles of (c, d) vertical mass flux from a numerical modeling sensitivity study in which profiles of (a) temperature and (b) mixing ratio were allowed to vary. Note in panel (c) that the level of maximum vertical mass flux is lowered in the presence of an upper-level warm temperature anomaly and cold low-level temperature anomaly (from Raymond and Sessions 2007). ....	32
Figure 11	Schematic from Dolling and Barnes (2012b) of how subsidence warming above the low-level circulation center (LLCC) is thought to have occurred during the formation of TS Humberto (2001). Ovals represent convective cells; red corresponds to cells 10 km in height, and white 16 km. Low-level flow is marked by blue arrows and is strongest away from LLCC. Subsidence and warm core are located at the trailing base of the anvil south of MCV. ....	33
Figure 12	Thermodynamic profiles representative of warm-core development via (a) WISHE and (c) subsidence and their associated temperature anomalies (b, d). Black lines in left panels represent a moist adiabatic environment. Red hatching corresponds to warming caused by latent heating (a) and subsidence (c) (from Dolling and Barnes 2012b). ....	33
Figure 13	Two pathways whereby low- $\theta_e$ air in the presence of vertical wind shear air can affect the thermodynamic cycle of a tropical cyclone: (a) mid-level low- $\theta_e$ air is directly entrained into eyewall convection and reduces $\theta_e$ within the eyewall, and as proposed by Riemer et al. (2010), (b) low- $\theta_e$ air is transported into the boundary layer via downdrafts and limits $\theta_e$ in the inflow layer. The blue regions represent the ocean surface and the storm center is located to the left in each figure. Black arrows represent air parcel trajectories within the idealized framework of a Carnot heat engine. Letters A, B, C, and D in the figures represent segments of the Carnot heat cycle (see Emanuel 1986). Black contours are lines of constant $\theta_e$ , with $\theta_e$ decreasing away from the storm center. Red wavy arrows represent processes that can change $\theta_e$ (i.e., surface fluxes and radiational cooling). ..	34

Figure 14	Schematic illustrating the combined impacts on convection that vertical wind shear (red outline) and rapid translation speed (orange outline) had in initiating convection in the down-shear direction (hatched) for Hurricane Irene (1997) (from Nguyen and Molinari 2012).	35
Figure 15	Illustration depicting a protected region where the mid-level and low-level circulations overlap. Boundary layer and mid-level circulations are oriented such that storm-relative flow (short black arrows) due to vertical wind shear is cancelled or minimized by the penetration depth of the circulation at each level (short green arrows) (from Raymond and Carrillo 2011).	35
Figure 16	Illustration of storm formation in the protective environment of an easterly wave pouch. The black dot marks the pouch center or intersection of the wave trough axis and critical latitude (i.e., “sweet spot”). The pouch center is where deep convection (gray shading) can be sustained and is the favored region for storm formation. Dashed streamlines represent ground-relative flow whereas solid streamlines correspond to flow in the storm-relative framework, which show a nearly closed recirculation region protected from the dry Saharan air layer (SAL) to the north (from Wang et al. 2010).	36
Figure 17	MTSAT IR brightness temperature overlaid on a streamline analysis of TY Nuri valid at 1200 UTC 16 August in (a) ground-relative reference frame and (b) storm-relative frame. Black dots mark the JTWC best track position. In (b), the thin black line is the wave trough axis and the purple line is the critical latitude; red arrows indicate where convective regions are converging upon the “sweet spot” (from Montgomery et al. 2010).	36
Figure 18	Approximate on-station (data collection) times of TCS025 aircraft missions. Numbers in parentheses correspond to the number of dropwindsondes deployed during each mission. The red line at the top of the figure corresponds to the simulation time of the multi-physics ensemble (including the control simulation), and the blue and green lines correspond to the first and second phases of the DART-WRF data assimilation experiments to be discussed in Chapter V.	54
Figure 19	Flight tracks for the five aircraft missions (listed in inset) in TCS025. Flights 0125W, 0325W, and 0525W were conducted by the USAF WC-130J aircraft and flights 0225W and 0425W were conducted by the NRL P-3. Colored dots correspond to GPS dropwindsonde locations and the numbers in parentheses in the inset correspond to the number of dropwindsondes deployed during each mission. Mission times are in day/UTC time next to the flight numbers. The black dashed line indicates the subjectively-determined center positions for TCS025 based on the ECMWF 850 hPa circulation and the black dots denote the 0000 UTC and 1200 UTC positions.	55
Figure 20	Example of the dropwindsonde center-finding technique computed at (a, b) 6 km altitude and (c, d) 2.5 km altitude during the second IOP. Center positions in (a) and (c) were computed following the simplified method	

	described in this study and those in (b) and (d) were computed based on the method described by Davis and Ahijevych (2012). Black wind barbs indicate dropwindsonde winds (1 full barb = 10 kt) interpolated to each height. Additional wind barbs at 2.5 km (bottom panels) are from the NRL P-3 that flew at an altitude of $\sim 3$ km. Shading represents the average tangential wind speed ( $\text{m s}^{-1}$ ) (see text for details). In (a) and (c), red and white dots correspond to the maximum average tangential wind speed and the circulation center determined from the centroid position of values within a threshold of the maximum value, respectively. Dashed ellipses in (a) and (c) represent an estimate of uncertainty in the circulation center position. White dots in (b) and (d) correspond to the circulation center position following the method of Davis and Ahijevych (2012), and black bars extending from the center position represent an estimate of uncertainty in the center position. ....	56
Figure 21	MTSAT IR brightness temperature ( $^{\circ}\text{C}$ ) valid at 0345 UTC 28 August. The subjectively determined center of MCS-G is marked by the white dot, and the red box defines the area used to compute the MCS intensity statistics for MCS-G at this time (see text). ....	57
Figure 22	(a) TRMM precipitation rate estimate ( $\text{mm h}^{-1}$ ) valid at 0000 UTC 28 August and (b) MTSAT IR brightness temperature ( $^{\circ}\text{C}$ ) valid at 2345 UTC 27 August. The blue box corresponds to the area used to compute the average TRMM precipitation rate estimates in Figure 90e. ....	57
Figure 23	(a) ELDORA tail-mounted dual radar geometry, where $\tau$ is the tilt angle (fore and aft) from a plane normal to the flight track and $\theta_r$ is the rotation angle in the plane normal to the flight track. (b) ELDORA flight track and radar sampling schematic for a hypothetical storm. Radar data are combined from the fore and aft beams to create an analysis of the velocity and reflectivity field on horizontal planes that intersect the storm. At locations where fore and aft radar beams intersect, the two-dimensional wind field can be constructed using measured radial velocities (adapted from Hildebrand et al. 1996). ....	58
Figure 24	(a) Total and (b) environmental vertical wind shear (200 – 850 hPa) from the global CFSR analysis valid at 0000 UTC 28 August. ....	59
Figure 25	Domain configurations used in this study. Black boxes correspond to the domains used for the multi-physics WRF ensemble and DART-WRF ensemble data assimilation system (see text for details). The domain “d04” (1-km grid spacing) was only used for simulation 20 (see Table 3). Colored boxes represent the SAMURAI analyses domains that encompassed data collection regions during the three IOPs (see Table 1). ....	60
Figure 26	Ensemble data assimilation cycle similar to that used for the DART-WRF simulations (see text for details). The model is represented by the green arrows and the state vector of each ensemble is represented by the blue stars; green tick marks correspond to the model state vector mapped to observation space by the forward operator $\mathbf{h}$ ; red tick marks represent observations, and red curves correspond to the observation probability.	

	The blue tick marks represent ensemble updates provided by the ensemble filter; blue arrows at top right are the increments in observation space, and the model increments correspond to the blue arrows near bottom center. Sources of error associated with each step of the data assimilation cycle are listed in the figure (from Anderson et al. 2009).....	61
Figure 27	ELDORA Doppler radial velocity ( $\text{m s}^{-1}$ ) displayed in range-elevation coordinates collected from the aft-pointing radar (TA) during the first NRL P-3 flight (0225W) from 0315:24 to 0315:28 UTC 28 August. Radial velocity data in (a) are full resolution, and in (b) after thinning as described in text. ....	62
Figure 28	Observation error standard deviation values used in the DART-WRF simulations for each observation platform for (a) temperature/dewpoint (K) and (b) wind speed ( $\text{m s}^{-1}$ ). Values are shown as probability density functions in percent of total number of observations available for assimilation. The standard deviation of ELDORA radial velocity error in (b) is shown with (cyan) and without (purple) the additional factor to account for uncertainty associated with precipitation fall speed. The total number of observations available for assimilation from both the second and third IOPs is shown in inset. ....	62
Figure 29	Observations assimilated at 0300 UTC 28 August using the DART-WRF ensemble data assimilation system. Colored dots denote the location observations assimilated and observation types are listed in inset. The numbers in parentheses in inset correspond to the total number of observations available for assimilation and the percentage of observations assimilated.....	63
Figure 30	850 hPa wind speed ( $\text{m s}^{-1}$ , shaded and vectors) for the DART-WRF ensemble mean (a) prior, (b) posterior, and (c) increment (posterior – prior) from the 3-km domain valid at 0300 UTC 28 August. ....	64
Figure 31	(a) MTSAT IR brightness temperature ( $^{\circ}\text{C}$ ) at 2345 UTC 26 August. Horizontal wind vectors ( $\text{m s}^{-1}$ , colored scale on right) and geopotential heights (m, black contours) at (b) 200 hPa and (c) 850 hPa from ECMWF analysis valid at 0000 UTC 27 August. The location of MCS-D is annotated in (a) and the red line and red circles in (b) and (c) correspond to the flight track and dropwindsonde deployment locations for USAF WC-130J flight 0125W. Blue circles in (b) and (c) correspond to AXBT deployment locations. Low-level circulations are labeled L1, L2, and L3 in (a) and (c) and G marks the location of Guam. ....	94
Figure 32	As in Figure 31, except (a) MTSAT IR brightness temperature at 2345 UTC 27 August and ECMWF analysis valid at 0000 UTC 28 August. The location of MCS-G is annotated in (a) and the red line and red circles in (b) and (c) correspond to the flight track and dropwindsonde deployment locations for USAF WC-130J flight 0325W. Blue line and blue circles in (b) and (c) correspond to the flight track and dropwindsonde deployment locations for NRL P-3 flight 0225W. South to north vertical cross section shown in Figure 48 is marked by black line in (b) and (c). ....	95

Figure 33	As in Figure 31, except (a) MTSAT IR brightness temperature at 2345 UTC 28 August and ECMWF analysis valid at 0000 UTC 29 August. Red line and red circles in (b) and (c) correspond to the flight track and dropwindsonde deployment locations for USAF WC-130J flight 0525W. Blue line and blue circles in (b) and (c) correspond to the flight track and dropwindsonde deployment locations for NRL P-3 flight 0425W. ....	96
Figure 34	As in Figure 31, except (a) MTSAT-IR brightness temperature valid at 2345 UTC 29 August and ECMWF analysis valid at 0000 UTC 30 August. ....	97
Figure 35	Vertical wind shear (200-850 hPa, kt) and direction (1 full barb = 10 kt) for TCS025. Computed using CFSR reanalysis data (see text for details).....	98
Figure 36	(a) Tracks of MCSs during TCS025 with open and closed circles indicating the formation and dissipation locations, respectively. The solid and dashed black lines mark the subjectively determined 850 hPa circulation and vorticity maximum tracks, respectively, which are based on a ECMWF analysis and are labeled at 0000 UTC positions (black circles). The approximate duration for each MCS is listed in the inset in (a) and shown as a time series in (b). ....	99
Figure 37	Ratio expressed as a percentage of area with MTSAT-IR brightness temperatures less than $-65^{\circ}\text{C}$ to that less than $-35^{\circ}\text{C}$ for MCSs that developed within the environment of TCS025. Dashed vertical black lines indicate the approximate time of the expected early morning convective maximum. ....	100
Figure 38	Radially averaged ( $0^{\circ}$ - $3^{\circ}$ ) half-hourly MTSAT IR brightness temperatures relative to the ECMWF 850 hPa vorticity maximum positions of TCS025. Colored bands along the ordinate represent USAF WC-130J and NRL P-3 aircraft missions flown into TCS025 with brown, blue and orange corresponding to the USAF WC-130J missions and red and green to the NRL P-3 missions. Abscissa axis labels correspond to directions along the azimuth. Short dashed horizontal lines mark the approximate time of diurnal convective maximum (1800 UTC) and long dashed horizontal line denotes the ending time of the 0225W NRL P-3 mission. The brightness temperature features associated with MCS-D and MCS-G are annotated....	101
Figure 39	MTSAT IR brightness temperature ( $^{\circ}\text{C}$ , shading) at 2345 UTC 26 August. The USAF WC-130J flight track (black line) and dropwindsonde deployment locations (white circles) are shown with wind barbs corresponding to 1500 m height (1 full barb = 10 kt) for first IOP (0125W). Red and blue dropwindsonde locations correspond to the dropwindsonde profiles shown in Figure 42.....	102
Figure 40	Earth-relative USAF WC-130J (0125W: 1930 UTC 26 August – 0257 UTC 27 August) flight track for TCS025. Black dots denote dropwindsonde locations and wind barbs correspond to heights shown in legend (1 full barb = 10 kt). Colored circles with black outlines mark dropwindsonde-derived circulation center locations at heights listed in inset, and dashed ellipses are estimates of the position uncertainty as described in text. ....	103



Figure 41	(a) Earth-relative wind speed (kt, shading) and vectors ( $\text{m s}^{-1}$ ) at 5-km altitude from the SAMURAI analysis and the (b) corresponding increment wind speed (kt, shading) and vector ( $\text{m s}^{-1}$ ) field valid at 0000 UTC 28 August. The red line indicates the flight track for the USAF WC-130J 0125W mission and black wind barbs correspond to dropwindsonde winds at 5-km altitude (1 full barb = 10 kt).....	104
Figure 42	Vertical profiles of (a) relative humidity (%) and (b) equivalent potential temperature (K) constructed from dropwindsondes at blue- and red-colored deployment locations in Figure 39 (see text for details).....	105
Figure 43	MTSAT IR brightness temperature ( $^{\circ}\text{C}$ , shading) at 2345 UTC 27 August. The USAF WC-130J flight track (black line), NRL P-3 flight track (red line), and dropwindsonde deployment locations (white circles) are shown with wind barbs corresponding to 1500 m height (1 full barb = 10 kt) for the second IOP (0225W and 0325W). Red-filled dropwindsonde locations near $151^{\circ}\text{E}$ were used in vertical cross section in Figure 51 and the bold black line near $151.8^{\circ}\text{E}$ denotes the location of the cross-section in Figure 48. Black dashed portion of the USAF WC-130J flight track corresponds with the locations where SFMR rain rate and IR brightness temperature data were analyzed in Figure 52. Skew-T log-P comparisons in Figure 123 were constructed from dropwindsondes “A” and “B”.....	106
Figure 44	As in Figure 40, except storm-relative USAF WC-130J (0325W: 2103 UTC 27 August – 0407 UTC 28 August) and NRL P-3 (0225W: 0130 UTC 28 August – 0520 UTC 28 August) flight tracks for the second IOP in TCS025. In addition to the circulation center locations from the dropwindsondes as in Figure 40, solid colored circles connected by a solid black line mark the subjectively determined circulation center locations at heights listed in inset from the SAMURAI analysis. White-centered colored circles connected by a dashed black line mark subjectively determined circulation center locations at heights listed in inset from the ECMWF analysis.....	107
Figure 45	Storm-relative wind speed (kt, shading) and vectors ( $\text{m s}^{-1}$ ) at (a) 5 km and (b) 1.5 km from SAMURAI analysis valid at 0000 UTC 28 August. The USAF WC-130J track for flight 0325W is in red and the NRL P-3 track for flight 0225W is in blue. Black wind barbs (1 full barb = 10 kt) correspond to dropwindsonde winds corrected for storm motion. Solid black line denotes location of the cross-section in Figure 48. The $2^{\circ} \times 2^{\circ}$ black and red boxes are centered on the circulation center positions at 1.5 (black dot) and 5 km (red dot), respectively, are used in the mesoscale vertical wind shear calculations in Figure 47 and discussed in text. ....	108
Figure 46	As in Figure 45, except for the increment wind speed (kt, shading) and vector ( $\text{m s}^{-1}$ ) field at 1.5 km that corresponds with the SAMURAI analysis in Figure 45b. ....	109
Figure 47	As in Figure 35, except also shown are wind barbs for the mesoscale vertical wind shear (system-relative flow) defined as the difference in the $2^{\circ} \times 2^{\circ}$ box-average wind (see Figure 45) between the 5- and 1.5-km height from	

- the 0000 UTC 28 August SAMURAI analysis for the pseudo-aligned (blue barb, 5.4 kt) and misaligned (red barb, 9.3 kt) cases described in text. .... 109
- Figure 48 South-to-north oriented vertical cross section of relative vorticity ( $10^{-5} \text{ s}^{-1}$ , shading), potential temperature anomaly (K, blue contours at 2.5 K with negative values dashed), divergence ( $10^{-5} \text{ s}^{-1}$ , black contours at  $2.0 \times 10^{-5} \text{ s}^{-1}$  with negative values dashed), and in-plane wind vectors ( $\text{m s}^{-1}$ ) constructed from (a) SAMURAI analysis and (b) ECMWF background field valid at 0000 UTC 28 August. The location of cross section corresponds to solid black lines shown in Figure 32, Figure 43, Figure 45, Figure 49, and Figure 50. Thick vertical black lines immediately below the abscissa in (a) correspond to southern and northern extent of ELDORA Doppler radar at the longitude of the cross-section (see Figure 50). .... 110
- Figure 49 (a) Average temperature (K, shading) in the 6-7 km layer and 6.5 km wind vectors ( $\text{m s}^{-1}$ ) from SAMURAI analysis valid at 0000 UTC 28 August. (b) As in (a), except for the 0-500 m layer and wind vectors correspond to 500 m height. The USAF WC-130J track for flight 0325W is in red and the NRL P-3 track for flight 0225W is in blue. Black wind barbs correspond to dropwindsonde winds at 6500 m in (a) and 500 m in (b) corrected for storm motion (1 full barb = 10 kt). Solid black lines denote location of cross-section in Figure 48. .... 111
- Figure 50 ELDORA reflectivity (dBZ, shading) at 5-km height from the NRL P-3 flight 0225W early on 28 August. The white horizontal wind vectors ( $\text{m s}^{-1}$ , with  $15 \text{ m s}^{-1}$  reference vector indicated at top right) correspond to the wind field at 5-km height derived using the SAMURAI analysis technique. The USAF WC-130J track for flight 0325W is in red and the NRL P-3 track for flight 0225W is in blue. Black wind barbs correspond to dropwindsonde winds corrected for storm motion (1 full barb = 10 kt). The solid black line denotes the location of the cross-section in Figure 48. .... 112
- Figure 51 South-to-north vertical cross section of equivalent potential temperature (K) constructed using dropwindsonde data (red-filled circles in Figure 43) collected during the second USAF WC-130J flight (0325W). Wind barbs depict the dropwindsonde horizontal wind (1 full barb = 10 kt) and follow standard convention (wind barb tails pointing toward the bottom of the figure represent a northerly wind). .... 113
- Figure 52 SFMR rain rate ( $\text{mm h}^{-1}$ , blue line and left ordinate) and MTSAT IR brightness temperatures ( $^{\circ}\text{C}$ , red line and right ordinate) interpolated spatially and temporally to the flight track during the second USAF WC-130J flight (0325W). Abscissa axis labels correspond to UTC time. Black dashed line in Figure 43 denotes the location along the flight track corresponding to this time interval. The black circle along the abscissa indicates the time of the 0046 UTC dropwindsonde in Figure 51. .... 114
- Figure 53 SAMURAI analyzed wind speed (kt, shading and vectors) at 1.5-km height from data collected during the third IOP in (a) the ground-relative frame and (b) storm-relative frame. The USAF WC-130J mission 0525W flight track is in red and the NRL P-3 mission 0425W flight track is in blue.

	Black wind barbs correspond to dropwindsonde winds (1 full barb = 10 kt), which have been corrected for storm motion in (b). The black star near 24°N, 152°E in (a) represents the surface circulation center determined from QuikSCAT scatterometer data valid at ~0747 UTC 29 August (see Figure 55).....	115
Figure 54	MTSAT IR brightness temperature (°C, shading) valid at 2345 UTC 28 August. The USAF WC-130J flight track (black line), NRL P-3 flight track (red line), and dropwindsonde deployment locations (white circles) are shown for third IOP (0425W and 0525W) with wind barbs corresponding to 1500 m height (1 full barb = 10 kt).....	116
Figure 55	Surface wind speed (kt) and direction (wind barbs, shading) valid at ~0747 UTC 29 August from the NASA QuikSCAT scatterometer. Black wind barbs denote possible rain contamination (from the T-PARC/TCS-08 Field Catalog: <a href="http://catalog.eol.ucar.edu/tparc_2008/report/weather/20080829/report.weather.200808292300.summary.image5.png">http://catalog.eol.ucar.edu/tparc_2008/report/weather/20080829/report.weather.200808292300.summary.image5.png</a> ).....	117
Figure 56	ELDORA reflectivity (dBZ, shading) at 3000 m height from the NRL P-3 flight (0425W) early on 29 August. The horizontal wind vectors correspond to the wind field derived using the SAMURAI analysis technique in the storm-relative frame. The USAF WC-130J track for flight 0525W is in red and the NRL P-3 track for flight 0425W is in blue. Black wind barbs correspond to dropwindsonde winds corrected for storm motion (1 full barb = 10 kt).....	118
Figure 57	As in Figure 40, except for storm-relative USAF WC-130J (0525W: 2234 UTC 28 August – 0510 UTC 29 August) and NRL P-3 (0425W: 0015 UTC 29 August – 0420 UTC 29 August) flight tracks for the third IOP. ....	119
Figure 58	Vertical profiles of (a) relative humidity (%), (b) $\theta_e$ (K), and (c) DCAPE ( $J\ kg^{-1}$ ) averaged for dropwindsondes for which the MTSAT IR brightness temperatures interpolated to the dropwindsonde time and location were less than -35°C (solid lines) and greater than -35°C (dashed lines) during USAF WC-130J aircraft missions shown in inset. The average MTSAT IR brightness temperatures of dropwindsondes used to compute each average are shown in inset. (d) Vertical profiles of temperature anomaly (K) from dropwindsondes averaged within 250 km of the analyzed ECMWF 850 hPa circulation center during aircraft missions shown in inset. Each mean profile used to compute the average temperature anomaly was constructed from all dropwindsondes from each flight. The number of dropwindsondes used to compute each average is shown in the inset of each figure.....	120
Figure 59	Equivalent potential temperature (K, shading), geopotential height (m, contours), and wind vectors ( $m\ s^{-1}$ , with $10\ m\ s^{-1}$ reference vector indicated at bottom right in panel (d)) at 500 hPa from the ECMWF analysis at times annotated in each panel. The black box in (c) corresponds to the area from which back trajectories in Figure 60 were selected at the end time of 0000 UTC 28 August.....	121

Figure 60	Equivalent potential temperature (K, shading) and geopotential height (m, contours) at 0000 UTC 25 August from the CFSR reanalysis at (a) 500 hPa, (b) 600 hPa and (c) 700 hPa. Colored lines correspond to 72-h back trajectories selected from grid points within the boxed region of 18-22°N, 148-152°E at (a) 500 hPa, (b) 600 hPa, and (c) 700 hPa in which the relative humidity at the ending time of 0000 UTC 28 August was < 70 %. Colored segments of trajectory lines indicate pressure levels in panel (c) inset. ....	122
Figure 61	Longitudinal average from 145°E to 160°E of MTSAT IR brightness temperatures (°C) as a function of latitude from 10°N to 35°N during the evolution of TCS025. ....	123
Figure 62	Flight tracks for the six USAF WC-130J aircraft missions flown to observe TY Fanapi (2010). Colored dots correspond to dropwindsonde deployment locations and the number of dropwindsondes deployed during each mission is shown in inset. The black dashed line marks the best track created using a combination of JTWC best-track locations and aircraft vortex fixes. ....	124
Figure 63	As in Figure 31, except (a) MTSAT-IR brightness temperature (°C) for pre-TY Fanapi at 0000 UTC 14 September 2010 and (b) 200 hPa and (c) 850 hPa from the ECMWF operational analysis valid at 0000 UTC 14 September (during second USAF WC-130J mission 0220W). Blue circles in (b) and (c) correspond to AXBT deployment. ....	125
Figure 64	(a) JTWC best-track maximum wind speed (kt, red line and left ordinate) and minimum sea-level pressure (hPa, blue line and right ordinate) during TY Fanapi. Red and blue dots denote the dropwindsonde maximum wind speed (kt) and minimum sea-level pressure (hPa), respectively, for each aircraft mission marked by the colored vertical bars. Asterisks denote maximum flight-level winds for each aircraft mission. (b) Magnitude of the 200-850 hPa vertical wind shear (kt) and direction (1 full barb = 10 kt) computed using CFSR reanalysis data (see text for details). ....	126
Figure 65	As in Figure 40, except storm-relative USAF WC-130J (0220W: 2014 UTC 13 September - 0258 UTC 14 September) flight tracks for TY Fanapi (2010). ....	127
Figure 66	Average profiles of $\theta_e$ (K) created from all dropwindsondes collected during the three USAF WC-130J flights in TCS025 and the first three TY Fanapi USAF WC-130J flights. Colored shading surrounding the average profiles denotes $\pm 1$ standard deviation. The number of dropwindsondes used to compute each average is shown in the legend. ....	128
Figure 67	Average oceanic temperature (°C) profiles constructed from AXBT data collected during the first USAF WC-130J mission (0125W) in TCS025 and the first three USAF WC-130J missions for TY Fanapi. The number of AXBTs used to compute each average is shown in the legend. ....	129
Figure 68	Minimum and maximum $\theta_e$ (K) for (a) TCS025 and (b) pre-TY Fanapi from individual dropwindsonde profiles during USAF WC-130J missions (shown in inset) for which the MTSAT IR brightness temperatures	

	interpolated to the dropwindsonde time and location were less than $-35^{\circ}\text{C}$ (filled circles) and greater than $-35^{\circ}\text{C}$ (open circles). Circles enclosed by thin black circles correspond to the mean $\theta_e$ extrema of the convective and non-convective environments for each flight. The numbers of dropwindsondes used to compute the average $\theta_e$ extrema are shown in the inset along with the average IR brightness temperature ( $^{\circ}\text{C}$ ) and average $\theta_e$ deficit (K) (maximum $\theta_e$ – minimum $\theta_e$ )......	130
Figure 69	Radially-averaged ( $0^{\circ}$ - $3^{\circ}$ ) MTSAT IR brightness temperature from (a) the ECMWF 850 hPa vorticity maximum position of TCS025 and (b) the modified best-track position of TY Fanapi computed using a combination of JTWC best-track locations and aircraft vortex fixes and were interpolated to 15-minute intervals. Solid colors along the time axis in (a) represent aircraft missions in TCS025 with brown, blue, and orange corresponding to the USAF WC-130J and red and green the NRL P-3 (see inset). Solid colors along the time axis in (b) represent USAF WC-130J pre-TY Fanapi missions. ....	131
Figure 70	Average profiles of $\theta_e$ (K) from the four dropwindsondes immediately surrounding the circulations of TCS025 (red line and shading) during the 0325W mission and pre-TY Fanapi (blue line and shading) during the 0220W mission. For TCS025, only dropwindsondes from the USAF WC-130J were used to compute the average. Colored shading surrounding the average profiles denotes $\pm 1$ standard deviation. ....	132
Figure 71	(a) Minimum sea-level pressure (hPa) and (b) maximum 10-m wind speed ( $\text{m s}^{-1}$ ) from 1200 UTC 27 August to 1200 UTC 30 August for the multi-physics WRF-ARW ensemble as indicated in the inset and described in Table 3 plus the ECMWF YOTC analysis. Bold lines denote simulations that are extensively compared in this chapter. ....	179
Figure 72	As in Figure 71, except the tracks based on minimum sea-level positions from WRF simulations and the ECMWF YOTC analysis from 1200 UTC 27 August to 1200 UTC 30 August. Large open and filled blue circles mark the starting and ending positions, respectively, of the ECMWF YOTC analysis. Small circles connected by dashed lines denote center positions from simulations of focus in this study (bold lines) at times annotated in figure. Latitude and longitude positions from the WRF simulations were smoothed using a 5-point running average. ....	180
Figure 73	Wind speed ( $\text{m s}^{-1}$ , shading) and geopotential height (m, contoured) at 200 hPa (top) and 850 hPa (bottom) valid at 0000 UTC 28 August ( $T + 12$ h) for (a, c) WRF simulation 25 and (b, d) WRF simulation 9. The red lines indicate the location of the vertical cross-sections in Figure 74. ....	181
Figure 74	Vertical cross sections along the red lines in Figure 73 of (top) relative vorticity ( $10^{-5} \text{ s}^{-1}$ , shading) and (bottom) equivalent potential temperature (K, shading) and virtual temperature perturbation (K, contours) valid at 0000 UTC 28 August for (a, c) WRF simulation 25 and (b, d) WRF simulation 9. The ordinate axis is in pressure (hPa). Vectors represent wind speeds in the plane of the cross section, and vertical velocity has	

	been rescaled by multiplying by a factor of 10. The average virtual temperature out to $6^\circ$ radius from the circulation center position was used as the reference state to determine the virtual temperature perturbations in (c) and (d).....	182
Figure 75	As in Figure 73, except valid at 0000 UTC 29 August (T + 36 h) and the red lines indicate the locations of the cross sections in Figure 76. ....	183
Figure 76	As in Figure 74, except for 0000 UTC 29 August (T + 36 h). The locations of the vertical cross sections in (a) and (b) correspond to the short, dashed red lines in Figure 75 (a, c) and (b, d), respectively. The locations of the vertical cross sections in (c) and (d) correspond to the longer solid red lines in Figure 75 (a, c) and (b, d), respectively. Note that the horizontal scaling in (a) and (b) is different from Figure 74a,b.....	184
Figure 77	As in Figure 73, except valid at 0000 UTC 30 August (T + 60 h) without red lines indicating cross section locations. ....	185
Figure 78	Time series of azimuthally-averaged 200 hPa radial wind speeds ( $\text{m s}^{-1}$ ) as a function of radius from (a) WRF simulation 25, (b) WRF simulation 9, and (c) the ECMWF analysis. Values were first transformed to cylindrical coordinates before azimuthal averaging using center positions determined from the 900 hPa PV centroid.....	186
Figure 79	850 hPa wind vectors ( $\text{m s}^{-1}$ , with $10 \text{ m s}^{-1}$ reference vector indicated at top) and 950-700 hPa average relative vorticity ( $10^{-5} \text{ s}^{-1}$ , color shading) from WRF simulation 25 at 6-h intervals from 1800 UTC 27 August to 1200 UTC 28 August. Boxed regions of various colors correspond to areas over which circulation budgets and averages were computed. ....	187
Figure 80	As in Figure 79, except for WRF simulation 9. ....	188
Figure 81	Time evolution from WRF simulation 25 from 1800 UTC 27 August to 0600 UTC 28 August for the blue-boxed region in Figure 79 of (a) relative vorticity ( $10^{-5} \text{ s}^{-1}$ ), (b) total circulation tendency ( $10^{-5} \text{ s}^{-1} \text{ h}^{-1}$ ), (c) circulation tendency due to stretching ( $10^{-5} \text{ s}^{-1} \text{ h}^{-1}$ ), (d) circulation tendency due to horizontal eddy fluxes ( $10^{-5} \text{ s}^{-1} \text{ h}^{-1}$ ), (e) circulation tendency due to tilting ( $10^{-5} \text{ s}^{-1} \text{ h}^{-1}$ ), and (f) integrated circulation budget contributions. Ordinate axes are in pressure (hPa). ....	189
Figure 82	As in Figure 81, except for WRF simulation 9 for the blue-boxed region in Figure 80. ....	190
Figure 83	Differences between WRF simulations 9 and 25 (9-25) averaged over the blue-boxed regions in Figure 79 and Figure 80 for (a) relative vorticity ( $10^{-5} \text{ s}^{-1}$ ), (b) total circulation tendency ( $10^{-5} \text{ s}^{-1} \text{ h}^{-1}$ ), (c) circulation tendency due to stretching ( $10^{-5} \text{ s}^{-1} \text{ h}^{-1}$ ), and the circulation tendency due to horizontal eddy fluxes ( $10^{-5} \text{ s}^{-1} \text{ h}^{-1}$ ) Note that the color scales in this figure are different from those used in Figure 81 and Figure 82. ....	191
Figure 84	As in Figure 81, except for simulation 25 in the red-boxed region in Figure 79.....	192
Figure 85	As in Figure 81, except for simulation 9 in the red-boxed region in Figure 80.	193
Figure 86	As in Figure 83, except for the red-boxed regions in Figure 79 and Figure 80.	194

Figure 87	Time evolution from the ECMWF operational forecast from 1200 UTC 27 August to 1200 UTC 28 August averaged over the blue-boxed region in Figure 79 of (a) relative vorticity ( $10^{-5} \text{ s}^{-1}$ ), (b) total circulation tendency ( $10^{-5} \text{ s}^{-1} \text{ h}^{-1}$ ), and (c) circulation tendency due to stretching ( $10^{-5} \text{ s}^{-1} \text{ h}^{-1}$ ). Note that the scales used in this figure are different from those in Figure 81 and Figure 82. ....	195
Figure 88	(a, c) Azimuthally-averaged cloud-top brightness temperatures ( $^{\circ}\text{C}$ ) and (b, d) integrated circulation budget contributions for the time period 0300-1200 UTC 28 August for the blue-boxed region in Figure 79 for WRF simulations (a, b) 25 and (c, d) 9. ....	196
Figure 89	Differences between WRF simulations 9 and 25 (9-25) averaged over the blue-boxed regions in Figure 79 and Figure 80 from 1200 UTC 27 August to 1200 UTC 28 August for (a) vertical velocity ( $\text{m s}^{-1}$ ), (b) diabatic heating rate ( $\text{K h}^{-1}$ ), (c) divergence ( $10^{-5} \text{ s}^{-1}$ ), and (d) equivalent potential temperature ( $\text{K}$ ). ....	197
Figure 90	Vertical profiles from the WRF simulations 9 (red), 12 (green), and 25 (purple) for grid points where the model-derived cloud-top brightness temperatures were $< -35^{\circ}\text{C}$ (solid lines) and $> -35^{\circ}\text{C}$ (dashed lines) averaged within the blue-boxed region in Figure 79 from 1800 UTC 27 August to 0600 UTC 28 August of (a) positive and negative vertical velocity ( $\text{m s}^{-1}$ ), and (b) diabatic heating rate ( $\text{K h}^{-1}$ ) corresponding with the positive and negative vertical velocities. (c) Total non-precipitating mixing ratio ( $\text{g kg}^{-1}$ ), (d) total precipitating mixing ratio ( $\text{g kg}^{-1}$ ), (e) average precipitation rate ( $\text{mm h}^{-1}$ ) as a function of time, and (f) CAPE ( $\text{J kg}^{-1}$ ). Black dots in (e) denote the average TRMM precipitation rate estimates for the blue-boxed region at the corresponding times. ....	198
Figure 91	Minimum sea-level pressure (hPa) from simulation 25 (solid purple), simulation 25 except hydrometeor drag was reduced by 50% (dashed purple), simulation 9 (solid red), and simulation 9 except the graupel fall speed was reduced to match the WSM6 formulation (dashed red). ....	199
Figure 92	Minimum sea-level pressure (hPa) for simulations that used the Purdue Lin microphysics scheme in which the diabatic heating rate was multiplied by a factor ranging from 0.5 to 1.1. The minimum sea-level pressure from the ECMWF analysis (black) is shown for reference. ....	200
Figure 93	Vertical profiles of diabatic heating rate ( $\text{K h}^{-1}$ ) for simulation 9 (red line), simulation 25 (purple line), and for simulations that used the Purdue Lin microphysics scheme in which the diabatic heating rates were multiplied by a factor of 0.95 (long dashed line) and 0.90 (short dashed line). ....	201
Figure 94	(a) MTSAT-IR brightness temperature ( $^{\circ}\text{C}$ ) at 2345 UTC 27 August and model-derived cloud-top brightness temperature at 0000 UTC 28 August from WRF simulations (c) 25 and (e) 9. Histograms as a function of time during the evolution of TCS025 of (b) MTSAT IR brightness temperature ( $^{\circ}\text{C}$ ) and of model-derived cloud-top brightness temperature ( $^{\circ}\text{C}$ ) from (d) WRF simulation 25 and (f) WRF simulation 9. Histograms were created	

	by binning brightness temperature values within a $\pm 3^\circ$ box of the respective center position for each case (see text). . . . .	202
Figure 95	Left panels: reflectivity (dBZ, shading) and horizontal wind vectors ( $\text{m s}^{-1}$ ) at 4-km height from (a) the NRL P-3 ELDORA dual Doppler radar, (c) WRF simulation 25, and (e) WRF simulation 9 valid at 0000 UTC 28 August. Right panels: vertical cross-sections of reflectivity (dBZ, shading) for (b) the NRL P-3 ELDORA dual Doppler radar, (d) WRF simulation 25, and (f) WRF simulation 9. Cross-section locations for (b, d, and f) correspond to the black lines in (a, c, and e), respectively. . . . .	203
Figure 96	Average (a) $\theta_e$ deficit (K), (b) mid-tropospheric $\theta_e$ minimum, and (c) lower- tropospheric $\theta_e$ maximum for the blue-boxed region in Figure 79 for WRF simulations 9 (red), 12 (green), and 25 (purple). . . . .	204
Figure 97	Potential vorticity centroid positions at 900 hPa (red) and 500 hPa (blue) for (a) WRF simulation 25 and (b) WRF simulation 9 from 1200 UTC 27 August to 1200 UTC 30 August. Red and blue dots indicate the PV centroid positions at 6 h intervals and are connected by dashed lines. Wind barbs correspond to the environmental vertical wind shear computed using the CFSR dataset (see Figure 35) (1 full barb = 10 kt). . . . .	205
Figure 98	(a) Separation distance (km, red line) between the 900 hPa and 500 hPa PV centroid positions and the direction of vortex tilt ( $^\circ$ , blue line) relative to the environmental vertical wind shear direction for WRF simulation 25. Positive angles correspond to a vortex tilt that is left of the shear vector. (b) Minimum sea-level pressure (hPa, green line), maximum 10-m wind speed ( $\text{m s}^{-1}$ , purple line), and radially averaged (0-100 km) model-derived cloud-top brightness temperature ( $^\circ\text{C}$ , brown line) for WRF simulation 25. (c) Radially averaged (0-100 km) relative vorticity ( $10^{-5} \text{ s}^{-1}$ ) at 900 hPa (red line) and 500 hPa (blue line) for WRF simulation 25. . . . .	206
Figure 99	As in Figure 98, except for WRF simulation 9. . . . .	207
Figure 100	(a, b) Equivalent potential temperature (K) and (c, d) radial wind speed ( $\text{m s}^{-1}$ ) at 500 hPa in cylindrical coordinate form from (a, c) WRF simulation 25 and (b, d) WRF simulation 9 at 1800 UTC 27 August. Data were interpolated to cylindrical coordinates using the 900 hPa PV centroid positions. North corresponds to the azimuth of $90^\circ$ , and dashed circles indicate range (km) from the center position. . . . .	208
Figure 101	Time series of averaged (a) $\theta_e$ advection by the radial wind ( $\text{K h}^{-1}$ ), (b) inertial stability ( $10^{-5} \text{ s}^{-2}$ ), (c) $\theta_e$ (K), and (d) total heat flux (latent and sensible) from the surface ( $\text{W m}^{-2}$ ) for simulations 9 (red) and 25 (purple). Quantities were averaged azimuthally ( $0^\circ$ - $360^\circ$ ) and radially (100-200 km) from the 900 hPa PV centroid positions between the 850 hPa and 400 hPa isobaric surfaces. . . . .	209
Figure 102	(a, b): Wind speed ( $\text{m s}^{-1}$ , shading), geopotential height (m, black contours), and vertical velocity ( $\text{m s}^{-1}$ , red contours with a $5 \text{ m s}^{-1}$ contour interval) at 200 hPa at 2000 UTC 27 August for (a) WRF simulation 9 and (b) WRF simulation 25. (c, d): As in (a, b), except color shading represents the 200-	



	850 hPa vertical wind shear ( $\text{m s}^{-1}$ ). The white-boxed area corresponds to the region where vertical wind shear was computed in Table 4 (see discussion in text). .....	210
Figure 103	Minimum sea-level pressure (hPa) from the control simulation (red), ECMWF analysis (blue), DART-WRF posterior ensemble mean (cyan), DART-WRF ensemble mean forecast-1 (magenta), DART-WRF ensemble mean forecast-2 (orange), DART-WRF posterior ensemble (ninety-six members, black), and the mean of the DART-WRF posterior ensemble (yellow). .....	230
Figure 104	Relative vorticity ( $10^{-5} \text{ s}^{-1}$ , shaded) at (a, b) 5- and (c, d) 1.5-km altitude for (a, c) WRF simulation 9 (control simulation) and (b, d) the DART-WRF ensemble mean at 0600 UTC 28 August (after the first ELDORA flight). The black lines denote the location of the vertical cross section shown in Figure 105. ....	231
Figure 105	South-to-north vertical cross sections of relative vorticity ( $10^{-5} \text{ s}^{-1}$ , shaded), potential temperature anomaly (K, blue contours every 0.25 K), divergence ( $10^{-5} \text{ s}^{-1}$ , black contours every $2.0 \times 10^{-5} \text{ s}^{-1}$ ), and in-plane wind vectors ( $\text{m s}^{-1}$ , with $10 \text{ m s}^{-1}$ reference vector indicated at the top right in each panel) from (a) WRF simulation 9 (control simulation) and (b) the DART-WRF ensemble mean at 0600 UTC 28 August. Dashed contours indicate negative values. The locations of the cross sections correspond to the solid black lines in Figure 104. ....	232
Figure 106	Wind speed ( $\text{m s}^{-1}$ , shaded) and geopotential height (m, contoured) at (a) 200 hPa and (b) 850 hPa, and south-to-north vertical cross sections of (c) relative vorticity ( $10^{-5} \text{ s}^{-1}$ , shading), and (d) $\theta_e$ (K, shading) and virtual temperature perturbation (K, contours) at the initial time of 0600 UTC 28 August for the DWEMF. The ordinate axis in (c) and (d) is in pressure (hPa). Vectors in (c) and (d) represent wind speeds in the plane of the cross sections, and vertical velocity has been rescaled by multiplying by a factor of 10. The average virtual temperature out to $6^\circ$ radius from the circulation center position was used as the reference state to determine the virtual temperature perturbation in (d). The red lines in (a) and (b) mark the location used for the vertical cross sections in (c) and (d). The vorticity cross section in (c) is similar to that in Figure 105b, except with different horizontal scaling. ....	233
Figure 107	As in Figure 106, except at 0000 UTC 29 August ( $T + 18 \text{ h}$ ). The dashed and longer solid red lines in (a) and (b) denote the locations used for the vertical cross sections in (c) and (d), respectively. Note that the cross-section location and horizontal scaling in (c) is different from (d). ....	234
Figure 108	As in Figure 106, except at 0000 UTC 30 August ( $T + 42 \text{ h}$ ). The solid red line in (a) and (b) denotes the location used for the vertical cross sections in (c) and (d). ....	235
Figure 109	950-700 hPa average relative vorticity, ( $10^{-5} \text{ s}^{-1}$ , shaded) and 850 hPa wind vectors ( $\text{m s}^{-1}$ , with a $10 \text{ m s}^{-1}$ reference vector indicated above the top left panel) at 6 h intervals from 1200 UTC 28 August to 1200 UTC 30 August	

	for WRF simulation 9 (control simulation). The purple boxed-region in the top panels corresponds to the area over which a circulation budget (see Figure 114) and averages (see Figure 116) were computed from 1200–1800 UTC 28 August. ....	236
Figure 110	As in Figure 109, except for the DART-WRF ensemble mean forecast (DWEMF). The purple boxed-region in the top panels corresponds to the area over which a circulation budget (see Figure 115) and averages (see Figure 116) were computed from 1200–1800 UTC 28 August. ....	237
Figure 111	As in Figure 109, except for the non-developing WRF simulation 25. The purple boxed-region in the top panels corresponds to the area over which averages (see Figure 116) were computed from 1200–1800 UTC 28 August. ....	238
Figure 112	As in Figure 97, except for the DWEMF. ....	239
Figure 113	As in Figure 98, except for the DWEMF. ....	240
Figure 114	Circulation budget tendencies as in Figure 81, except for the purple-boxed region in Figure 109 from 1200 UTC 28 August to 1800 UTC 28 August for WRF simulation 9 (control simulation). ....	241
Figure 115	Circulation budget tendencies as in Figure 81, except for the purple-boxed region in Figure 110 from 1200 UTC 28 August to 1800 UTC 28 August for the DART-WRF ensemble mean forecast (DWEMF). ....	242
Figure 116	Average profiles of (a) vertical velocity ( $\text{m s}^{-1}$ ), (b) diabatic heating rate ( $\text{K h}^{-1}$ ), (c) precipitation rate ( $\text{mm h}^{-1}$ ), (d) divergence ( $10^{-5} \text{ s}^{-1}$ ), (e) $\theta_e$ (K), and relative vorticity ( $10^{-5} \text{ s}^{-1}$ ) the for the WRF simulation 9 (control simulation, red), WRF simulation 12 (green), WRF simulation 25 (purple), DART-WRF ensemble mean forecast (magenta), and the DART-WRF posterior mean (cyan). Quantities were averaged within the purple-boxed region in Figure 72, and averaged in time for (a, b, d, e, f) from 1200 UTC 28 August to 1800 UTC 28 August. Black dots in (c) denote the average TRMM precipitation estimate for the purple-boxed region at the corresponding times. ....	243
Figure 117	Minimum sea-level pressure (hPa) from the control simulation (red), ECMWF analysis (blue), DART-WRF posterior ensemble mean (cyan), DART-WRF ensemble mean forecast-1 (magenta), DART-WRF ensemble mean forecast-2 (orange), DART-WRF ensemble initialized at 0600 UTC 28 August and integrated in forecast mode (no further data assimilation) (ninety-six members, black), and the mean of the DART-WRF ensemble integrated in forecast mode (yellow). ....	244
Figure 118	Minimum sea-level pressure tracks for the control simulation (red), ECMWF analysis (blue), DART-WRF posterior ensemble mean (cyan), DART-WRF ensemble mean forecast-1 (magenta), DART-WRF ensemble mean forecast-2 (orange), DART-WRF ensemble initialized at 0600 UTC 28 August and integrated in forecast mode (no further data assimilation) (96 members, thin red, green and blue lines), and the mean of the DART-WRF ensemble integrated in forecast mode (yellow). Tracks for ensemble members with a minimum sea-level pressure at 1200 UTC 30 August >	

	1004 hPa are colored blue, between 1000 hPa and 1004 hPa are colored green, and < 1000 hPa are colored red. Latitude and longitude positions were smoothed using a 3-point running average. ....	245
Figure 119	As in Figure 117, except minimum sea-level pressure (hPa) for the DART-WRF ensemble initialized at 0600 UTC 29 August and integrated in forecast mode (ninety-six members, black), and the mean of the DART-WRF ensemble integrated in forecast mode (yellow).....	246
Figure 120	Average profiles of (a) vertical velocity ( $\text{m s}^{-1}$ ), (b) diabatic heating rate ( $\text{K h}^{-1}$ ), (c) relative vorticity ( $10^{-5} \text{ s}^{-1}$ ), (d) divergence ( $10^{-5} \text{ s}^{-1}$ ), and (e) precipitation rate ( $\text{mm h}^{-1}$ ) for WRF simulations 9 (red), 12 (green), 25 (purple), DART-WRF ensemble mean forecast (magenta), and the DART-WRF posterior mean (cyan). Quantities were averaged within the <b>magenta</b> -boxed region in Figure 72, and averaged in time for (a, b, c, d) from 1200 UTC 27 August to 1800 UTC 27 August. (f) Profiles of integrated circulation budget contributions for WRF simulation 9 for the time period from 1200 UTC 27 August to 1800 UTC 27 August. Black dots in (e) denote the average TRMM precipitation estimate for the magenta-boxed region at corresponding times. ....	263
Figure 121	Same as Figure 120, except quantities were averaged within the <b>brown</b> -boxed region in Figure 72, and averaged in time for (a, b, c, d) from 1800 UTC 27 August to 0000 UTC 28 August. (f) Profiles of integrated circulation budget contributions for WRF simulation 9 for the time period from 1800 UTC 27 August to 0000 UTC 28 August.....	264
Figure 122	Same as Figure 120, except quantities were averaged within the <b>blue</b> -boxed region in Figure 72, and averaged in time for (a, b, c, d) from 1800 UTC 27 August to 0600 UTC 28 August. (f) Profiles of integrated circulation budget contributions for WRF simulation 9 for the time period from 1800 UTC 27 August to 0600 UTC 28 August. ....	265
Figure 123	Skew-T log-P comparisons in (a) and (b) constructed from dropwindsondes “A” and “B” in Figure 43, respectively, (dashed colors), and the ECMWF analysis at the same locations (solid colors), valid at 0000 UTC 28 August. Red and blue profiles correspond to temperature and dewpoint, respectively. Black wind barbs represent winds from the ECMWF analysis, and red wind barbs are for dropwindsonde winds (1 full barb = 10 kt). ....	270
Figure 124	Vertical profiles of (a) average relative humidity (%), (b) average $\theta_e$ (K), (c) average relative humidity difference (%), and (d) average $\theta_e$ difference (K) from dropwindsonde data collected during the second USAF WC-130J mission (0325W), and the ECMWF analysis at the same locations, valid at 0000 UTC 28 August. Red and blue profiles correspond to dropwindsondes for which the MTSAT IR brightness temperature (interpolated to the dropwindsonde time and location) was less than $-35^\circ\text{C}$ and greater than $-35^\circ\text{C}$ , respectively. ....	271
Figure 125	Relative vorticity (shaded, $10^{-5} \text{ s}^{-1}$ ) averaged between (a) 600-400 hPa and (b) 950-700 hPa and wind speed at (a) 500 hPa and (b) 850 hPa (vectors)	

	for the non-developing WRF simulation 25 at 0000 UTC 30 August. The blue and red open circles correspond to the diagnosed PV-weighted center positions at 500 hPa and 900 hPa, respectively. The blue- and red-boxed regions correspond to the area over which the PV-weighted center positions were calculated. ....	274
Figure 126	Relative vorticity (shaded, $10^{-5} \text{ s}^{-1}$ ) averaged between (a, b) 600-400 hPa and (c, d) 950-700 hPa and wind speed at (a, b) 500 hPa and (c, d) 850 hPa (vectors) for the WRF control simulation 9 at 1800 UTC 28 August. The blue and red open circles correspond to the diagnosed PV-weighted center positions at 500 hPa and 900 hPa, respectively. The blue- and red-boxed regions correspond to the area over which the PV-weighted center positions were calculated. PV center positions were determined using exponential weighting factors of 1 in (a, c) and 2 in (b, d).....	275

## LIST OF TABLES

Table 1	SAMURAI analyses of the TCS025 disturbance at the UTC times (day/hour) indicated in the second column. All analyses used the ECMWF YOTC analysis as the background field. For reference frame (third column), “E” and “S” denote earth-relative and storm-relative analyses, respectively. Abbreviations for “data used” (seventh column) are as follows: “C” is USAF WC-130J flight-level data, “P” is NRL P-3 flight level data, “D” is dropwindsonde data, and “E” is ELDORA Doppler radar radial velocity data. Other characteristics of the SAMURAI configuration are indicated in the other columns (see text). .....	65
Table 2	Observation error values used for different observation types in the SAMURAI analyses. Error values were chosen to account for instrumentation and representativeness error. ....	66
Table 3	List of TCS025 multi-physics ensemble simulations conducted using the WRF model. Model initialization times (start time) are given in dd/hh (UTC). Abbreviations not mentioned in text are as follows: WSM5 is the WRF single-moment 5-class microphysics scheme, and MYJ is the Mellor-Yamada-Janjic boundary layer scheme. The cumulus parameterization scheme (cumulus) is that used on the highest-resolution grid: KF represents the Kain-Fritsch scheme and “-” indicates no cumulus scheme. The development column indicates the rate of intensification exhibited: “N” is no development, “S” is slow development, “M” is moderate development, and “R” represents rapid development. ....	67
Table 4	Vertical wind shear values (200 hPa – 850 hPa) corresponding to the white-boxed regions in Figure 102 for WRF simulations 25 and 9 at 1800 UTC and 2000 UTC 27 August (see text for details). ....	211

THIS PAGE INTENTIONALLY LEFT BLANK

## LIST OF ACRONYMS AND ABBREVIATIONS

3DVAR	three-dimensional variational analysis
4DVAR	four-dimensional variational analysis
ARW	Advanced Research WRF
ARWO	Air Force Reconnaissance Weather Officer
ASPEN	Atmospheric Sounding Processing ENvironment
AXBT	airborne expendable bathometry thermograph
CAPE	convective available potential energy
CFSR	Climate Forecast System Reanalysis
COAMPS	Coupled Ocean/Atmosphere Mesoscale Prediction System
DA	data assimilation
DART	Data Assimilation Research Testbed
DART-WRF	Data Assimilation Research Testbed / WRF
DCAPE	downdraft convective available potential energy
DWEM	DART-WRF ensemble mean
DWEMF	DART-WRF ensemble mean forecast
EAKF	ensemble adjustment Kalman filter
EnKF	ensemble Kalman filter
ECMWF	European Center for Medium-range Weather Forecasts
ELDORA	ELectra DOppler RAdar
EOL	Earth Observing Laboratory
GPS	global positioning system
GTS	Global Telecommunications System
INS	inertial navigation system
IOP	intensive observing period
IR	infrared
ITOP	Impact of Typhoons on the Ocean in the Pacific
JMA	Japan Meteorological Agency
JTWC	Joint Typhoon Warning Center
KF	Kain-Fritsch cumulus parameterization scheme
LLCC	low-level circulation center
MCS	mesoscale convective system
MCV	mesoscale convective vortex
MM5	Fifth-generation Pennsylvania State University–NCAR Mesoscale Model
MTSAT	Multifunctional Transport Satellite
MYJ	Mellor-Yamada-Janjic boundary layer parameterization scheme
NAM	North American Mesoscale model
NASA	National Aeronautics and Space Administration
NCAR	National Center for Atmospheric Research
NCEP	National Centers for Environmental Prediction
NHC	National Hurricane Center
NOAA	National Oceanic and Atmospheric Administration
NOGAPS	Navy Operational Global Atmospheric Prediction System

NRL	Navy Research Lab
OHC	ocean heat content
PREDICT	PRE-Depression Investigation of Cloud systems in the Tropics
PRF	pulse repetition frequency
PV	potential vorticity
QuikSCAT	Quick Scatterometer
RHS	right hand side
RMW	radius of maximum winds
RPM	revolutions per minute
RRTM	Rapid Radiative transfer Model
SAL	Saharan air layer
SAMURAI	Spline Analysis at Mesoscale Utilizing Radar and Aircraft Instrumentation
SFMR	Stepped Frequency Microwave Radiometer
STY	supertyphoon
TCM-93	Tropical Cyclone Motion-1993
TCS-08	Tropical Cyclone Structure-2008
TD	tropical depression
TEXMEX	Tropical Experiment in Mexico
THORPEX	The Observing System Research and Predictability Experiment
T-PARC	THORPEX Pacific Regional Campaign
TRMM PR	Tropical Rainfall Measuring Mission Precipitation Radar
TS	tropical storm
TUTT	tropical upper tropospheric trough
$T_v$	virtual temperature
TY	typhoon
USAF	United States Air Force
UTC	coordinated universal time
VHT	vortical hot tower
VORTEX	Verification of the Origins of Rotation in Tornadoes Experiment
WISHE	Wind Induced Surface Heat Exchange
WRF	Weather Research and Forecasting model
WSM3	WRF Single-Moment 3-class microphysics parameterization scheme
WSM5	WRF Single-Moment 5-class microphysics parameterization scheme
WSM6	WRF Single-Moment 6-class microphysics parameterization scheme
WSM6 DM	WRF Double-Moment 6-class microphysics parameterization scheme
YOTC	Year of Tropical Convection
YSU	Yonsei University boundary layer parameterization scheme
$\theta_e$	equivalent potential temperature



## ACKNOWLEDGMENTS

I would like to thank my advisor, Professor Pat Harr, for his guidance and patience, and for helping me to see the big picture when, at times, I felt lost in the details. And my committee members: Professors Michael Bell, Russ Elsberry, Josh Hacker, Michael Montgomery, and Rebecca Stone. I am very appreciative of their constructive feedback and willingness to serve on my committee.

A special thanks to the National Science Foundation and Office of Naval Research–Marine Meteorology for funding the T-PARC and TCS-08 field programs, and to the flight crews of the USAF WC-130J and NRL P-3 aircraft for collecting the data used in this study.

This work greatly benefited from scientific discussions with Heather Archambault, Pete Black, Chris Davis, Jim Doyle, Christian Grams, Sarah Jones, and Myung-Sook Park. Thanks for sharing your insight and expertise.

I received a great deal of technical help with this project. I'd like to thank Nancy Collins, Glen Romine, Josh Hacker, and Jared Lee for their help with the setup of the DART experiments. I'd also like to thank Leonhard Scheck for providing code for the circulation budget calculations, Heather Archambault for assistance with the trajectory analysis, and Michael Bell for helping with the ELDORA radar data and SAMURAI analyses. This project would not have been possible without the computing resources provided by the U.S. Army Engineer Research and Development Center DoD Supercomputing Resource Center. I'd also like to thank Bob Creasey and Donna Burych for maintaining the computer and data archive systems in the department that I heavily relied upon.

A special thank you to my fellow PhD students (past and present) for their help and support: Sue Chen, Corey Cherrett, Jack Evans, Joel Feldmeier, Paul Homan, Heather Hornick, Bill Ryerson, and Beth Sanabia. I'm also grateful to the professors in the Meteorology Department who allowed me to audit classes, and for the postdoc group discussions, which I've greatly appreciated. I'm especially grateful for the

encouragement and friendship I've received from Bob Creasey, Mary Jordan, Walter Kolczynski, Jared Lee, and Kurt Nielsen.

I'm very grateful for my brothers and my parents, who encouraged and helped me along the way, and for my grandfather, whose keen interest in weather was passed down to me at an early age. Most of all I'd like to thank my family, for their love, support, and sacrifice: my wife Sarah, and children Isabel, Brian, and Simon.

I'd also like to give thanks to God for creating an amazingly complex and beautiful world of which I am fortunate to study.

# **I. INTRODUCTION**

## **A. MOTIVATION**

Much attention has been given to defining the key mechanisms responsible for tropical cyclone formation or tropical cyclogenesis. Although great strides have been made toward increasing our understanding of the process, a lack of consensus remains within the scientific community as to how tropical disturbances develop a near-surface warm-core vortex, and transform into a self-sustaining tropical cyclone. The National Hurricane Center (NHC) defines a tropical cyclone as “a warm-core non-frontal synoptic-scale cyclone, originating over tropical or subtropical waters, with organized deep convection and a closed surface wind circulation about a well-defined center” (NHC 2012).

The western North Pacific basin is one of the most active areas globally for tropical cyclones, as about one third of all tropical cyclones occur there (Gray 1968). However, similar to other ocean basins, only a small fraction of the tropical disturbances go on to develop into tropical cyclones (Gray 1982; Lee 1989a; Simpson et al. 1997; Peng et al. 2012; Fu et al. 2012). Gray (1998) commented that to adequately understand the process of tropical cyclogenesis we must “thoroughly document the physical differences between those systems which develop into tropical cyclones from those prominent tropical disturbances which have a favorable climatological and synoptic environment, look very much like they will develop but still do not.” Despite this statement by Gray (1998) and the broad focus given toward analyzing developing systems, there are relatively few detailed analyses of non-developing tropical disturbances.

During the combined The Observing system Research and Predictability Experiment (THORPEX) Pacific Regional Campaign (T-PARC) and Tropical Cyclone Structure-2008 (TCS-08) field program in the western North Pacific (Elsberry and Harr 2008), approximately 50 tropical cloud clusters were identified in satellite imagery as potential precursors to tropical cyclone formation. Of these, only 12 reached or exceeded

tropical depression (TD) status. TCS025, which was the 25th synoptic circulation monitored by the TCS-08 scientists, was a tropical disturbance considered to be a likely candidate for development as global models consistently forecast intensification (Figure 1; figures and tables are located at the end of each chapter). The system was closely monitored from 24 August until 3 September 2008. Five aircraft missions were conducted over three intensive observing periods (IOPs) to observe TCS025 (see Figure 18): three reconnaissance flights with the United States Air Force (USAF) WC-130J, and two with the Naval Research Laboratory (NRL) P-3. Both aircraft deployed Global Positioning System (GPS) dropwindsondes (Hock and Franklin 1999), and the NRL P-3 was able to observe the three-dimensional cloud and precipitation structure of TCS025 with a tail-mounted dual-Doppler ELectra DOppler RADar (ELDORA) (Hildebrand et al. 1996; Wakimoto et al. 1996). Ultimately the TCS025 disturbance failed to develop, but this allowed for an unprecedented high-quality dataset detailing the evolution of a non-developing tropical disturbance.

Following a summary of previous tropical cyclogenesis studies (next subsection) and a discussion in Chapter II of the data and methodology used for this study, Chapter III will present an analysis of observations that help identify factors associated with the lack of development of the TCS025 disturbance. Numerical simulations from a multi-physics ensemble will be examined in Chapter IV in which a variety of development scenarios result. In Chapter V, data assimilation (DA) experiments are conducted with the special T-PARC/TCS-08 dataset to improve model initial conditions and diagnose the relative importance of differences in vortex structure and precipitation characteristics that exist between the observations and model initial conditions. Chapter VI will summarize the findings from this study, and future work and recommendations will be provided in Chapter VII.

## **B. PREVIOUS TROPICAL CYCLOGENESIS STUDIES**

Average environmental conditions of developing and non-developing tropical disturbances were compared by McBride (1981) and McBride and Zehr (1981) in an attempt to identify key differences. McBride (1981) and McBride and Zehr (1981)

constructed a composite of developing and non-developing tropical systems in the western North Pacific (spanning 10 years) and North Atlantic (spanning 14 years) using rawinsonde data. The most notable differences between the developing and non-developing composites were: (i) larger values of low-level relative vorticity for the developing cases; (ii) areas of nearly zero vertical wind shear centered on developing systems; and (iii) a surrounding vertical wind shear structure that was indicative of an anticyclone aloft.

Expanding on the work of McBride (1981) and McBride and Zehr (1981), Lee (1989a) and Lee (1989b) composited radiosonde data, but in the frame of reference moving with the systems. They discovered that the cloud clusters that went on to develop into tropical cyclones exhibited an increase in low- to mid-level cyclonic circulation during the formation process.

Peng et al. (2012) and Fu et al. (2012) used Navy Operational Global Atmospheric Prediction System (NOGAPS) model output to create composites of developing and non-developing systems in the North Atlantic and western North Pacific basins to identify key environmental differences. In the western North Pacific, Fu et al. (2012) found that dynamical parameters were better at discriminating between developing and non-developing disturbances, whereas Peng et al. (2012) found that thermodynamic factors were more important in the North Atlantic.

Kerns and Chen (2013) objectively tracked 435 developing and 2,311 non-developing cloud clusters over eight years in the western North Pacific. They found the environment generally became more favorable for developing systems, but less so for non-developing systems. However, they found that many developing systems formed within an environment that appeared unfavorable (and vice versa).

In addition to comparing the composite mean large-scale conditions of developing and non-developing disturbances, recent tropical cyclogenesis studies have utilized increasingly detailed datasets to focus on precipitation processes and environmental influences and how they relate to storm formation and early intensification.

## 1. Precipitation Processes

Convective and stratiform precipitation processes are thought to play an important role in the thermodynamic and kinematic evolution during storm formation. Radar echo signatures (Houze 2004) indicate convective precipitation regions are characterized by intense, deep vertical cores, whereas stratiform precipitation is generally uniform in appearance and characterized by light precipitation. Stratiform precipitation regions form either from decaying convective cells or through regions of broad mesoscale ascent (Houze 2004).

### *a. Stratiform Precipitation Processes: Mid-level Vortex Formation and Its Possible Role in Storm Formation*

Mesoscale convective systems (MCSs) form when deep convective cells organize upscale to create large contiguous areas of precipitation (~100 km or more in at least one direction) (Houze 2004). These MCSs exhibit a variety of embedded cloud and precipitation structures, which often includes a large region of stratiform precipitation (Figure 2).

It has been well documented that MCSs are often observed prior to and during tropical storm formation. For example, Ritchie and Holland (1999) found that in 70% of all tropical cyclogenesis cases over a 3-year period in the western North Pacific basin a MCS was present at more than one time in the 72-hour period prior to formation. For 44% of the cases, multiple MCSs existed at a single time.

Mid-level vortices often form within the stratiform precipitation regions of MCSs (Raymond and Jiang 1990; Bartels and Maddox 1991; Houze 2004). Bartels and Maddox (1991) constructed a climatology of mid-level vortices over the United States based on satellite data and suggested that the mid-level vortices form as a result of convergence and vertical vorticity stretching. As stratiform precipitation evaporates below the cloud base in the mid-troposphere, air cools, and a deep layer of subsidence forms. At the same time, condensational warming within the stratiform cloud deck contributes to the formation of a broad region of ascent above the region of subsidence. The vertical profile of latent heating in the stratiform rain region (Figure 3) has low-level

cooling with warming in the mid- and upper-levels. Vertical stretching of the columns associated with ascent aloft and subsidence below leads to a positive mid-level potential vorticity (PV) anomaly (see Figure 6).

Potential vorticity is conserved in the absence of diabatic and frictional processes, and in isentropic coordinates PV is defined as:

$$PV_{\theta} = -g(\zeta + f) \frac{\partial \theta}{\partial p}, \quad (1)$$

where  $g$  is gravitation acceleration,  $f$  is planetary vorticity,  $\zeta$  is the vertical component of relative vorticity, and  $\partial \theta / \partial p$  is the change in potential temperature with pressure, which is analogous to static stability. Because  $PV_{\theta}$  is conserved under adiabatic conditions, Equation 1 defines a relationship between relative vorticity and a form of the static stability for a given latitude. Following Holton (2004), the relative vorticity in Equation 1 can be further expanded using the frictionless relative vorticity tendency equation in isobaric coordinates as:

$$\frac{\partial \zeta}{\partial t} = -\bar{v} \cdot \bar{\nabla}(\zeta + f) - \omega \frac{\partial \zeta}{\partial p} - (\zeta + f) \left( \frac{\partial u}{\partial x} + \frac{\partial v}{\partial y} \right) + \left( \frac{\partial u}{\partial p} \frac{\partial \omega}{\partial y} - \frac{\partial v}{\partial p} \frac{\partial \omega}{\partial x} \right), \quad (2)$$

where  $\partial \zeta / \partial t$  is the time rate of change of the vertical component of relative vorticity,  $p$  is pressure,  $\bar{v}$  is the horizontal wind vector,  $f$  is the planetary vorticity,  $u$  is the zonal wind component,  $v$  is the meridional wind component,  $\omega$  is the vertical velocity in pressure coordinates,  $x$  is eastward distance, and  $y$  is northward distance. In the absence of friction, horizontal advection (term 1 right hand side (RHS)), vertical advection (term 2 RHS), divergence (term 3 RHS), and tilting effects (term 4 RHS) may contribute to change the relative vorticity over time. As a result of the vertical velocity profile that is characteristic of the stratiform precipitation region (ascending motion above areas of descent) in the presence of a positive PV anomaly, mid-level relative vorticity is enhanced through vertical stretching, and a mesoscale convective vortex (MCV) often forms (Figure 4).

A number of studies have examined MCV characteristics as a potential precursor to tropical cyclogenesis (Chen and Frank 1993; Fritsch et al. 1994; Harr et al. 1996b; Ritchie and Holland 1997; Simpson et al. 1997; Bister and Emanuel 1997; Rogers and Fritsch 2001; Houze 2004). However, the exact role that MCVs (which often accompany MCSs) have in the process of tropical cyclogenesis remains elusive due to a lack of observations on the necessary temporal and spatial scales. Harr et al. (1996a) hypothesized that the vorticity contribution from MCSs was a vital component in the transformation of a large monsoon depression into a tropical storm during the Tropical Cyclone Motion (TCM-93) mini-field experiment. For the near-surface circulation to form, Harr et al. (1996a) suggested that mid-level vorticity would need to have been transported downward to the surface. However, they state that observations available for their study failed to reveal such a process.

It has been noted that simply because MCVs are often observed during the tropical cyclogenesis process, their presence alone is not evidence that they play a vital role (Tory et al. 2006a). The existence of a MCV in thermal wind balance necessitates from geostrophic considerations a low-level cold thermal structure that is characteristic of a stratiform precipitation region (Figure 3). In combination with downward motion in the stratiform rain region, net divergence is present in the lower troposphere, whereas the level of maximum convergence resides in the mid-troposphere. The resultant vertical divergence profile dominated by divergence in the lower troposphere is argued by Tory et al. (2006a) to be counter-productive to tropical storm spin-up by reducing low-level relative vorticity (term 3 RHS of Equation 2). In contrast, the vertical divergence profile of convective clouds is considered by Tory et al. (2006a) to be favorable for tropical cyclone formation.

Several theories have been proposed to address the change in vertical divergence and thermal characteristics that must be realized for a MCV to transition into a near-surface vortex with warm-core characteristics. In their observation and modeling study of the formation of Hurricane Guillermo (1991), Bister and Emanuel (1997) stated (but did not show) that the cyclonic circulation of a MCV could be identified as low as 300 m above the surface in the stratiform precipitation region of a MCS. Shortly thereafter, a surface-based warm core was observed in the midst of the larger-scale cold core associated with the elevated MCV.



Bister and Emanuel (1997) hypothesized (Figure 5) that the saturation of the lower and mid-troposphere beneath a MCV through precipitation would reduce the strength of subsequent downdrafts. It is thought that if downdrafts are strong enough, they can disrupt the organization of low-level convergence (Raymond et al. 2007) and import mid-level low equivalent potential temperature ( $\theta_e$ ) air into the boundary layer (Bister and Emanuel 1997) that would inhibit spin-up of the cyclone. Since relative humidity values tend to be higher in a cold-core system for a given amount of moisture, Bister and Emanuel (1997) argued that evaporative downdrafts would be less fatal to an incipient disturbance than if present within a warm-core system.

Bister and Emanuel (1997) outlined a three-step process by which tropical cyclogenesis might occur in the presence of a MCS (Figure 5). They speculated that for warm-core development to occur, relative flow through the system must remain weak and stratiform rain must persist long enough to drive the mid-level vortex down to the boundary layer through evaporative cooling. As evaporation takes place below the stratiform rain region, air cools and moistens, and over time the level of maximum evaporation extends closer to the surface. The increased static stability contributes to a positive PV anomaly. Bister and Emanuel (1997) argued that the recovery of boundary layer  $\theta_e$  would allow subsequent convection to develop. Furthermore, the penetration of the cold-core circulation into the boundary layer would enhance surface fluxes, while the remnant cold-core aloft would act to further destabilize the vertical temperature profile to promote deep convection and an increase in near-surface vorticity through convergence.

Raymond and Jiang (1990) examined the role of vertical wind shear in the presence of a MCV as being favorable for the redevelopment of deep convection. Under favorable shear, the near-surface negative temperature anomaly (i.e., cold pool) beneath a MCV contributes to isentropic lift of low-level, high- $\theta_e$  air (Figure 6). This lifting contributes to the formation or re-development of deep convection in close proximity to the MCV. In addition, the low-level vertical wind shear profile in conjunction with the near-surface cold pool could serve as a source of horizontal vorticity that could later be tilted into the vertical plane (term 4 RHS of Equation 2) through convective updrafts (Figure 6 and Figure 7).

Ritchie and Holland (1997) hypothesized that the development of Typhoon Irving (1992) was related to the merger of multiple MCVs that allowed for the increase of near-surface relative vorticity. Ritchie and Holland (1997) stated that if the horizontal extent of the MCV is increased through vortex merger, or if the background cyclonic vorticity increases, the penetration depth of the positive PV anomaly will also increase, and this larger penetration depth of the circulation could eventually lead to the existence of a near-surface vortex. The penetration depth of a PV anomaly is defined as:

$$H = fL/N , \quad (3)$$

where  $H$  is the penetration depth,  $f$  is the planetary vorticity,  $L$  is the horizontal length scale of the anomaly, and  $N^2$  is the static stability, which can be expanded as:

$$N^2 = \frac{g}{\theta} \frac{\partial \theta}{\partial z} . \quad (4)$$

At constant latitude ( $f$  remains unchanged), an increase in the penetration depth can be achieved through a reduction of  $N$  or by increasing the horizontal scale of the anomaly. Simpson et al. (1997) also noted that a reduction in the local deformation radius would allow for more efficient vortex mergers. The deformation radius is the spatial scale over which geostrophic adjustment occurs (Webster 1972; Holland 1987), and can be written as:

$$L_d = NH/I , \quad (5)$$

where  $N$  is the Brunt-Väisälä frequency,  $I^2$  is the inertial stability (see Equation 6), and  $H$  is the scale height. Simpson et al. (1998) suggested that if the deformation radius is lowered from the ambient tropical value of  $\sim 3000$  km to 200-300 km (closer to the horizontal scale of the disturbance), mid-level vortices would be closer to being in geostrophic balance. Simpson et al. (1998) hypothesized that a balanced vortex would be able to persist longer as less energy would be dispersed during geostrophic adjustment. In regions that can be considered neutral to moist processes, the local deformation radius reduces close to zero, and vortices, if they exist, are able to persist and potentially interact with other vortices that might be present. Simpson et al. (1997) hypothesized that under

these conditions and in the presence of a favorable horizontal shear profile, which is characteristic of a monsoon trough environment, the cycle of convection, MCV development, and vortex merger could continue until the vertical extent of the circulation reaches the surface. In their study of the formation of Tropical Cyclone Oliver (1993), Simpson et al. (1997) analyzed two separate vortices that interacted such that one formed the eye of Oliver, while the other was horizontally sheared into the developing circulation to form a major rainband.

The presence of a mid-level vortex would also allow for a more efficient development of a warm core by increasing the inertial stability in the mid-troposphere (Schubert and Hack 1982). Following Holland (1987), inertial stability can be written as:

$$I^2 = (\zeta + f)(f + 2v/r), \quad (6)$$

where  $r$  is radial distance from the center of curvature and  $v$  is the tangential velocity. As inertial stability is increased through either an increase in the magnitude of the cyclonic wind field ( $\zeta$  and  $v$ ) or a reduction in the radius of maximum winds (RMW), there is increased resistance to radial displacements within the flow. This helps to increase the efficiency by which local warming occurs through diabatic heating as  $I^2$  becomes larger and  $L_d$  decreases (Figure 8). Therefore, the potential energy generated by latent heat release is not easily dispersed by gravity waves (Chen and Frank 1993; Schubert and Hack 1982), which allows for a more rapid development of an inner warm core.

#### ***b. Convective Processes: Deep Vortical Convection***

The high-resolution modeling studies by Hendricks et al. (2004) and Montgomery et al. (2006) labeled plumes of deep convection that possess high values of cyclonic vorticity as “vortical hot towers” (VHTs) (see Figure 2). Furthermore, they argued that the VHTs are the essential building blocks for tropical cyclone formation. In their numerical modeling study of Hurricane Diana (1984), Hendricks et al. (2004) hypothesized that increased vorticity within individual VHTs trapped the latent heat released in moist convection, and reduced lateral entrainment, which led to a net increase

in the efficiency of convection. They suggested a two-stage development of tropical cyclogenesis in which deep convection first pre-conditions the atmosphere by the diabatic production of lower-tropospheric positive PV anomalies, then this is followed by the concentration and axisymmetrization of low-level PV that is enhanced through vortex mergers. Hendricks et al. (2004) argued that the combined effects of the diabatic heating associated with multiple VHTs is to produce a net influx of angular momentum, which aids cyclogenesis and allows for the upscale cascade of vertical vorticity from the VHT scale to the tropical cyclone scale. Following Raymond et al. (1998), Hendricks et al. (2004) noted that for vortex spin-up to occur, the low-level convergence of absolute angular momentum must overcome the spin-down due to surface friction. Their modeling study contained VHTs with strong updrafts in their cores that acted to “converge and stretch ambient low-level vorticity into intense small-scale vortex tubes.” Hendricks et al. (2004) stated that in their simulations, warm core development did not occur as a result of subsidence warming, but rather from the aggregate effect of diabatic heating from multiple VHTs and their subsequent merger.

Montgomery et al. (2006) suggested that even though VHT-induced downdrafts bring low- $\theta_e$  air down near the surface, continued formation and dissipation of VHTs tends to pre-condition the atmosphere by increasing mid-level moisture and cyclonic vorticity in the lower troposphere. As convection subsides and individual VHTs dissipate, they leave behind low-level cyclonic relative vorticity, which allows the near-surface mesoscale circulation to continue to intensify through several convective cycles. In their idealized numerical simulations, Montgomery et al. (2006) determined that VHT development and subsequent near-surface spin-up was dependent on the presence of a MCV in the initial conditions. However, they concluded that the MCV serves the tropical cyclogenesis process primarily by providing a favorable environment characterized by increased horizontal and vertical vorticity. During the formation of updrafts early in the simulation, vertical vorticity is generated from the tilting of horizontal vorticity into the vertical plane (term 4 RHS of Equation 2, Figure 9). As the updrafts continued to evolve and strengthen, the stretching of cyclonic vorticity became the dominant mechanism (terms 2 and 3 RHS of Equation 2). In addition, Montgomery et al. (2006) found that the

developing secondary circulation acted to concentrate cyclonic vorticity associated with the initial MCV and the vorticity generated by VHTs on the convective scale.

Using the Tropical Cyclone Limited Area Prediction System (TC-LAPS) numerical model, Tory et al. (2006b, 2007) simulated a central low-level core of increased PV that formed from the merger of diabatically-produced lower-tropospheric PV anomalies generated in convective updrafts. Tory et al. (2006a) suggested that although mid-level stratiform processes that lead to MCV formation can increase mid-tropospheric cyclonic vorticity and create favorable conditions for continued convection, tropical cyclogenesis will not proceed without vortex intensification in a convective low- to mid-level convergence region. Tory et al. (2006a) argued that lower tropospheric vortex enhancement occurs primarily through the convergence and stretching in vigorous convective updrafts that originate in the lower troposphere.

In the idealized tropical cyclogenesis modeling study by Nolan (2007), a weak warm-core, near-surface vortex was initialized in the presence of a MCV. The simulated path to genesis was marked by an initial rise in mid-level relative humidity near the core (above 80%) followed by the formation and contraction of a mid-level vortex. Although the simulation developed a mid-level vortex en route to genesis, the penetration of mid-level cyclonic vorticity down to the surface was not observed prior to genesis. Nolan (2007) stated that genesis was triggered by a strong, prolonged updraft near the center of the mid-level vortex and hypothesized that the increased mid-level relative humidity that occurred during the formation of the mid-level vortex prior to genesis helped to pre-condition the atmosphere in a similar manner as proposed by Montgomery et al. (2006). This pre-conditioning provided for stronger updrafts, increased upper-level heating, and an intensified secondary circulation.

*c. Cooperative Stratiform and Convective Processes: VHT Development in the Presence of a MCV*

In their airborne Doppler radar analysis of the formation of Hurricane Dolly, Reasor et al. (2005) identified multiple low-level and mid-level cyclonic circulations during the formation of the storm. Although the radar analysis did not

provide conclusive evidence as to the role that the mid-level vortices played in the development of Hurricane Dolly, Reasor et al. (2005) stated that VHTs seemed to readily develop in the presence of mid-level vortices. They concluded that the formation of Hurricane Dolly followed a stochastic pathway through the interaction of low-level circulations that formed as a result of deep convection occurring in an environment rich in cyclonic relative vorticity.

More recently, a number of studies have suggested the importance of low-level convective processes acting in conjunction with a MCV. Raymond et al. (2011) noted that treating a MCV as a source of vertical vorticity that could be transported down to the surface is dynamically incorrect as there cannot be a direct transport of vertical vorticity from mid-troposphere to the low levels. Raymond et al. (2011) contended that any spin-up of a near-surface vortex must occur through the horizontal flux convergence of vertical vorticity in the lower troposphere. Therefore, focus has been given as to how a MCV might be beneficial in promoting low-level vorticity convergence.

Raymond and Carrillo (2011) analyzed the spin up of Typhoon Nuri (2008) using a three-dimensional variational analysis (3DVAR) technique that employed dual-Doppler radar and dropwindsonde observations. Raymond and Carrillo (2011) noted that as Typhoon (TY) Nuri intensified, regions where stretching of the vorticity was occurring became fewer and more intense. Furthermore, the level of maximum vertical mass flux lowered from 10 km while a tropical wave to 5 km as a tropical depression. They suggested the lowering of the level of maximum vertical mass flux is significant since vortex spin-up dominated by vorticity flux convergence (term 3 RHS of Equation 2) will be greatest at the level where the product of vorticity and convergence is maximized (Figure 10). They noted that the greatest horizontal mass convergence will occur where the vertical mass flux increases most rapidly with height.

Based on the tropical experiment in Mexico (TEXMEX) field campaign, Raymond et al. (1998) noted that the circulation was strongest in the mid-troposphere (near 5 km) for developing disturbances. It was also observed that the development of a warm core occurred following the formation of a larger cold core in the lower- or mid-troposphere. Raymond and Sessions (2007) and Raymond et al. (2011) suggested that the

thermodynamic structure resulting from a strong mid-level circulation, with a warm temperature anomaly above a cold anomaly in the lower troposphere, would act to increase rainfall and lower the level of maximum vertical mass flux (Figure 10). They argued that this in turn necessitates an increase in convergence of mass and vorticity in the lower troposphere while suppressing the lateral detrainment of moist entropy, which allows moisture to increase in the atmospheric column.

Raymond et al. (2011) also argued that a cold core resulting from a mid-level balanced vortex would persist longer and have a greater horizontal extent than one resulting solely from evaporative cooling. The longer time scales make the formation of an embedded warm core more likely, and following Equation 3, a considerably large horizontal spatial scale might allow the penetration depth to reach the surface.

However, Park and Elsberry (2013) and Park et al. (2013) found that considering only stratiform and convective processes of mesoscale convective systems (see Figure 3) in the Tropical Rainfall Measuring Mission Precipitation Radar (TRMM PR) and in two mesoscale models is too simplistic. An assumption that the convective precipitation is vertical in the TRMM retrievals, and representing the deep convection in the numerical models as being too vertical, leads to inaccurate latent heating and evaporative cooling profiles in tropical MCSs. The contributions from tilted convective updrafts that lead to coupled saturated convective-scale downdrafts are omitted. Park and Elsberry (2013) argue that the impacts of these processes on the diabatic heating profile also need to be considered. In their study examining ELDORA Doppler radar data collected during TCS-08, Park and Elsberry (2013) and Park et al. (2013) found that two non-developing tropical disturbances exhibited relatively uniform latent heating and cooling rates through a deep layer, which implies a mixture of stratiform and convective rain areas and their respective latent heating profiles. Park and Elsberry (2013) focused on the less-frequently occurring, but intense convective regions as being most important for TC formation. They found that the maximum heating rates are larger than the maximum cooling rates in the developing cases examined, and note that a shift in the heating maximum to the lower troposphere was more favorable for inducing low-level convergence and spin-up of a cyclone.

*d. Subsidence-induced Warm-core Development*

Dolling and Barnes (2012a) stated that the prevailing convective- and stratiform-based hypotheses for tropical cyclone formation rely on claims that do not appear to be supported by observations. They suggested that little evidence exists for a cool, saturated layer marked by heavy stratiform precipitation beneath the MCV, which is argued to be important for the “top-down” route to storm formation dominated by stratiform processes. Instead, they suggested that a dry, warm layer is often observed beneath the MCV, as was the case for Hurricane Humberto (2001). Dolling and Barnes (2012a) state that numerical simulations suggesting a convectively-driven “bottom-up” pathway exhibit updraft velocities within VHTs that are stronger than observations suggest actually occur, and the subsequent merger of VHT-generated vorticity anomalies has not yet been verified by observations.

Dolling and Barnes (2012a) suggested that stratiform precipitation under a MCV leads to subsiding air that might act to suppress convection and allow for the buildup of high- $\theta_e$  air near the surface via sensible and latent heat fluxes. They claimed that deep convection will eventually break out along the periphery of the subsidence region when the convective available potential energy (CAPE) values reach a critical level. In the case of Hurricane Humberto (2001), an arc of deep convection formed along the periphery of the subsidence region and later became the eyewall (Figure 11). Dolling and Barnes (2012b) suggested that having convection form away from the low-level circulation center avoids the potential issue of deep convection forming near the circulation center only to be later replaced by unsaturated warm air that is characteristic of a tropical cyclone eye.

During the formation of Humberto, Dolling and Barnes (2012b) suggested that the anvil cloud was advected overtop of the low-level circulation center by a MCV located to the north (Figure 11). Flight-level data identified an area of mesoscale subsidence over the low-level circulation center that is thought to have warmed the low-levels. They noted that the maximum temperature anomaly (+7 K) was located at 2 km above the low-level circulation center, and only slight warming (+1 K) was identified in the upper levels. Dolling and Barnes (2012b) argued that the warm, dry layer extending



from the surface to 5 km could account for 90% of the surface pressure deficit through hydrostatic considerations. Since the greatest warming occurred in the lower troposphere instead of the upper levels (Figure 12), Dolling and Barnes (2012b) suggested that at this stage in the evolution of Tropical Storm (TS) Humberto, subsidence was the dominant process responsible for pressure falls.

Dolling and Barnes (2012b) also pointed out that since the region of highest  $\theta_e$  was not co-located with the area of strongest winds, TS Humberto had not yet entered the Wind Induced Surface Heat Exchange (WISHE) phase of tropical cyclone formation, which is a proposed tropical cyclone intensification mechanism (Emanuel 1986; Rotunno and Emanuel 1987) that relies on the positive feedback between an increase in surface heat fluxes (latent and sensible) and an increase in the strength of the low-level circulation. Dolling and Barnes (2012b) hypothesized that for tropical cyclogenesis to occur via the subsidence pathway, precipitation beneath the anvil must remain light, as a moist adiabatic profile would reduce the amount of warming that could occur. They also speculated that subsidence and stratiform rain should persist for many hours, and suggested that convection needs to remain in close proximity to the stratiform rain/subsidence area.

## **2. Environmental Influences**

Tropical cyclogenesis is known to be a cooperative multi-scale process (Sippel et al. 2006, Figure 2), and thus the characteristics of the background flow also need to be considered. Often, the background environmental factors are hostile to a disturbance. Vertical wind shear and the entrainment of dry air can prohibit formation and limit storm intensity. It is therefore imperative to understand how the surrounding environment might impact an incipient disturbance, and examine mechanisms by which it could remain protected from the otherwise negative influences.

### ***a. Vertical Wind Shear***

Although the interaction of vertical wind shear and mature tropical cyclones has been studied extensively, relatively little attention has been given to

examining the effects that vertical wind shear has during storm formation. As previously indicated, McBride and Zehr (1981) noted that cyclogenesis occurred under an area of minimum vertical wind shear and found that the vertical wind shear pattern surrounding the disturbance was characteristic of an upper-level anticyclone above a low-level cyclonic circulation.

Nolan and McGauley (2011) have recently suggested that the vast majority of tropical cyclogenesis events occur in the presence of vertical wind shear and noted that the strength of vertical wind shear often is the most important factor when forecasting whether storm formation will occur. They examined the climatological relationship between vertical wind shear and storm formation, and after normalizing for typical shear conditions, found that shear between  $1.25 - 5 \text{ m s}^{-1}$  was most favorable, although shear less than this was not unfavorable. Nolan and McGauley (2011) pointed out that regions with climatologically low values of mean vertical wind shear are most favorable for storm formation because vertical wind shear in these areas is often less than the mean value during storm formation.

To address whether some vertical wind shear might be favorable for tropical cyclogenesis, Nolan and McGauley (2011) conducted numerical simulations and found that surface pressure falls occurred more rapidly in cases where vertical shear was present. Simulations with shear magnitudes of  $5\text{-}7 \text{ m s}^{-1}$  achieved genesis earlier than in cases with weaker shear. Nolan and McGauley (2011) hypothesized that without some vertical wind shear, convection remains scattered and less organized. Consequently, updrafts are more susceptible to entrainment of mid-level dry air, and evaporative cooling between updrafts can be detrimental such that convection is less effective in producing net diabatic heating necessary for significant pressure falls.

Riemer et al. (2010) conducted a modeling study and found that vertical wind shear could negatively impact mature storm energetics through the downward transport of low- $\theta_e$  air via downdrafts (termed “anti-fuel”) into the boundary layer outside the eyewall. If this boundary layer  $\theta_e$  is not able to recover before reaching the eyewall convection, this may limit the energy available to a storm. Riemer et al. (2010)

argued that the shear-induced boundary layer response is more important for modulating storm intensity than vertical wind shear effects realized in the mid- and upper-troposphere (Figure 13).

Based on the environmental vertical wind shear, surface and mid-level entropy deficit, and the theoretical potential intensity of a system, Tang and Emanuel (2012) developed a ventilation index to quantify the negative effect that the flux of cooler, drier air via vertical wind shear could have on tropical cyclone intensity. In agreement with Riemer et al. (2010), Tang and Emanuel (2012) argue that ventilation allows low-entropy air to penetrate into the high-entropy reservoir of the inner core of a tropical cyclone, which can partially neutralize the positive energy supplied by surface fluxes and limit the potential energy available to the tropical cyclone.

In their analysis of episodic down-shear convection associated with TS Edouard (2002), Molinari et al. (2012) hypothesized that the repeated outbreaks and lulls in convection were the result of downdrafts of low- $\theta_e$  air during deep convection resulting from ventilation caused by vertical wind shear. As deep convection subsided, so did the downdrafts of low- $\theta_e$  air, and this allowed boundary layer  $\theta_e$  to recover via surface fluxes before the next episode of deep convection. Molinari et al. (2012) concluded that because low- $\theta_e$  air in the boundary layer was coincident with deep convection, it originated from downdrafts rather than from the outer radii of the storm. Molinari et al. (2012) found that the low- $\theta_e$  air associated with the convective downdrafts occurred only below 700 m, and suggested this might explain why cold pools are difficult to observe in tropical cyclones.

Recently, the orientation of vertical wind shear in relation to the mean surface wind has received some attention. Rappin and Nolan (2012) used numerical simulations initialized with varying surface wind and vertical shear combinations to examine how an incipient vortex would develop under different vertical wind shear regimes. They found the configuration most favorable for storm formation to be when the direction of the mean surface wind opposed the environmental shear vector. Rappin and Nolan (2012) showed that although the vertical motion field is more symmetric in this

configuration due to offsetting convective asymmetries caused by vertical wind shear and storm translation (Shapiro 1983), they attributed the favorability of this configuration to enhanced surface fluxes left of the shear vector caused by the superposition of the mean and vortex flow. Right of the shear vector, surface fluxes are reduced due to weaker surface flow, and the trajectory through the subsidence branch of the vertical circulation causes the air circulating down-shear to be relatively dry. This air is moistened as it enters the down-shear flank where upward motion and moist convection are favored due to the wavenumber-one asymmetry in vertical motion that results from the vortex being in sheared flow. As the air leaves the down-shear region and enters the up-shear flank (left of shear vector), enhanced surface fluxes act to moisten the boundary layer, which permits the cyclonic propagation of convection around the core. Rappin and Nolan (2012) noted that when the shear vector and mean surface wind are aligned, the driest boundary layer air is located cyclonically down-wind from the shear-induced convection, and this prevents convection from building up-shear where forced subsidence is acting to limit convection.

Rappin and Nolan (2012) also suggested that without up-shear propagation of deep convection, vortex tilt becomes large and coupling between the mid- and lower-tropospheric circulation is weakened. They noted that the “showerhead” mechanism (after Bister and Emanuel 1997) acts to moisten the up-shear circulation prior to the onset of deep convection by advecting frozen condensate originating from down-shear convection in the up-shear direction. The frozen condensate melts and evaporates as it falls, which tends to increase low-level moisture.

Nguyen and Molinari (2012) examined the rapid intensification of Hurricane Irene (1997) despite its presence in strong vertical wind shear. They hypothesized that the rapid storm translation speed ( $18 \text{ m s}^{-1}$ ) to the northeast coupled with strong southwesterly vertical wind shear ( $10 - 13 \text{ m s}^{-1}$ ) contributed to the rapid intensification of Irene (Figure 14). Nguyen and Molinari (2012) noted that convection tended to form in the down-shear direction instead of down-shear-left as previous studies suggested. In a numerical modeling study examining the role of tropical cyclone translation on storm asymmetry, Shapiro (1983) found that upward vertical motion was

avored slightly to the right of the direction of motion. Asymmetric frictional effects caused by stronger boundary layer winds on the right side of the storm (superposition of translation speed and tangential wind) were the primary factors for the asymmetric distribution of vertical motion. Nguyen and Molinari (2012) speculated that the rapid forward speed of Irene increased the impact of translation and induced asymmetries that were also in the down-shear direction (Figure 14). The combined effects then contributed to rapid intensification. They hypothesized that the location of Irene over the Gulf Stream allowed large enthalpy fluxes to offset detrimental effects that downdrafts might have had on such a highly asymmetric system. Nguyen and Molinari (2012) pointed out that the formation of deep convection inside the RMW close to the circulation center was crucial for intensification but also stated that it was unclear why convection formed so close to the center under the influence of strong shear. Nguyen and Molinari (2012) speculated that the symmetry of diabatic heating was not important in this case as Irene responded more to the azimuthal average of diabatic heating, which allowed the storm to intensify despite the highly asymmetric convective structure.

In their analysis of TY Nuri, Raymond and Carrillo (2011) found that overlapping closed circulations (in the storm reference frame) existed in the boundary layer and at 5 km elevation to provide a deep region protected from hostile environmental influences (Figure 15). They argued that vortex tilt in the down-shear-left direction occurs such that the induced vorticity of the parent circulation would act to oppose system-relative flow at that level caused by vertical wind shear (Figure 15). Raymond and Carrillo (2011) also examined a non-developing tropical disturbance (TCS030) that experienced vertical wind shear of similar magnitude as the pre-Nuri disturbance to conclude that non-development resulted from a lack of overlapping closed circulations.

#### ***b. Protective Environment of the Pouch***

Dunkerton et al. (2009) developed the “marsupial pouch” paradigm to describe how synoptic-scale easterly waves could serve as a protective environment and transition to tropical depressions. Dunkerton et al. (2009) defined the critical latitude for easterly waves that are equatorward of the easterly jet axis to be the latitude at which the

mean flow and wave phase speed are equal. This critical latitude is where wave breaking and roll-up of cyclonic vorticity occurs, and is argued to be a favorable environment for the aggregation of vorticity anomalies created by VHTs (Figure 16). In addition, the quasi-closed Lagrangian circulation region allows air to be continually moistened by convection while being protected from intrusions of surrounding dry air. Dunkerton et al. (2009) suggested that upscale feedback might also occur in which the parent wave circulation is maintained and even strengthened through diabatic processes within the recirculation region. They proposed that the intersection of the critical latitude and easterly wave trough axis coincides with a preferred region for tropical cyclogenesis that they called the “sweet spot” (Figure 16).

In their analysis of the formation of Typhoon Nuri (2008), Montgomery et al. (2010) suggested that despite the detrimental influences of strong vertical wind shear and dry air, the presence of an easterly wave critical layer protected the incipient vortex until it could reach a more favorable environment. The critical latitude and a closed circulation were identified in the co-moving frame (moving with the parent wave) (Figure 17). Montgomery et al. (2010) concluded that the inhibiting factor early in the evolution of TY Nuri was the presence of low ocean heat content (OHC), which acted to stabilize the lower troposphere and limit the intensity of deep convection. They further hypothesized that an increase in the vertical extent of the wave pouch is a favorable condition for storm formation and appears to have occurred prior to the formation of TY Nuri.

In their comparison of the convective environments (i.e., pouch) of developing and non-developing tropical disturbances observed during the PRE-Depression Investigation of Cloud systems in the Tropics (PREDICT) field campaign, Smith and Montgomery (2012) observed a tendency for the lower troposphere to moisten with time in both the developing and non-developing systems. However, the mid- and upper-troposphere became progressively drier for the non-developing system. They found that the  $\theta_e$  deficit between the surface and the level of minimum  $\theta_e$  was considerably different for the non-developing system compared to those that proceeded to develop, as  $\theta_e$  differences of only 15 K were observed for the developing systems compared to 25 K

for the non-developing system. Instead of focusing on the effect that dry air might have on supporting stronger downdrafts, Smith and Montgomery (2012) suggested that mid-level dry air observed in the non-developing systems might act to dilute updraft intensity and limit the amplification (via stretching) of lower-tropospheric vorticity (Bell and Montgomery 2010). Smith and Montgomery (2012) pointed to a lack of evidence of lower-tropospheric cooling and drying, which would be expected if downdrafts were being enhanced as a result of dry air. Instead, their composites showed progressive moistening and slight warming in the lower troposphere of both developing and non-developing disturbances. Unlike the analysis of the same dataset by Raymond et al. (2011), Smith and Montgomery (2012) did not find any evidence of cooling throughout the lower-troposphere of the pouch. They suggested that the hypotheses of Bister and Emanuel (1997), Raymond and Sessions (2007), Raymond and Carrillo (2011), and Raymond et al. (2011) are thus incomplete, as each paradigm requires cooling in the lower troposphere. However, it is unclear what effect sampling and analysis method had on the different conclusions purported by Raymond et al. (2011) and Smith and Montgomery (2012).

Davis and Ahijevych (2012) conducted a dropwindsonde analysis of several cases observed during PREDICT and concluded that the combination of dry air and vortex misalignment were important inhibiting factors in the non-developing case. They suggested the vertical misalignment of the vortex would lead to stronger relative flow (relative to the vortex), making the incipient disturbance more susceptible to dry air that might exist in the surrounding environment. Davis and Ahijevych (2012) suggested the deep convection could lead to vortex realignment by initiating new lower-tropospheric circulations below the mid-tropospheric circulation. They pointed out that convection tended to pulsate over a quasi-diurnal time scale, and suggested that a consistent convective structure that persists over several convective cycles might help overcome weakening caused by shear and friction and allow genesis to occur more rapidly.

On one hand, the findings of Davis and Ahijevych (2012) support those of Smith and Montgomery (2012) in that the developing systems showed an increase in

mid-tropospheric moist static energy over time, while the non-developing system exhibited a decrease in moist static energy and an increase in downdraft convective available potential energy (DCAPE). However, Davis and Ahijevych (2012) concluded that the mid-tropospheric circulation in two developing systems strengthened and lower-tropospheric cooling occurred prior to storm formation. They suggested differences from the findings of Smith and Montgomery (2012) could be due to the inclusion of dropwindsondes outside of the central convective region in the average computed by Smith and Montgomery (2012), which would act to dilute a lower-tropospheric cooling signal if present.

### **C. OBJECTIVES AND HYPOTHESES**

The foregoing literature review of recent tropical cyclogenesis theories highlights differences in the perceived role that precipitation processes and environmental influences have in storm formation. The goals of this study are to examine the relative importance of vortex alignment and precipitation processes during tropical cyclogenesis. In particular, three hypotheses are analyzed with respect to the non-development of the tropical disturbance TCS025 observed during TCS-08. Observations will be carefully examined and compared to high-resolution numerical simulations to help identify factors that impacted the non-development of the TCS025 disturbance.

In this analysis, GPS dropwindsondes (Hock and Franklin 1999), aircraft flight-level and Stepped Frequency Microwave Radiometer (SFMR) (Uhlhorn et al. 2007) observations, airborne ELDORA radar observations (Hildebrand et al. 1996), geostationary Multifunctional Transport Satellite (MTSAT) infrared (IR) brightness temperature, and gridded model analyses and forecasts will be used. Observational datasets will initially be examined individually. Subsequently, analyses will be constructed utilizing the Spline Analysis at Mesoscale Utilizing Radar and Aircraft Instrumentation (SAMURAI) analysis package (Bell et al. 2012) to create a single set of analyzed fields that span each aircraft surveillance mission.

High-resolution simulations will be conducted using the Advanced Weather Research and Forecasting (WRF-ARW) (hereafter WRF) numerical model with and



without data assimilation. Differences in circulation structure and convective intensity will be compared with observations to help elucidate the sensitivity of tropical cyclone development to vortex alignment and precipitation processes.

## **1. Hypothesis #1**

*The tropical disturbance TCS025 failed to develop in part due to poor vertical alignment of the vortex structure that increased system-relative flow and prevented enhancement and organization of deep convection.*

Based on an observational analysis, it will be shown that TCS025 was under the presence of northerly vertical wind shear and possessed a circulation structure that was poorly aligned in the vertical. System-relative flow was larger due to the vertical misalignment of the circulation, and this, combined with persistent northerly vertical wind shear, allowed mid-level low- $\theta_e$  air to penetrate into the inner-core region of TCS025, which weakened convection and hindered further development.

An implication of this hypothesis is that the convective environment of tropical disturbances contributes to the generation of mesoscale features that can maintain vertical alignment, and environmental factors (i.e., vertical wind shear, mid-level moisture, inflow source region) can impact the character and evolution of the convectively-driven circulation in the vertical. Vertical alignment of the initial, pre-tropical cyclone vortex structure is critical for a tropical disturbance to develop into a self-sustaining tropical cyclone. It is argued that a vertically coherent vortex structure minimizes system-relative flow and protects the warm, moist inner core, and allows for a more efficient system-scale response to diabatic heating (Vigh and Schubert 2009). In cases of poor vertical alignment, the magnitude of system-relative flow is larger, and combined with vertical wind shear in the presence of mid-level low- $\theta_e$  air can cause dry air entrainment into the mid-level circulation of an incipient disturbance. This can weaken convection and slow or inhibit further development.

A similar method to that described by Davis and Ahejivech (2012), which is based on dropwindsonde data, will be used to objectively identify the circulation center as a function of height for each aircraft mission. Circulation center positions based on

SAMURAI analyses will also be determined in an attempt to define the mesoscale vortex structure based on ELDORA radar observations. Factors to be examined include whether multiple circulation centers existed in the vertical, whether there was vortex tilt, and whether the strength of the circulation varied as a function of height. Vortex alignment will be analyzed with regards to the environmental and self-induced vertical wind shear following the method of Davis et al. (2008b). Furthermore, the effects of vortex alignment and shear on the thermodynamic and convective structure will be examined in light of recent studies of vertical wind shear (Riemer et al. 2010; Nolan and McGauley 2011; Rappin and Nolan 2012).

## **2. Hypothesis #2**

*High-resolution simulations consistently overdevelop the TCS025 disturbance due to overly intense convective precipitation processes.*

Although the operational European Center for Medium-range Weather Forecasts (ECMWF) Year of Tropical Convection (YOTC) global forecasts and analysis correctly represent the non-development of TCS025, high-resolution WRF simulations that used the ECMWF analysis as initial and boundary conditions (no data assimilation) unrealistically intensified the TCS025 disturbance.

In both the ECMWF forecasts and WRF simulations, the circulation structure of TCS025 was better aligned vertically than observations suggest. However, some down-shear (southward) tilt with height was still present. It is hypothesized that overly intense convective precipitation processes in the high-resolution WRF simulations allowed TCS025 to develop despite the poor vertical alignment of the vortex structure. In contrast, convection in the ECMWF global forecasts and analysis was relatively weak and intermittent, which was consistent with IR brightness temperature and ELDORA reflectivity observations. The ECMWF solution was dominated by a mid-level vortex and its associated stratiform precipitation processes, which were unfavorable for development.

Since deep convection is considered to be a necessary and vital component for tropical cyclogenesis (Montgomery et al. 2006; Raymond et al. 2011), an examination of

the nature of the convective events in the observations and numerical simulations is critical to understanding the non-development of TCS025. Davis and Ahijevich (2012) state that vortex re-alignment might occur via the formation of a new low-level circulation below a mid-level circulation via deep convection. In this study, the ECMWF forecasts and the multi-physics WRF ensemble will be examined to assess the relative roles of vertical alignment, stratiform processes, and convective processes. The examination will be based on a diagnosis of tendencies related to precipitation processes through the use of a vorticity budget of the TCS025 circulation.

### **3. Hypothesis #3**

*High-resolution simulations that assimilate ELDORA radar observations will result in a more accurate vortex structure in the vertical. The relative roles of precipitation processes will be dependent upon the vertical structure of the vortex.*

It is hypothesized that a more realistic vortex structure that reflects the vertical variation of TCS025, which is attained through the assimilation of high-resolution Doppler winds, will inhibit or slow development of the disturbance to a tropical cyclone. Whether development does or does not occur will depend on the dominant precipitation process. If the vertical misalignment is too severe such that convective processes are not able to re-align the vortex in the vertical as suggested by Davis and Ahijevich (2012), then stratiform processes will dominate and development will not occur or will be delayed.

An ensemble of simulations employing data assimilation will be conducted using the Data Assimilation Research Testbed (DART) software package (Anderson et al. 2009) in conjunction with the WRF model (DART-WRF). Simulations will be configured to match the configurations of previous simulations in which no data assimilation was used. Vortex structure and the convective response will be analyzed and compared with observations and control simulations to help identify key processes responsible for the over-development of TCS025 in the high-resolution simulations.

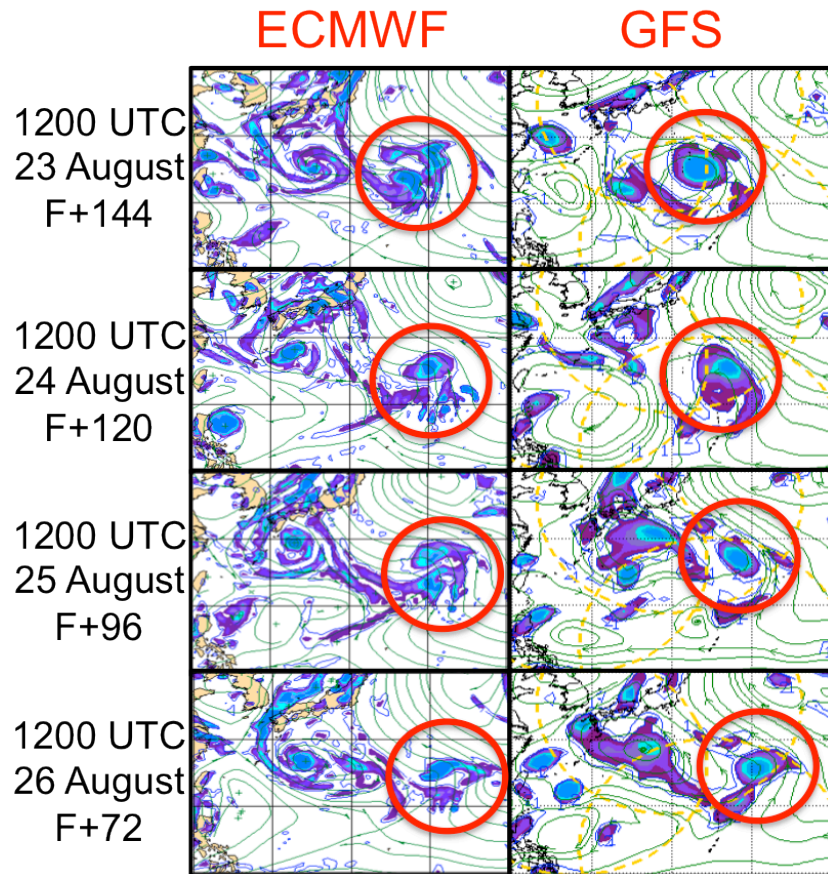


Figure 1 Operational forecasts of 850 hPa relative vorticity and streamlines valid at 1200 UTC 29 August from the ECMWF (left panels) and GFS (right panels). Model initialization times (UTC) and forecast lead times (hours) are listed to the left of each set of graphics. Red circles indicate the vorticity features associated with the model development of the TCS025 disturbance. Forecast graphics taken from the NCAR EOL online T-PARC/TCS-08 field catalog: <http://catalog.eol.ucar.edu/tparc/>.

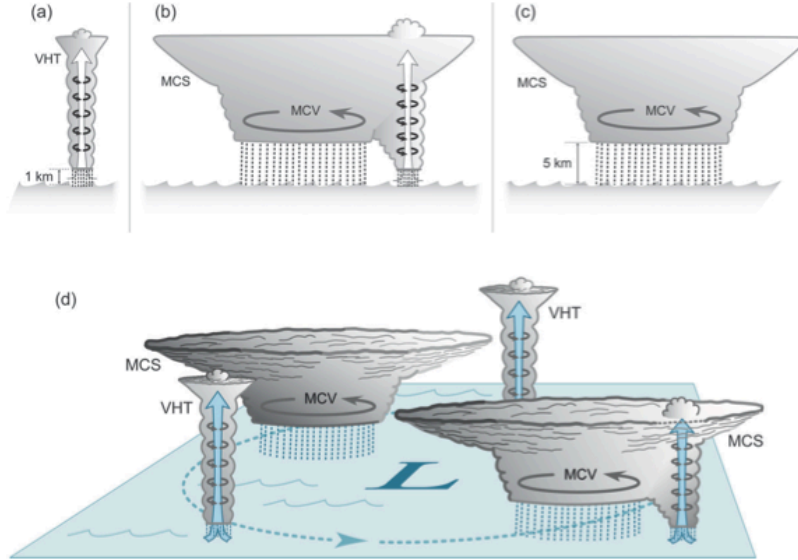


Figure 2 Schematic illustration of the mesoscale convective system (MCS) lifecycle in the presence of a developing tropical cyclone from Houze et al. (2009). (a) Deep convection possessing increased relative vorticity or “vortical hot towers” (VHTs) is followed by (b) MCS and mesoscale convective vortex development in the trailing stratiform precipitation region. After deep convection dissipates, the (c) stratiform precipitation region of MCS and associated MCV remain. Panel (d) depicts MCS development at various stages within the context of a preexisting disturbance.

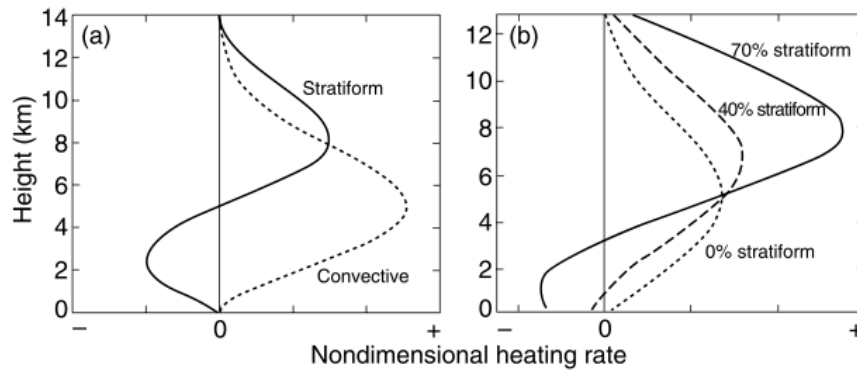


Figure 3 (a) Idealized net heating and cooling profiles for stratiform (solid line) and convective (dashed line) precipitation regions of a MCS. (b) Idealized heating rate profiles for various fractions of stratiform precipitation (from Houze 2004).

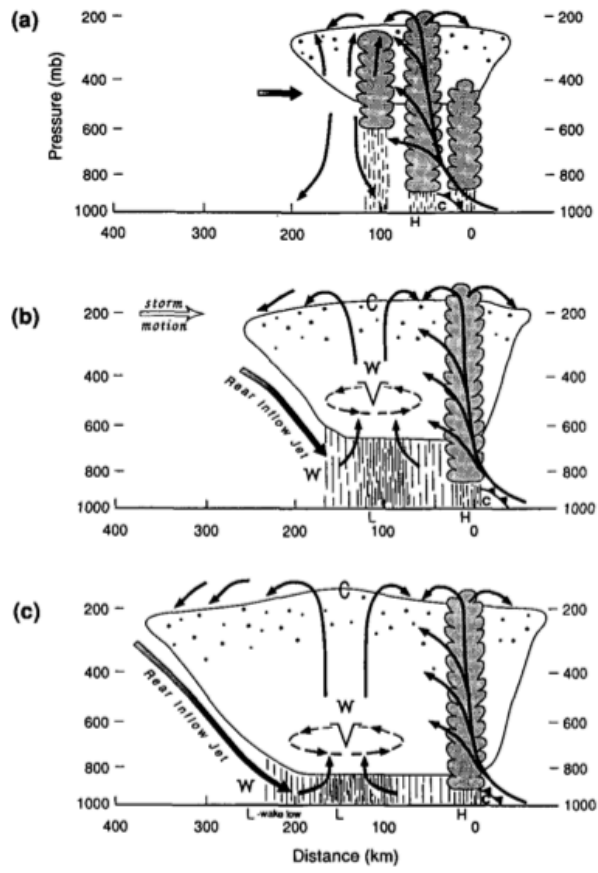


Figure 4 Diagram illustrating the formation of a MCV with a leading convective line (dark shaded areas) and trailing stratiform precipitation region. Panel (a) depicts the initial stage, and the MCV (denoted by "V") formation and intensification are shown in panels (b) and (c), respectively. Warm temperature anomalies are indicated by "W" and cold anomalies "C" (from Chen and Frank 1993).

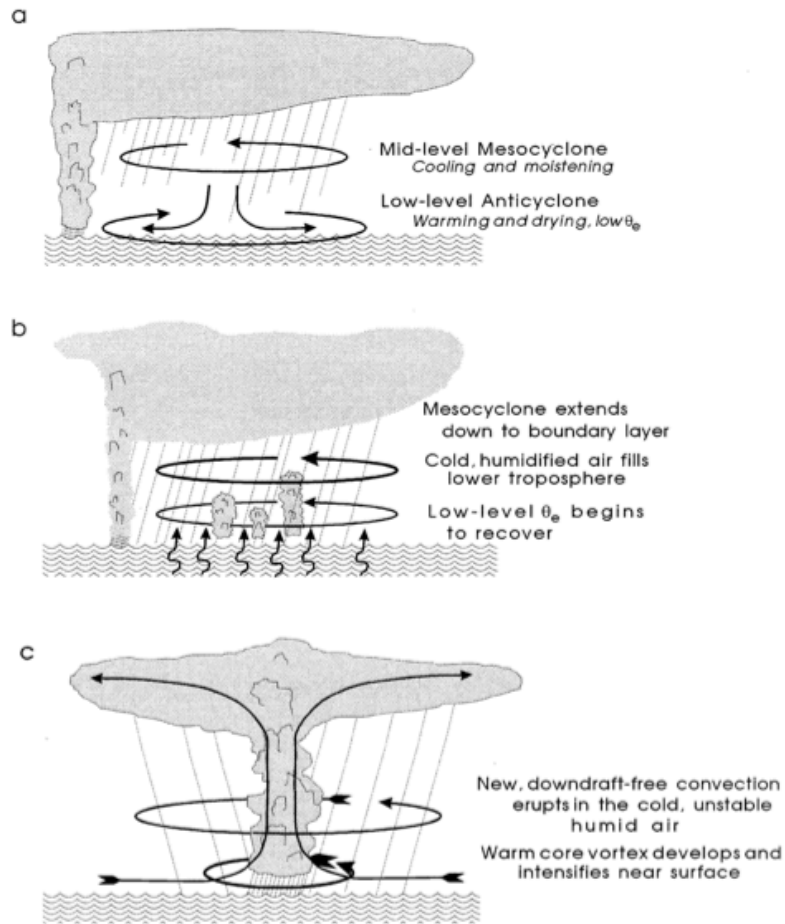


Figure 5 Illustration from Bister and Emanuel (1997) depicting the three-stage process of how tropical cyclogenesis is hypothesized to occur from a pre-existing MCS.

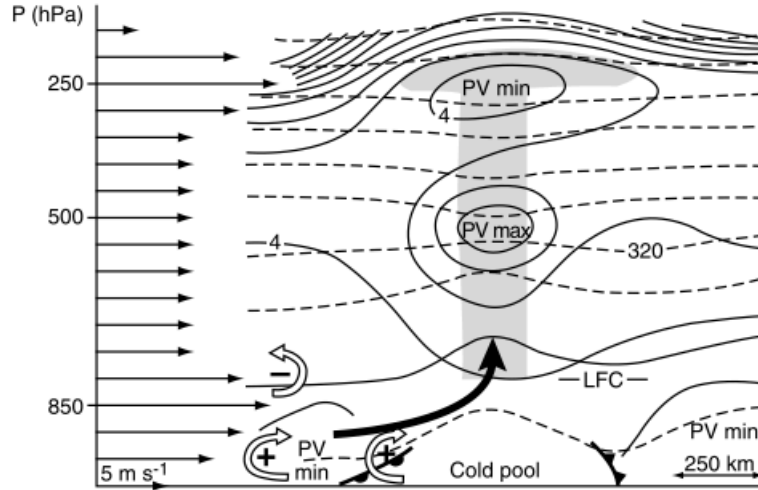


Figure 6 Graphic depicting how the thermal structure of a MCV could contribute to new convection. The environmental wind profile is shown at the left of diagram. Potential temperature and PV are contoured with dashed and solid lines, respectively. Open arrows indicate where horizontal vorticity is generated at the base of the cold pool associated with the vertical wind shear profile. The cold pool acts to lift low-level, high-equivalent potential temperature air inflowing relative to the system and trigger deep convection (from Raymond and Jiang 1990 and adapted by Houze 2004).

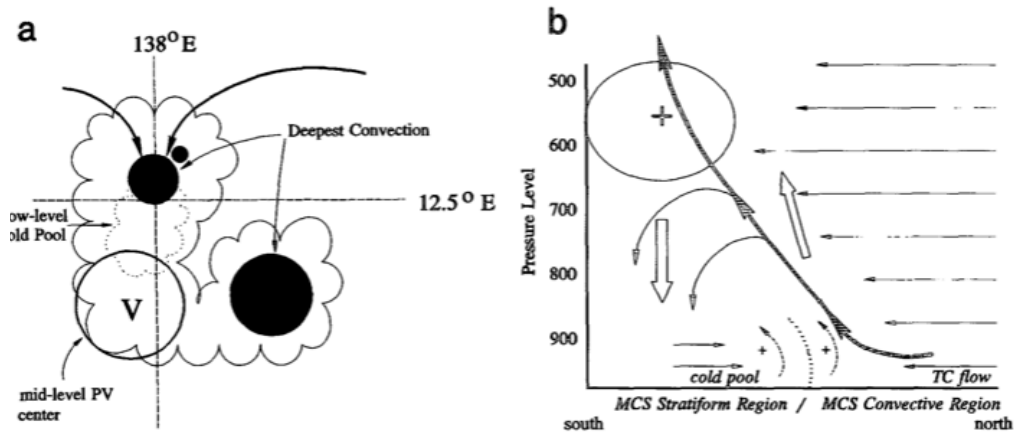


Figure 7 (a) Schematic from Harr and Elsberry (1996) illustrating where deep convection occurred in relation to the near-surface cold pool and MCV during the formation of TY Robyn (1993). Bold dark arrows denote low-level inflow. (b) Idealized south to north vertical cross-section through the convective structure depicted in (a) demonstrating how horizontal vorticity could be generated at the leading edge of the cold pool. Ellipse near 650 hPa marks the positive PV anomaly. Dark continuous arrow corresponds to the main MCS updraft. Dashed curved arrows at the leading edge of the cold pool mark the region where horizontal vorticity generation is occurring.



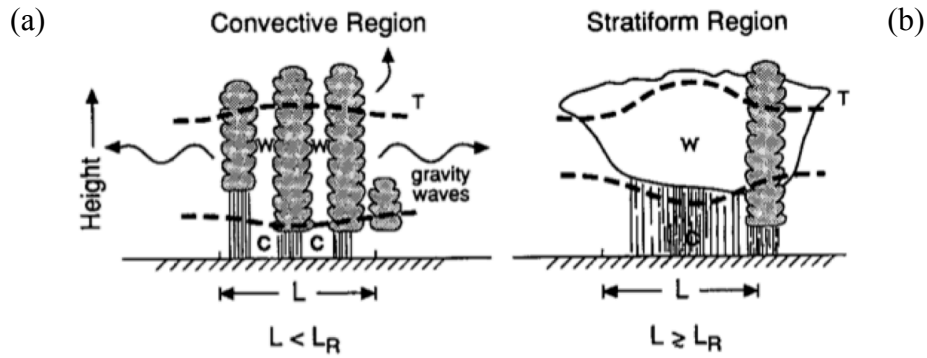


Figure 8 Schematic from Chen and Frank (1993) of the response to diabatic heating when the characteristic length scale ( $L$ ) of the disturbance is (a) less than the deformation radius ( $L_R$ ) and (b) greater than the deformation radius. “W” corresponds to warm temperature anomalies and “C” denotes cold anomalies.

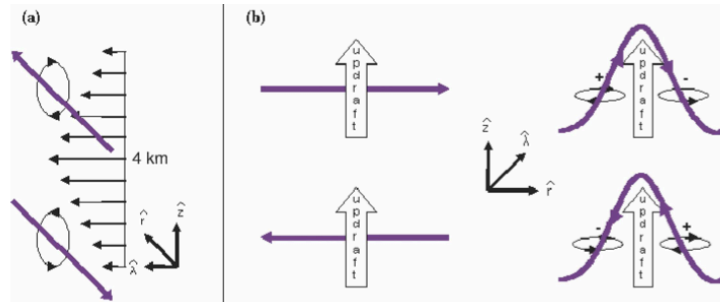


Figure 9 Schematic from Montgomery et al. (2006) showing horizontal vorticity filaments (purple lines) tilted into vertical plane by MCV updrafts. Panel (a) is an illustration of how vorticity in the radial plane ( $\hat{r}$ ) is generated from a vertical wind shear profile and panel (b) illustrates how updrafts tilt horizontal vorticity to create vertical vorticity dipoles.

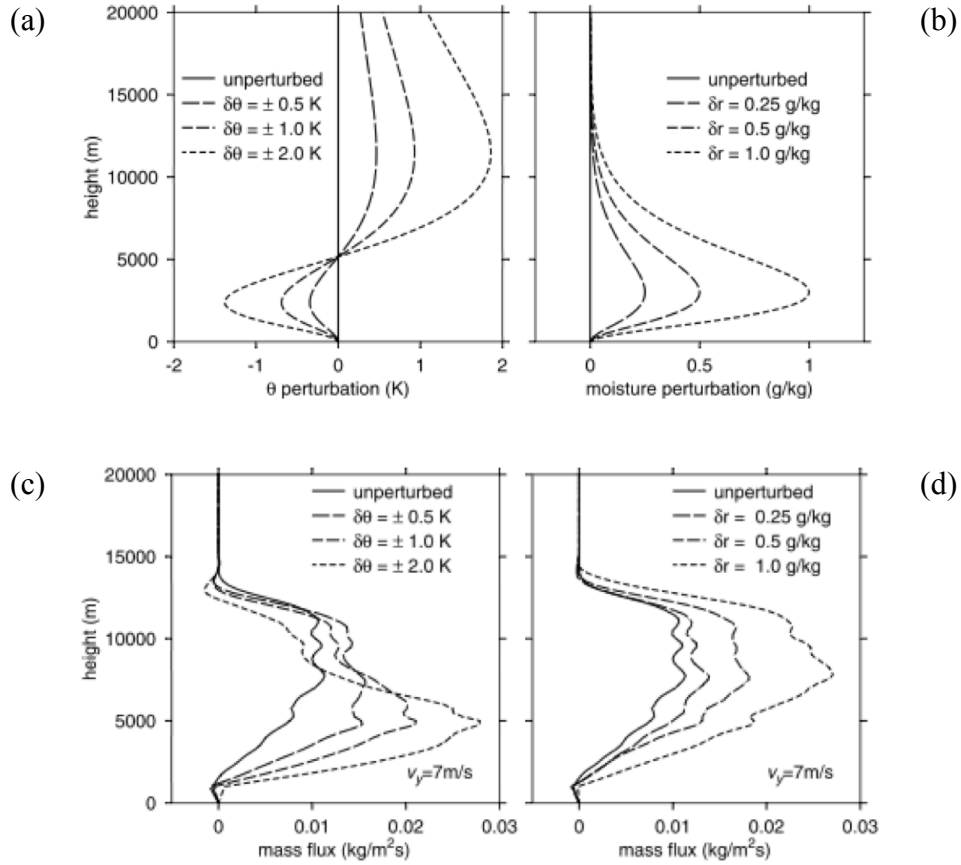


Figure 10 Profiles of (c, d) vertical mass flux from a numerical modeling sensitivity study in which profiles of (a) temperature and (b) mixing ratio were allowed to vary. Note in panel (c) that the level of maximum vertical mass flux is lowered in the presence of an upper-level warm temperature anomaly and cold low-level temperature anomaly (from Raymond and Sessions 2007).

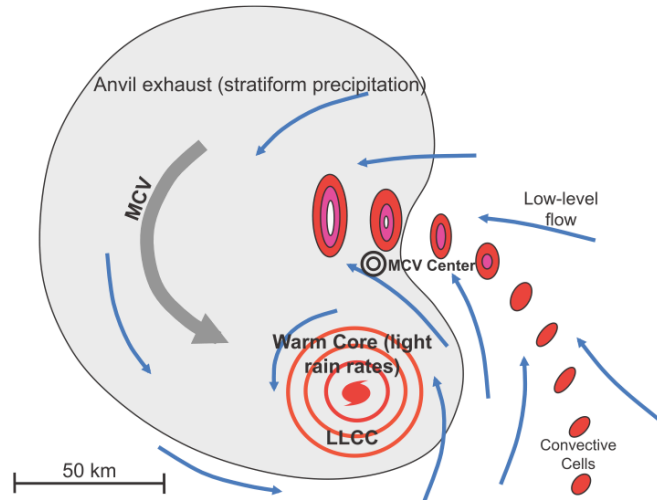


Figure 11 Schematic from Dolling and Barnes (2012b) of how subsidence warming above the low-level circulation center (LLCC) is thought to have occurred during the formation of TS Humberto (2001). Ovals represent convective cells; red corresponds to cells 10 km in height, and white 16 km. Low-level flow is marked by blue arrows and is strongest away from LLCC. Subsidence and warm core are located at the trailing base of the anvil south of MCV.

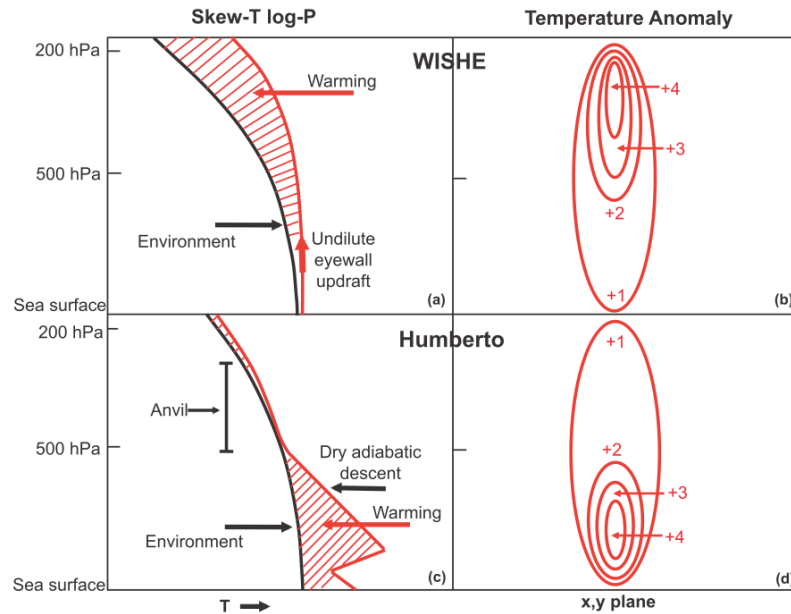


Figure 12 Thermodynamic profiles representative of warm-core development via (a) WISHE and (c) subsidence and their associated temperature anomalies (b, d). Black lines in left panels represent a moist adiabatic environment. Red hatching corresponds to warming caused by latent heating (a) and subsidence (c) (from Dolling and Barnes 2012b).

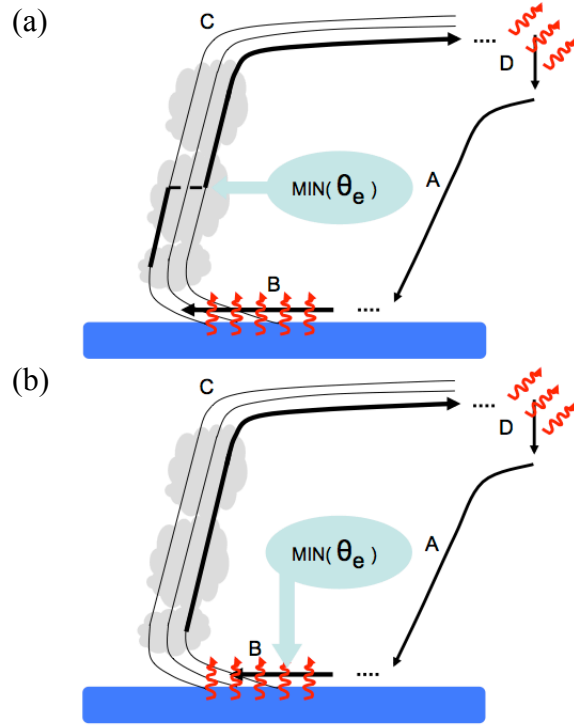


Figure 13 Two pathways whereby low- $\theta_e$  air in the presence of vertical wind shear air can affect the thermodynamic cycle of a tropical cyclone: (a) mid-level low- $\theta_e$  air is directly entrained into eyewall convection and reduces  $\theta_e$  within the eyewall, and as proposed by Riemer et al. (2010), (b) low- $\theta_e$  air is transported into the boundary layer via downdrafts and limits  $\theta_e$  in the inflow layer. The blue regions represent the ocean surface and the storm center is located to the left in each figure. Black arrows represent air parcel trajectories within the idealized framework of a Carnot heat engine. Letters A, B, C, and D in the figures represent segments of the Carnot heat cycle (see Emanuel 1986). Black contours are lines of constant  $\theta_e$ , with  $\theta_e$  decreasing away from the storm center. Red wavy arrows represent processes that can change  $\theta_e$  (i.e., surface fluxes and radiational cooling).

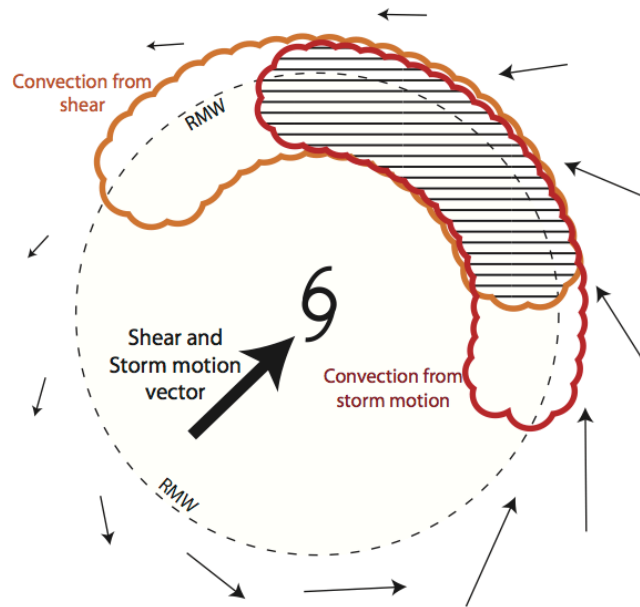


Figure 14 Schematic illustrating the combined impacts on convection that vertical wind shear (red outline) and rapid translation speed (orange outline) had in initiating convection in the down-shear direction (hatched) for Hurricane Irene (1997) (from Nguyen and Molinari 2012).

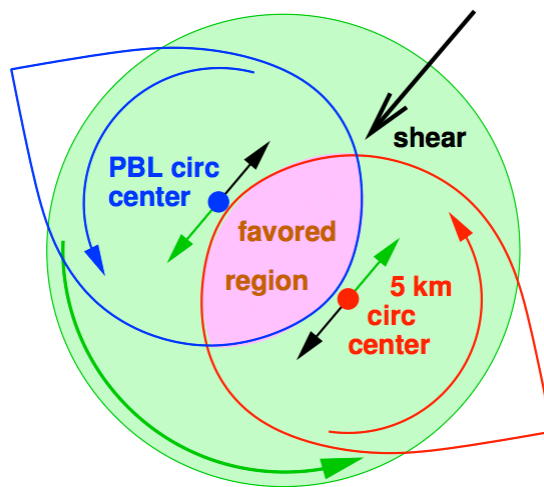


Figure 15 Illustration depicting a protected region where the mid-level and low-level circulations overlap. Boundary layer and mid-level circulations are oriented such that storm-relative flow (short black arrows) due to vertical wind shear is cancelled or minimized by the penetration depth of the circulation at each level (short green arrows) (from Raymond and Carrillo 2011).

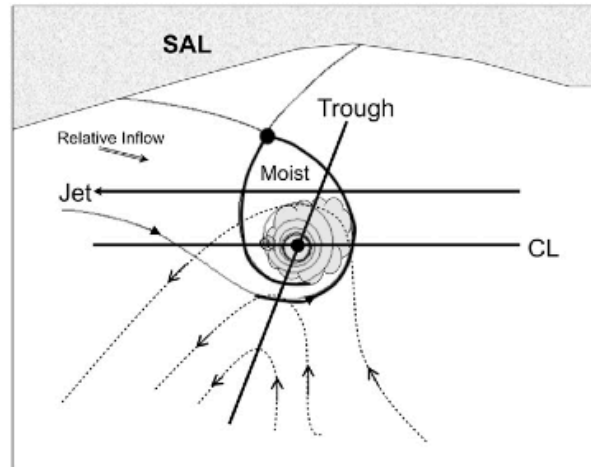


Figure 16 Illustration of storm formation in the protective environment of an easterly wave pouch. The black dot marks the pouch center or intersection of the wave trough axis and critical latitude (i.e., “sweet spot”). The pouch center is where deep convection (gray shading) can be sustained and is the favored region for storm formation. Dashed streamlines represent ground-relative flow whereas solid streamlines correspond to flow in the storm-relative framework, which show a nearly closed recirculation region protected from the dry Saharan air layer (SAL) to the north (from Wang et al. 2010).

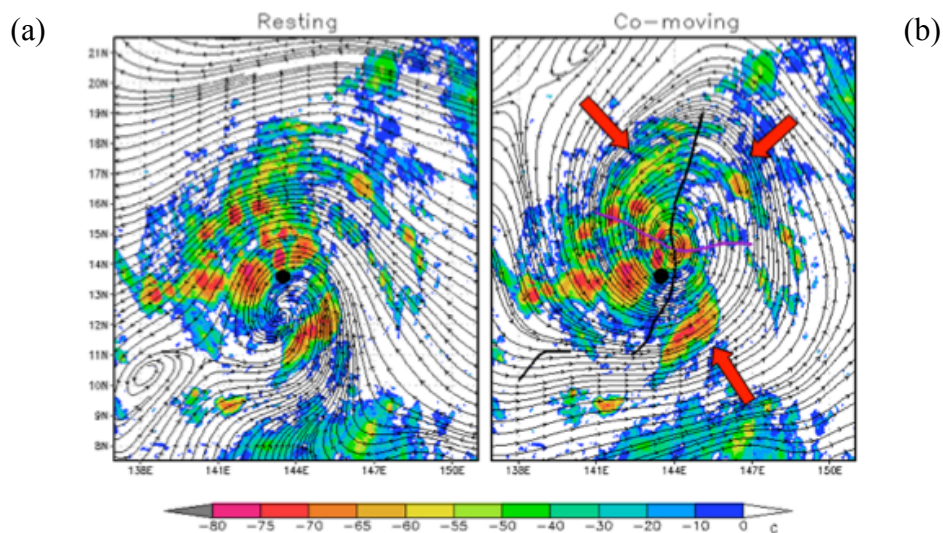


Figure 17 MTSAT IR brightness temperature overlaid on a streamline analysis of TY Nuri valid at 1200 UTC 16 August in (a) ground-relative reference frame and (b) storm-relative frame. Black dots mark the JTWC best track position. In (b), the thin black line is the wave trough axis and the purple line is the critical latitude; red arrows indicate where convective regions are converging upon the “sweet spot” (from Montgomery et al. 2010).

## **II. DATA AND METHODOLOGY**

### **A. OBSERVATIONS COLLECTED DURING TCS025 IOPS**

Since TCS025 was consistently forecast to develop in most of the global models (see Figure 1), it was closely monitored for potential development from 24 August until 3 September 2008. Three reconnaissance flights were conducted with the USAF WC-130J, and two flights were conducted with the Naval Research Laboratory (NRL) P-3 (Figure 18). Both aircraft deployed global positioning system (GPS) dropwindsondes during each flight, collected flight-level data, and the NRL P-3 was able to observe the three-dimensional cloud and precipitation structure of TCS025 with the tail-mounted ELectra DOppler Radar (ELDORA).

In addition to the observations collected during the IOPs, other data sources included geostationary MTSAT infrared brightness temperatures, and 6-h gridded fields from the ECMWF YOTC analysis and the National Centers for Environmental Prediction (NCEP) Climate Forecast System Reanalysis (CFSR).

Since TCS025 failed to develop, the Joint Typhoon Warning Center (JTWC) best-track post-season analysis positions and intensity estimates were not made available for this system. As a result, circulation and vorticity center positions were subjectively determined at 850 hPa using the ECMWF YOTC analysis for the time period encompassing the IOPs (see Figure 19). When a closed circulation was not present, wind speed minima that provided the best continuity with previous and future center positions were chosen. After the 6-h center positions were identified, center positions were interpolated to 15-minute intervals. These interpolated center positions allowed for analyses of several datasets in storm-relative coordinates (described below).

#### **1. GPS Dropwindsondes and AXBTs**

Vertical profiles of atmospheric pressure, temperature, humidity, and horizontal winds were obtained via the deployment of GPS dropwindsondes (Hock and Franklin 1999). Dropwindsonde data collected during the USAF WC-130J and NRL P-3 missions were quality controlled using the Atmospheric Sounding Processing ENvironment

(ASPEN) software by the National Center for Atmospheric Research (NCAR) Earth Observing Laboratory (EOL) and made available at half-second temporal resolution (Young et al. 2009a,b). Pressure, temperature, and relative humidity were measured directly, while dewpoint temperature was derived from the temperature and relative humidity data. Horizontal wind speed and direction were computed using GPS navigational signals received by the dropwindsonde. In addition, vertical velocities were computed during the quality control procedure following the method described by Wang et al. (2009).

A total of 143 dropwindsondes were deployed during the five aircraft missions flown to observe TCS025 and its surrounding environment (Figure 19). Dropwindsondes were deployed from about 10 km altitude with regular horizontal spacing during the three USAF WC-130J missions. Since the NRL P-3 was tasked to investigate convective features using the ELDORA radar, its flight tracks were far more irregular and thus dropwindsondes were deployed with variable spacing and generally from below 3 km altitude.

For dropwindsondes that were determined to have transmitted data all the way down to the surface, geopotential heights were computed by integrating the hydrostatic equation from the surface upward. All 53 NRL P-3 dropwindsondes deployed during TCS025 missions were identified as having reached the surface. For 10 of the 90 dropwindsondes from the USAF WC-130J that failed to reach the surface, geopotential height was integrated downwards from the altitude of the aircraft at launch time.

Dropwindsonde data were interpolated to various height and pressure levels. Individual dropwindsonde profiles were examined and average profiles were constructed based on distance from the analyzed circulation center and the MTSAT IR brightness temperature interpolated to the time and location of the dropwindsonde. Dropwindsonde data were incorporated into the SAMURAI analyses analyzed in Chapter III and used in the DART-WRF ensemble data assimilation system in Chapter V.

Dropwindsonde data were also used to analyze the vertical alignment of the TCS025 circulation based on the method used by Davis and Ahijevych (2012) (Figure



20). Dropwindsonde data were interpolated to 500 m height intervals and tangential wind speeds were computed on a grid encompassing the dropwindsonde locations. Tangential wind speeds at each height were then averaged and grid points with a tangential wind speed within 2% of the maximum value were identified. The circulation center position at each height was defined as the centroid position of grid points within 2% of the maximum value threshold. Uncertainty ellipses were created based on the areal extent of grid points within 2% of the maximum tangential wind speed value. The method employed by Davis and Ahijevych (2012) attempted to correct for sampling bias by first averaging observations by storm quadrant. However, due to the relatively weak and highly asymmetric wind structure of TCS025, this procedure did not yield results consistent with expectations (Figure 20b,d). Therefore the simpler method of employing all dropwindsonde data was used (Figure 20a,c). A secondary reason for employing the dropwindsonde center-finding method was to allow for a comparison with circulation center estimates based on ELDORA radar during the second and third IOPs. Because routine reconnaissance is not conducted in the western North Pacific, high-resolution dual Doppler radar data are rarely available.

In addition to dropwindsondes, the USAF WC-130J aircraft also deployed Airborne eXpendable BathyThermographs (AXBTs) during the first IOP, which measure ocean temperature as a function of depth. These AXBTs were primarily deployed along the eastern half of the flight track (see Figure 31b, c). The AXBT profiles allowed for a comparison of the ocean temperature characteristics of TCS025 and TY Fanapi, which was a developing system observed during the ITOP field campaign in 2010 (see Figure 67).

## **2. MTSAT IR Brightness Temperature and TRMM Precipitation**

Digital MTSAT IR brightness temperatures at 0.05°-spatial and 30-minute-temporal resolutions were provided by the Japan Meteorological Agency (JMA), and made available on the T-PARC/TCS-08 NCAR EOL data archive. MTSAT-IR data were azimuthally and radially averaged in cylindrical coordinates based on the subjectively-

determined center positions, which allowed for a diagnosis of the convective characteristics relative to the circulation center position of TCS025.

Histograms of IR brightness temperature during the evolution of TCS025 were also created following Raymond and Carrillo (2011; their Figure 3) by binning IR values within a  $\pm 3^\circ$  box surrounding the 850 hPa circulation center position of TCS025 determined from the ECMWF YOTC dataset.

To assist in analyzing the convective nature of TCS025, contiguous areas of deep convection that could be loosely identified as MCSs based on MTSAT IR brightness temperature were subjectively tracked during TCS025. Convective intensity was defined based on the ratio of pixels with brightness temperature less than  $-65^\circ\text{C}$  to those less than  $-35^\circ\text{C}$  within a box surrounding the identified MCSs (Figure 21).

As an additional model evaluation tool, the Tropical Rainfall Measuring Mission (TRMM) merged precipitation estimates were used to compare with precipitation output from the model simulations. The TRMM precipitation estimates were available at 3-h intervals at 0.25 degree grid spacing from  $50^\circ\text{S}$  to  $50^\circ\text{N}$  (NASA 2013). These precipitation estimates are computed from an algorithm that uses a combination of available passive microwave data, such as TCI, TMI, AMSR-E, AMSU-B, SSM/I, and variable rain-rate estimates from infrared brightness temperature (NASA 2013). An example of the TRMM precipitation rate estimate and corresponding IR brightness temperature valid at 0000 UTC 28 August is shown in Figure 22.

### **3. NRL P-3 ELDORA Dual-Doppler Radar**

The ELDORA radar, which was mounted on the tail of the NRL P-3 during T-PARC/TCS-08, allowed for an unprecedented examination of the precipitation and circulation structure of the non-developing TCS025 disturbance over two consecutive days. Because of the importance of the ELDORA data in this study, the original motivation for deployment on the NCAR Electra will first be provided as described by Hildebrand et al. (1996) and Wakimoto et al. (1996). Then differences in the ELDORA deployment on the NRL P-3 aircraft for the T-PARC/TCS-08 field experiment will be summarized.

Plans for the ELDORA radar were originally proposed based on the success of the National Oceanic and Atmospheric Administration (NOAA) P-3 airborne radar system that was designed to study tropical storms (Hildebrand et al. 1996). Due to the geometric considerations of the NCAR Electra aircraft (in which the ELDORA radar was originally housed), and a need for the highest spatial sampling resolution possible, a radar wavelength of 3.2 cm (X-band) was chosen. Wavelengths shorter than 3.2 cm suffer from extreme attenuation in heavy precipitation. The 3.2 cm wavelength and antenna diameter of 1.4 m dictates a beamwidth of  $1.8^\circ$ , which translates to 0.9 km of beam spreading at 30 km range from the aircraft (Hildebrand et al. 1996).

The dual-Doppler ELDORA configuration consists of two radar antennas housed inside a “rotadome” that rotates about the aircraft’s longitudinal axis. One antenna points  $\sim 18.5^\circ$  forward of a plane normal to the flight track, and the other points  $\sim 18.5^\circ$  aft. Based on the tilt angles and a flight speed of  $120 \text{ m s}^{-1} - 125 \text{ m s}^{-1}$ , a  $\sim 1$  minute lag time exists between when the fore and aft radar beams sample the same location in space for each 11 km range from the aircraft (Hildebrand et al. 1996). Where the two radar beams intersect, the two dimensional wind field can be constructed from the radial velocities (Figure 23), and vertical motion can be computed by integrating the horizontal divergence through a vertical column by assuming appropriate boundary conditions (Hildebrand et al. 1996). Beam intersection angles are required to be  $\geq 30^\circ$ , and long, straight flight tracks between turns are desirable.

The ELDORA dual-beam orientation and scanning technique was dictated by the need for an along-track sampling interval of 0.3 – 0.5 km while achieving a radial velocity measurement uncertainty of  $\leq 1 \text{ m s}^{-1}$ . To achieve this desired level of radial velocity uncertainty with a signal-to-noise ratio of 10 dB using a pulse repetition frequency (PRF) of 2 KHz, an adequate number ( $\geq 10$ ) of independent measurements are needed. Independent measurements provide a spatial “pre-filtering,” which reduces the possibility of aliasing finer-scale fluctuations into the signal returned to the radar (Hildebrand et al. 1996). Obtaining independent samples can be achieved by sampling a different location of the storm, or by allowing time for turbulent motions to rearrange precipitation particles relative to the wavelength of the radar beam (Wakimoto et al.

1996), which is estimated to take about 2 milliseconds when using airborne radar (Jorgensen et al. 1983). With a horizontal beamwidth of 0.9 km at 30 km range from the aircraft, measurements taken at 0.3 km intervals along the flight track would be only 30% independent, and using a  $1^\circ$  sampling interval in elevation ( $\sim 0.5$  km) only allows for  $\sim 50\%$  independence between adjacent rays in elevation (Hildebrand et al. 1996). With an aircraft speed of  $120 \text{ m s}^{-1} - 125 \text{ m s}^{-1}$ , the desired 0.3 km sampling interval along the flight track would provide no more than 7 milliseconds of dwell time, which is only enough time to permit  $\sim 3$  independent samples through the reshuffling of precipitation particles through turbulent motions (Hildebrand et al. 1996). These effects combine to increase the Doppler radial velocity uncertainty closer to  $2 \text{ m s}^{-1}$ . To obtain a radial velocity uncertainty of  $1 \text{ m s}^{-1}$  with this configuration would require the scanning rate of the antenna be reduced, but this would significantly degrade the along-track sampling resolution (Wakimoto et al. 1996). Thus, ELDORA uses a complex waveform such that the transmitted radar pulse is divided into 2-5 discrete sub-pulses with slightly different frequencies. Averaging the returns from the separate frequencies helps to reduce the sampling error (Hildebrand et al. 1996).

With a pulse repetition frequency of 2 KHz, the largest Doppler-shifted frequency that can be unambiguously measured translates to an unambiguous (Nyquist) velocity of only  $\pm 16 \text{ m s}^{-1}$ . Based on the need to sample radial velocities near  $100 \text{ m s}^{-1}$  during the Verification of the Origins of Rotation in Tornadoes Experiment (VORTEX), dual PRFs were used to increase the Nyquist velocity to  $\pm 80 \text{ m s}^{-1}$  (Wakimoto et al. 1996).

During T-PARC/TCS-08, the ELDORA radar system was mounted on the tail of the NRL P-3. Details of the NRL P-3 ELDORA specifications can be found in Lee et al. (2009). Due to the slightly faster flight speed ( $130 \text{ m s}^{-1}$ ) of the NRL P-3 compared to the NCAR Electra, an antenna rotation rate of 24 revolutions per minute (RPM) was needed to sample at 0.3 – 0.5 km resolution along the flight track. However, due to a technical failure with the fourth sub-pulse frequency, a slower rotation rate had to be used ( $78^\circ \text{ sec}^{-1}$  or  $\sim 13 \text{ RPM}$ ), such that the dwell time was increased to 18 milliseconds so that additional independent samples could be measured. The beamwidth was  $1.8^\circ$  in the

horizontal direction and  $2.0^\circ$  in the vertical direction. Fore and aft radar beam tilt angles were  $15.6^\circ$  and  $16.5^\circ$ , respectively, and the Nyquist velocity was  $\pm 62 \text{ m s}^{-1}$ .

Only minor issues were experienced with the operation of the radar during the two flights (RF05 and RF06) analyzed in this study (Lee et al. 2009). Radial velocity data were corrected for aircraft motion at EOL by using the “THL” or Testud-Hildebrand-Lee method (Lee et al. 2009). The reflectivity and radial velocity fields underwent an additional quality control step to remove radar artifacts, noise, ground clutter etc. using an automated procedure described by Bell et al. (2013).

The ELDORA reflectivity and radial velocity data for the two NRL P-3 flights were first analyzed independent of other data by interpolating to a Cartesian grid using the variational approach described by Reasor et al. (2009). Following this, the ELDORA radial velocity data were combined with other data collected during the three IOPs to create three-dimensional SAMURAI analyses of the storm structure (see Chapter III), and were assimilated using the DART-WRF ensemble data assimilation system (see Chapter V).

#### **4. USAF WC-130J and NRL P-3 Flight-level Data**

Flight-level pressure, temperature, dewpoint temperature, horizontal wind, and SFMR data were collected on the USAF WC-130J and inspected inflight by the Air Force Reconnaissance Weather Officer (ARWO). The USAF WC-130J flight-level data did not go through a thorough post-flight quality control process. Since the TCS025 disturbance possessed a relatively shallow circulation and the WC-130J flight level was close to 10 km altitude ( $\sim 300 \text{ hPa}$ ), flight-level data were not directly used to analyze the disturbance. However, WC-130J flight-level data were used to diagnose the large-scale synoptic environment above the TCS025 disturbance through SAMURAI analyses and DART-WRF simulations.

The SFMR instrument onboard the USAF WC-130J aircraft measures nadir microwave brightness temperature at six C-band frequencies. An algorithm using a geophysical model function is then used to retrieve surface wind speeds and rain rates based on the surface emissivity underneath the flight track (Uhlhorn et al. 2007). These

SFMR precipitation and surface wind data were analyzed for individual flight legs to identify the presence of convectively-generated cold pools.

The NRL P-3 was flown close to 3 km altitude for best performance of the ELDORA radar. Flight-level data from the NRL P-3 were quality controlled by NCAR/EOL (Jensen 2009): (i) pressures were corrected for airflow effects; (ii) temperatures were selected from the sensor determined to be least affected by wetting, icing, and radio interference effects (of two possible sensors); (iii) aircraft positions were determined from the inertial navigation system (INS) and, along with horizontal winds, were corrected for drift using GPS; (iv) spikes were removed from the HGM232 radar altimeter data; and (v) intervals determined to contain bad data were filled with missing values.

## **B. GLOBAL FORECAST ANALYSES**

### **1. ECMWF YOTC: Synoptic Evolution**

Analysis and forecast fields from the ECMWF YOTC dataset were used extensively in the analysis of TCS025. The  $\sim 0.25^\circ$  horizontal resolution ECMWF YOTC dataset consisted of 6-h global analysis fields and multi-day forecast fields, which also included subgrid-scale tendency terms. The ECMWF four-dimensional variational (4DVAR) data assimilation system during 2008 used a triangular truncation of T799 with 91 vertical model levels (see [http://www.ecmwf.int/products/data/operational\\_system/evolution](http://www.ecmwf.int/products/data/operational_system/evolution)).

The ECMWF YOTC dataset was used to analyze the synoptic background and evolution of TCS025 and was used to identify the low-level circulation and vorticity maxima of the TCS025 disturbance (see Figure 19). As will be discussed in a following section, a comparison of dropwindsonde data and the ECMWF analysis showed good agreement, suggesting dropwindsonde data were being assimilated during the forecast cycle. Initial and lateral boundary conditions for the WRF simulations and DART-WRF ensemble data assimilation simulations were constructed from the 6-h ECMWF YOTC analysis fields. Tendency fields from ECMWF forecasts were used to compute a vorticity budget analysis of the TCS025 disturbance (see Chapter IV).

## **2. NCEP CFSR: Environmental Vertical Wind Shear**

Since the ECMWF operational analysis used to analyze pre-TY Fanapi was not global in coverage, it could not be used in the environmental shear calculation. Therefore, the NCEP CFSR dataset was used to compute the vertical wind shear for both TCS025 and TY Fanapi. The environmental vertical wind shear was calculated using the method of Davis et al. (2008b) whereby the irrotational and non-divergent components of the vertical wind shear associated with the TCS025 disturbance were removed within a radius of 450 km (Figure 24). The vertical wind shear was computed as the difference between the 200 hPa and 850 hPa wind at the circulation center position. Vertical shear was computed for various radii, and 450 km corresponded to the distance needed to remove the shear resulting from the TCS025 disturbance.

Park et al. (2013) suggested that the vertical wind shear computed by averaging over a symmetric area from the storm center would be different from the actual vertical wind shear experienced by an asymmetric system such as TCS025. As will be discussed in Chapter III, an analysis of the mesoscale structure of the TCS025 circulation (see Figure 45) indicates that the vertical wind shear on the mesoscale differed in magnitude and direction from the environmental vertical wind shear computed using the Davis et al. (2008b) method (see Figure 47). In addition, an examination of individual dropwindsonde wind profiles (see Figure 40, Figure 44, and Figure 57) revealed that the local vertical wind shear values were often different from the mesoscale and environmental average values, especially near areas of active convection (also see Figure 102 and Table 4). However, since the spatial and temporal coverage of dropwindsonde winds and ELDORA radar winds were limited, the environmental vertical wind shear was used to assess the evolution of the average large-scale vertical wind shear for TCS025.

Since the TCS025 circulation was relatively shallow, it was essentially separate from the upper-level flow. As a consequence, it appears as though part of the upper-level circulation of a tropical upper tropospheric trough (TUTT) cell was removed in the vertical wind shear calculation (see Figure 24b) while the TUTT cell was in close proximity to the low-level circulation of TCS025. However, there was little difference

quantitatively between using the method of Davis et al. (2008b) and computing the vertical wind shear over a boxed-area centered on the circulation (not shown), even during the period when the TUTT cell was close to TCS025.

### **C. SAMURAI ANALYSES**

To achieve a more accurate assessment of the true atmospheric state, analysis fields were constructed from data collected during the IOPs utilizing the Spline Analysis at Mesoscale Utilizing Radar and Aircraft Instrumentation (SAMURAI) analysis package (Bell et al. 2012) with the ECMWF analysis as the background field. The SAMURAI analyses combined observations, estimates of the observation error, and a background field to provide a maximum likelihood estimate of the atmospheric conditions at the time of the TCS025 IOPs through the minimization of a variational cost function.

Data used in the SAMURAI analysis consisted of dropwindsondes, ELDORA dual-Doppler radar data (for the second and third IOPs), and flight-level data. SAMURAI domains were configured to encompass data collection regions during each IOP (Figure 25). When appropriate, the analyses were computed in the storm-relative frame; observations were space- and time-corrected, and wind observations were adjusted for storm motion.

Settings used for the various SAMURAI analyses are listed in Table 1. Due to an ill-defined circulation center during the first IOP, that SAMURAI analysis was in the earth-relative reference frame. Analyses in the earth- and storm-relative reference frames were almost identical during the second IOP due to the slow translation speed of the disturbance during this time. By the time of the last IOP, the translation speed of the disturbance had increased significantly, thus analyses were conducted in both reference frames.

Observation errors were assigned for each observation type (Table 2) based on Bell et al. (2012), and were specified to account for both instrumentation and representativeness error. Except for the ELDORA radar data, the error values used for other observation types remained constant for all observations during the analysis. Error values for each radar radial velocity observation were determined from the spectrum



width, which is a measure of the standard deviation of radial velocity within a single radar volume, and elevation angle. Radial velocity error was increased for observations at large elevation angles because a significant component of the measured radial velocity might result from hydrometeor fall speed. To reduce the computational expense of SAMURAI analyses that utilized ELDORA radial velocity data, input data were thinned by averaging along each beam (range gates) using a stride of two (radar stride), and by only retaining every second beam (radar skip).

The background error values associated with the ECMWF analysis were generally set quite high to give increased weight to the observations. During the second IOP, the flight track of the NRL P-3 (0225W) was made up of a large number of turns (see Figure 19), which led to higher uncertainty in the ELDORA radar radial velocities (Hildebrand et al. 1996). Consequently, small errors in the horizontal wind can translate to large vertical velocity error in these regions. As a result, background vertical velocity error values were set lower for the second IOP SAMURAI analysis to reduce the weight given to the radar vertical velocity observations.

The spatial influence of the observations was determined using a Gaussian recursive filter of various lengths (in grid points). For the analyses employing 25-km grid spacing, a horizontal filter length of 4 grid points was used. For the higher-resolution analyses (5- and 2-km grid spacing) that utilized ELDORA radar data, a horizontal filter length of 8 grid points was used. Using a larger filter length for the high-resolution SAMURAI analyses helped to eliminate “bulls-eyes” in the thermodynamic fields that were otherwise apparent.

Although the SAMURAI analysis technique allowed observations to be adjusted in space and time with respect to the storm center, one may question whether the stationarity assumption is valid for these IOPs. Depending on the transit time, data collection times were generally close to six hours in duration. Since it is likely that the thermodynamic and dynamic structure of TCS025 evolved during this time interval, it was considered an additional source of uncertainty when interpreting the SAMURAI analyses.

#### **D. MULTI-PHYSICS ENSEMBLE: WRF-ARW MODEL**

To expand upon the observational analysis and examine aspects of the evolution of TCS025, numerical simulations of TCS025 were conducted using versions 3.1.1 and 3.2.1 of the Advanced Weather Research and Forecasting (WRF-ARW) non-hydrostatic, mesoscale model (Skamarock et al. 2008). Each model simulation was comprised of three nested domains at 27-, 9-, and 3-km grid spacing with 33 vertical levels. Grid dimensions were 188 by 147 grid points (east-west by north-south direction) for the 27-km grid, 493 by 337 grid points for the 9-km grid, and 718 by 634 grid points for the 3-km grid (Figure 25). Two-way feedback was used in each simulation such that the lateral boundary conditions for the nested domains were interpolated from the parent domain (coarse grid). The solution obtained from the nested domains replaced parent-domain grid values where grid points of the parent domain coincided with nested grid points.

Cumulus convection was parameterized using the Kain-Fritsch scheme (Fritsch and Kain 1993; Kain 2004) for the two outer domains, but was explicitly represented for the inner-most domain. Radiative processes were calculated using the Rapid Radiative Transfer Model (RRTM; Mlawer et al. 1997) for longwave radiation and Dudhia (1989) for shortwave radiation. Although the lower boundary was primarily comprised of ocean surface, surface temperature was predicted for land areas using the five-layer thermal diffusion land surface scheme (Dudhia 1996).

Most simulations employed the Yonsei University (YSU) boundary layer scheme (Hong et al. 2006), which is a non-local K parameterization that uses a parabolic K profile in an unstable mixed layer and includes an explicit entrainment layer, and the fifth-generation Pennsylvania State University–NCAR Mesoscale Model (MM5) similarity theory surface-layer scheme (Skamarock et al. 2008). However, one simulation used the Mellor-Yamada-Janjic (MYJ) boundary layer scheme (Mellor and Yamada 1984; Janjic 1990; Janjic 1996; Janjic 2002) and the Eta surface layer scheme (Janjic 1996; Janjic 2002).

Based on the study by Park and Elsberry (2013) that found different diabatic heating profiles for developing and non-developing disturbances, the multi-physics

ensemble (see Chapter IV) was constructed primarily by using different cloud microphysics schemes (Table 3). The three simulations that were thoroughly analyzed in this study employed the WSM3 cloud microphysics scheme (Hong et al. 2004), the WRF Double-Moment 6-class (WSM6 DM) scheme (Lim and Hong 2010), and the Purdue Lin scheme (Lin et al. 1983; Chen and Sun 2002). The WSM6 DM and Purdue Lin schemes account for the effects of water vapor, cloud water, cloud ice, rain, snow, and graupel, whereas the WSM3 scheme uses single variables to account for the mixing ratios of cloud water and cloud ice and the mixing ratios of rain and snow, which precludes the representation of mixed phase processes.

Initial and lateral boundary conditions for the WRF simulations were constructed from the 6-h ECMWF YOTC analysis. Significant differences were noted in the ECMWF analysis before and after the first IOP when flight-level and dropwindsonde data of the TCS025 disturbance were first made available to the ECMWF data assimilation system. As a result, most WRF simulations were initialized at 1200 UTC 27 August (after the first IOP). In addition, it was readily apparent that vertical wind shear played an important role in the evolution of TCS025. Therefore, it was deemed important that the evolution of the two large-scale TUTT cells that modulated vertical wind shear be realistically resolved in the WRF simulations. The evolution of the TUTT cells seemed to agree better with the ECMWF analysis when the WRF model was initialized at 1200 UTC 27 August. Model fields were output every thirty minutes for analysis.

#### **E. DART-WRF ENSEMBLE DATA ASSIMILATION EXPERIMENTS**

To assess the impact of observations collected during TCS025 on the simulated development in the WRF-ARW numerical model, data assimilation experiments were conducted using the Data Assimilation Research Testbed (DART) (Anderson et al. 2009) software package in conjunction with the WRF model. The ensemble filters provided by the DART system allow for data assimilation without the need for a sophisticated and extremely costly variational assimilation system similar to those used by most operational numerical weather prediction agencies.

## 1. Data Assimilation Cycle

The following is a summary of the DART data assimilation cycle as described by Anderson et al. (2009) and illustrated in Figure 26. Using a numerical model, an ensemble of simulations is integrated until the time corresponding with the next observation to be assimilated. At the observation time, a forward operator is used to map the model state vector into observation space to provide a prior estimate of the observation. While the instrument measures the observed value, the instrument error characteristics provide the observation likelihood, or probability of obtaining the measured value given a true value of the observed quantity. Using an ensemble filter algorithm, the prior ensemble, observation, and observation probability are combined to yield an ensemble estimate and increments that can be applied to the prior ensemble as an update. The model is then used to integrate each ensemble member forward to the next observation time.

The linearized Kalman filter was proposed by Kalman and Bucy (1961) to solve for the analyzed model state,  $\mathbf{x}^a$ , such that the error variance is minimized:

$$\mathbf{x}^a = \mathbf{x}^f + \mathbf{K}(\mathbf{y}^o - \mathbf{H}\mathbf{x}^f). \quad (7)$$

Here  $\mathbf{x}^a$  is computed as the sum of the model forecast,  $\mathbf{x}^f$ , and the analysis increment  $\mathbf{K}(\mathbf{y}^o - \mathbf{H}\mathbf{x}^f)$ . The analysis increment is the difference between the observations,  $\mathbf{y}^o$ , and the model forecast state mapped to observation space using the linear forward operator,  $\mathbf{H}$ , before being weighted by the gain matrix,  $\mathbf{K}$ , which is defined as:

$$\mathbf{K} = \mathbf{P}^f \mathbf{H}^T (\mathbf{H} \mathbf{P}^f \mathbf{H}^T + \mathbf{R})^{-1}. \quad (8)$$

The covariance matrix of the forecast errors is  $\mathbf{P}^f$  (in this case estimated from the ensemble statistics),  $\mathbf{H}^T$  is the transpose of  $\mathbf{H}$ , and  $\mathbf{R}$  is the covariance matrix of the observation error. The analysis error covariance,  $\mathbf{P}^a$ , that results is:

$$\mathbf{P}^a = (\mathbf{I} - \mathbf{K}\mathbf{H})\mathbf{P}^f. \quad (9)$$

Using a Monte Carlo approximation to the Kalman filter, Evensen (1994) proposed the ensemble Kalman filter (EnKF), which is computationally more tractable. Based on the EnKF, Anderson (2001) developed the ensemble adjustment Kalman filter (EAKF), which was used for data assimilation in this study. The EAKF is a deterministic filter that can solve Equations 7–9 sequentially (Anderson 2003), which precludes the need for matrix inversion that can be computationally and memory intensive.

The DART-WRF data assimilation system in this study included 96 ensemble members with an identical domain and parameter configuration to that used in simulation 9 of the multi-physics ensemble (Purdue Lin microphysics scheme) (see Table 3), except 45 vertical levels were used instead of 33. A 1-hour data assimilation cycle was used whereby the 96-member WRF-ARW model ensemble was integrated forward an hour at a time (until the next data assimilation time). At the data assimilation time, observations within the  $\pm 25$  minute window (Figure 29) and their corresponding error characteristics were combined with the ensemble prior state (Figure 30a) using the EAKF to generate an increment for each ensemble state (Figure 30c). Given the finite ensemble size, which leads to sampling error, a spatially varying state-space inflation was also used to increase spread among the ensemble members. The increment was then applied to the ensemble prior state to generate the ensemble posterior state (Figure 30b), which was then integrated forward in time by the model until the next assimilation time.

To reduce computational expense and limit spurious correlations between the state vector and observations, a localization cutoff radius (Gaspari-Cohn covariance) was used to limit how far (spatially) the impact of the observations extended. The localization cutoff radius was determined according to observation type due to differences in observation density (e.g., radial velocity observations were more closely spaced than other observation types). A localization value of 15 km was used for radial velocity observations and 25 km was used for flight-level observations. Other observation types used a localization value of 125 km.

Data assimilation was carried out in two phases (see Figure 18). The first phase extended from 1200 UTC 27 August to the end of the first NRL P-3 ELDORA flight (second IOP). The second data assimilation phase extended from 0600 UTC 28 August to

the end of the second NRL P-3 ELDORA flight (third IOP). Data were assimilated every hour except during the time period from 0600 28 August to 1800 UTC 28 August when 3-hour intervals were used. Prior to and between the second and third IOPs, data were limited to “synoptic” observations available to the Global Telecommunications System (GTS). Data coverage in the region of interest was limited during this time period.

## **2. Data Preparation**

Due to the enormous amount of data collected during the second and third IOPs, several data thinning strategies were implemented. Data thinning reduced the computational expense and allowed the spatial resolution of the data to more closely match the background analysis grid. In addition, it was found that numerical instabilities would often result during the next model integration phase if too many observations were included for assimilation. To reduce the frequency of the instabilities, the localization cutoff radius was increased (i.e., the impact of the observations was spread over a larger area). However, a larger localization radius increased the computational resources needed during an assimilation cycle. This was another reason for reducing the total number of observations included for assimilation.

About 80,000,000 ELDORA radial velocity observations were collected during a 6 h flight. Therefore, multiple approaches had to be used to thin the data. The horizontal resolution of radar radial velocities collected during T-PARC/TCS-08 was close to 0.5 km, whereas the grid spacing of the highest-resolution domain used for the ensemble data assimilation simulations was 3 km. After the radial velocity data were quality controlled following the procedure outlined by Bell et al. (2013), only data from every fifth “sweep” of the fore and aft antennas were retained (each sweep contained about 4 seconds of data collected during one rotation of the antenna). This increased the along-track observation spacing from about 600 m to 3 km.

Individual radar sweeps were thinned further by only retaining every fifth beam in elevation. Radial velocity and spectrum width, which is a measure of the standard deviation of radial velocity within a single radar volume, were averaged along each beam using a stride (bin size) of twenty (Figure 27). Assuming there are enough independent

samples in each radar volume, the spectrum width can be averaged by taking the square root of the average of the variances (M. Bell, 2013, personal communication). For a horizontal beam, averaging along the beam increased the observation spacing from 150 m to about 3 km. Finally, only radial velocity observations with a corresponding spectrum width  $\leq 6 \text{ m s}^{-1}$  were retained (see Figure 28b), which removed radial velocities with large observational error that would have had a minimal impact on the analysis state.

The NRL P-3 flight-level data (1-Hz) were thinned by only retaining every twenty-fifth set of observations (horizontal wind, temperature, and humidity). With a typical ground speed of about  $135 \text{ m s}^{-1}$ , the observation spacing of the thinned NRL P-3 flight-level data was about 3.4 km. Since the USAF WC-130J flight-level data were of 30-second temporal resolution, additional thinning was not required as the WC-130J ground speed of  $\sim 155 \text{ m s}^{-1}$  is equivalent to a spacing of  $\sim 4.7 \text{ km}$ . Dropwindsonde data collected from the NRL P-3 and USAF WC-130J flights were thinned by only retaining every fifth set of observations in the vertical, which corresponds to a spacing of about 40 m.

Observation error (standard deviation) values for flight-level and dropwindsonde data were determined for each observation as a function of pressure from look-up tables used by the North American Mesoscale (NAM) model. Error values for the ELDORA radial velocity data, which accounted for the largest number of observations available for assimilation, were determined in a manner similar to that used in the SAMURAI analyses. The observation error standard deviation values used for the data assimilation are indicated in Figure 28, as well as the number of observations available for assimilation.

In preparing the radial velocity data for assimilation, coordinates of the NRL P-3 aircraft and radar beam azimuth and elevation angles were paired with each observation. Hydrometeor species accounted for by the bulk microphysics scheme in the WRF-ARW model were used by the forward operator to determine an additional component of radial velocity due to precipitation fall speed. The fall speed was then added to the model-derived radial velocity, which allowed the forward operator to map the model wind speed to observation space in a manner representative of actual radar observations during the assimilation cycle.

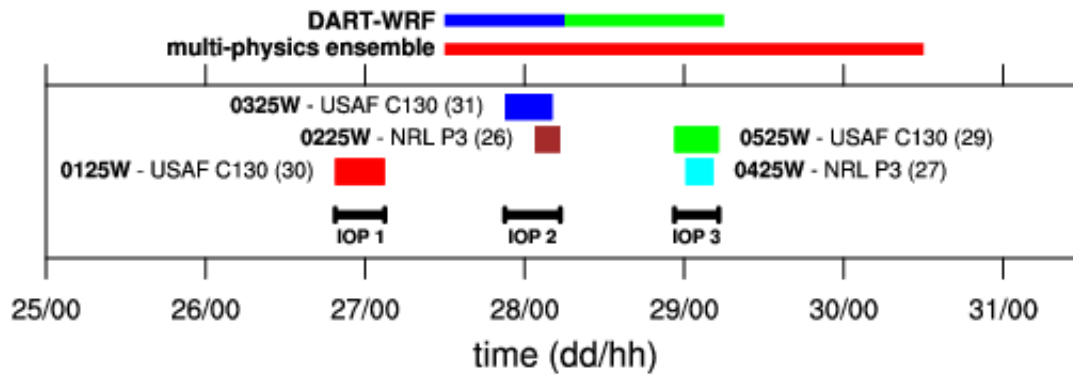


Figure 18 Approximate on-station (data collection) times of TCS025 aircraft missions. Numbers in parentheses correspond to the number of dropwindsondes deployed during each mission. The red line at the top of the figure corresponds to the simulation time of the multi-physics ensemble (including the control simulation), and the blue and green lines correspond to the first and second phases of the DART-WRF data assimilation experiments to be discussed in Chapter V.



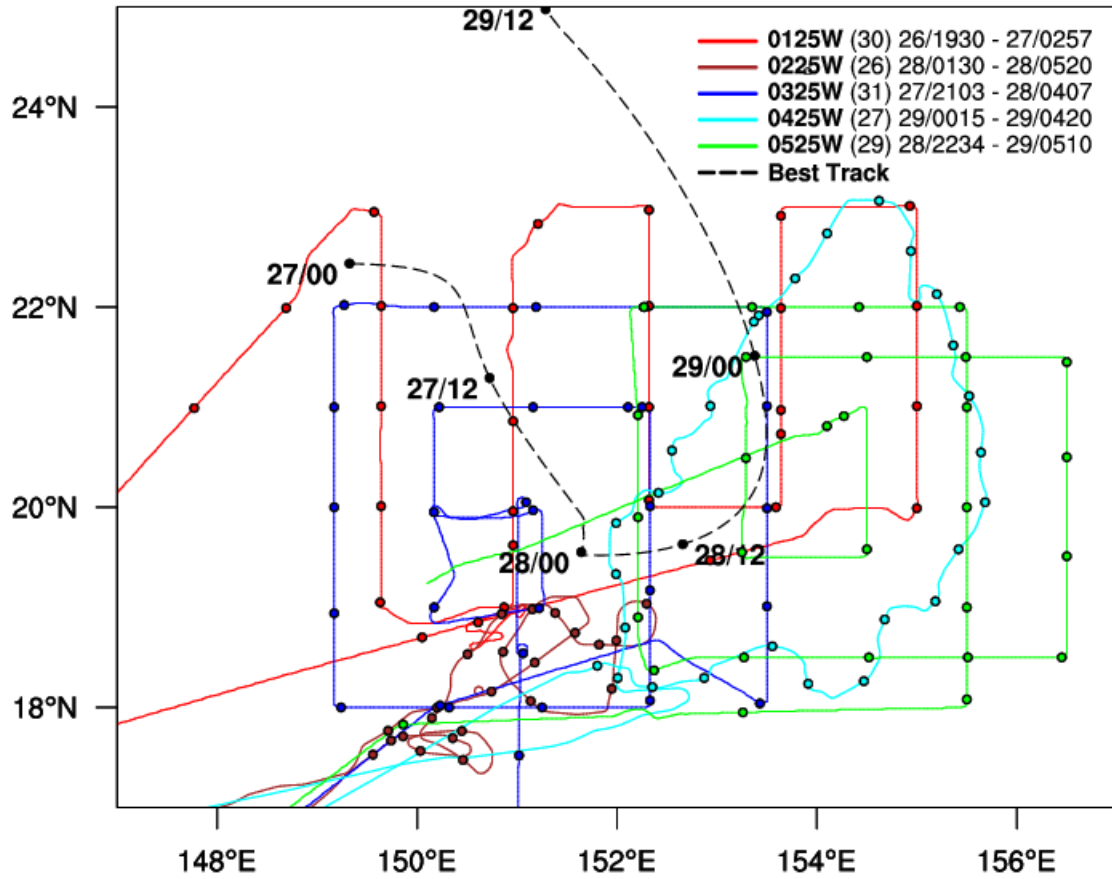


Figure 19 Flight tracks for the five aircraft missions (listed in inset) in TCS025. Flights 0125W, 0325W, and 0525W were conducted by the USAF WC-130J aircraft and flights 0225W and 0425W were conducted by the NRL P-3. Colored dots correspond to GPS dropwindsonde locations and the numbers in parentheses in the inset correspond to the number of dropwindsondes deployed during each mission. Mission times are in day/UTC time next to the flight numbers. The black dashed line indicates the subjectively-determined center positions for TCS025 based on the ECMWF 850 hPa circulation and the black dots denote the 0000 UTC and 1200 UTC positions.

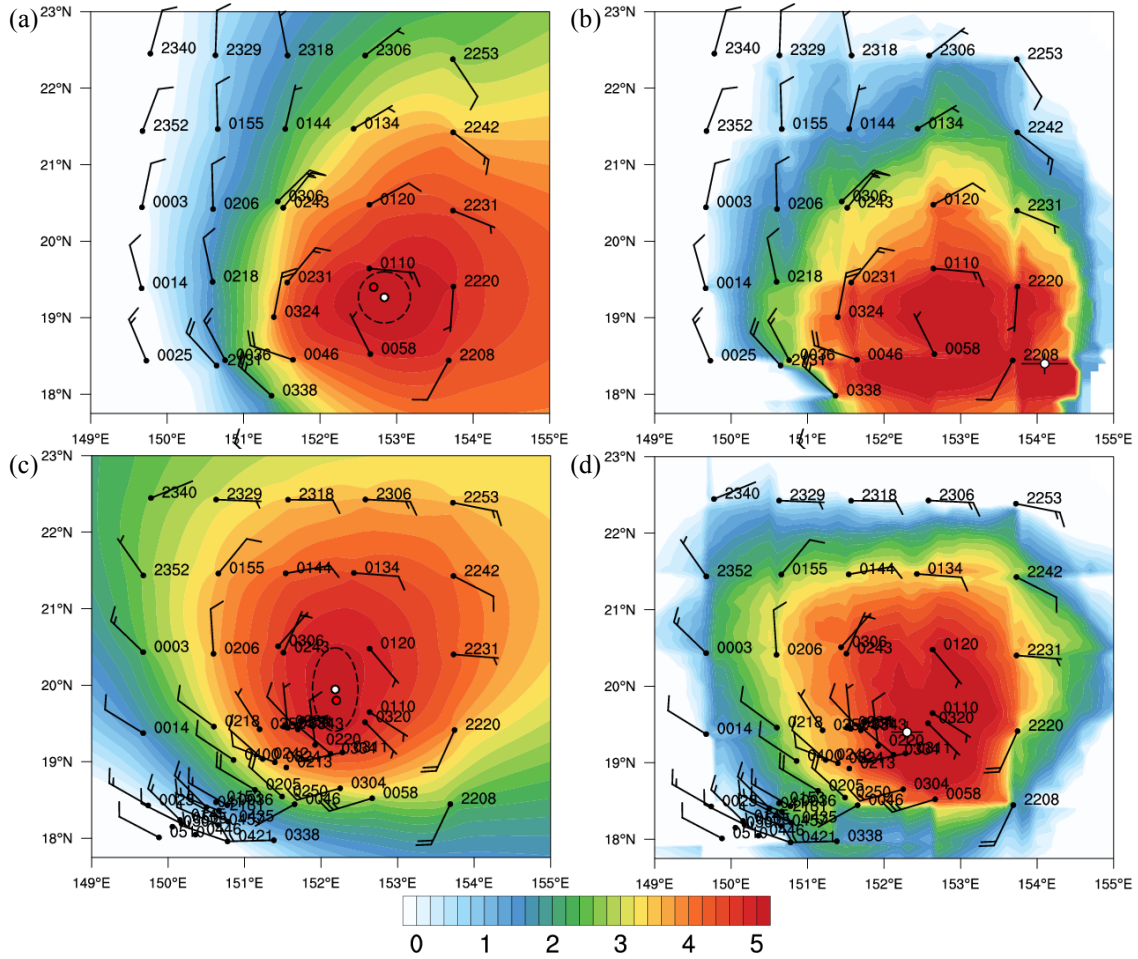


Figure 20 Example of the dropwindsonde center-finding technique computed at (a, b) 6 km altitude and (c, d) 2.5 km altitude during the second IOP. Center positions in (a) and (c) were computed following the simplified method described in this study and those in (b) and (d) were computed based on the method described by Davis and Ahijevych (2012). Black wind barbs indicate dropwindsonde winds (1 full barb = 10 kt) interpolated to each height. Additional wind barbs at 2.5 km (bottom panels) are from the NRL P-3 that flew at an altitude of  $\sim 3$  km. Shading represents the average tangential wind speed ( $\text{m s}^{-1}$ ) (see text for details). In (a) and (c), red and white dots correspond to the maximum average tangential wind speed and the circulation center determined from the centroid position of values within a threshold of the maximum value, respectively. Dashed ellipses in (a) and (c) represent an estimate of uncertainty in the circulation center position. White dots in (b) and (d) correspond to the circulation center position following the method of Davis and Ahijevych (2012), and black bars extending from the center position represent an estimate of uncertainty in the center position.

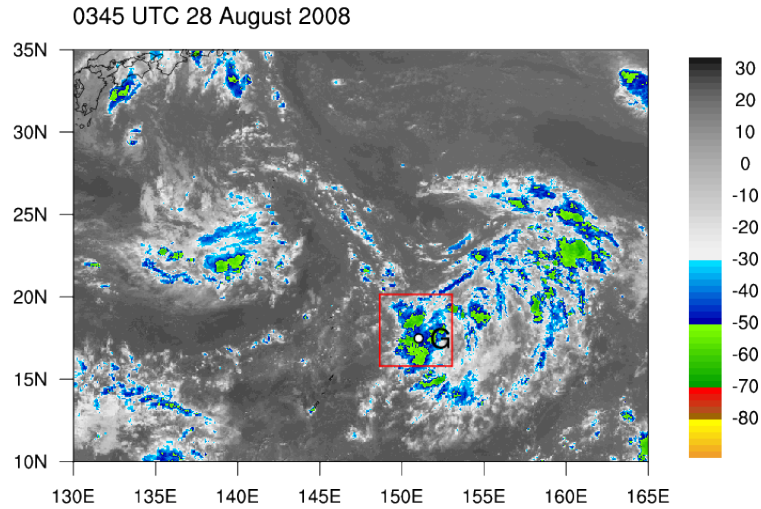


Figure 21 MTSAT IR brightness temperature ( $^{\circ}\text{C}$ ) valid at 0345 UTC 28 August. The subjectively determined center of MCS-G is marked by the white dot, and the red box defines the area used to compute the MCS intensity statistics for MCS-G at this time (see text).

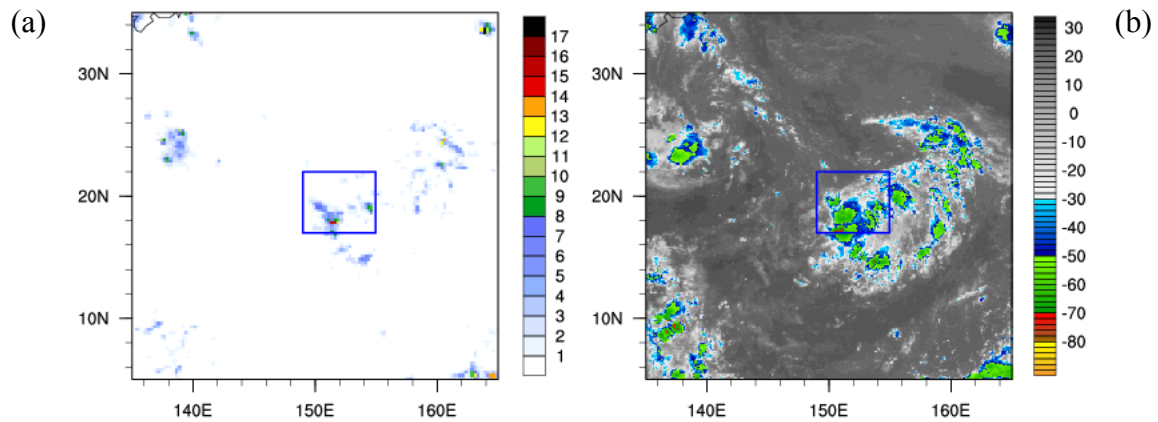
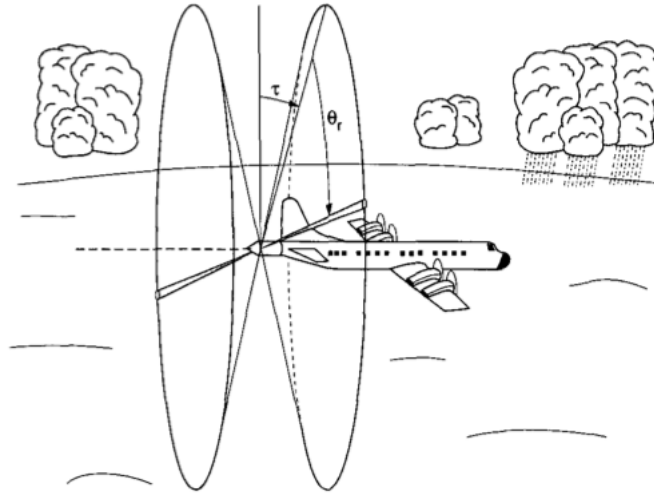


Figure 22 (a) TRMM precipitation rate estimate ( $\text{mm h}^{-1}$ ) valid at 0000 UTC 28 August and (b) MTSAT IR brightness temperature ( $^{\circ}\text{C}$ ) valid at 2345 UTC 27 August. The blue box corresponds to the area used to compute the average TRMM precipitation rate estimates in Figure 90e.

(a)



(b)

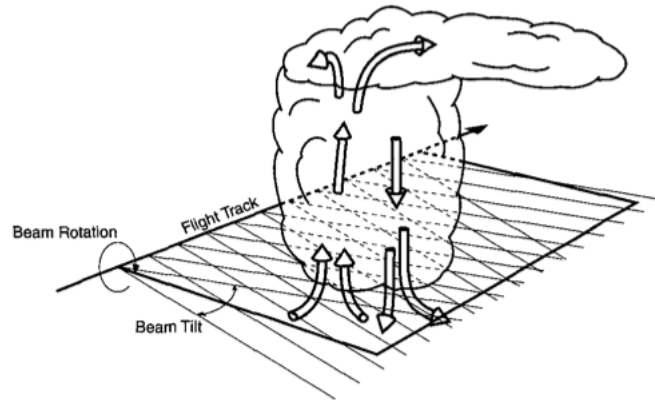


Figure 23 (a) ELDORA tail-mounted dual radar geometry, where  $\tau$  is the tilt angle (fore and aft) from a plane normal to the flight track and  $\theta_r$  is the rotation angle in the plane normal to the flight track. (b) ELDORA flight track and radar sampling schematic for a hypothetical storm. Radar data are combined from the fore and aft beams to create an analysis of the velocity and reflectivity field on horizontal planes that intersect the storm. At locations where fore and aft radar beams intersect, the two-dimensional wind field can be constructed using measured radial velocities (adapted from Hildebrand et al. 1996).

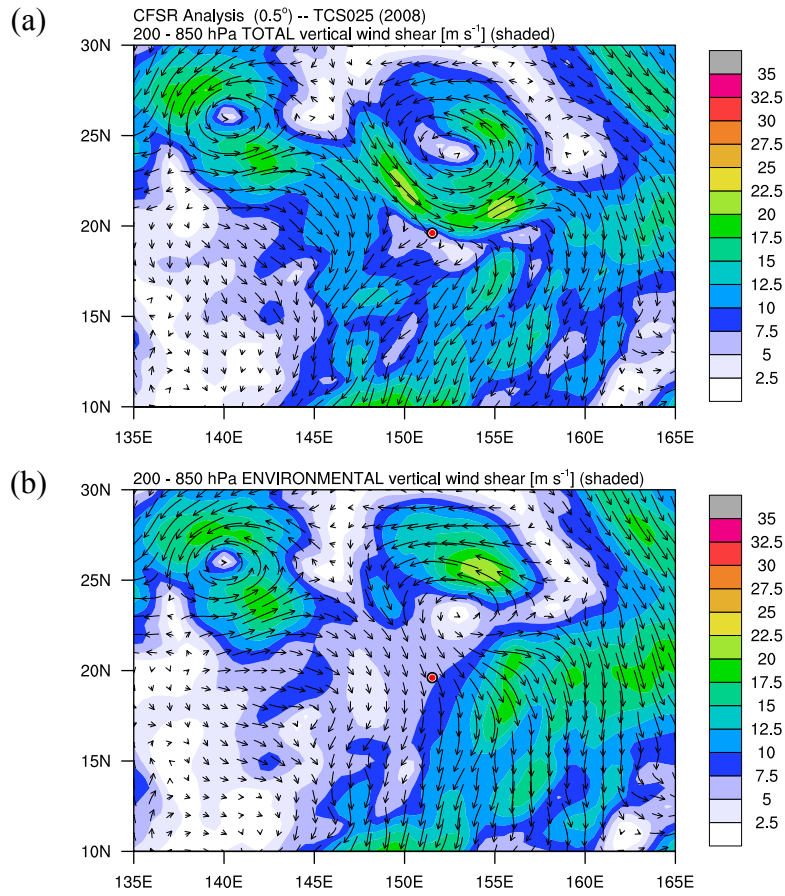


Figure 24 (a) Total and (b) environmental vertical wind shear (200 – 850 hPa) from the global CFSR analysis valid at 0000 UTC 28 August.

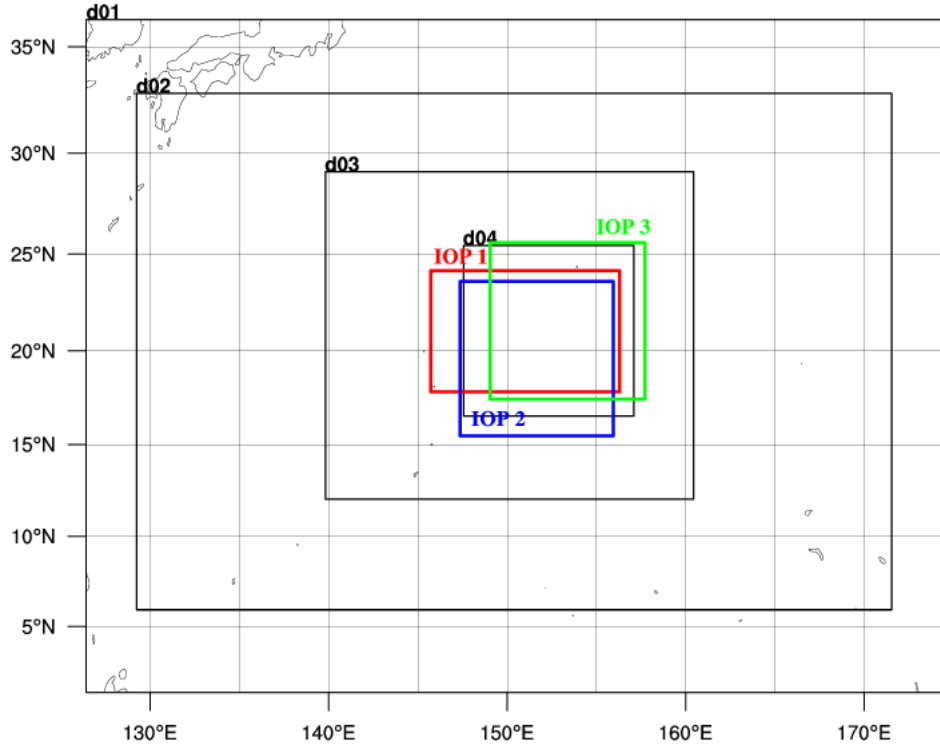


Figure 25 Domain configurations used in this study. Black boxes correspond to the domains used for the multi-physics WRF ensemble and DART-WRF ensemble data assimilation system (see text for details). The domain “d04” (1-km grid spacing) was only used for simulation 20 (see Table 3). Colored boxes represent the SAMURAI analyses domains that encompassed data collection regions during the three IOPs (see Table 1).

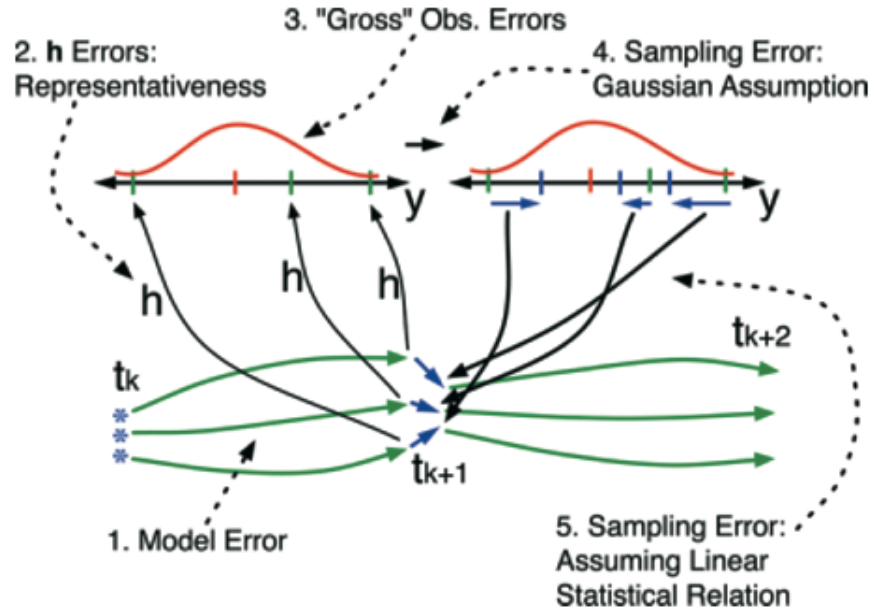


Figure 26 Ensemble data assimilation cycle similar to that used for the DART-WRF simulations (see text for details). The model is represented by the green arrows and the state vector of each ensemble is represented by the blue stars; green tick marks correspond to the model state vector mapped to observation space by the forward operator  $h$ ; red tick marks represent observations, and red curves correspond to the observation probability. The blue tick marks represent ensemble updates provided by the ensemble filter; blue arrows at top right are the increments in observation space, and the model increments correspond to the blue arrows near bottom center. Sources of error associated with each step of the data assimilation cycle are listed in the figure (from Anderson et al. 2009).

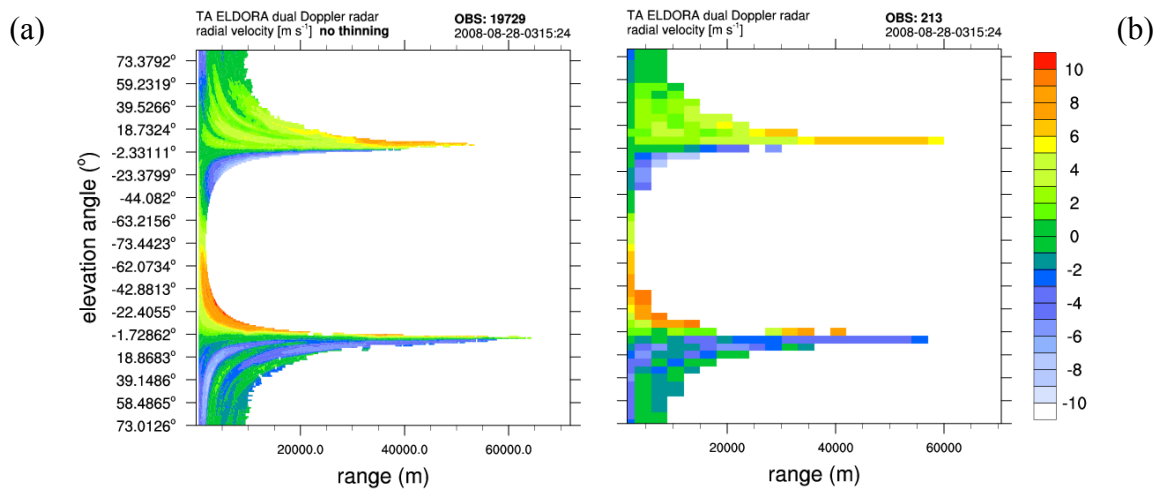


Figure 27 ELDORA Doppler radial velocity ( $\text{m s}^{-1}$ ) displayed in range-elevation coordinates collected from the aft-pointing radar (TA) during the first NRL P-3 flight (0225W) from 0315:24 to 0315:28 UTC 28 August. Radial velocity data in (a) are full resolution, and in (b) after thinning as described in text.

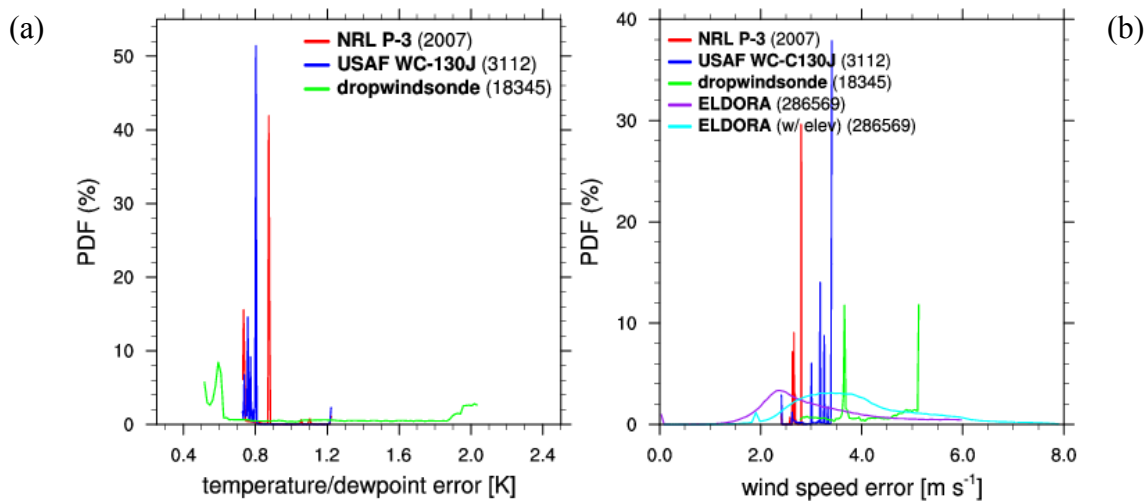


Figure 28 Observation error standard deviation values used in the DART-WRF simulations for each observation platform for (a) temperature/dewpoint (K) and (b) wind speed ( $\text{m s}^{-1}$ ). Values are shown as probability density functions in percent of total number of observations available for assimilation. The standard deviation of ELDORA radial velocity error in (b) is shown with (cyan) and without (purple) the additional factor to account for uncertainty associated with precipitation fall speed. The total number of observations available for assimilation from both the second and third IOPs is shown in inset.



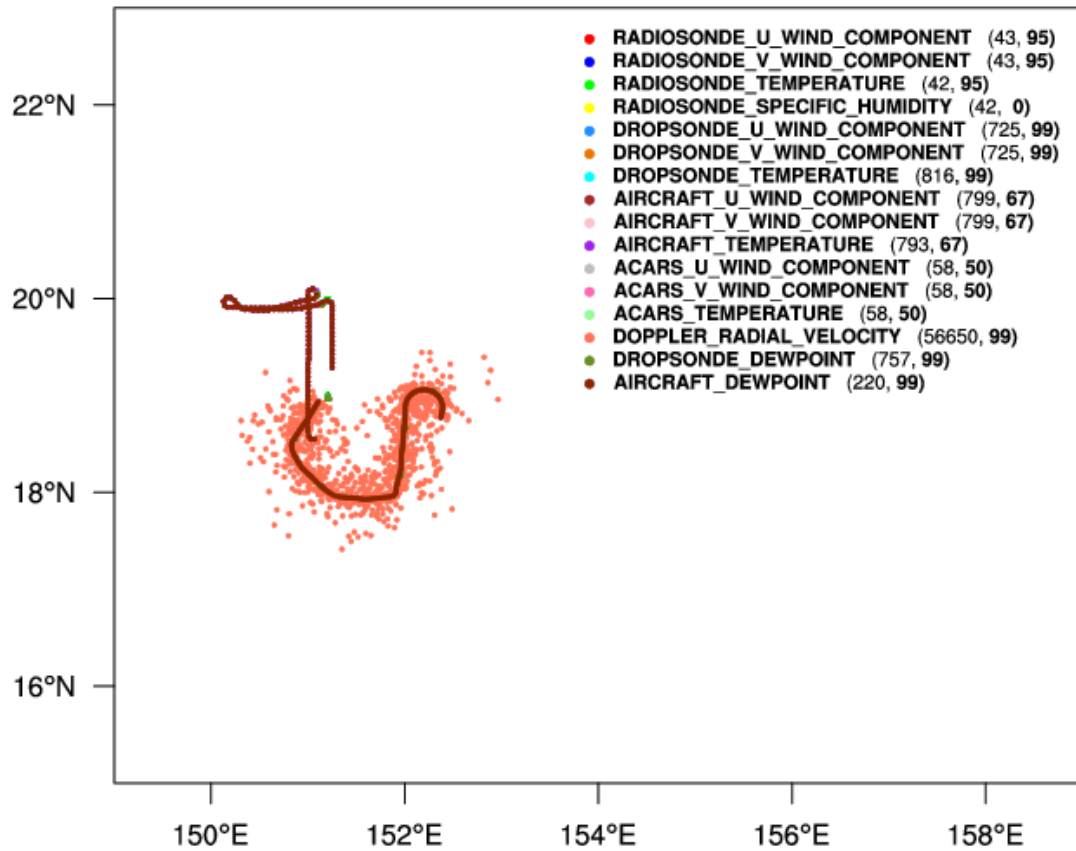


Figure 29 Observations assimilated at 0300 UTC 28 August using the DART-WRF ensemble data assimilation system. Colored dots denote the location observations assimilated and observation types are listed in inset. The numbers in parentheses in inset correspond to the total number of observations available for assimilation and the percentage of observations assimilated.

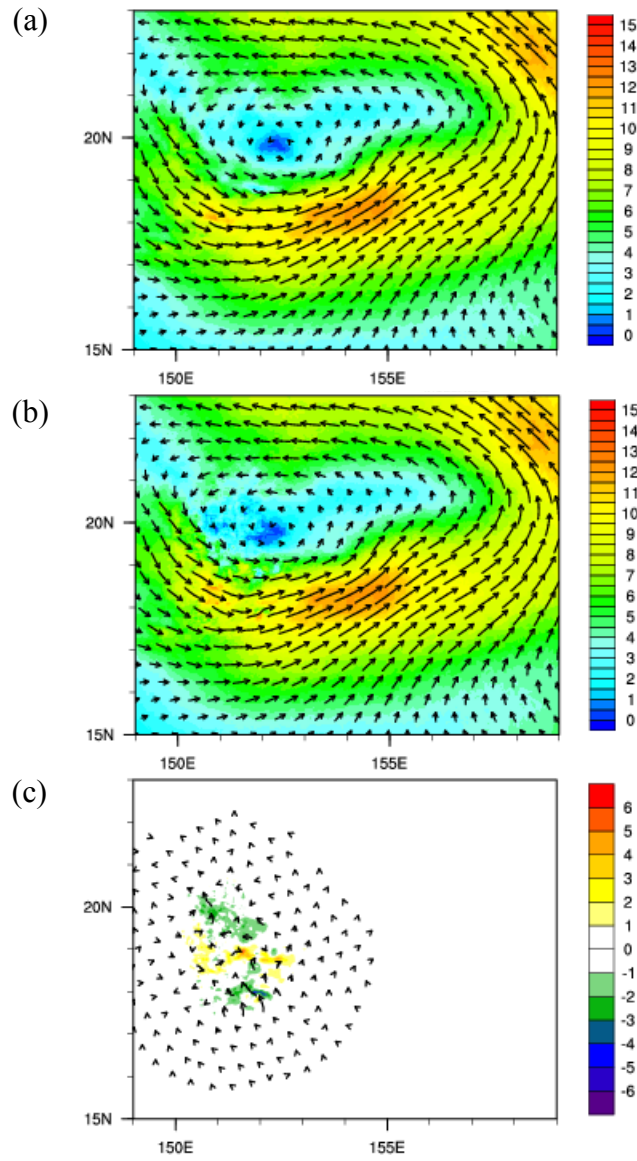


Figure 30 850 hPa wind speed ( $\text{m s}^{-1}$ , shaded and vectors) for the DART-WRF ensemble mean (a) prior, (b) posterior, and (c) increment (posterior – prior) from the 3-km domain valid at 0300 UTC 28 August.

<b>SAMURAI analysis</b>	<b>analysis time (day/UTC)</b>	<b>reference frame</b>	<b>resolution (km) (horizontal, vertical)</b>	<b>domain extent (km) (E-W, N-S, vertical)</b>	<b>background error (standard deviation) (<math>\rho u</math>, <math>\rho v</math>, <math>\rho w</math>)</b>	<b>data used</b>	<b>filter length (grid points) (i, j, k)</b>	<b>radar skip, radar stride</b>
0125W_3	27/00	E	25, 0.1	1100, 700, 12.5	15, 15, 1	C, D	4, 4, 2	-
RF05_28	28/00	S	2, 0.5	460, 320, 12.5	15, 15, 0.1	C, P, D, E	8, 8, 2	2, 2
RF05_39	28/00	S	5, 0.1	600, 650, 12.5	5, 5, 0.1	C, P, D, E	8, 8, 2	2, 2
RF06_11	29/00	S	5, 0.1	900, 900, 12.5	5, 5, 0.1	C, P, D, E	8, 8, 2	2, 2
RF06_12	29/00	E	5, 0.1	900, 900, 12.5	5, 5, 0.1	C, P, D, E	8, 8, 2	2, 2

Table 1 SAMURAI analyses of the TCS025 disturbance at the UTC times (day/hour) indicated in the second column. All analyses used the ECMWF YOTC analysis as the background field. For reference frame (third column), “E” and “S” denote earth-relative and storm-relative analyses, respectively. Abbreviations for “data used” (seventh column) are as follows: “C” is USAF WC-130J flight-level data, “P” is NRL P-3 flight level data, “D” is dropwindsonde data, and “E” is ELDORA Doppler radar radial velocity data. Other characteristics of the SAMURAI configuration are indicated in the other columns (see text).

observation platform	observation	error value (standard deviation)	units
dropwindsonde	horizontal momentum density ( $\rho u, \rho v$ )	1.0	$\text{kg m}^{-3} \bullet \text{m s}^{-1}$
	vertical momentum density ( $\rho w$ )	2.0	$\text{kg m}^{-3} \bullet \text{m s}^{-1}$
	temperature	1.0	K
	specific humidity	0.5	$\text{g kg}^{-1}$
USAF WC-130J and NRL P-3 flight-level data	horizontal momentum density ( $\rho u, \rho v$ )	1.0	$\text{kg m}^{-3} \bullet \text{m s}^{-1}$
	vertical momentum density ( $\rho w$ )	2.0	$\text{kg m}^{-3} \bullet \text{m s}^{-1}$
	temperature	1.0	K
	specific humidity	0.5	$\text{g kg}^{-1}$
ELDORA radar	radial velocity	varies (see text)	$\text{m s}^{-1}$

Table 2 Observation error values used for different observation types in the SAMURAI analyses. Error values were chosen to account for instrumentation and representativeness error.

simulation #	start time	microphysics	boundary layer	cumulus	# of domains	highest resolution	development
6	26/12	WSM6	YSU	-	3	3-km	M
7	27/12	WSM6	YSU	KF	2	9-km	M
9	27/12	Purdue Lin	YSU	-	3	3-km	M
12	27/12	WSM6 DM	YSU	-	3	3-km	S
14	27/12	WSM6	YSU	-	3	3-km	M
15	27/12	Thompson	YSU	-	3	3-km	M
16	27/12	Milbrandt	YSU	-	3	3-km	M
17	27/12	Morrison	YSU	-	3	3-km	M
18	27/12	WSM6 DM	YSU	KF	3	3-km	R
19	27/12	Kessler	YSU	-	3	3-km	R
20	27/12	WSM6	YSU	-	4	1-km	M
22	28/00	WSM6	YSU	-	3	3-km	M
24	27/12	WSM6	MYJ	-	3	3-km	S
25	27/12	WSM3	YSU	-	3	3-km	N
26	27/12	WSM5	YSU	-	3	3-km	M

Table 3 List of TCS025 multi-physics ensemble simulations conducted using the WRF model. Model initialization times (start time) are given in dd/hh (UTC). Abbreviations not mentioned in text are as follows: WSM5 is the WRF single-moment 5-class microphysics scheme, and MYJ is the Mellor-Yamada-Janjic boundary layer scheme. The cumulus parameterization scheme (cumulus) is that used on the highest-resolution grid: KF represents the Kain-Fritsch scheme and “-” indicates no cumulus scheme. The development column indicates the rate of intensification exhibited: “N” is no development, “S” is slow development, “M” is moderate development, and “R” represents rapid development.

THIS PAGE INTENTIONALLY LEFT BLANK

### **III. OBSERVATIONAL ANALYSIS**

#### **A. SYNOPTIC BACKGROUND AND SYSTEM EVOLUTION**

The TCS025 disturbance formed on the eastern periphery of a low-level trough over the subtropical western North Pacific (Figure 31c). At 0000 UTC 27 August, the trough consisted of three low-level circulations and extended from the northwest to southeast. Two TUTT cells were in close proximity to the low-level trough (Figure 31b). At this time, upper-level diffluence between the TUTT cells to the north coincided with an area of deep convection (hereafter MCS-D) that was associated with the central low-level circulation (L2) (Figure 31a).

By 28 August (Figure 32), the eastern-most TUTT cell was to the north-northeast (Figure 32b) of the low-level circulation L2 (Figure 32c) and convection organized to form MCS-G (Figure 32a). Compared to the previous day, the low-level circulation L3 had weakened and was absorbed by the circulation L2 to the west (compare Figure 31c and Figure 32c). At this time the eastern edge of the low-level trough near 155°E was marked by strong confluence and southerly low-level winds as the low-level circulation (L2 in Figure 32c) intensified.

By 29 August (Figure 33), the TUTT cell had weakened considerably (Figure 33b) and was well to the northwest of the low-level circulation (Figure 33c). An area of deep convection was present near a region of upper-level diffluence east of the TUTT cell and extended farther east to the upper-level ridge (Figure 33a). A separate cloud cluster existed to the southeast of L2 in the region of strong confluence with the southerly flow. The pressure gradient and southerly winds had increased along the eastern side of the low-level circulation, but the western branch of the low-level circulation remained weak (Figure 33c).

By 0000 UTC 30 August (Figure 34), the low-level circulation of TCS025 was no longer closed and had moved rapidly northwestward as a low-level ridge strengthened to the south and east of TCS025 (Figure 34c). Strong confluence of the southwesterly flow was contributing to an increase in convective activity (Figure 34a), and a broad

anticyclone existed aloft (Figure 34b), so conditions appeared favorable for development. However, the deep convection was trailing the low-level circulation and was not wrapped around the western side of the circulation.

Throughout its evolution, TCS025 was located in a region of moderate northerly vertical wind shear (Figure 35) as computed from the CFSR reanalysis as described in Chapter II. Although the northerly vertical wind shear relaxed somewhat as the easternmost TUTT passed north of TCS025 and an upper-level anticyclone developed aloft during 28 and 29 August (Figure 32b and Figure 33b), northerly vertical wind shear increased again on 30 August as another TUTT cell approached from the east (not shown). This increase in vertical wind shear coupled with a weakening of the low-level trough inhibited development at this time. However, the remnants of TCS025 underwent some extratropical development several days later (Davis et al. 2013).

## **B. CONVECTION AND MCS DEVELOPMENT**

Convection associated with TCS025 was intermittent and marked by repeated MCS development and decay (Malvig 2009). Periods of deep convection occurred as early as 24 August in the general region where TCS025 would later develop before the eastward extension of the low-level trough (not shown). The pulsating of convection continued and organized into a broad MCS (MCS-A) centered near 22°N, 152°E that reached peak intensity by 1130 UTC 25 August (see Figure 36 and Figure 37). This MCS moved quickly to the southeast and by 0000 UTC 26 August, only weak and relatively disorganized convection remained.

Deep convection continued to develop and decay, predominantly to the southeast of the low-level circulation center (labeled L2 in Figure 31c). At 0645 UTC 26 August, MCS-D formed near 20°N, 150°E, which was south (i.e., down-shear) of the low-level circulation L2 (see Figure 31a). During the ensuing hours, MCS-D fluctuated in intensity and structure and moved southward (Figure 36a), presumably due to the northerly flow aloft between the two TUTT cells (Figure 31b). While MCS-D was located relatively close to the low-level circulation L2 that was near 22°N, 150°E (Figure 31c), there was limited convection along the eastern periphery of the low-level trough close to the low-



level circulation L3. At 0845 UTC 27 August, MCS-D dissipated. An additional area of scattered convection near 15°N, 160°E that included MCS-E appears to have been associated with upper-level diffluence from the TUTT located to the north (Figure 31b).

Convection remained relatively disorganized and weak until after 1200 UTC 27 August when the eastern-most TUTT cell moved north-northeast of the low-level circulation (Figure 32b). At 0215 UTC 27 August, MCS-F formed (Figure 36) to the southeast of the low-level circulation L2, and was characterized by an elongated band of deep convection that was related to the low-level confluence along the eastern edge of the low-level trough (Figure 31c). At 1045 UTC 27 August MCS-G formed near 20°N, 150°E (Figure 32a), which was very close to the location of MCS development the day before. Evidently due to the influence of the northerly flow between the two TUTT cells, MCS-G moved southward. Although its structure based on IR brightness temperature fluctuated, it remained a coherent feature before dissipating by 1145 UTC 28 August. MCS-G and its surrounding environment was the primary focus during the second IOP (aircraft missions 0225W and 0325W).

After the dissipation of MCS-G, convection remained disorganized and weak until about 1800 UTC 28 August when deep convection formed (MCS-H) in a region of low-level convergence near 18°N, 154°E, which was east of the low-level circulation. Convection also formed to the north and northeast of TCS025 (MCS-I and MCS-J) (Figure 33a), which was east of the TUTT cell and near the developing anticyclone (Figure 33b). These two areas of deep convection appeared to merge around 1200 UTC 29 August (not shown), and by 0000 UTC 30 August a cyclonically banded cloud structure became evident in MTSAT brightness temperature (Figure 34a). By 1200 UTC August 30, inner-core convection had become very disorganized and weak (not shown), and by 1800 UTC August 30 the cloud structure of TCS025 began to shear apart. An area of convection formed around 0000 UTC 1 September, but failed to show signs of organization and moved quickly southward under the influence of strong northerly shear.

Prior to 28 August, the majority of MCSs formed in close proximity to the circulation center of TCS025 and propagated southward before dissipating (Figure 36a). The MCSs that developed on or after 28 August tended to propagate northward as

convection formed in the strong confluent flow at the eastern edge of the low-level trough while the trough weakened and began to accelerate northward.

Convective episodes varied in intensity with the diurnal cycle (Figure 37). The area containing IR brightness temperature values less than  $-65^{\circ}\text{C}$  relative to those less than  $-35^{\circ}\text{C}$  was largest around 1800 UTC daily, which approximately corresponds to the early morning oceanic convective maximum time (Yang and Smith 2006; Park et al. 2011). Except for 29 August, the minimum in convective intensity occurred shortly after 0000 UTC. Note that the convective minimum also corresponded to the time that the majority of aircraft observations of TCS025 were collected (see Figure 18).

The IR brightness temperatures were radially averaged relative to the 850 hPa vorticity maxima positions (Figure 38). The majority of convection formed south of the center position in the down-shear direction (Figure 35). While convection to the south of the low-level center would be consistent with previous studies (Jones 1995; Frank and Ritchie 1999; Frank and Ritchie 2001) that examined the tropical cyclone convective response to vertical wind shear, this region was also where low-level confluence was strongest.

### **C. MESOSCALE ANALYSIS**

SAMURAI analyses were conducted for each IOP using dropwindsonde data, flight-level data, ELDORA dual-Doppler radar data (when available), and the ECMWF YOTC analysis fields to examine the mesoscale structure of the TCS025 disturbance. Although dropwindsonde data were available for assimilation into the ECMWF YOTC analysis fields, flight-level data and ELDORA dual-Doppler radar data were not. Therefore, the examination of the mesoscale structure of TCS025 will focus on the impact of these additional datasets, and especially the ELDORA data. Additionally, since the sampling coverage relative to the circulation center was superior during the second IOP, data collected during the second IOP will receive the majority of attention in the analysis.

## 1. First IOP (1930 UTC 26 August – 0257 UTC 27 August)

During the first IOP centered on 0000 UTC 27 August, the USAF WC-130J conducted a “lawnmower” flight pattern (Figure 39) and deployed dropwindsondes to sample the environment of MCS-D that was beginning to decay while propagating southward, as well as the broader environment of the low-level trough.

Dropwindsondes from the first IOP sampled only a small portion of the southern branch of the low-level circulation L2 (Figure 31c), and only the western edge of the circulation L3 was sampled (Figure 40). Circulation center positions were determined as a function of height from dropwindsonde data based on the method used by Davis and Ahijevych (2012) (colored dots and ellipses in Figure 40). Although there was a significant sampling bias in that the dropwindsonde coverage failed to encompass either of the low-level circulations (L2 and L3), the dropwindsonde method identified two low-level circulations that agree relatively well with the ECMWF analysis (see Figure 31c). The circulation center location method indicated the maximum average tangential wind near the surface corresponded to circulation L2, but was closer to the location of L3 in the mid-levels. Uncertainties in the center positions were too large to evaluate the vertical alignment of the circulation during the first IOP.

The SAMURAI analysis for the first IOP agreed quite closely with the ECMWF analysis, as the low-level wind field resembled the broad trough evident in the ECMWF analysis (see Figure 31c). This is not surprising as only USAF WC-130J dropwindsonde and flight-level data were available for the SAMURAI analysis. However, the SAMURAI analysis and increment of wind speed at 5-km height indicates that a stronger mid-level circulation was present to the southeast of the flight domain (Figure 41) corresponding to the low-level circulation L3 in Figure 31c, which agrees with the dropwindsonde analysis (see Figure 40).

Profiles of relative humidity and equivalent potential temperature ( $\theta_e$ ) from the dropwindsonde deployed at the northeast corner of the USAF WC-130J flight pattern (Figure 42, blue lines) reveal dry, cool air associated with the approaching TUTT cell to the east (see Figure 31b). By contrast, the dropwindsonde near 19°N, 151°E (Figure 42, red lines) indicates the warm and moist thermodynamic environment associated with MCS-D.

## **2. Second IOP (2103 UTC August 27 – 0520 UTC 28 August)**

At the time of the second IOP, translation of the low-level circulation was slow and beginning a turn towards the northeast (see Figure 36a). Since the TCS025 disturbance remained nearly stationary during the second IOP, the earth- and storm-relative SAMURAI analyses were nearly identical (not shown). Because the first IOP aircraft mission had identified a circulation center, the second USAF WC-130J aircraft mission was defined as a “square spiral” centered on the estimated circulation center (Figure 43). Similar to the previous day, a large MCS (MCS-G) was present south of the circulation center (Figure 43).

An examination of the dropwindsonde winds from the second IOP reveals that the circulation of TCS025 was highly asymmetric (Figure 44). The strongest low-level winds were westerlies and southwesterlies in the south and southeast portions of the USAF WC-130J flight domain, and the western branch of the low-level circulation was relatively weak. The ECMWF analysis also implies the pressure gradient was increasing along the eastern edge of the low-level trough during this time (see Figure 32b and Figure 33b). In contrast, the strongest mid-level winds from the dropwindsondes were northerlies and northwesterlies on the western side of the mid-level circulation near 18.5°N, 151°E (Figure 44). This was consistent with the ECMWF analysis that exhibited a strong pressure gradient on the western side of a broad mid-level circulation that was south of the L2 low-level circulation (not shown).

Circulation center positions were determined as a function of height from dropwindsonde data collected during the second IOP: USAF WC-130J mission 0325W and NRL P-3 mission 0225W (Figure 44). Dropwindsonde coverage relative to the circulation center was much more evenly distributed than during the first IOP. The dropwindsonde-based analysis reveals that the circulation centers were poorly aligned in the vertical; the low-level circulation tilted toward the east with height, while above 2 km the circulation tilted toward the southeast (Figure 44).

Circulation center positions were also subjectively identified as a function of height for the ECMWF and SAMURAI analyses (Figure 44). The ECMWF analysis

exhibited a strong low-level circulation that tilted toward the southeast with height and extended from the surface to near 4 km. A separate mid-level circulation was evident above this, but was located farther to the southeast. In contrast, the SAMURAI analysis, which included ELDORA Doppler radar data, revealed a more fractured circulation structure in the vertical. A relatively weak low-level circulation was located near 19.5°N, 152.5°E and only extended to 2-km height. The circulation centers from 2.5-km to 6-km height were a considerable distance southwest of the low-level circulation.

The large differences in center positions from the dropwindsonde method compared to the subjectively identified centers based on gridded analysis fields (Figure 44) may be a result of including all dropwindsondes in the average tangential wind analysis and not correcting for sampling bias (see Figure 20 and in-text description). In addition, disparity in data coverage among the datasets may have also contributed to the differences in circulation center positions. Whereas dropwindsondes were generally deployed with 100-km spacing, the ECMWF analysis had of ~25-km grid spacing and the SAMURAI analysis had 5-km grid spacing. Thus, the scales of motion sampled by the dropwindsondes were much larger than for the ELDORA radar winds, or resolved by the ECMWF analysis. It is possible that the center positions identified from the ECMWF and SAMURAI analyses represent small-scale centers embedded in the larger circulations whose centers were identified using the dropwindsonde method.

The SAMURAI analysis for the second IOP reveals an asymmetric vortex structure in the low- and mid-levels (Figure 45a,b). The SAMURAI wind speed increment field at 1.5 km (Figure 46) suggests the low-level circulation was much weaker than in the ECMWF analysis that was utilized as the background field. Additionally, the cyclonic circulation in the mid-troposphere in the SAMURAI analysis was stronger than the low-level circulation, which is indicative of a cold-core circulation. At this time, the mid-level circulation center was positioned ~110 km to the south-southwest of the low-level circulation center. Low- to mid-tropospheric vertical wind shear induced from the mid-level circulation was impacting the low-level circulation. Strong northeasterly winds in the northwest quadrant of the mid-level circulation (Figure 45a) were near the center of the low-level circulation (black dot in Figure 45a).

The potential impact of the vertical misalignment was examined by comparing the mesoscale vertical wind shear (system-relative flow) in the SAMURAI analysis between

5- and 1.5-km height (Figure 45) with an identical circulation structure that was pseudo-aligned in the vertical (i.e., as if the mid- and low-level circulations were vertically aligned). The system-relative flow for the misaligned circulation was computed as the difference between the box-average 5-km wind vector centered over the 1.5-km circulation (dashed black box in Figure 45a) and the box average 1.5 km wind vector centered on the 1.5-km circulation (solid black box in Figure 45b). In contrast, the pseudo-aligned system-relative flow was defined as the difference between the box-average 5-km wind vector centered on the 5-km circulation (solid red box in Figure 45a) and the box average 1.5 km wind vector centered on the 1.5-km circulation (solid black box in Figure 45b). The system-relative flow for the misaligned circulation was 9.3 kt from the northeast (Figure 47), whereas the system-relative flow for the pseudo-aligned circulation was only 5.4 kt from the north-northwest. This indicates that the misalignment of the circulation resulted in a larger system-relative flow compared to if the circulation had been vertically aligned. As will be discussed later in this chapter, the large system relative flow allowed low- $\theta_e$  air of the background environment to infiltrate the circulation of TCS025, which negatively impacted the inner-core thermodynamic environment and limited development.

A south to north vertical cross section through the mid- and low-level circulation centers from the SAMURAI analysis (Figure 48a) reveals that two distinct vorticity centers existed at this time. To the north, and mostly outside the range of the ELDORA Doppler radar, a shallow area of enhanced relative vorticity existed below 1-km height. Above this, weak negative vorticity extended upwards to 10 km. An area of positive vorticity was present farther to the south in the mid-levels, and was almost entirely separate from the low-level cyclonic vorticity to the north. Relative vorticity was greatest near 6.5-km height for the mid-level vorticity feature in the SAMURAI analysis.

Although separate low- and mid-level vorticity maxima can be identified in the vertical cross section constructed from the ECMWF analysis (Figure 48b), the vorticity structure appears to be better aligned vertically than in the SAMURAI analysis. The ECMWF analysis had an area of low-level vorticity that extended upward to 2.5-km height, which is considerably higher than in the SAMURAI analysis. A second vorticity

maximum near 3-km height that was not present in the SAMURAI analysis existed just south of the low-level feature. Near 6-km height in the ECMWF analysis there is a broad vorticity feature associated with the southward shift in the circulation center at this level (see Figure 44), but it is much weaker compared to the SAMURAI analysis.

The contrasts in the low-level wind fields (see Figure 46) and vorticity analyses (Figure 48) suggest that the ECMWF and SAMURAI analyses exhibited fundamental differences in vortex structure. The ECMWF analysis possessed a much stronger low-level circulation that tilted southward into the mid-troposphere. In contrast, the SAMURAI analysis depicted a strong mid-level circulation near 6-km height that was almost entirely separate from a shallow low-level circulation to the north. The low-level circulation was also much weaker than in the ECMWF analysis. Therefore, it is possible that the low-level wind field more closely resembled the broad trough observed the day before (see Figure 31c) rather than the well-defined low-level circulation of the ECMWF analysis. Because the low-level circulation in the SAMURAI analysis was outside the range of the ELDORA Doppler radar (see Figure 48a), it is uncertain whether the low-level vorticity feature in the SAMURAI analysis was realistic or due to an over-reliance on the ECMWF background field where there was limited data.

Potential temperature anomalies in Figure 48 were defined using a domain-mean SAMURAI profile that was roughly limited to where dropwindsonde data were available. Negative anomalies were present below the positive mid-level vorticity feature, and were greatest in magnitude near the surface and at 4-km height. Above the mid-level vorticity feature, a positive potential temperature anomaly was present, and was a maximum near 8.5 km.

The vertical cross section of the SAMURAI analysis (Figure 48a) also indicates that vertical motions were relatively weak at this time. An area with positive vertical motion was present near 8-km height south of the near-surface vorticity feature and above the low-level negative potential temperature anomaly. The divergence profile in Figure 48a indicates strong low-level convergence was collocated with the low-level vorticity feature, which is characteristic of a convective divergence profile. In contrast, strong mid-level convergence and low-level divergence were associated with the midlevel vorticity feature, which is typical of a MCV (Raymond and Jiang 1990; Bartels

and Maddox 1991; Houze 2004). In addition, the positive temperature anomaly in the SAMURAI analysis above 6.5 km height (Figure 49a) over the negative low-level temperature anomaly (Figure 49b) is also characteristic of the thermal structure of a balanced mid-level vortex (Chen and Frank 1993), and based on the reflectivity pattern observed by the ELDORA radar at 5-km height during flight 0225W (Figure 50), the region surrounding the mid-level circulation was predominantly characterized by stratiform precipitation.

A south-to-north vertical cross section of  $\theta_e$  constructed using dropwindsonde data (Figure 51) just west of the midlevel circulation center during the second IOP indicates the presence of convectively-generated, low-level cold pools. Note the lower values of  $\theta_e$  near the surface in the dropwindsonde deployments at 0338, 0046, 0324, and 0231 UTC (Figure 51). As indicated in Figure 43, the USAF WC-130J was passing through the southern region of MCS-G at the time of the 0046 UTC dropwindsonde release. Stepped-Frequency Microwave Radiometer (SFMR) rain rates (Figure 52, blue line) corresponding to the time of the 0046 UTC dropwindsonde release confirm the presence of precipitation, and MTSAT IR brightness temperature, which was interpolated spatially and temporally to the USAF WC-130J flight track (Figure 52, red line), reveals that cloud-top temperature values were suggestive of a convective environment. Above the near-surface cold pool in the 0046 UTC profile (Figure 51), a plume of increased  $\theta_e$  relative to the background environment extended into the upper levels, which is an indication of deep moist convection. By contrast, an extensive region of low- $\theta_e$  air in the mid-troposphere north of the convective region (up-shear) is also evident in Figure 51, which was relatively cold, dry air associated with the TUTT cell to the north (near 24°N, 154°E in Figure 32b).

### **3. Third IOP (2234 UTC 28 August – 0510 UTC 29 August)**

At the time of the third IOP, the translation speed of the low-level circulation had increased significantly toward the north-northwest (see Figure 36a). Due to the rapid forward movement of TCS025 in association with the tightening of the low-level pressure gradient along the eastern side of the circulation (see Figure 33c), the wind structure was highly asymmetric.



The SAMURAI analysis for the third IOP in the ground-relative frame (Figure 53a) indicates that strong southerlies existed along the east side of the low-level circulation with almost no northerly return flow on the western side of the circulation. The strongest winds existed near 1.5-km height. The SAMURAI analysis in the storm-relative frame (Figure 53b) reveals a more symmetric wind structure, with a weak, elongated low-level circulation consisting of two circulation centers. The northern-most circulation center near 23.7°N, 154.5°E originated from an area of enhanced low-level convergence and vorticity to the southeast of the low-level circulation that can be identified during the second IOP (not shown). This vorticity feature wrapped cyclonically around to the north of the original circulation center as the TCS025 system moved northward.

Flight plans for the third IOP were designed based on the broad cyclonically banded convective structure of MCS-H, which was almost entirely south of the circulation center (Figure 54). This resulted in a south-southeastward bias relative to the circulation center for observations collected during the third IOP. Surface wind data from the National Aeronautics and Space Administration (NASA) Quick Scatterometer (QuikSCAT) reveals the low-level circulation center was near 24°N, 152°E at ~0747 UTC 29 August (Figure 55). However, the low-level circulation center diagnosed from the SAMURAI analysis in Figure 53a valid at 0000 UTC 29 August (~8 hours earlier) was near 21.6°N, 153.8°E, which indicates the system was rapidly moving toward the northwest away from the convective area during this time.

Because the NRL P-3 flight track was designed to circumnavigate the disturbance to aid in a post-storm budget analysis, this limited the area covered by the ELDORA radar to a narrow swath around the periphery of the disturbance (Figure 56). Unfortunately, this coverage does not allow for a detailed analysis within the convective structure or near the circulation center to the north.

A dropwindsonde analysis of the circulation structure in the vertical implies the vortex exhibited increased vertical alignment in the lowest 4 km compared to the previous IOP (Figure 57), but an appreciable eastward shift of the vortex with height was

analyzed from 5 - 6 km. However, similar to the first IOP (see Figure 40), dropwindsonde coverage during the third IOP was strongly biased to the south of the circulation center. Due to the asymmetric wind field of TCS025 at this time, and this bias in dropwindsonde coverage, caution must be used when interpreting the circulation center positions obtained from this method. A diagnosis of the circulation structure from the SAMURAI analysis (not shown) suggests the low-level circulation on the northern periphery of the flight domain was quite shallow as it only extended from the surface to 2-km height. Furthermore, the mid-level circulation was displaced to the south, which was similar to the vertical structure observed during the second IOP.

#### **D. THERMODYNAMIC EVOLUTION**

For each of the three USAF WC-130J flights, MTSAT IR brightness temperatures were interpolated to the location and time of each dropwindsonde. Average vertical profiles of relative humidity,  $\theta_e$ , and DCAPE were created for each flight for all dropwindsondes with a corresponding IR brightness temperature less than  $-35^{\circ}\text{C}$  and for dropwindsondes with an IR brightness temperature greater than  $-35^{\circ}\text{C}$ , which allowed for a comparison of the thermodynamic conditions of the convective and non-convective environments, respectively.

The average profiles reveal low-level relative humidity (Figure 58a) was quite high throughout all IOPs ( $> 80\%$ ) in both the convective and non-convective environments. However, mid- and upper-level relative humidity in the non-convective environment decreased during the second IOP (0325W) compared to the first IOP (0125W) before increasing during the last IOP (0525W). Average profiles of  $\theta_e$  reveal similar trends in the mid- and upper-troposphere during the second IOP (Figure 58b). Low- $\theta_e$  air observed during this time was a result of the TUTT cell to the north being in close proximity to TCS025 (see Figure 32b and Figure 51). The largest values of DCAPE in the non-convective environment existed during the second IOP (Figure 58c). This indicates there was a potential for strong downdrafts if dry environmental air associated with the TUTT mixed into the convective environment. The importation of low- $\theta_e$  air into the boundary layer via strong downdrafts may have limited further convection

(Riemer et al. 2010). By the time of the last IOP, the TUTT cell had weakened considerably and had moved a significant distance away from TCS025 such that its thermodynamic influences no longer impacted TCS025 (see Figure 33b).

Profiles of average temperature anomalies (Figure 58d) constructed from dropwindsondes deployed close to the circulation center (within 250 km) reveal that the lower-tropospheric near-surface layer was  $\sim 0.5$  K colder relative to the dropwindsonde mean, and the mid- and upper levels were generally warmer. During the second IOP (missions 0225W and 0325W), the inner-core environment was colder than during the first or third IOPs. Similar to the relative humidity,  $\theta_e$ , and DCAPE profiles, this is believed to have been due to the thermodynamic influence of the TUTT cell to the north. The large negative low-level temperature anomaly observed during NRL P-3 flight 0225W might have in part been due to a sampling bias, as a large number of dropwindsondes were deployed near the low-level circulation center that was dominated by negative low-level temperature anomalies (see Figure 49b). A sampling bias might have also contributed to the increase in  $\theta_e$  during the last IOP relative to the first two IOPs (Figure 58b), as the majority of dropwindsondes were deployed south of the circulation center (see Figure 57).

The evolution of mid-level  $\theta_e$  prior to and extending past the second IOP reveals low- $\theta_e$  air to the north of the broad mid-level circulation at 1200 UTC 27 August (Figure 59a). The lowest  $\theta_e$  air was near  $23.5^\circ\text{N}$ ,  $156^\circ\text{E}$  and was associated with the upper-level TUTT cell. By 0000 UTC 28 August (Figure 59c), low- $\theta_e$  air had moved westward to become positioned north of the strengthening mid-level circulation. The low- $\theta_e$  air was being advected southward along the western side of the mid-level circulation (Figure 59c-e). By 1200 UTC 28 August (Figure 59e), low- $\theta_e$  air had reached  $18^\circ\text{N}$ ,  $151^\circ\text{E}$  while the lowest  $\theta_e$  air associated with the TUTT cell continued to move farther to the northwest (Figure 59f).

Back trajectories were computed from the CFSR dataset by selecting grid points at various pressure levels within the boxed region of  $18^\circ\text{--}22^\circ\text{N}$ ,  $148^\circ\text{--}152^\circ\text{E}$  that had a

relative humidity  $< 70\%$  at the ending time of 0000 UTC 28 August. The back trajectories ending at 500 hPa (Figure 60a), and at 400 hPa (not shown), all originated from the northeast in a region of low- $\theta_e$  air near the eastern TUTT, which later became positioned close to TCS025 on 28 August. These air parcels were advected around the circulation of the TUTT and descended slowly while moving westward with the TUTT. Eventually these air parcels became positioned immediately north (up-shear) of the low-level circulation at 500 hPa. These trajectories define the mid-level low- $\theta_e$  air along the north side of the vertical cross section of  $\theta_e$  constructed from dropwindsonde data in Figure 51.

The majority of back trajectories ending at 600 hPa (Figure 60b) originated from a different source region to the west of TCS025. Low- $\theta_e$  air near  $23^\circ\text{N}$ ,  $135^\circ\text{E}$  was advected eastward along the southern side of the TUTT cell that was west of TCS025. Although the circulation of the TUTT cell was a maximum near 200 hPa, a weak circulation could still be identified at 600 hPa with westerly winds to the south of the geopotential height minimum. Below this level, westerly winds were also present and merged with the southern part of the broad low-level trough in which TCS025 formed (see Figure 31c) that extended from the northwest to the southeast. This deep layer of westerly flow advected low- $\theta_e$  air eastward to the south of TCS025 (down-shear). This air stream can be identified as a relatively shallow region of low- $\theta_e$  air in Figure 51 along the south side of the dropwindsonde vertical cross section. In addition, a few of the trajectories ending at 600 hPa followed a similar path to the relatively dry air that ended up at 500 hPa. These trajectories define the lowest levels of the influx from the eastern TUTT cell. Finally, several trajectories originated from regions of higher- $\theta_e$  air to the west that experienced drying while moving to the east. These parcels were positioned north of TCS025 at 0000 UTC 28 August.

The trajectories ending at 700 hPa with relative humidity  $< 70\%$  (Figure 60c) all originated from the same low- $\theta_e$  air region to the west that was responsible for the bulk of the 600 hPa trajectories. These trajectories all ended up south of the TCS025 circulation at 0000 UTC 28 August.

Two main source regions of low- $\theta_e$  air can be identified from the trajectory analysis. The mid-level low- $\theta_e$  air to the north of TCS025 that originated from the TUTT cell to the east (Figure 60a) had a larger negative impact on the thermodynamic environment of TCS025 due to presence of northerly environmental vertical wind shear (see Figure 35) and enhanced system-relative flow that resulted from the vertical misalignment of the circulation (Figure 47). This is consistent with the southward penetration of low- $\theta_e$  air from this northern air stream along the western edge of the mid-level circulation in Figure 59.

Near the end of the second IOP, deep convection associated with MCS-G was beginning to diminish in intensity, which is indicated by the broad areas of weak reflectivity in Figure 50 and the increase in IR brightness temperature (see long dashed line in Figure 38). This absence of deep convection may have been partially due to diurnal fluctuations in convective intensity (Figure 37), however, deep convection near the low-level circulation ( $\sim 20^\circ\text{N}$ ) failed to redevelop after this time based on longitudinally averaged IR brightness temperature (Figure 61). This suggests that the low- $\theta_e$  air associated with the TUTT to the north of TCS025 inhibited deep convection after this time. Vertical wind shear coupled with poor vertical alignment of the circulation structure were responsible for increased system-relative flow that allowed mid-level low- $\theta_e$  air up-shear of TCS025 to penetrate the disturbance and deplete boundary layer  $\theta_e$  through convective downdrafts. Synoptic conditions became less favorable before the boundary layer could replenish  $\theta_e$  via surface fluxes, and this suppressed subsequent convection and frustrated further development of the TCS025 disturbance.

#### **E. OBSERVATIONAL COMPARISON WITH TY FANAPI (2010)**

During the Impact of Typhoons on the Ocean in the Pacific (ITOP) field program, six USAF WC-130J missions observed the development and intensification of TY Fanapi over six days (Figure 62). TY Fanapi originated from an easterly wave (Figure 63c) and developed slowly as it moved toward the west-northwest. The atmospheric data set collected during TY Fanapi is noteworthy in that the first three flights employed a high-altitude ( $\sim 300$  hPa) surveillance pattern similar to that used for TCS025 and collected

observations prior to the intensification to a tropical storm. At this time, the intensity of Fanapi was comparable to that of TCS025 (Figure 64a), which allowed for a comparison with observations collected during TCS025. Vertical wind shear during this time was very weak (Figure 64b), and based on IR brightness temperatures (Figure 63a), convection appeared scattered and relatively disorganized.

Circulation center positions for Fanapi (Figure 65) derived from dropwindsonde data collected during the second USAF WC-130J flight 0220W (2014 UTC 13 September to 0258 UTC 14 September) reveal the circulation of Fanapi was much better aligned in the vertical compared to TCS025 (see Figure 44). Dropwindsonde winds in Figure 65 also indicate Fanapi possessed a symmetric wind field compared to the highly asymmetric structure exhibited by TCS025 (see Figure 44).

Average profiles of  $\theta_e$  were constructed from all dropwindsondes deployed during each USAF WC-130J mission for TCS025 and the first three USAF WC-130J missions for Fanapi (Figure 66). These profiles reveal that the average thermodynamic structure of TCS025 and Fanapi were quite similar during the early stages of the development of Fanapi (first two USAF WC-130J flights). Furthermore, the lowest  $\theta_e$  in the mid-troposphere was actually observed during the second Fanapi mission (0220W) to the northwest of the low-level circulation. Thus, the thermodynamic environment of Fanapi was not more favorable for development than it was for TCS025. In addition, average ocean temperature profiles from AXBT data indicate that TCS025 and Fanapi had very similar oceanic conditions. The sea-surface temperatures (SSTs) were generally greater than 29°C, and the ocean mixed layer extended down to about 50 m depth (Figure 67).

Smith and Montgomery (2012) found a large difference in the  $\theta_e$  deficit between developing and non-developing systems. Deficits of  $\theta_e$ , which are defined as the differences between the low-level maximum and mid-tropospheric minimum values of  $\theta_e$ , had similar trends for both disturbances (Figure 68). Following the first flights in TCS025 and Fanapi, the  $\theta_e$  deficit declined in the convective environments while increasing in the non-convective environments. For TCS025, this corresponded to when the TUTT was in closest proximity to TCS025 (see Figure 32), and according to the

ECMWF operational analysis, a TUTT was also present to the northwest of the low-level circulation during the second Fanapi flight (0220W) (see Figure 63b). Thus, except for a slightly smaller  $\theta_e$  deficit within the convective environment of Fanapi, there was very little discernable difference in  $\theta_e$  deficit between Fanapi and TCS025.

Similar to TCS025, convection associated with Fanapi was intermittent during its early stages of development (Figure 69). The early convective pulses experienced by Fanapi appeared to cover a slightly larger area (extending farther from the center of circulation) than those associated with TCS025. Convection remained relatively scattered and did not organize into coherent MCS structures as it did for TCS025. While TCS025 may have had too large vertical wind shear (Figure 35), vertical wind shear for Fanapi may have been too small (Figure 64b), since Trier and Davis (2002) and Musgrave et al. (2008) suggest some vertical wind shear may help in the organization of convection.

Both TCS025 and Fanapi experienced a lull in convective activity near the time of the second USAF WC-130J flights (0225W and 0220W, respectively) (Figure 69). Convection associated with Fanapi was spread out relative to the circulation center, which may have exposed the convection to the negative effects of the dry mid-tropospheric air in the surrounding environment (Nolan and McGauley 2011). During this period, low- $\theta_e$  air was able to penetrate areas of convection, deplete boundary layer  $\theta_e$ , and inhibit subsequent convection for a period of time.

However, because Fanapi possessed a more symmetric and vertically-aligned circulation, the thermodynamic impact of the low- $\theta_e$  air on the inner-core of the system may have been minimized. A comparison of dropwindsondes near the two circulation centers confirms the  $\theta_e$  values were larger for Fanapi in both the mid-troposphere and near the surface (Figure 70). Weak system-relative flow due to the vertically aligned circulation protected the inner-core environment from low- $\theta_e$  air and permitted convection to quickly recover, which likely aided in the development of Fanapi. Since TCS025 and Fanapi had very similar oceanic conditions, it is unlikely that the rebound in convective activity for Fanapi was a result of larger surface fluxes.

In contrast to Fanapi, the inner-core region of TCS025 was left exposed to the negative effects of vertical wind shear and dry air due to its asymmetric, poorly aligned circulation. Larger system-relative flow due to the vertical misalignment of the circulation caused low- $\theta_e$  air to penetrate the low-level circulation of TCS025 through convective downdrafts, which retarded subsequent convection. Deep convection near the inner-core could not recover before synoptic conditions became unfavorable for further development.

## **F. OBSERVATIONAL SUMMARY AND DISCUSSION**

Gray (1975) stated that high SST ( $>26.5^{\circ}\text{C}$ ), abundant low-level and mid-level moisture, convective instability, small vertical wind shear, and increased low-level relative vorticity constituted an environment conducive to storm formation. Perhaps except for vertical wind shear, these favorable large-scale conditions for tropical cyclogenesis existed, yet TCS025 failed to develop. Although the TCS025 disturbance appeared to have been a system on the verge of some development, the combination of vertical wind shear, low- $\theta_e$  air associated with the TUTT to the north, coupled with its weak, asymmetric, and misaligned circulation prevented it from developing.

During the first IOP, a weak low-level circulation was present to the northwest of the flight track, but appeared separate from the midlevel circulation that was farther to the east (see Figure 40). The mesoscale analysis of data collected during the second IOP (centered on 0000 UTC 28 August) revealed the midlevel circulation was now positioned closer to the low-level circulation, but a significant vertical misalignment of the vortex still existed with a relatively weak low-level circulation to the north of a stronger midlevel circulation (see Figure 48). This misalignment persisted during the third IOP on 29 August.

Davis and Ahejivech (2012) state that vortex re-alignment might occur via the formation of a new low-level circulation below the mid-level circulation through deep convection. Between the first and second IOPs of TCS025, several episodes of deep convection occurred in close proximity to the mid-level circulation and organized into persistent MCS features (MCS-D and MCS-G). It is unclear from this analysis of TCS025 whether a new low-level circulation center formed in close proximity to the



midlevel center, or if the preexisting low-level circulation observed during the first IOP was drawn closer as a result of the convective bursts. It is possible that both processes occurred. Within the broad cyclonic circulation of the trough evident during the first IOP (Figure 31c), episodes of deep convection might have formed low-level pressure minima via latent heat release and thereby established new lower-tropospheric circulation centers. Alternatively, a weak low-level circulation center that existed some relatively small distance from the mid-level circulation where deep moist convection developed may have been drawn into the developing low-level circulation and absorbed. Therefore, it might appear as though a preexisting low-level circulation center had become vertically aligned with the mid-level circulation. For example, the eastern-most circulation embedded in the trough (circulation L3 in Figure 31c) was relatively free of deep convection during the first IOP. However, deep convection was present near the circulation L2 to the west, which allowed this circulation to strengthen and eventually absorb the circulation L3 to the east.

Although vertical alignment of the vortex in the second IOP had somewhat improved compared to the first IOP based on the dropwindsonde center analyses, an appreciable distance (~110 km) between the low- and mid-level circulations still remained. Vertical misalignment of the circulation caused the low- to mid-tropospheric vertical wind shear (system-relative flow) to be larger in magnitude relative to a well-aligned circulation (see Figure 47). Furthermore, the tangential wind field appeared relatively weak and asymmetric (see Figure 45b), which suggests that the convective activity associated with TCS025 lacked sufficient intensity to promote increased alignment of the circulation while in the presence of northerly vertical wind shear. Deep convection that did form tended to move southward away from the low-level circulation (see Figure 36). In addition, the convection was relatively short-lived as it did not persist through the diurnal convective minimum (see Figure 37).

The large-scale environment of TCS025 was modulated by TUTT cells that moved westward to the north of TCS025. A trajectory analysis (Figure 60) reveals that mid-level low- $\theta_e$  air to the north of TCS025 during the second IOP originated from the TUTT cell to the east. As the TUTT cell became positioned close to the low-level

circulation during the second IOP (see Figure 32b), low- $\theta_e$  air associated with the TUTT cell began to affect the thermodynamic environment of TCS025 (see Figure 42). Although vertical wind shear weakened somewhat as the TUTT cell was immediately to the north of TCS025, the infiltration of low- $\theta_e$  air below the mid-level circulation seemed to offset any positive impact associated with the reduction in vertical wind shear. Mid-tropospheric  $\theta_e$  was lowest during the second IOP (see Figure 58) and this is considered to have increased the negative impact potential of downdrafts (increased DCAPE).

Molinari et al. (2012) hypothesized that the repeated lulls in convective activity for TS Edouard (2002) were a result of vertical wind shear-induced ventilation that caused low- $\theta_e$  air to be transported into the boundary layer via downdrafts. It is hypothesized that similar processes occurred for TCS025; strong downdrafts depleted boundary layer  $\theta_e$  in precipitation regions through the transport of low- $\theta_e$  air down into the boundary layer (see Figure 51 and Figure 52), which is thought to have further limited the convective intensity as proposed by Riemer et al. (2010). A long convective lull near the circulation center occurred just after MCS-G dissipated (see Figure 61), suggesting the cooling and drying of the boundary layer was acting to inhibit subsequent convection. In their analysis of latent heating and cooling rates retrieved from ELDORA radar data, Park and Elsberry (2013) reached a similar conclusion regarding the demise of TCS025: despite the presence of deep convection during TCS025, evaporative cooling and strong downdrafts counteracted low-level spin-up.

During the second IOP, convection associated with MCS-G remained to the south-southwest of the low-level circulation (see Figure 43 and Figure 44). Vertical cross sections through this area reveal that upward vertical motion was located near the northern boundary of the low-level cold pool (Figure 48a). This suggests isentropic lift was helping to initiate or sustain deep convection (Raymond and Jiang 1990; Harr and Elsberry 1996). However, while isentropic lift appeared to be assisting the development of convection, dry mid-level air associated with the TUTT was also present. Beyond increasing downdraft strength and importing low- $\theta_e$  air into the boundary layer, it has

been argued by Smith and Montgomery (2012) that dry air entrainment can weaken updraft intensity, limiting the vorticity amplification process. Thus, when vertical wind shear was beginning to weaken on 28 August and vortex alignment appeared to improve somewhat, thermodynamic conditions became less favorable such that the convective intensity diminished and this limited further development.

After the second IOP, the vertical wind shear weakened for a period of time as the result of an upper-level ridge centered over TCS025 (Figure 34b). This pattern coincides with the large-scale composite structure for developing systems found by McBride (1981) and McBride and Zehr (1981). However, based on the SAMURAI analysis, the reduction in vertical wind shear and anticyclone aloft did not correspond with a significant improvement in the vertical alignment of the circulation relative to the second IOP (see Figure 53). Consequently, in addition to the large-scale environmental conditions, the interplay between vertical wind shear, circulation alignment, and the intensity of convection also needs to be considered.

By 0000 UTC 29 August, the TUTT cell had moved some distance away from the immediate environment of TCS025, which provided more favorable thermodynamic conditions compared to the second IOP (see Figure 58). Smith and Montgomery (2012) and Davis and Ahejivech (2012) noted that mid-level  $\theta_e$  declined over time in the non-developing disturbance they examined. Even though the low-level  $\theta_e$  was highest during the third IOP, there was essentially no difference in mid-level  $\theta_e$  between the first and third IOPs.

Smith and Montgomery (2012) found that the  $\theta_e$  deficit of a developing system they analyzed was about 15 K, while a  $\theta_e$  deficit of 25 K was observed for a non-developing system. A comparison of the  $\theta_e$  deficits computed from dropwindsondes within the convective environment of TCS025 revealed the average deficit declined from 19.4 K after the first IOP to 16.2 K in the second IOP, and remained nearly unchanged during the third IOP (see Figure 68a). In the non-convective environment, the average  $\theta_e$  deficits for the first, second, and third IOPs were 18.9 K, 22.9 K, and 19.6 K, respectively. The fact that the  $\theta_e$  deficits for the first and third IOPs were close to the

values exhibited by the developing system analyzed by Smith and Montgomery (2012) also suggests that the thermodynamic environment of TCS025 had improved between the second and third IOPs.

Despite the apparent improvement in thermodynamic conditions during the third IOP, a strengthening low-level ridge south and east of TCS025 caused the pressure gradient to increase along the eastern edge of the trough, and the TCS025 circulation moved northward rapidly (see Figure 33c and Figure 34c). This caused the low-level convective forcing of the trough environment to be displaced farther from the mid-level circulation. Even though the cloud structure in IR imagery appeared favorable for development with cyclonic banding south of TCS025 (see Figure 34a), rapid northward translation and weakening of the low-level trough coupled with increasing vertical wind shear (see Figure 35) from another TUTT approaching from the east (not shown) prevented further development, and convection quickly dissipated.

Whereas TCS025 existed in an environment of persistent northerly vertical wind shear (see Figure 35), it could be argued that vertical wind shear was not necessarily of sufficient magnitude to be considered detrimental for storm formation (DeMaria et al. 1996). Throughout the evolution of TCS025, MCSs that developed tended to move southward (i.e., down-shear) (see Figure 36), and the tilt of the circulation with height was predominantly in the down-shear direction (see Figure 44). Nolan and McGauley (2011) stated that the vast majority of tropical cyclogenesis events occur in the presence of some vertical wind shear, and found that in numerical simulations the sea-level pressure declined more rapidly for systems experiencing weak vertical wind shear ( $5\text{--}7\text{ m s}^{-1}$ ). Nolan and McGauley (2011) suggested that weak vertical wind shear could help organize and protect convection from the negative influences of dry air. Because the vertical wind shear in the TCS025 environment was generally greater than  $7\text{ m s}^{-1}$ , the impacts from vertical wind shear on the TCS025 disturbance appear to have been mostly negative.

Hendricks et al. (2004) and Montgomery et al. (2006) argued that VHTs are the essential building blocks for tropical storm formation. Although there were periods of deep convection associated with the TCS025 disturbance based on the MTSAT IR

brightness temperatures (see Figure 37), a careful examination of ELDORA radar data failed to reveal convective elements that might have been classified as VHTs. Instead, the ELDORA observations suggest stratiform precipitation processes were more prevalent. This might have been due to the fact that the ELDORA-equipped NRL P-3 sampled the TCS025 disturbance during the waning stages of the diurnal convective cycle. In addition, Park and Elsberry (2013) found that the latent heating and cooling rates from the ELDORA radar retrievals for TCS025 were more uniformly distributed over a deep layer, which implies that there was a mix of stratiform and convective precipitation.

The mesoscale analysis during the second IOP revealed divergence and thermal structures in the vertical that were consistent with the presence of a MCV (see Figure 48a). The reflectivity pattern evident in Figure 50 along with MTSAT IR brightness temperature analyses suggests significant periods existed during which MCSs that formed in close proximity to TCS025 were dominated by stratiform precipitation. It is likely that the large fraction of stratiform precipitation within the MCSs allowed for the strengthening and maintenance of the midlevel vortex via stratiform precipitation processes during the evolution of TCS025. As argued by Tory et al. (2006a), the divergence profile associated with stratiform precipitation processes (low-level divergence and mid-level convergence) would be detrimental to the spin-up of the low-level circulation. Therefore, during the periods of time when deep convection had subsided and large regions of stratiform precipitation were present, the stratiform divergence profile would have been an inhibiting factor for storm formation.

Raymond and Sessions (2007) and Raymond et al. (2011) hypothesized that the stable thermodynamic profile of a MCV (low-level negative temperature anomaly below a positive temperature anomaly) would lower the level of maximum vertical mass flux for subsequent convection, and lead to increased vorticity convergence and spin-up in the lower troposphere. Temperature anomaly profiles (see Figure 58d) indicate that a negative temperature anomaly was present below a positive anomaly for all five aircraft missions in TCS025. The low-level negative temperature anomaly was largest during the second IOP. However, the mid-level positive temperature anomaly was largest during the first IOP and almost nonexistent during the second IOP before again increasing in

magnitude by the time of the third IOP. Perhaps as a result of the non-development of the TCS025 disturbance, a clear trend did not exist of increasing stabilization as hypothesized by Raymond and Sessions (2007) and Raymond et al. (2011) that is believed to lead to a lowering of the level of maximum mass flux. In their analysis of TCS025, Raymond et al. (2011) found that the level of maximum vertical mass flux during the third IOP was lower than during the second IOP. Unfortunately, due to the large number of turns during the NRL P-3 mission 0225W, the magnitude of the vertical velocity derived from the ELDORA radial velocities was not considered reliable enough to attempt a vertical mass flux analysis similar to that computed by Raymond et al. (2011).

Dolling and Barnes (2012b) argued that subsidence warming beneath a MCV led to the formation of Hurricane Humberto (2001). To determine whether subsidence warming might have been present during the evolution of TCS025 despite its non-development, NRL P-3 flight-level data were examined for evidence of mesoscale descent. However, there were no areas of large-scale subsidence identified from any of the NRL P-3 flight legs for the TCS025 case.

Comparisons with pre-TY Fanapi, which was a developing system observed during ITOP, suggest differences in circulation structure and alignment were most important. Although Fanapi and TCS025 had similar thermodynamic environments (see Figure 66 and Figure 67), vertical wind shear was less for Fanapi, and this allowed the circulation to remain more vertically aligned than for TCS025 (see Figure 65). Both systems exhibited periods of deep convection early in their development followed by lulls in convective activity (Figure 69). The decline in convection is thought to have resulted from a reduction in boundary layer  $\theta_e$  through evaporative downdrafts, as low- $\theta_e$  air in the mid-troposphere was in close proximity to both systems during this time (see Figure 68). It is thought that low- $\theta_e$  air was not able to penetrate the inner-core of Fanapi due to the well-aligned circulation and weak system-relative flow, while the inner core of TCS025 was relatively unprotected. As a result, deep convection associated with TCS025 failed to redevelop near the same area, whereas convection was able to redevelop within the well-protected inner-core environment of Fanapi. As deep convection redeveloped within the protected inner-core environment of Fanapi, mid-level moisture increased rapidly, which helps maximize the impact of diabatic heating, and

allowed Fanapi to intensify. Based on the modeling studies of Nolan (2007), it was found that adequate mid-level moisture is a necessary condition for tropical cyclogenesis. Adequate mid-level moisture ensures that diabatic heating is maximized, and reduces dry air entrainment, which may act to limit updraft strength and its contribution to the amplification of vertical vorticity (Smith and Montgomery 2012).

In conclusion, the convection associated with the disturbance was not of sufficient intensity, areal extent, or duration to reduce the appreciable vortex misalignment of TCS025. The system-relative flow was larger due to the vertical misalignment of the circulation and this allowed dry, cool air originating from the TUTT cell to penetrate into the inner core of TCS025, which acted to suppress subsequent convection. These observations confirm the first hypothesis of this study: TCS025 failed to develop in part due to poor vertical alignment of the vortex structure that prevented enhancement and organization of deep convection. Had deep moist convection continued to occur near the midlevel circulation center, vortex re-alignment or the development of a new low-level circulation below the mid-level vortex might have occurred. The comparison with pre-TY Fanapi suggests that a coherent vertical vortex structure might have helped protect TCS025 from the intrusion of dry air that was present on 28 August, while at the same time providing a protective enclosure whereby the system could develop a warm core. Instead, the tangential wind structure remained weak and highly asymmetric, and this coupled with vertical misalignment of the circulation allowed negative thermodynamic influences to limit intensification when other factors (i.e., reduced vertical wind shear) were otherwise favorable. For a weak and highly asymmetric system such as TCS025 that exhibited poor vortex alignment and lacked convective intensity, 10-15 kt of vertical wind shear in the presence of dry, cool environmental air was enough to prevent development.

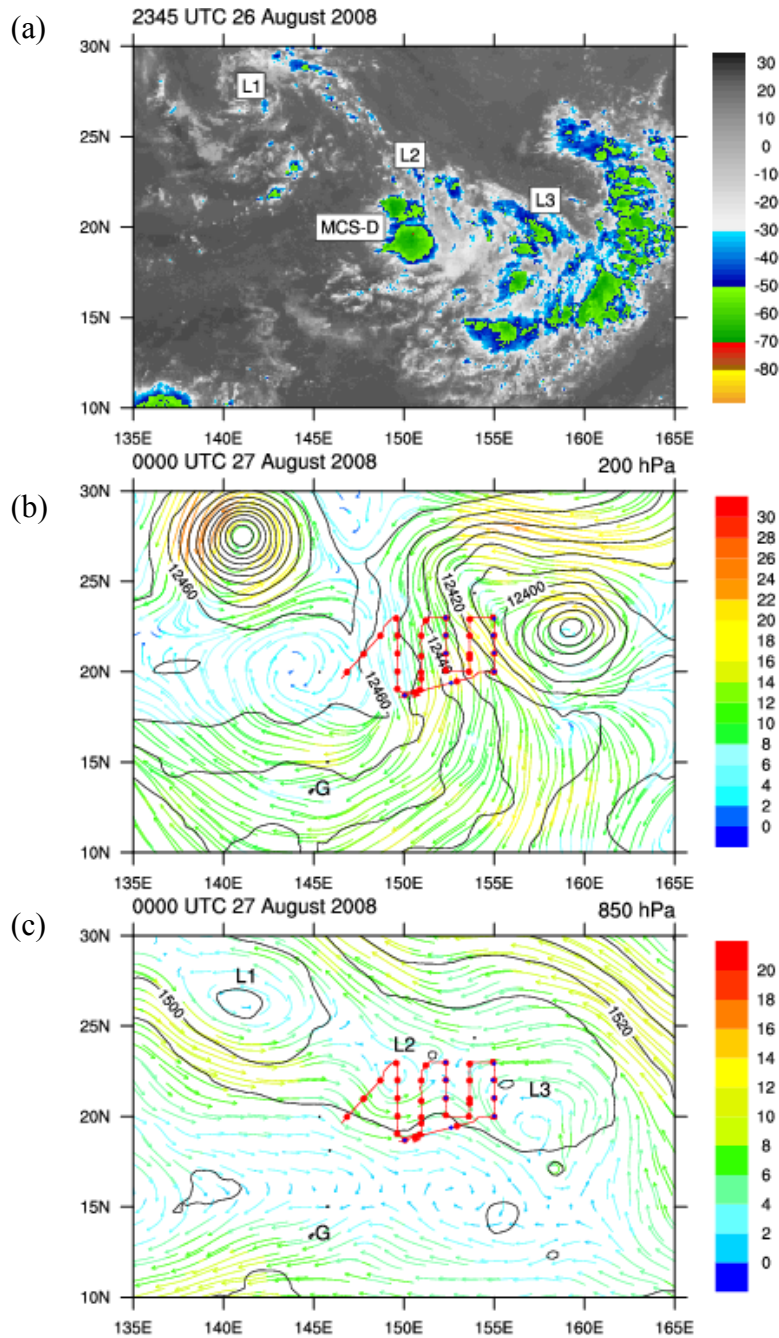


Figure 31 (a) MTSAT IR brightness temperature ( $^{\circ}\text{C}$ ) at 2345 UTC 26 August. Horizontal wind vectors ( $\text{m s}^{-1}$ , colored scale on right) and geopotential heights (m, black contours) at (b) 200 hPa and (c) 850 hPa from ECMWF analysis valid at 0000 UTC 27 August. The location of MCS-D is annotated in (a) and the red line and red circles in (b) and (c) correspond to the flight track and dropwindsonde deployment locations for USAF WC-130J flight 0125W. Blue circles in (b) and (c) correspond to AXBT deployment locations. Low-level circulations are labeled L1, L2, and L3 in (a) and (c) and G marks the location of Guam.



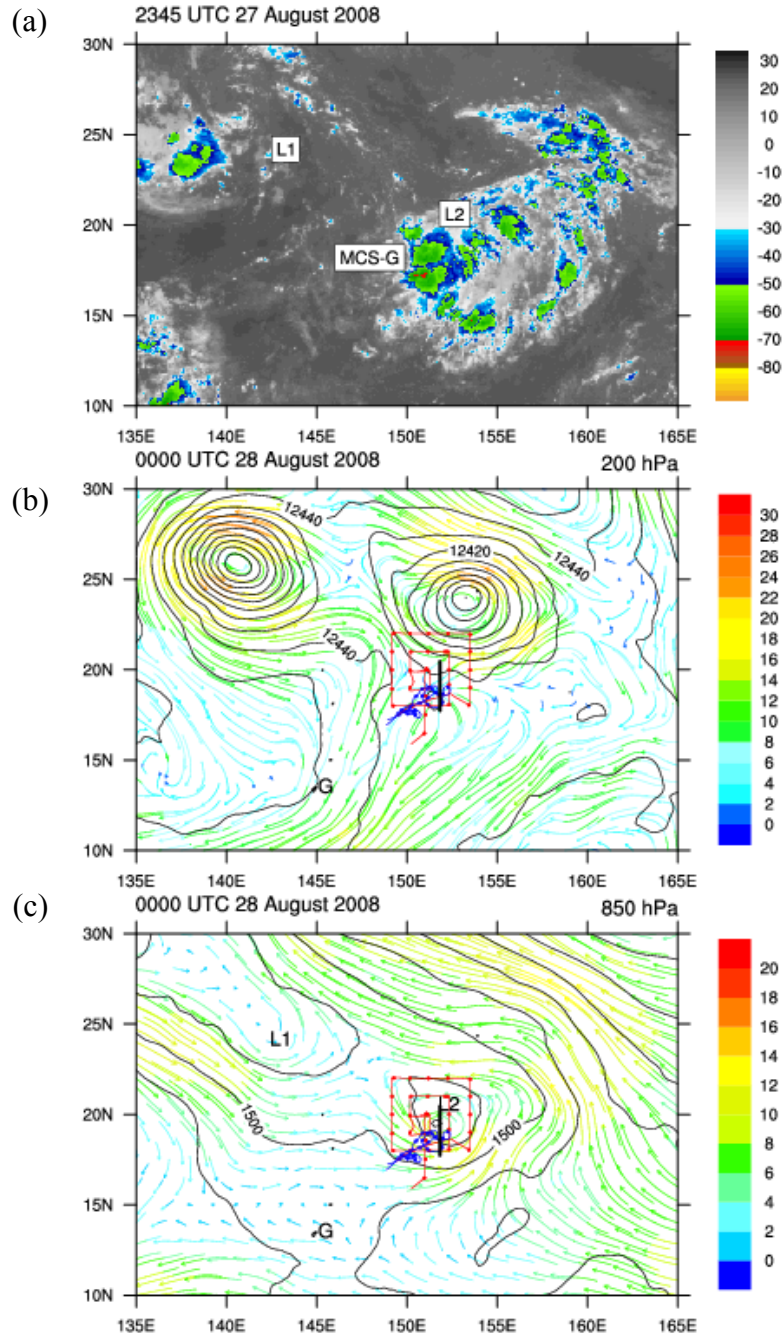


Figure 32 As in Figure 31, except (a) MTSAT IR brightness temperature at 2345 UTC 27 August and ECMWF analysis valid at 0000 UTC 28 August. The location of MCS-G is annotated in (a) and the red line and red circles in (b) and (c) correspond to the flight track and dropwindsonde deployment locations for USAF WC-130J flight 0325W. Blue line and blue circles in (b) and (c) correspond to the flight track and dropwindsonde deployment locations for NRL P-3 flight 0225W. South to north vertical cross section shown in Figure 48 is marked by black line in (b) and (c).

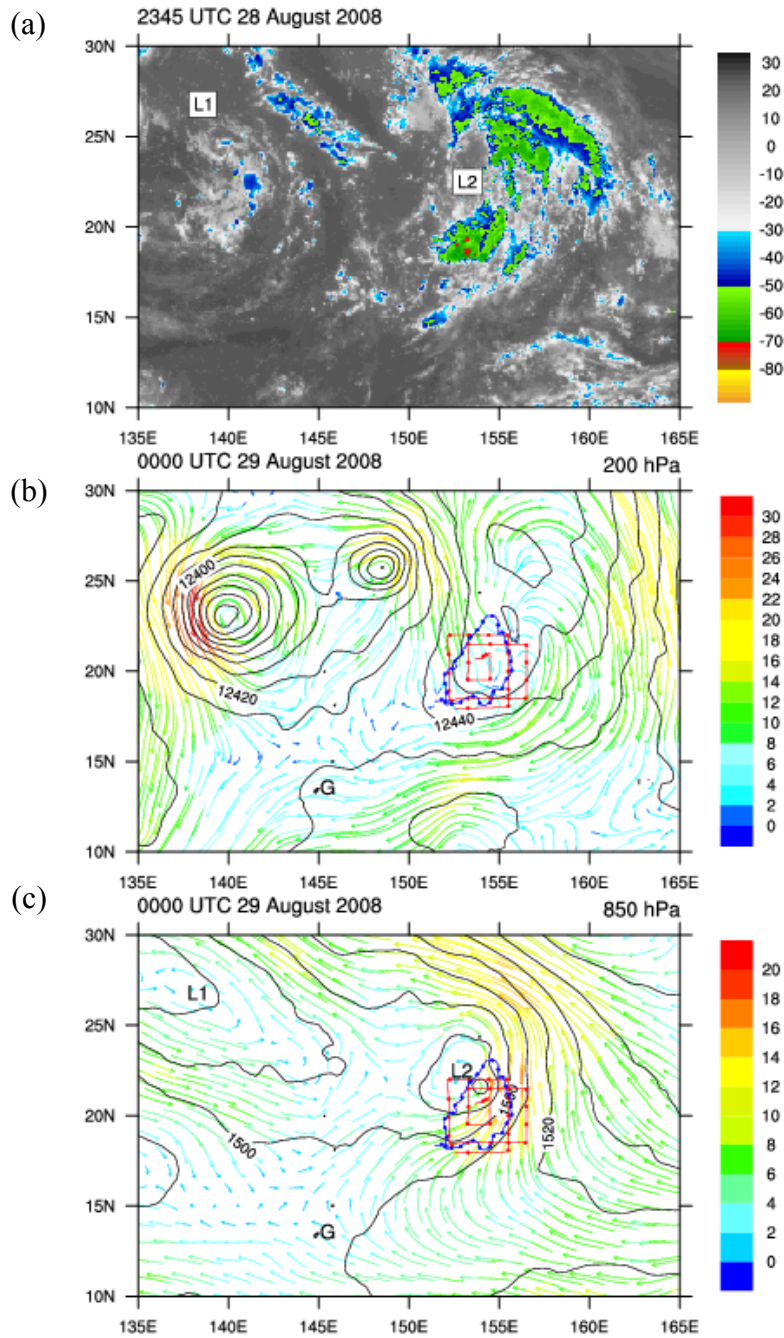


Figure 33 As in Figure 31, except (a) MTSAT IR brightness temperature at 2345 UTC 28 August and ECMWF analysis valid at 0000 UTC 29 August. Red line and red circles in (b) and (c) correspond to the flight track and dropwindsonde deployment locations for USAF WC-130J flight 0525W. Blue line and blue circles in (b) and (c) correspond to the flight track and dropwindsonde deployment locations for NRL P-3 flight 0425W.

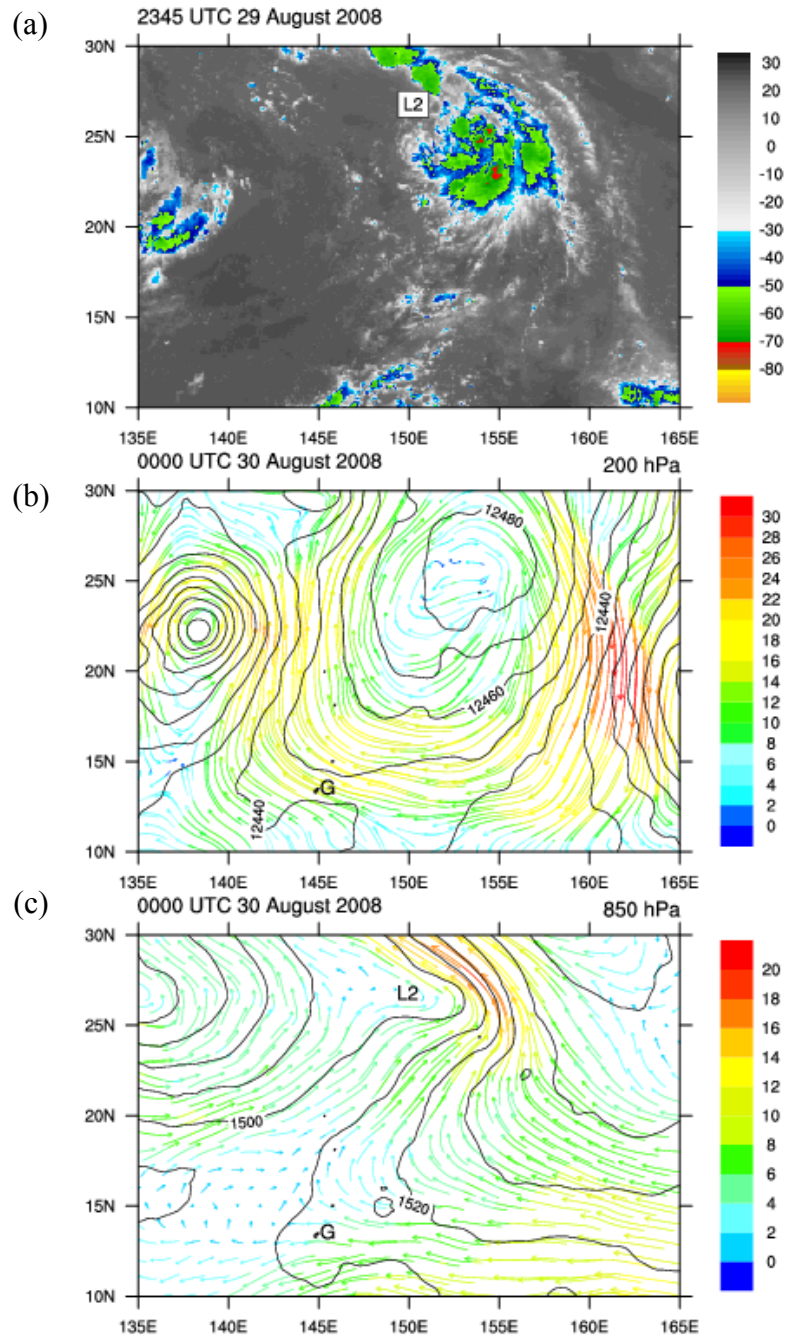


Figure 34 As in Figure 31, except (a) MTSAT-IR brightness temperature valid at 2345 UTC 29 August and ECMWF analysis valid at 0000 UTC 30 August.

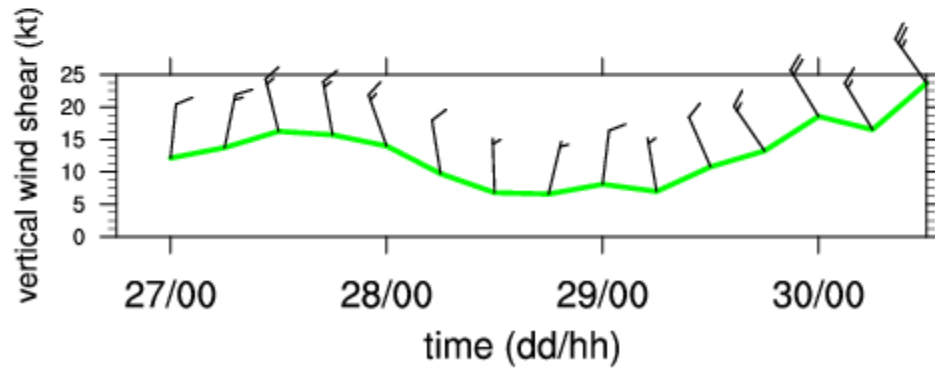


Figure 35 Vertical wind shear (200-850 hPa, kt) and direction (1 full barb = 10 kt) for TCS025. Computed using CFSR reanalysis data (see text for details).

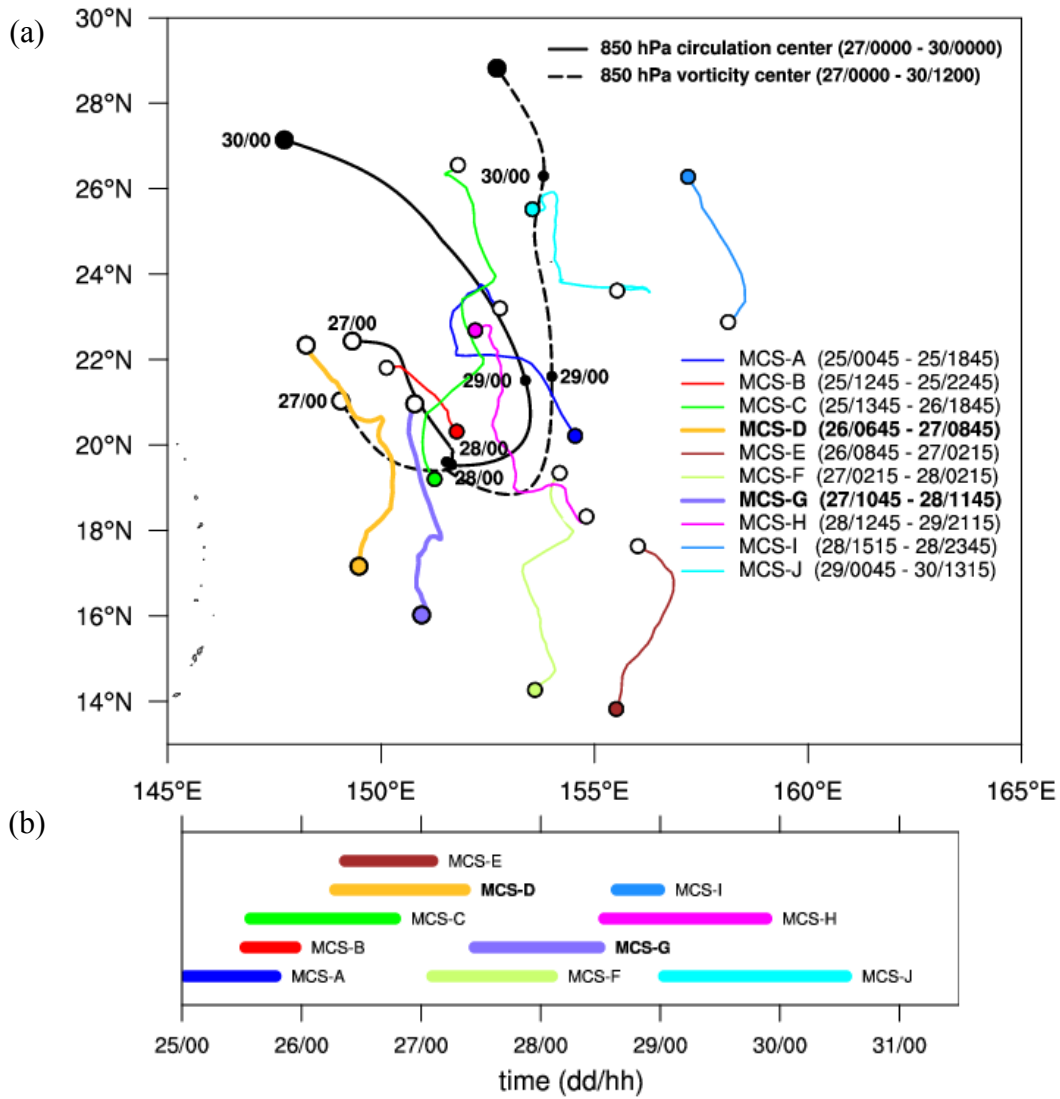


Figure 36 (a) Tracks of MCSs during TCS025 with open and closed circles indicating the formation and dissipation locations, respectively. The solid and dashed black lines mark the subjectively determined 850 hPa circulation and vorticity maximum tracks, respectively, which are based on a ECMWF analysis and are labeled at 0000 UTC positions (black circles). The approximate duration for each MCS is listed in the inset in (a) and shown as a time series in (b).

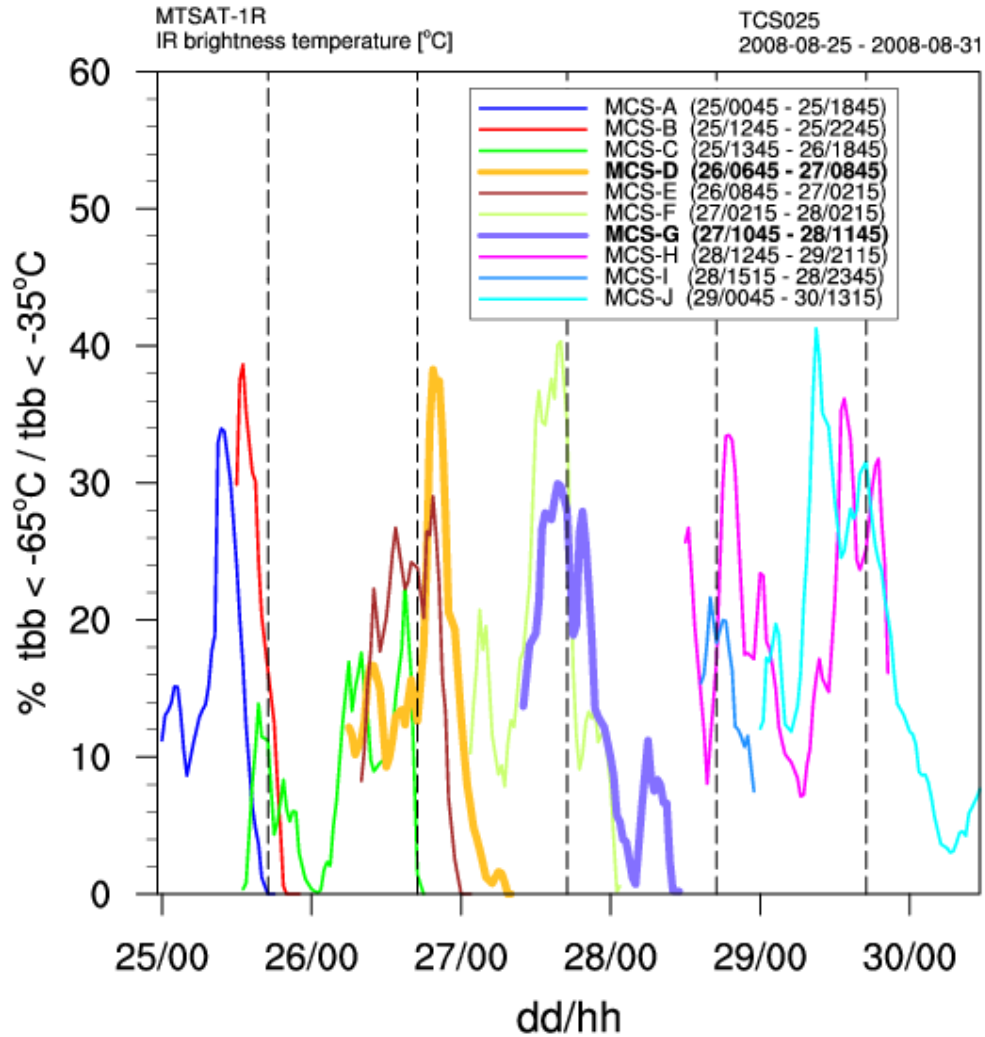


Figure 37 Ratio expressed as a percentage of area with MTSAT-IR brightness temperatures less than -65°C to that less than -35°C for MCSs that developed within the environment of TCS025. Dashed vertical black lines indicate the approximate time of the expected early morning convective maximum.



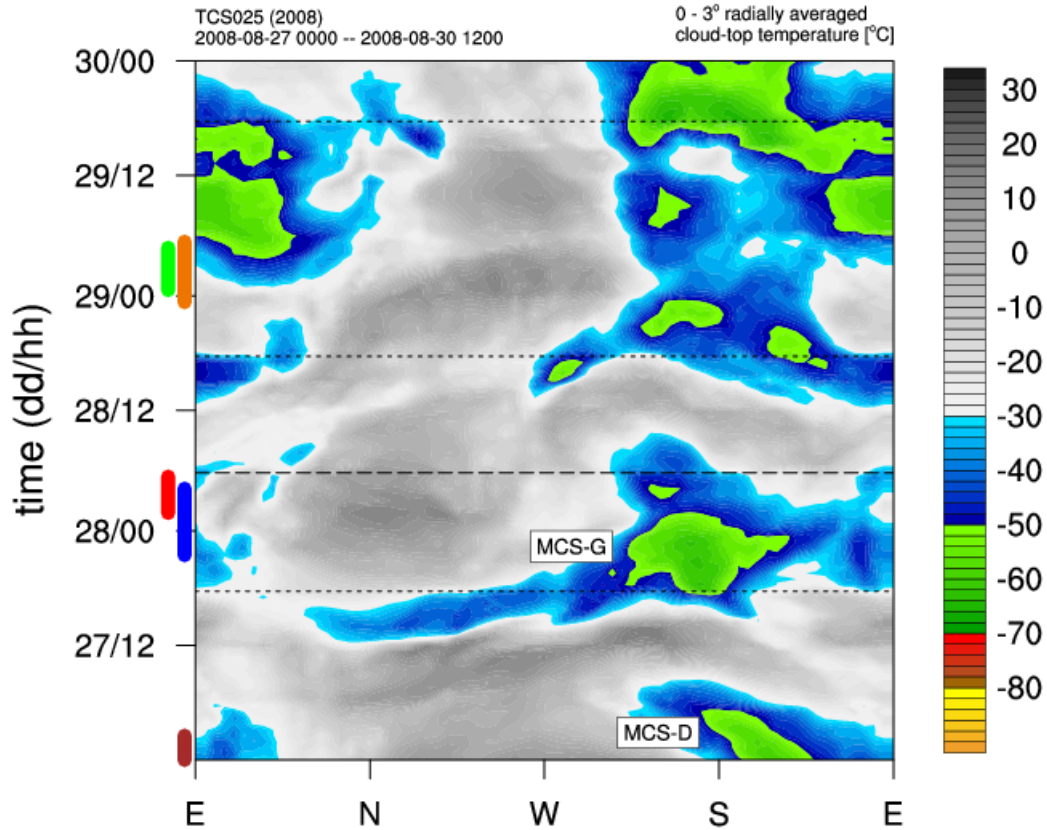


Figure 38 Radially averaged ( $0^{\circ}$ - $3^{\circ}$ ) half-hourly MTSAT IR brightness temperatures relative to the ECMWF 850 hPa vorticity maximum positions of TCS025. Colored bands along the ordinate represent USAF WC-130J and NRL P-3 aircraft missions flown into TCS025 with brown, blue and orange corresponding to the USAF WC-130J missions and red and green to the NRL P-3 missions. Abscissa axis labels correspond to directions along the azimuth. Short dashed horizontal lines mark the approximate time of diurnal convective maximum (1800 UTC) and long dashed horizontal line denotes the ending time of the 0225W NRL P-3 mission. The brightness temperature features associated with MCS-D and MCS-G are annotated.

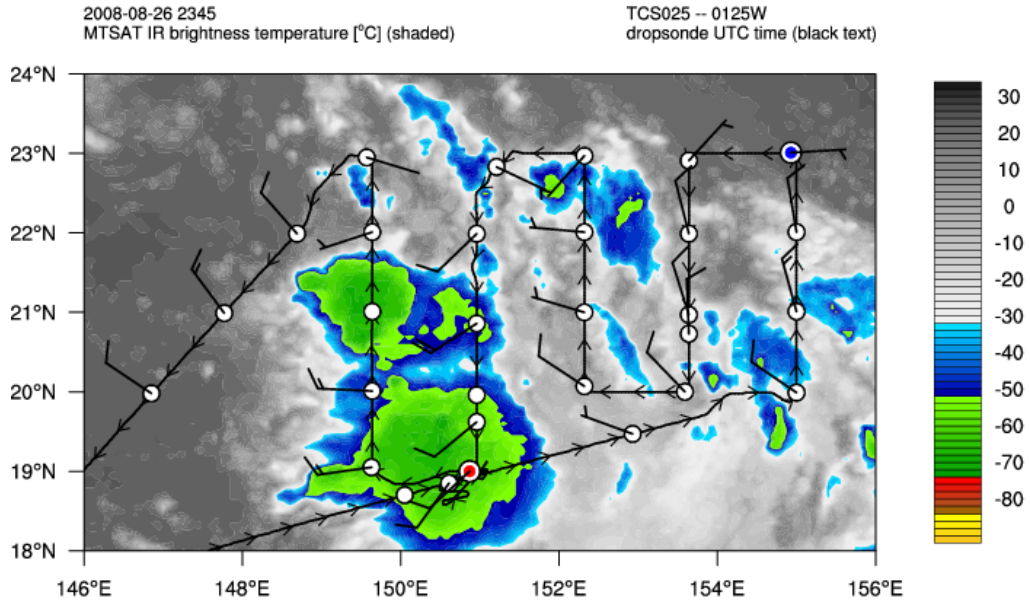


Figure 39 MTSAT IR brightness temperature (°C, shading) at 2345 UTC 26 August. The USAF WC-130J flight track (black line) and dropwindsonde deployment locations (white circles) are shown with wind barbs corresponding to 1500 m height (1 full barb = 10 kt) for first IOP (0125W). Red and blue dropwindsonde locations correspond to the dropwindsonde profiles shown in Figure 42.



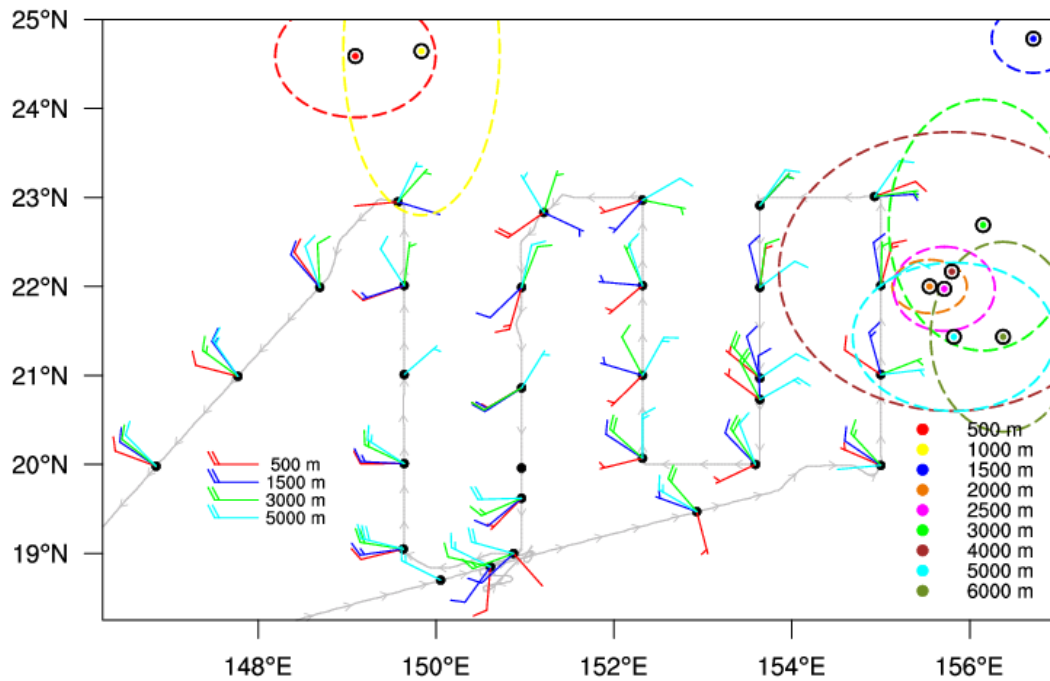


Figure 40 Earth-relative USAF WC-130J (0125W: 1930 UTC 26 August – 0257 UTC 27 August) flight track for TCS025. Black dots denote dropwindsonde locations and wind barbs correspond to heights shown in legend (1 full barb = 10 kt). Colored circles with black outlines mark dropwindsonde-derived circulation center locations at heights listed in inset, and dashed ellipses are estimates of the position uncertainty as described in text.

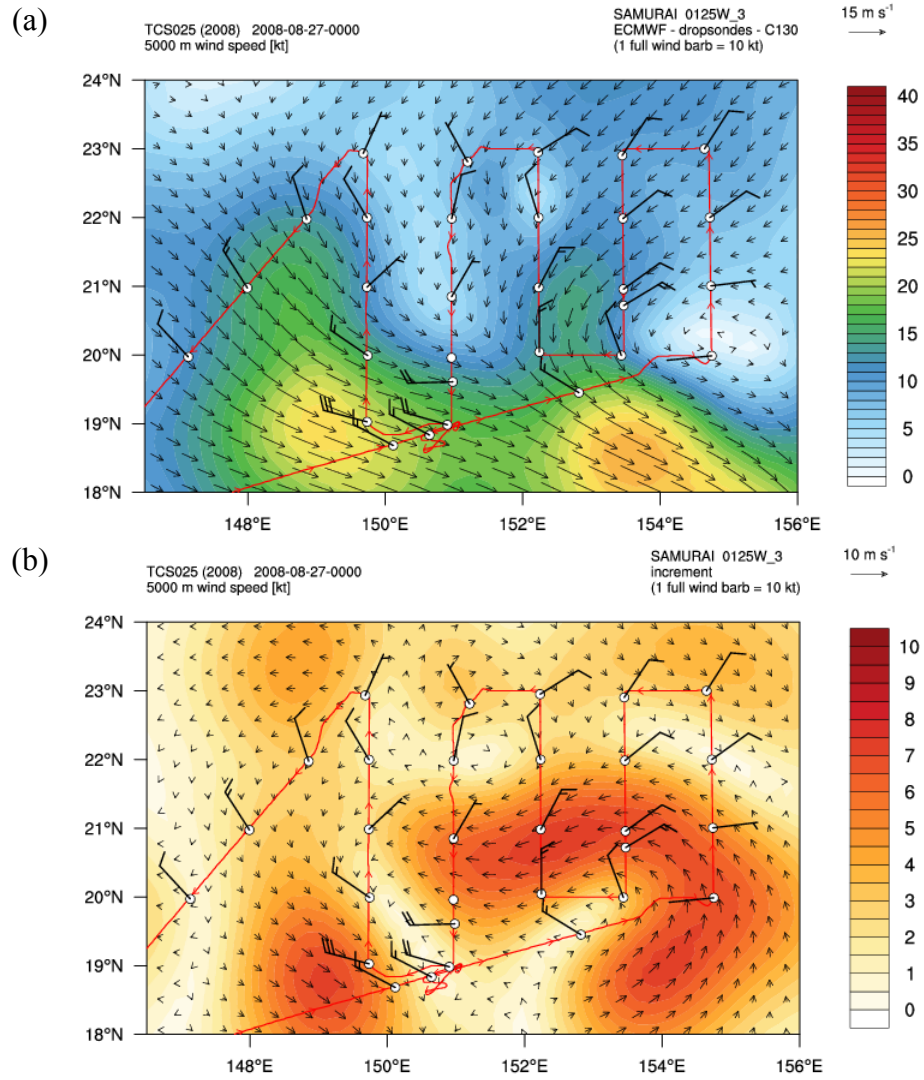


Figure 41 (a) Earth-relative wind speed (kt, shading) and vectors ( $\text{m s}^{-1}$ ) at 5-km altitude from the SAMURAI analysis and the (b) corresponding increment wind speed (kt, shading) and vector ( $\text{m s}^{-1}$ ) field valid at 0000 UTC 28 August. The red line indicates the flight track for the USAF WC-130J 0125W mission and black wind barbs correspond to dropwindsonde winds at 5-km altitude (1 full barb = 10 kt).

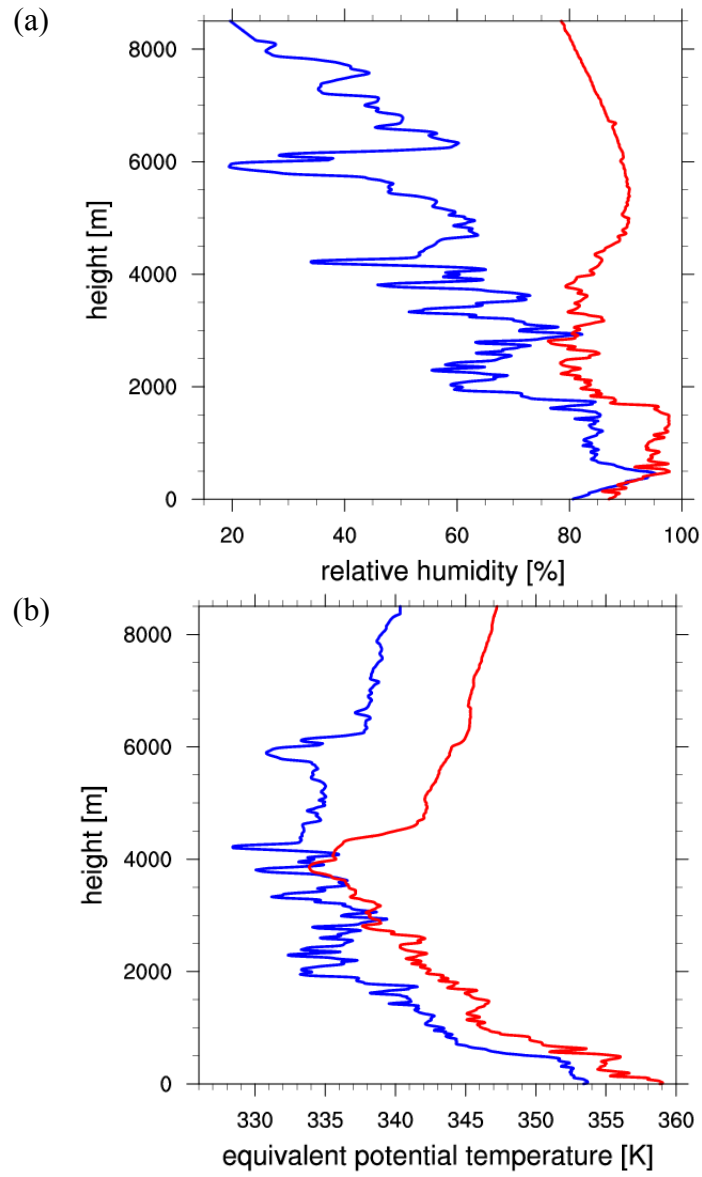


Figure 42 Vertical profiles of (a) relative humidity (%) and (b) equivalent potential temperature (K) constructed from dropwindsondes at blue- and red-colored deployment locations in Figure 39 (see text for details).

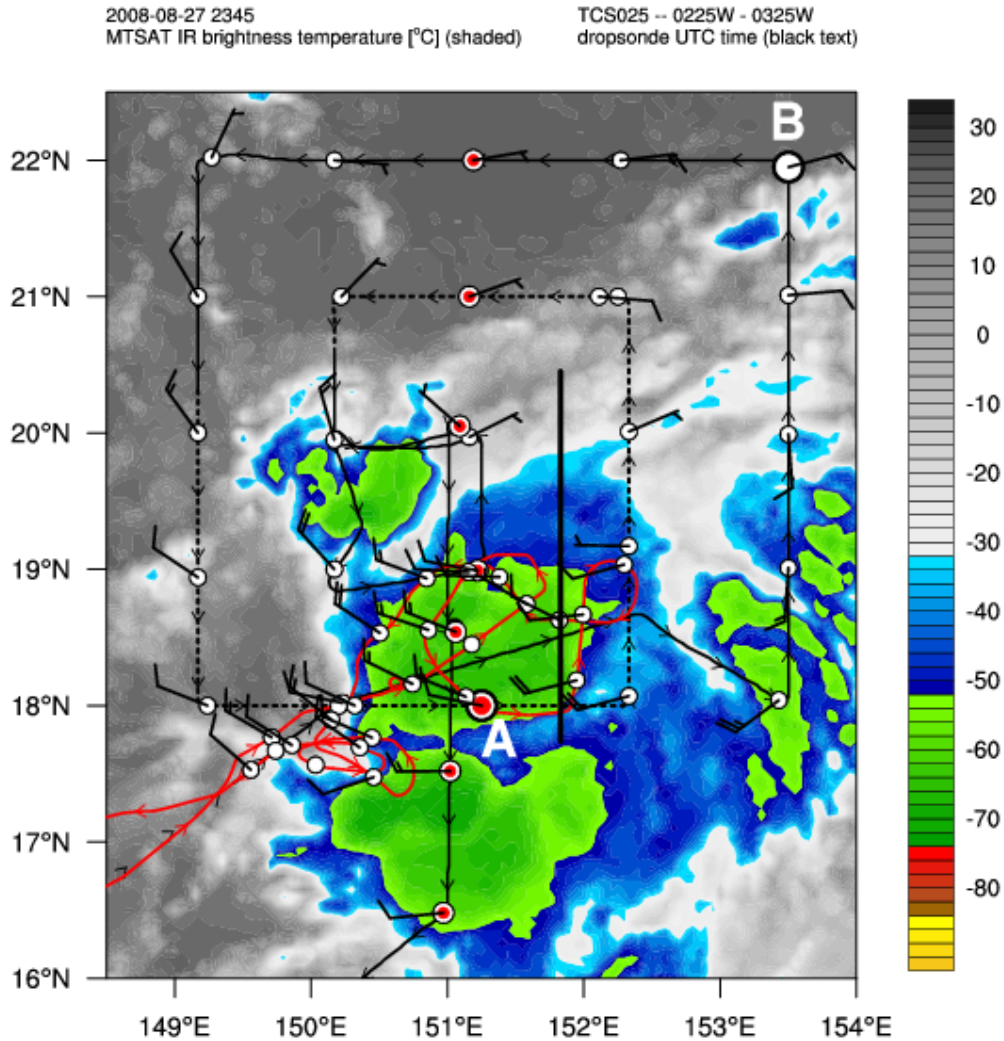


Figure 43 MTSAT IR brightness temperature (°C, shading) at 2345 UTC 27 August. The USAF WC-130J flight track (black line), NRL P-3 flight track (red line), and dropwindsonde deployment locations (white circles) are shown with wind barbs corresponding to 1500 m height (1 full barb = 10 kt) for the second IOP (0225W and 0325W). Red-filled dropwindsonde locations near 151°E were used in vertical cross section in Figure 51 and the bold black line near 151.8°E denotes the location of the cross-section in Figure 48. Black dashed portion of the USAF WC-130J flight track corresponds with the locations where SFMR rain rate and IR brightness temperature data were analyzed in Figure 52. Skew-T log-P comparisons in Figure 123 were constructed from dropwindsondes "A" and "B".

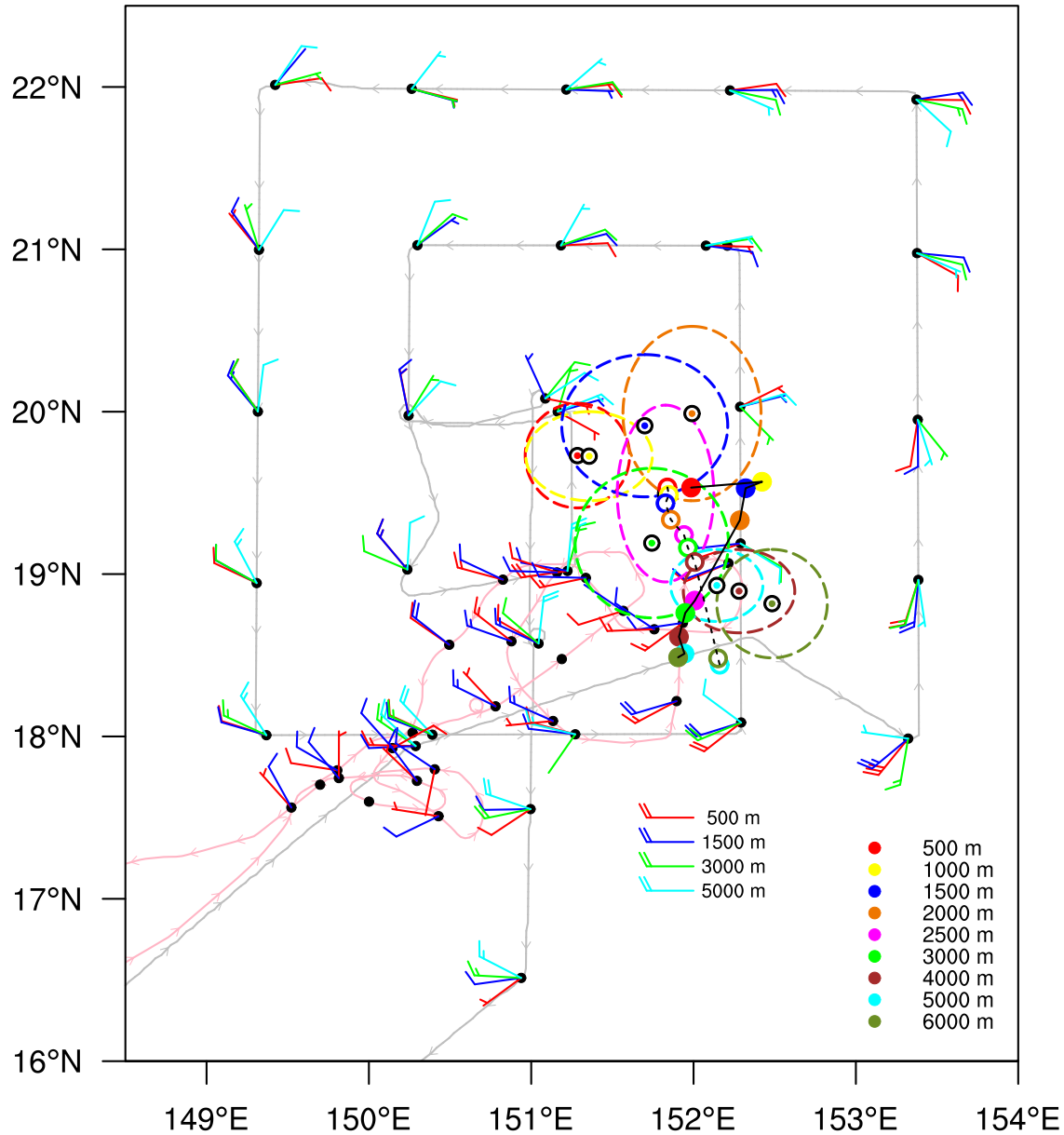


Figure 44 As in Figure 40, except storm-relative USAF WC-130J (0325W: 2103 UTC 27 August – 0407 UTC 28 August) and NRL P-3 (0225W: 0130 UTC 28 August – 0520 UTC 28 August) flight tracks for the second IOP in TCS025. In addition to the circulation center locations from the dropwindsondes as in Figure 40, solid colored circles connected by a solid black line mark the subjectively determined circulation center locations at heights listed in inset from the SAMURAI analysis. White-centered colored circles connected by a dashed black line mark subjectively determined circulation center locations at heights listed in inset from the ECMWF analysis.

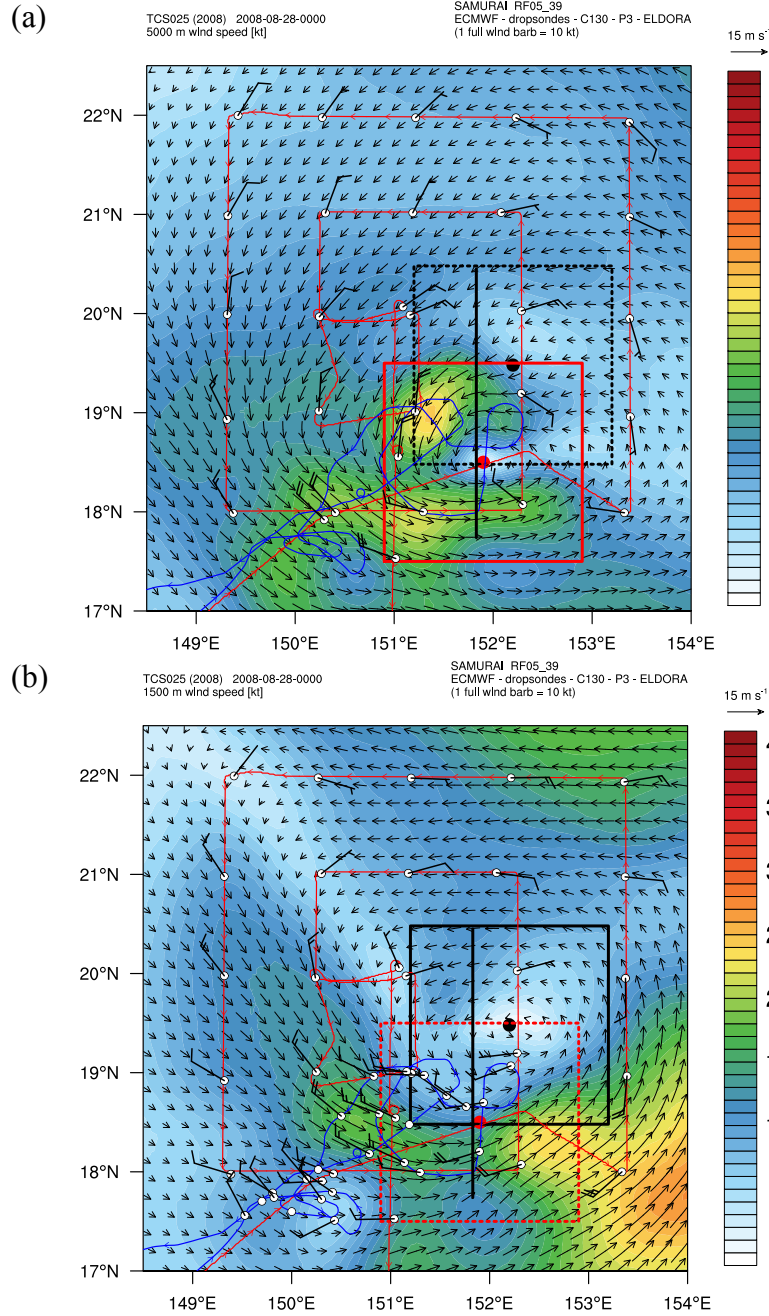


Figure 45 Storm-relative wind speed (kt, shading) and vectors ( $\text{m s}^{-1}$ ) at (a) 5 km and (b) 1.5 km from SAMURAI analysis valid at 0000 UTC 28 August. The USAF WC-130J track for flight 0325W is in red and the NRL P-3 track for flight 0225W is in blue. Black wind barbs (1 full barb = 10 kt) correspond to dropwindsonde winds corrected for storm motion. Solid black line denotes location of the cross-section in Figure 48. The  $2^\circ \times 2^\circ$  black and red boxes are centered on the circulation center positions at 1.5 (black dot) and 5 km (red dot), respectively, are used in the mesoscale vertical wind shear calculations in Figure 47 and discussed in text.



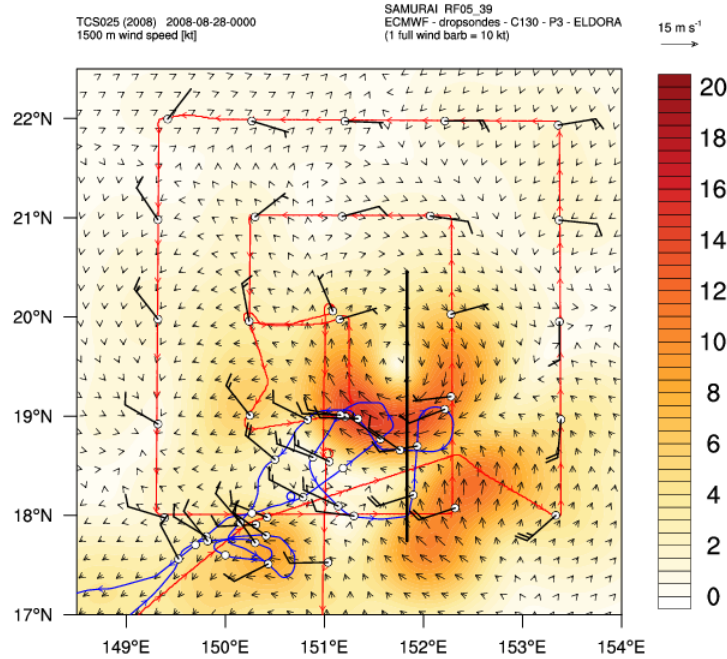


Figure 46 As in Figure 45, except for the increment wind speed (kt, shading) and vector ( $\text{m s}^{-1}$ ) field at 1.5 km that corresponds with the SAMURAI analysis in Figure 45b.

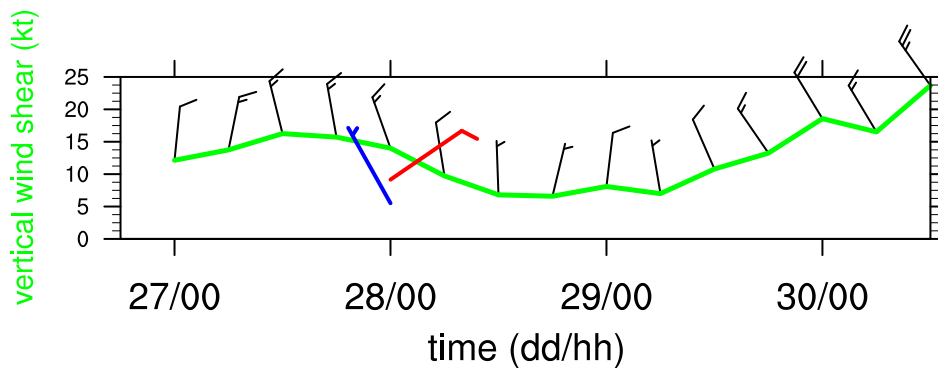


Figure 47 As in Figure 35, except also shown are wind barbs for the mesoscale vertical wind shear (system-relative flow) defined as the difference in the  $2^\circ \times 2^\circ$  box-average wind (see Figure 45) between the 5- and 1.5-km height from the 0000 UTC 28 August SAMURAI analysis for the pseudo-aligned (blue barb, 5.4 kt) and misaligned (red barb, 9.3 kt) cases described in text.

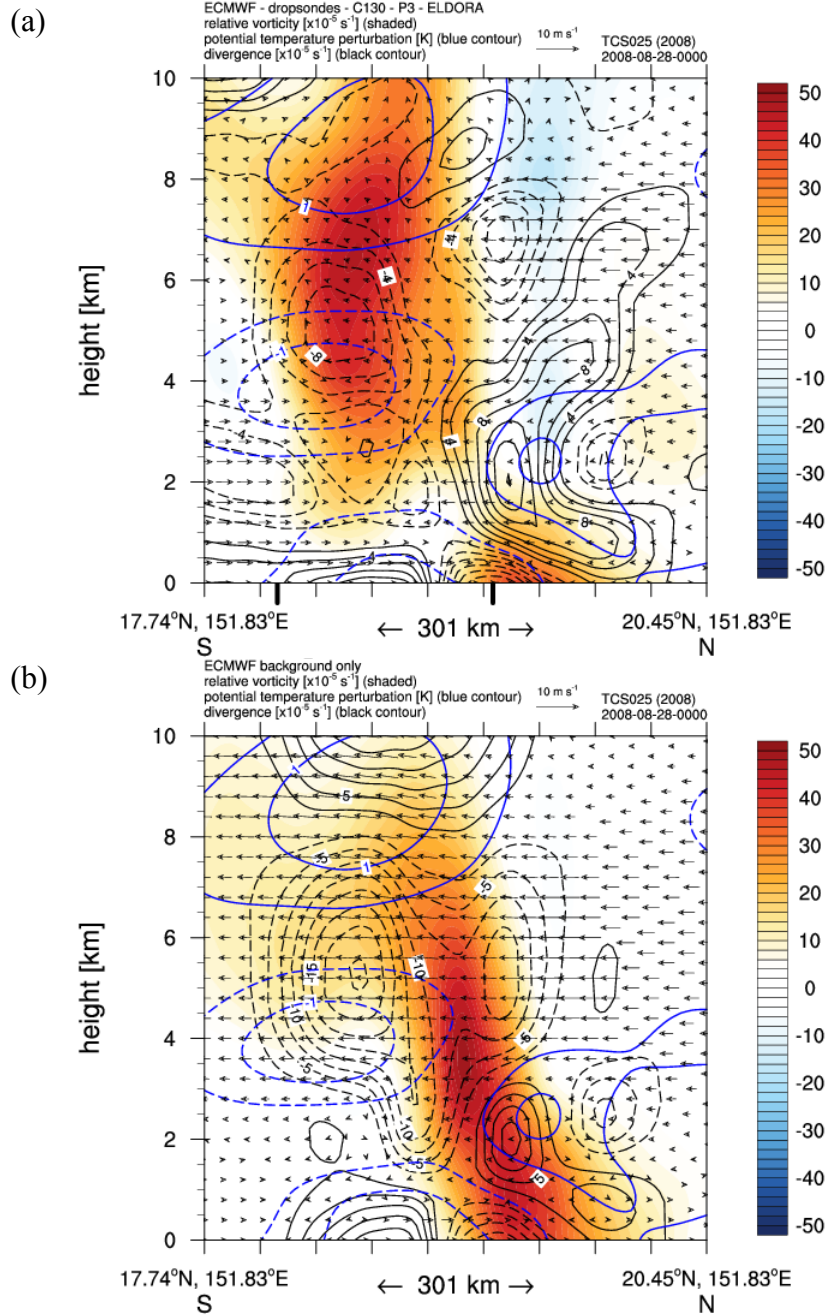


Figure 48 South-to-north oriented vertical cross section of relative vorticity ( $10^{-5} \text{ s}^{-1}$ , shading), potential temperature anomaly (K, blue contours at 2.5 K with negative values dashed), divergence ( $10^{-5} \text{ s}^{-1}$ , black contours at  $2.0 \times 10^{-5} \text{ s}^{-1}$  with negative values dashed), and in-plane wind vectors ( $\text{m s}^{-1}$ ) constructed from (a) SAMURAI analysis and (b) ECMWF background field valid at 0000 UTC 28 August. The location of cross section corresponds to solid black lines shown in Figure 32, Figure 43, Figure 45, Figure 49, and Figure 50. Thick vertical black lines immediately below the abscissa in (a) correspond to southern and northern extent of ELDORA Doppler radar at the longitude of the cross-section (see Figure 50).



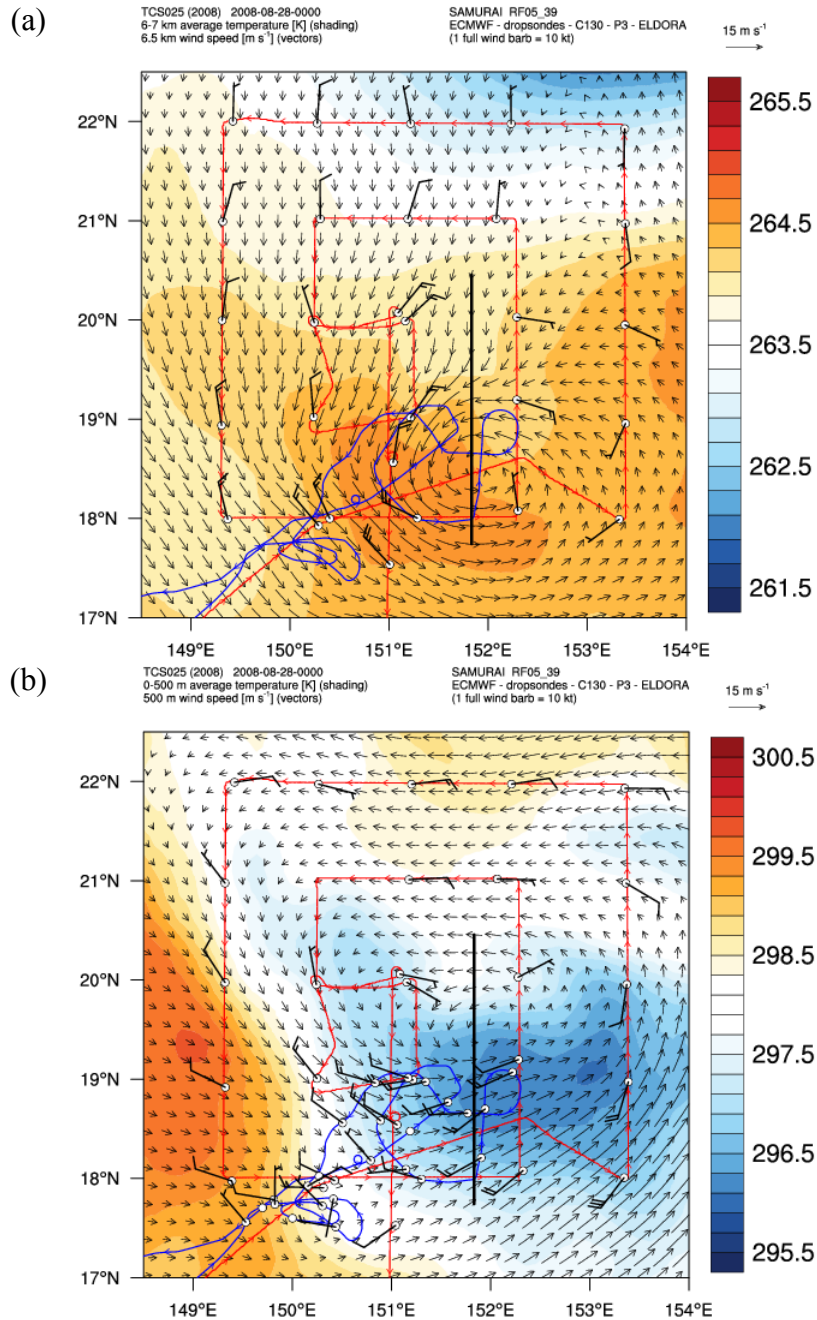


Figure 49 (a) Average temperature (K, shading) in the 6-7 km layer and 6.5 km wind vectors ( $\text{m s}^{-1}$ ) from SAMURAI analysis valid at 0000 UTC 28 August. (b) As in (a), except for the 0-500 m layer and wind vectors correspond to 500 m height. The USAF WC-130J track for flight 0325W is in red and the NRL P-3 track for flight 0225W is in blue. Black wind barbs correspond to dropwindsonde winds at 6500 m in (a) and 500 m in (b) corrected for storm motion (1 full barb = 10 kt). Solid black lines denote location of cross-section in Figure 48.

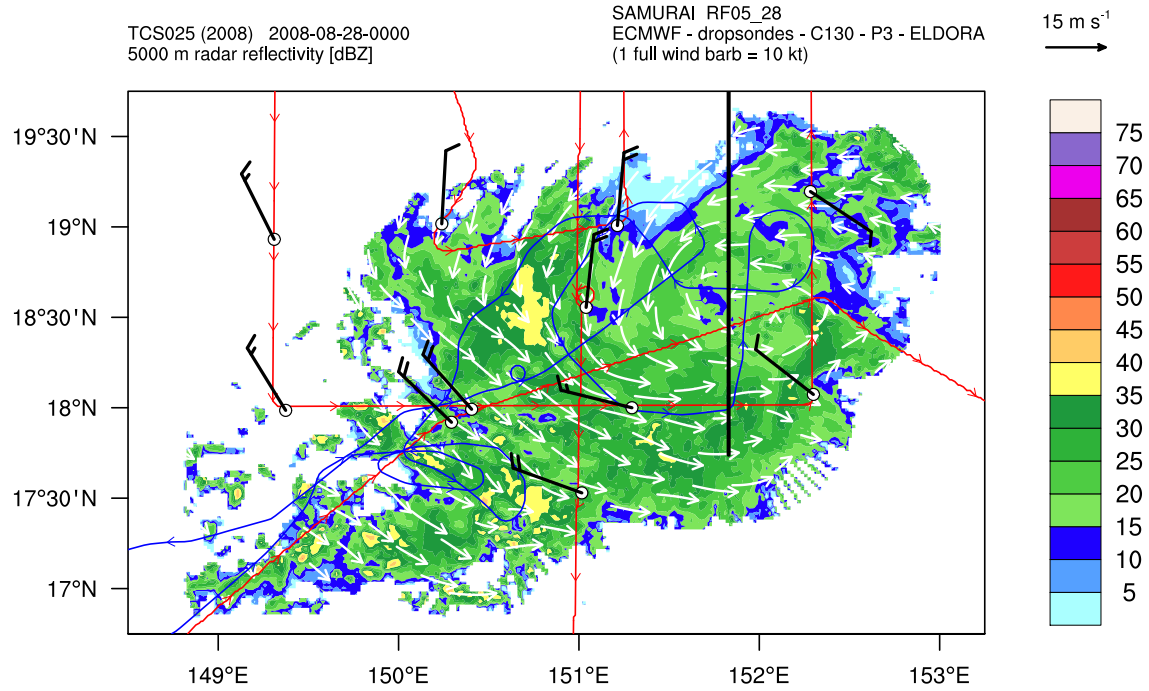


Figure 50 ELDORA reflectivity (dBZ, shading) at 5-km height from the NRL P-3 flight 0225W early on 28 August. The white horizontal wind vectors ( $\text{m s}^{-1}$ , with  $15 \text{ m s}^{-1}$  reference vector indicated at top right) correspond to the wind field at 5-km height derived using the SAMURAI analysis technique. The USAF WC-130J track for flight 0325W is in red and the NRL P-3 track for flight 0225W is in blue. Black wind barbs correspond to dropwindsonde winds corrected for storm motion (1 full barb = 10 kt). The solid black line denotes the location of the cross-section in Figure 48.

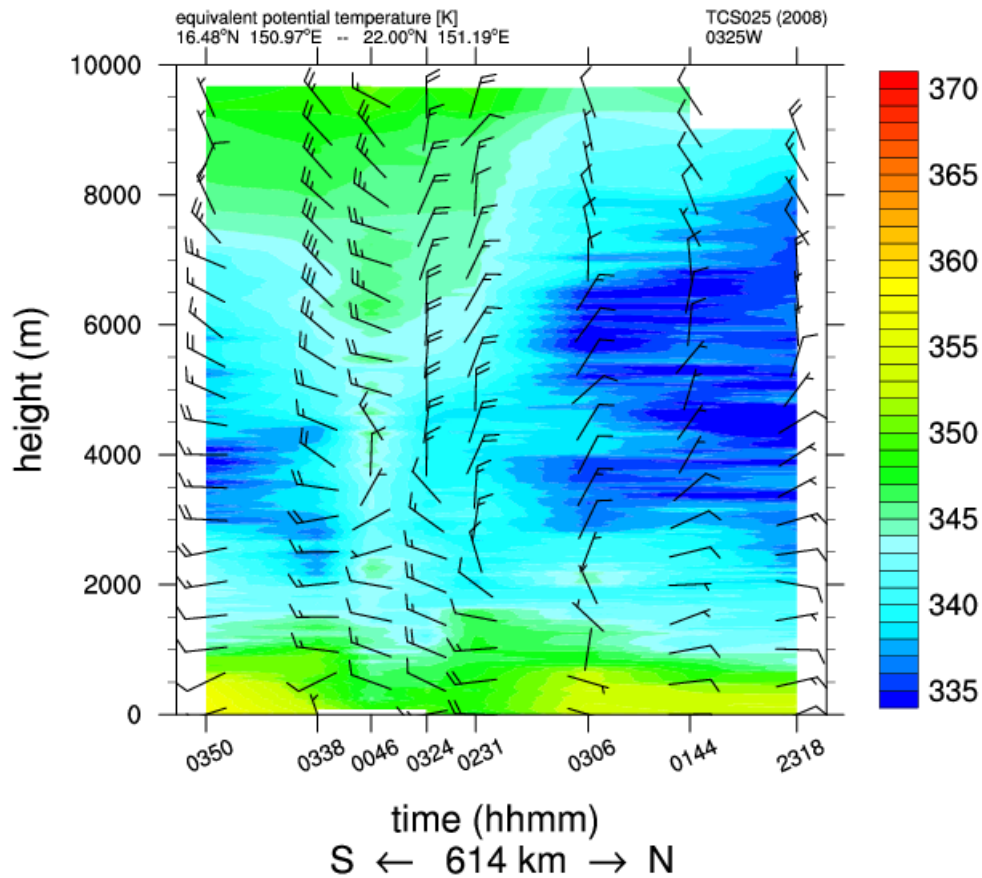


Figure 51 South-to-north vertical cross section of equivalent potential temperature (K) constructed using dropwindsonde data (red-filled circles in Figure 43) collected during the second USAF WC-130J flight (0325W). Wind barbs depict the dropwindsonde horizontal wind (1 full barb = 10 kt) and follow standard convention (wind barb tails pointing toward the bottom of the figure represent a northerly wind).

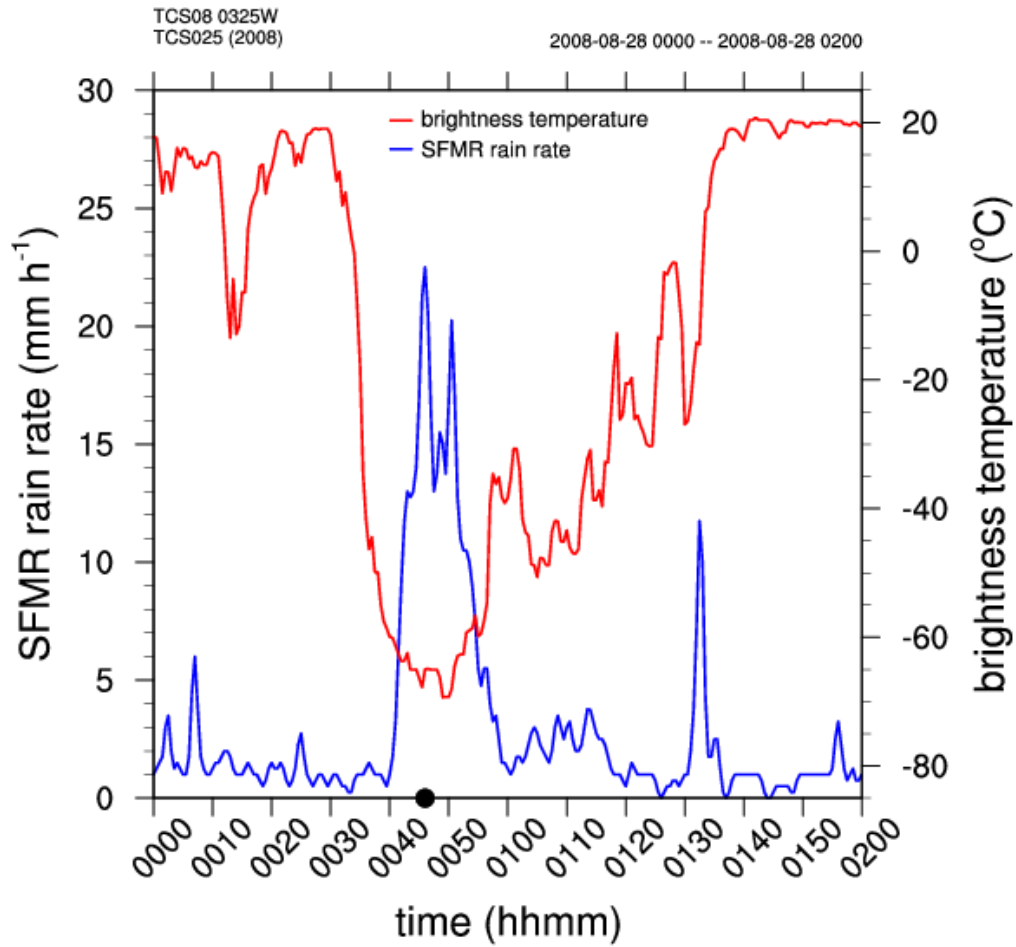


Figure 52 SFMR rain rate ( $\text{mm h}^{-1}$ , blue line and left ordinate) and MTSAT IR brightness temperatures ( $^{\circ}\text{C}$ , red line and right ordinate) interpolated spatially and temporally to the flight track during the second USAF WC-130J flight (0325W). Abscissa axis labels correspond to UTC time. Black dashed line in Figure 43 denotes the location along the flight track corresponding to this time interval. The black circle along the abscissa indicates the time of the 0046 UTC dropwindsonde in Figure 51.

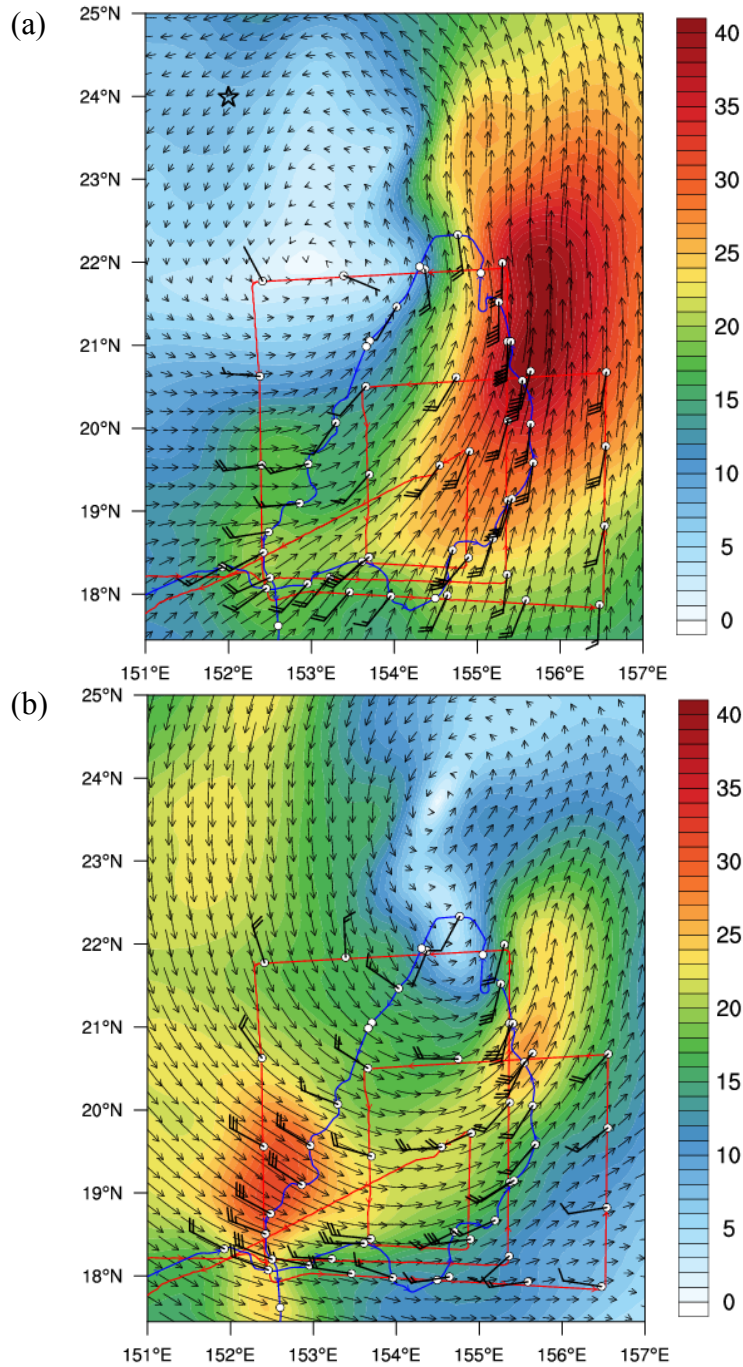


Figure 53 SAMURAI analyzed wind speed (kt, shading and vectors) at 1.5-km height from data collected during the third IOP in (a) the ground-relative frame and (b) storm-relative frame. The USAF WC-130J mission 0525W flight track is in red and the NRL P-3 mission 0425W flight track is in blue. Black wind barbs correspond to dropwindsonde winds (1 full barb = 10 kt), which have been corrected for storm motion in (b). The black star near 24°N, 152°E in (a) represents the surface circulation center determined from QuikSCAT scatterometer data valid at ~0747 UTC 29 August (see Figure 55).



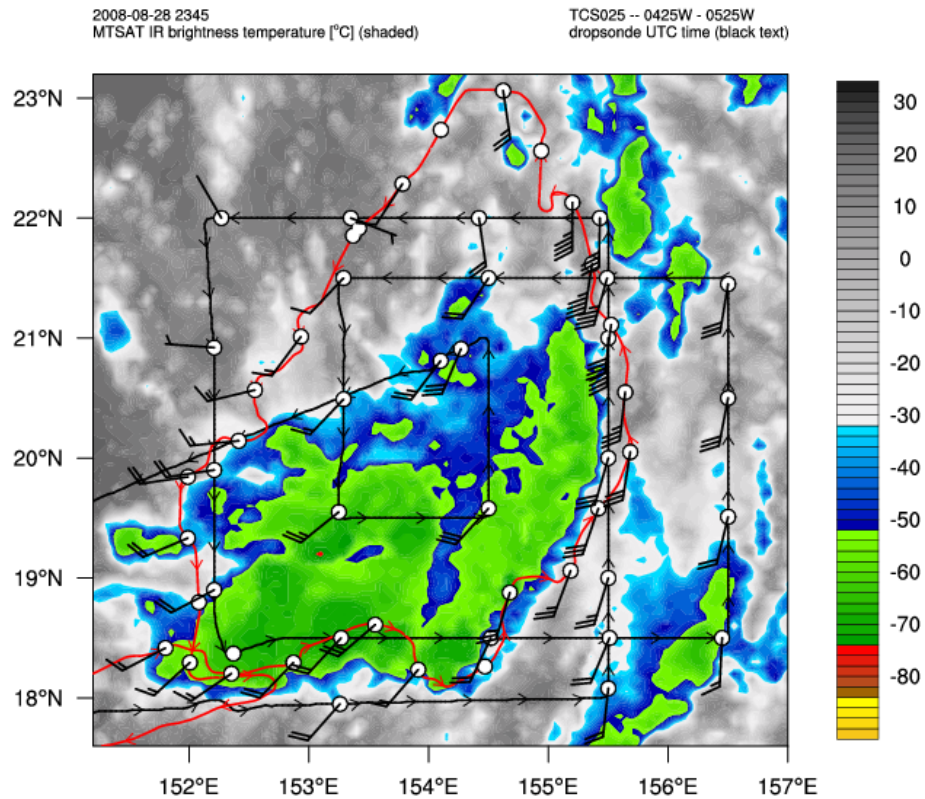


Figure 54 MTSAT IR brightness temperature (°C, shading) valid at 2345 UTC 28 August. The USAF WC-130J flight track (black line), NRL P-3 flight track (red line), and dropwindsonde deployment locations (white circles) are shown for third IOP (0425W and 0525W) with wind barbs corresponding to 1500 m height (1 full barb = 10 kt).

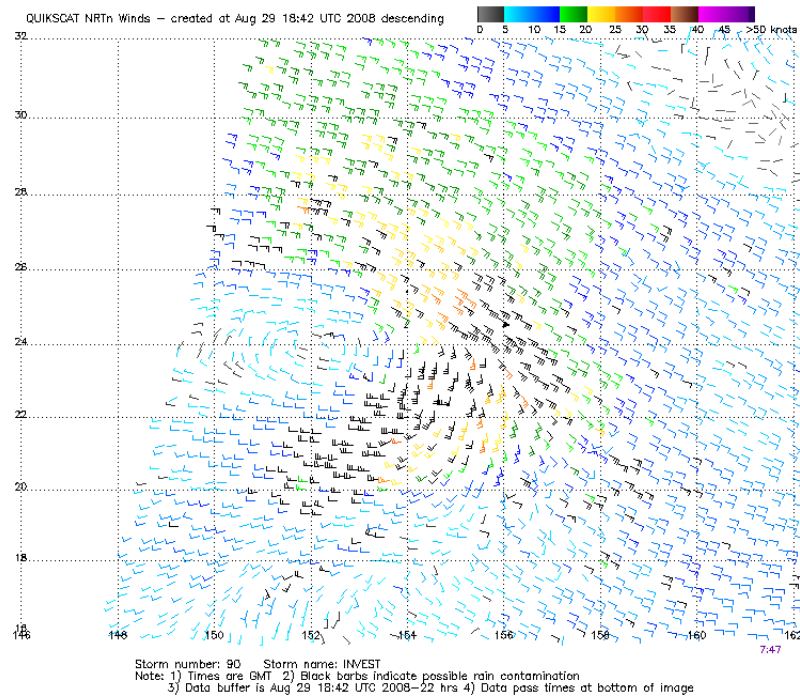


Figure 55 Surface wind speed (kt) and direction (wind barbs, shading) valid at ~0747 UTC 29 August from the NASA QuikSCAT scatterometer. Black wind barbs denote possible rain contamination (from the T-PARC/TCS-08 Field Catalog: [http://catalog.eol.ucar.edu/tparc\\_2008/report/weather/20080829/report.weather.200808292300.summary.image5.png](http://catalog.eol.ucar.edu/tparc_2008/report/weather/20080829/report.weather.200808292300.summary.image5.png)).

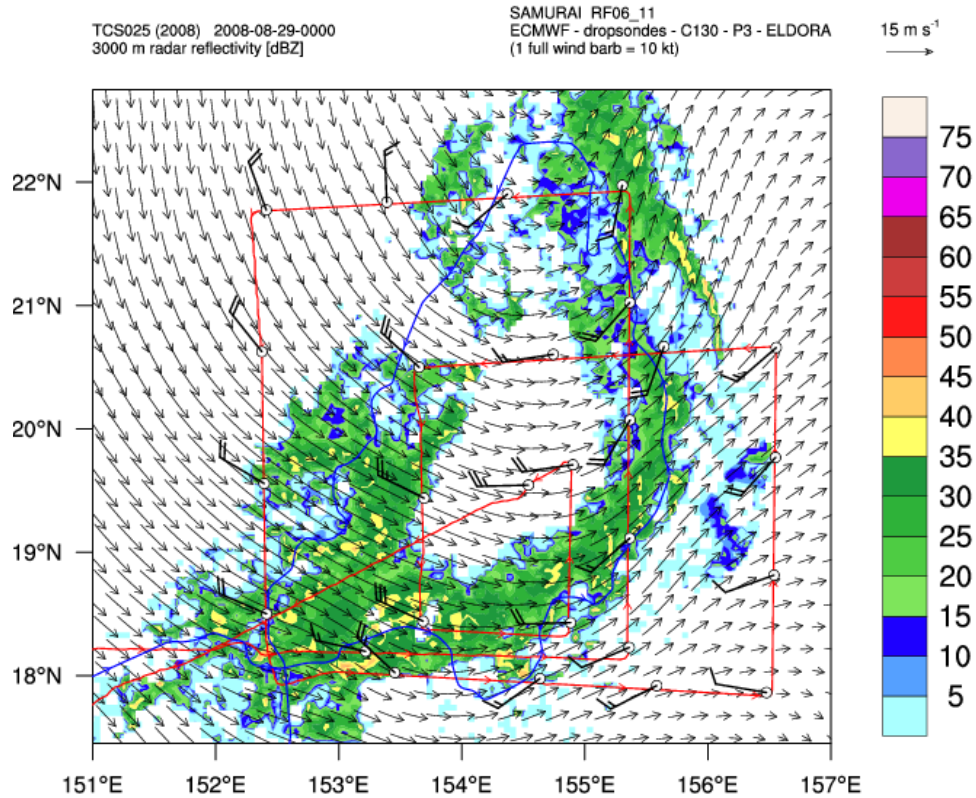


Figure 56 ELDORA reflectivity (dBZ, shading) at 3000 m height from the NRL P-3 flight (0425W) early on 29 August. The horizontal wind vectors correspond to the wind field derived using the SAMURAI analysis technique in the storm-relative frame. The USAF WC-130J track for flight 0525W is in red and the NRL P-3 track for flight 0425W is in blue. Black wind barbs correspond to dropwindsonde winds corrected for storm motion (1 full barb = 10 kt).



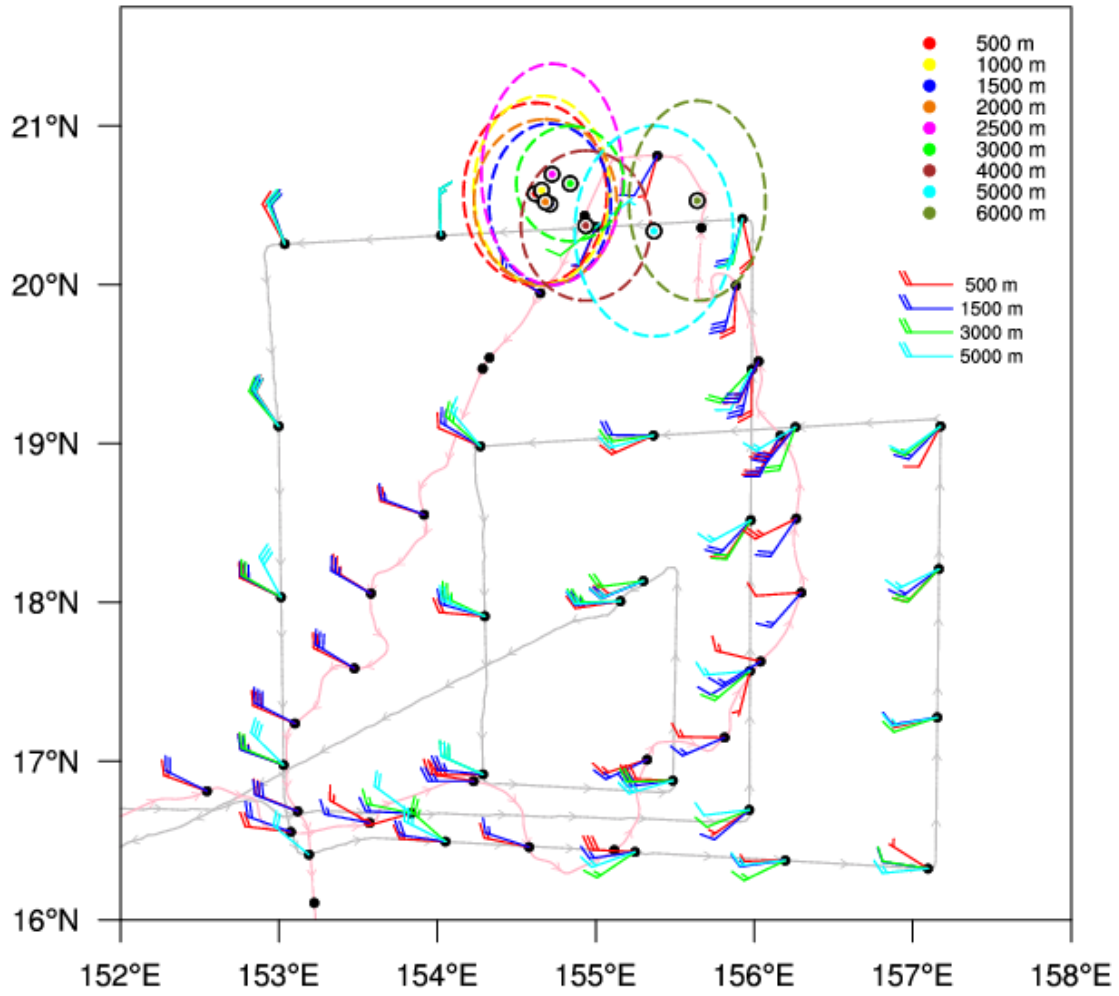


Figure 57 As in Figure 40, except for storm-relative USAF WC-130J (0525W: 2234 UTC 28 August – 0510 UTC 29 August) and NRL P-3 (0425W: 0015 UTC 29 August – 0420 UTC 29 August) flight tracks for the third IOP.

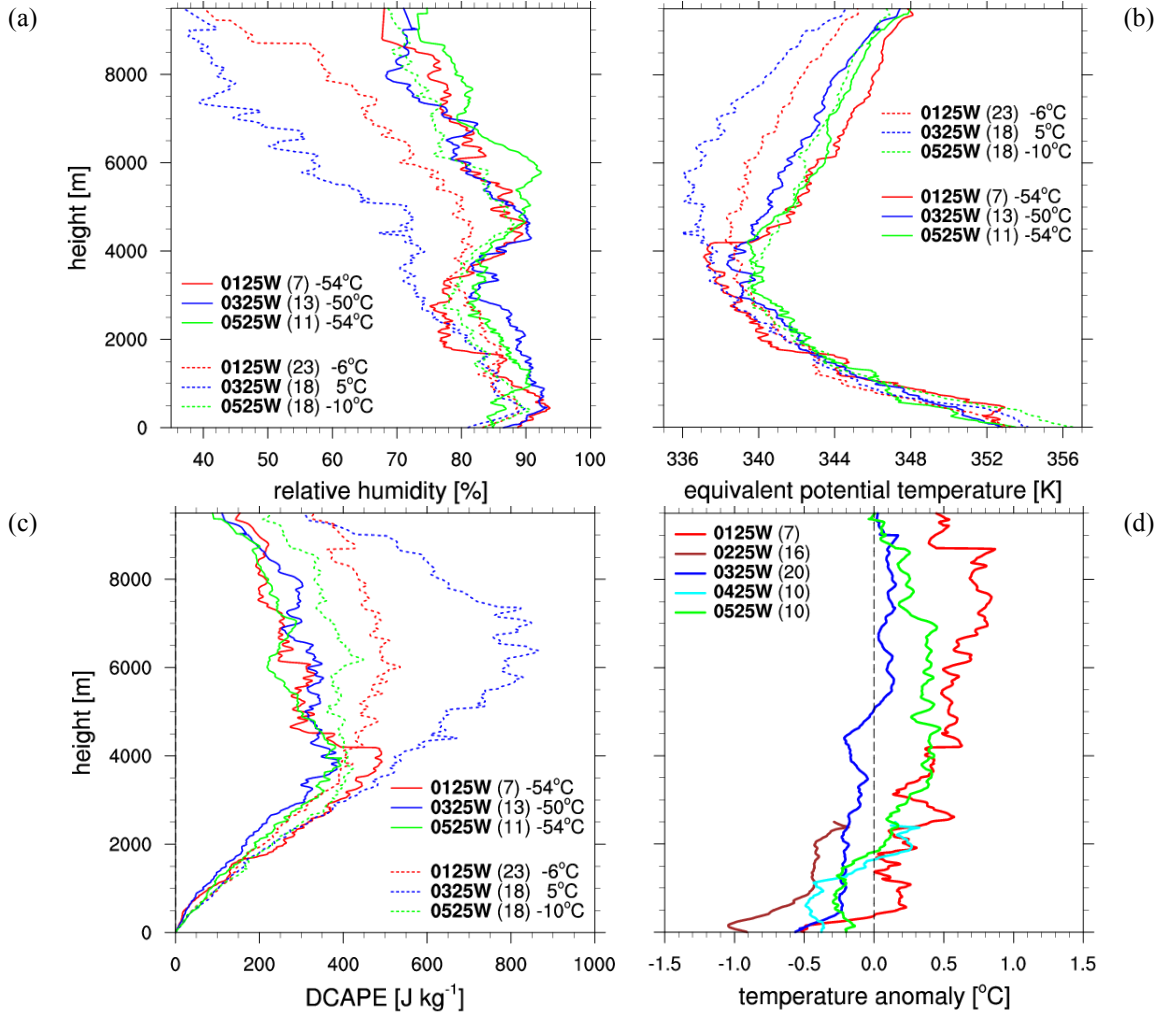


Figure 58 Vertical profiles of (a) relative humidity (%), (b)  $\theta_e$  (K), and (c) DCAPE ( $\text{J kg}^{-1}$ ) averaged for dropwindsondes for which the MTSAT IR brightness temperatures interpolated to the dropwindsonde time and location were less than  $-35^\circ\text{C}$  (solid lines) and greater than  $-35^\circ\text{C}$  (dashed lines) during USAF WC-130J aircraft missions shown in inset. The average MTSAT IR brightness temperatures of dropwindsondes used to compute each average are shown in inset. (d) Vertical profiles of temperature anomaly (K) from dropwindsondes averaged within 250 km of the analyzed ECMWF 850 hPa circulation center during aircraft missions shown in inset. Each mean profile used to compute the average temperature anomaly was constructed from all dropwindsondes from each flight. The number of dropwindsondes used to compute each average is shown in the inset of each figure.

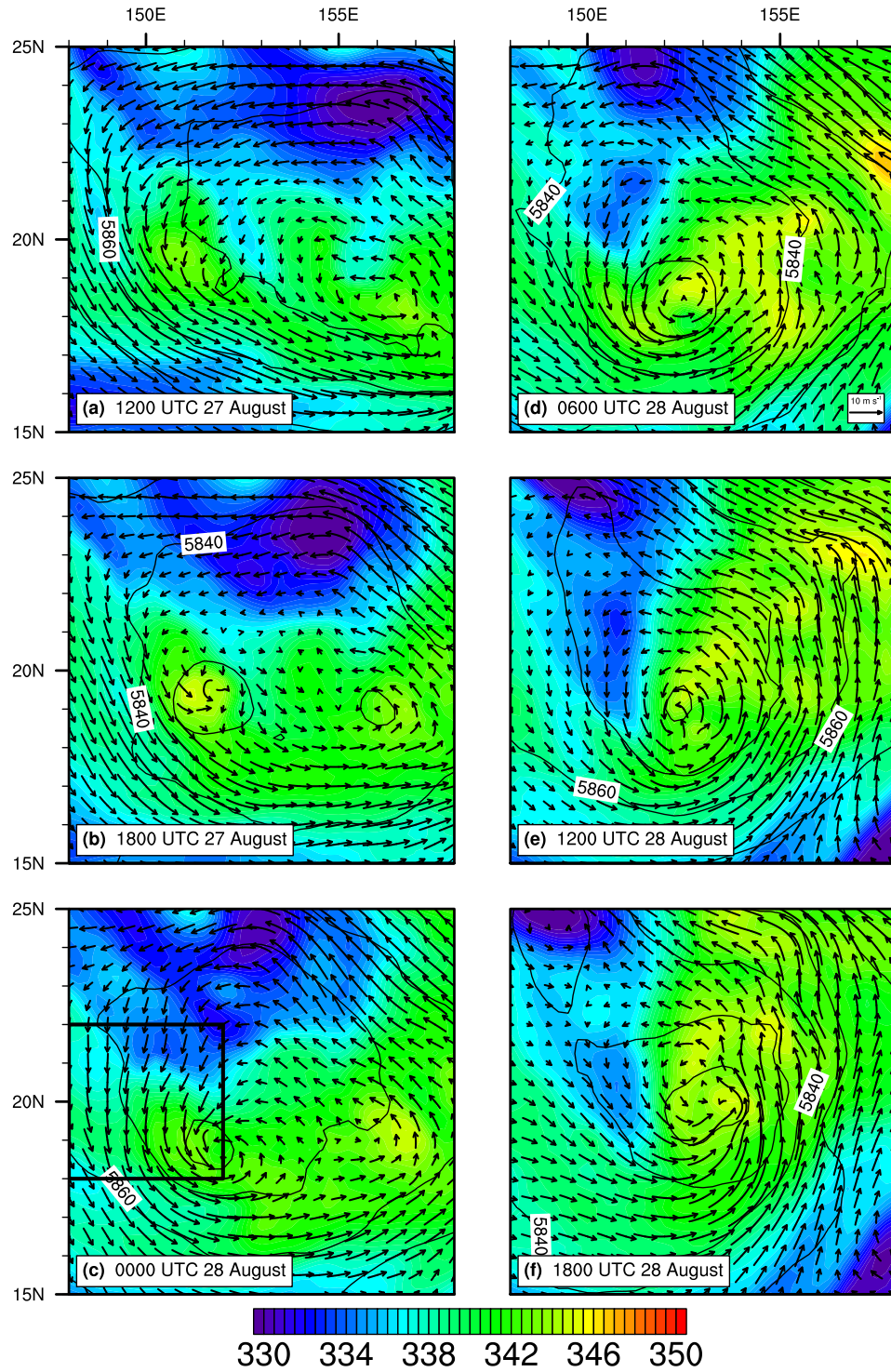


Figure 59 Equivalent potential temperature (K, shading), geopotential height (m, contours), and wind vectors ( $\text{m s}^{-1}$ , with  $10 \text{ m s}^{-1}$  reference vector indicated at bottom right in panel (d)) at 500 hPa from the ECMWF analysis at times annotated in each panel. The black box in (c) corresponds to the area from which back trajectories in Figure 60 were selected at the end time of 0000 UTC 28 August.

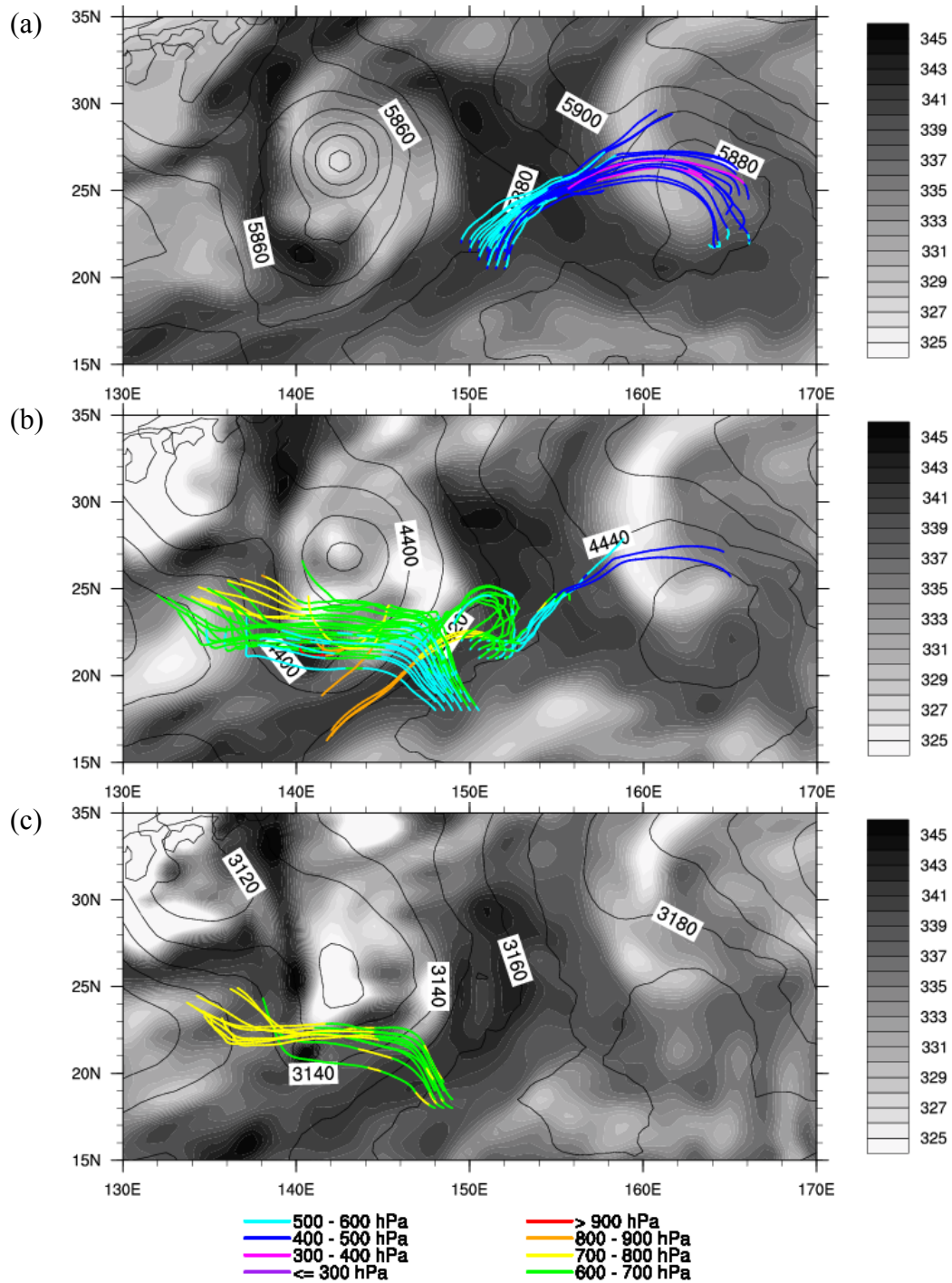


Figure 60 Equivalent potential temperature (K, shading) and geopotential height (m, contours) at 0000 UTC 25 August from the CFSR reanalysis at (a) 500 hPa, (b) 600 hPa and (c) 700 hPa. Colored lines correspond to 72-h back trajectories selected from grid points within the boxed region of 18-22°N, 148-152°E at (a) 500 hPa, (b) 600 hPa, and (c) 700 hPa in which the relative humidity at the ending time of 0000 UTC 28 August was < 70 %. Colored segments of trajectory lines indicate pressure levels in panel (c) inset.

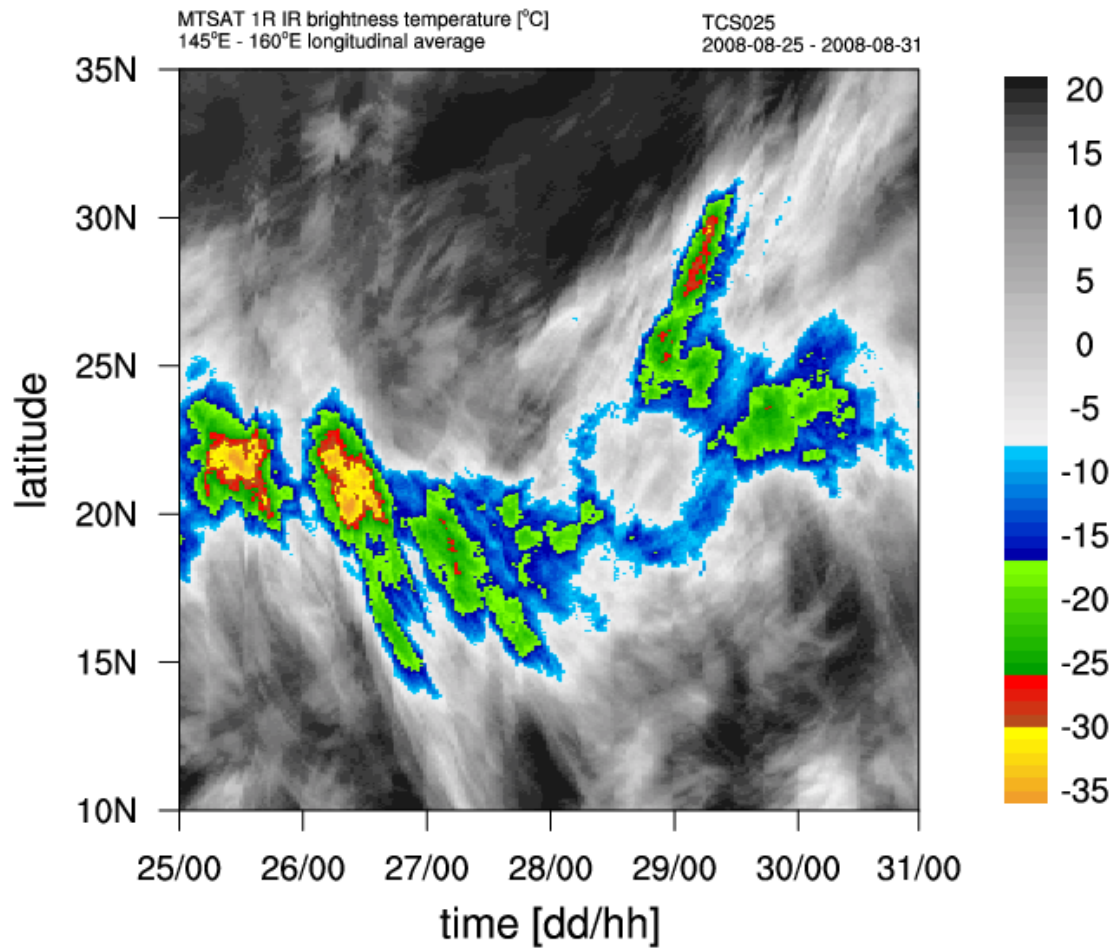


Figure 61 Longitudinal average from 145°E to 160°E of MTSAT IR brightness temperatures (°C) as a function of latitude from 10°N to 35°N during the evolution of TCS025.



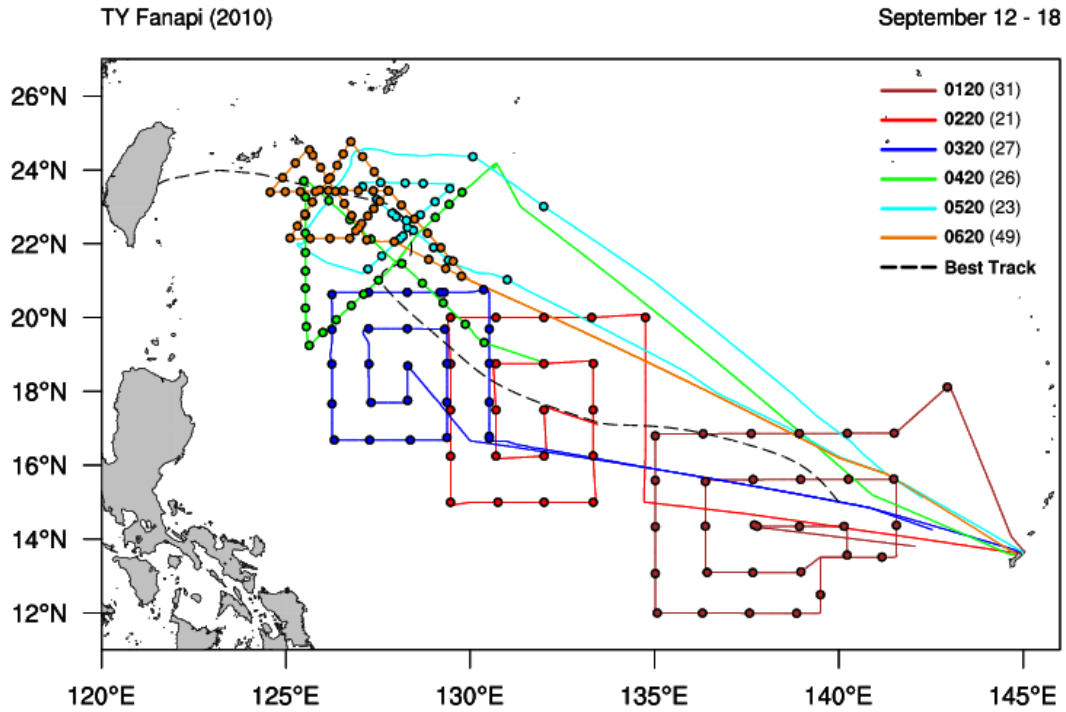


Figure 62 Flight tracks for the six USAF WC-130J aircraft missions flown to observe TY Fanapi (2010). Colored dots correspond to dropwindsonde deployment locations and the number of dropwindsondes deployed during each mission is shown in inset. The black dashed line marks the best track created using a combination of JTWC best-track locations and aircraft vortex fixes.

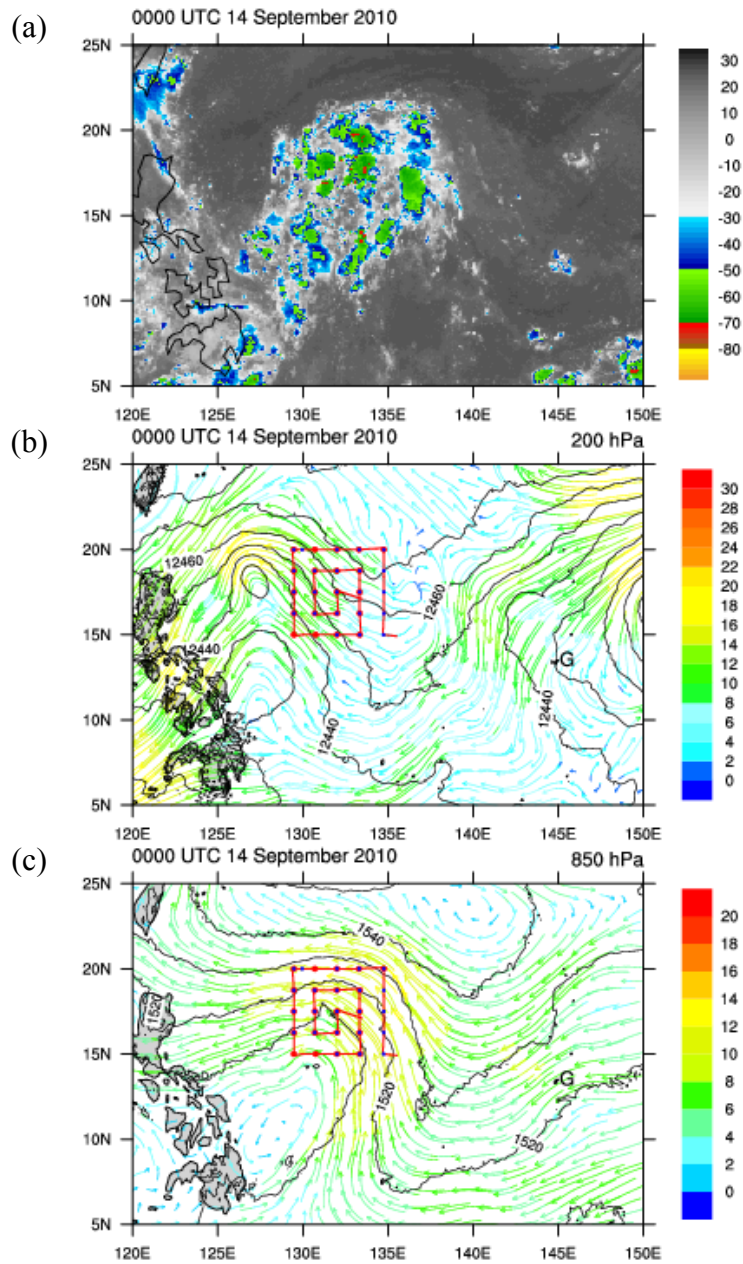


Figure 63 As in Figure 31, except (a) MTSAT-IR brightness temperature (°C) for pre-TY Fanapi at 0000 UTC 14 September 2010 and (b) 200 hPa and (c) 850 hPa from the ECMWF operational analysis valid at 0000 UTC 14 September (during second USAF WC-130J mission 0220W). Blue circles in (b) and (c) correspond to AXBT deployment.

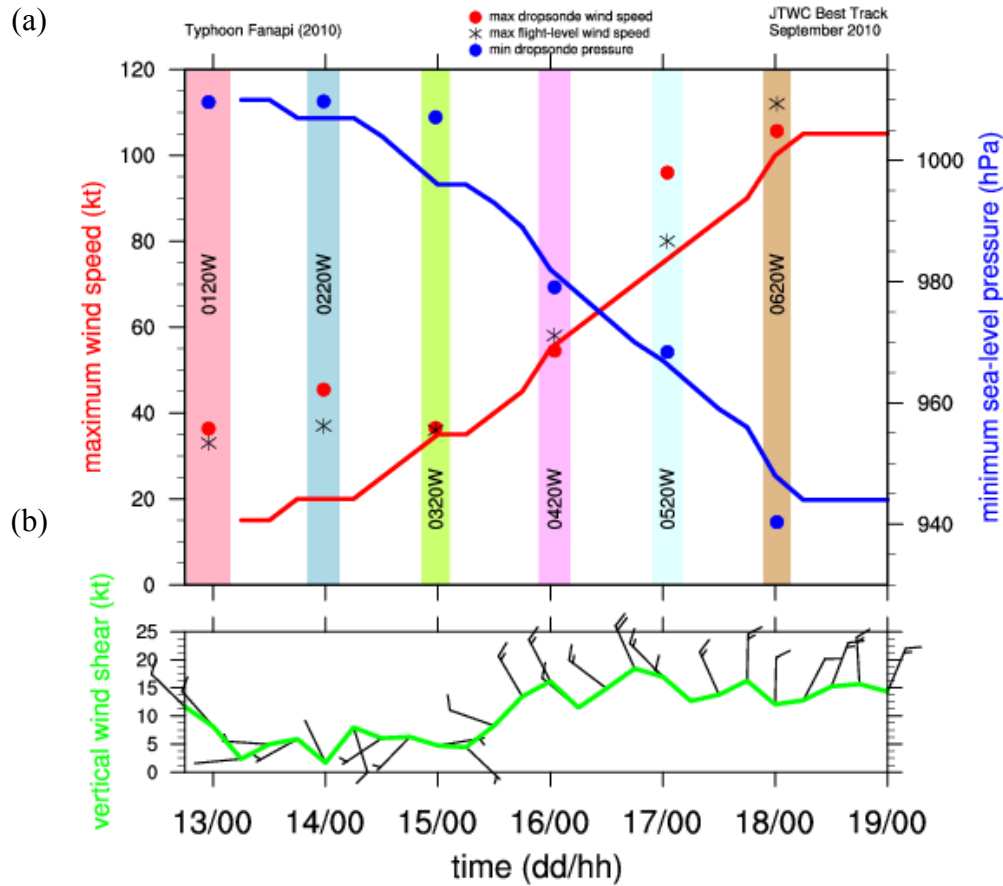


Figure 64 (a) JTWC best-track maximum wind speed (kt, red line and left ordinate) and minimum sea-level pressure (hPa, blue line and right ordinate) during TY Fanapi. Red and blue dots denote the dropwindsonde maximum wind speed (kt) and minimum sea-level pressure (hPa), respectively, for each aircraft mission marked by the colored vertical bars. Asterisks denote maximum flight-level winds for each aircraft mission. (b) Magnitude of the 200-850 hPa vertical wind shear (kt) and direction (1 full barb = 10 kt) computed using CFSR reanalysis data (see text for details).



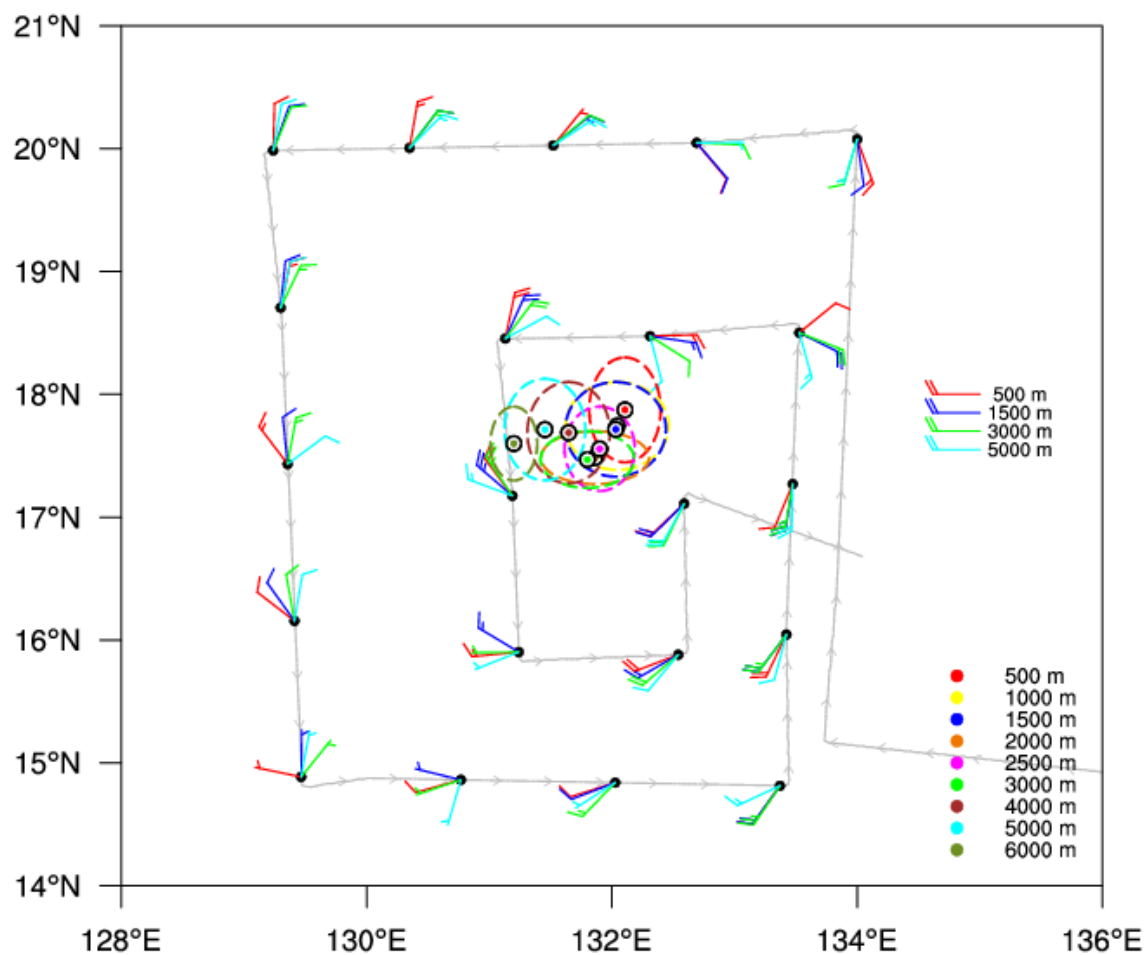


Figure 65 As in Figure 40, except storm-relative USAF WC-130J (0220W: 2014 UTC 13 September - 0258 UTC 14 September) flight tracks for TY Fanapi (2010).

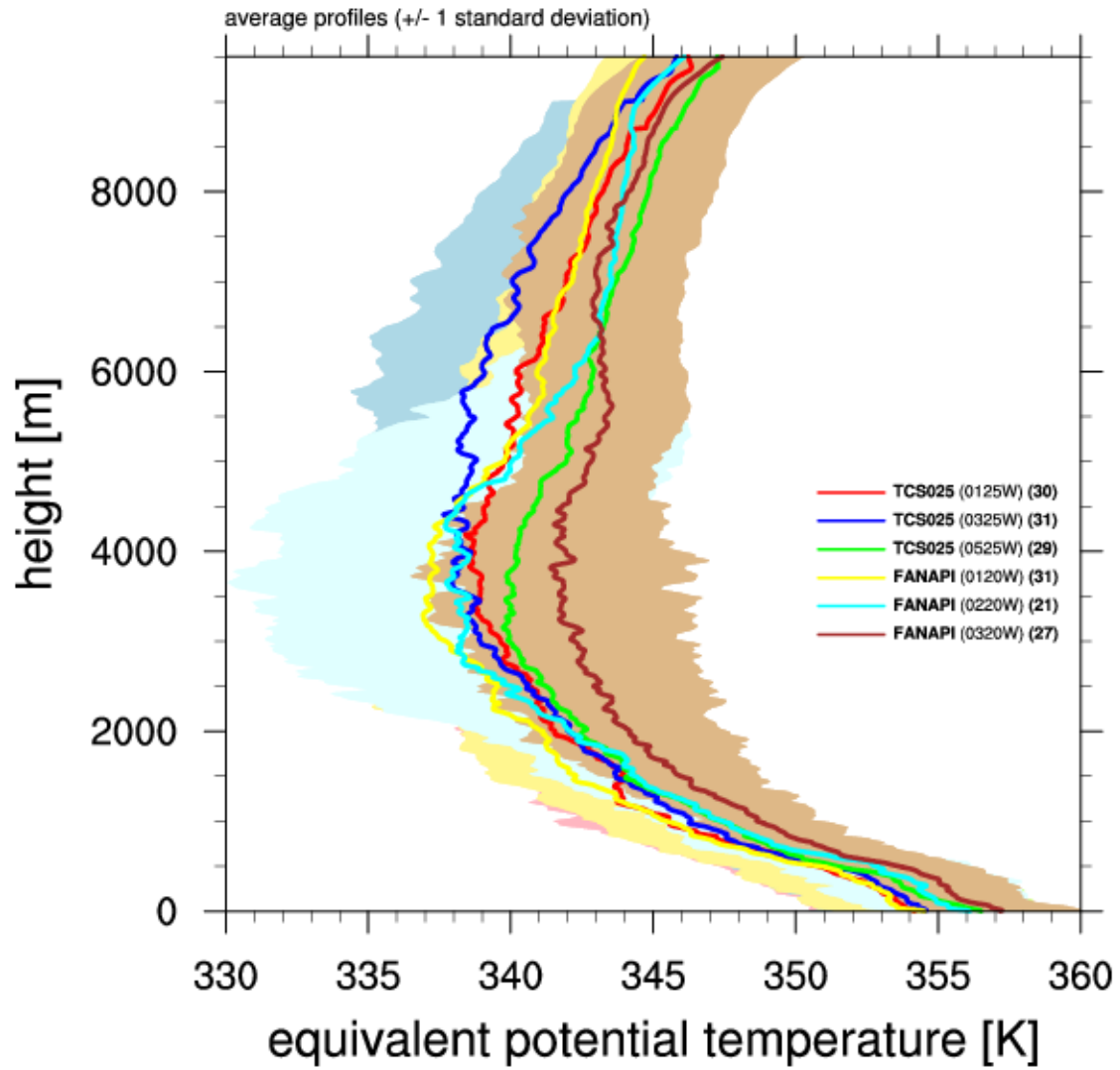


Figure 66 Average profiles of  $\theta_e$  (K) created from all dropwindsondes collected during the three USAF WC-130J flights in TCS025 and the first three TY Fanapi USAF WC-130J flights. Colored shading surrounding the average profiles denotes  $\pm 1$  standard deviation. The number of dropwindsondes used to compute each average is shown in the legend.

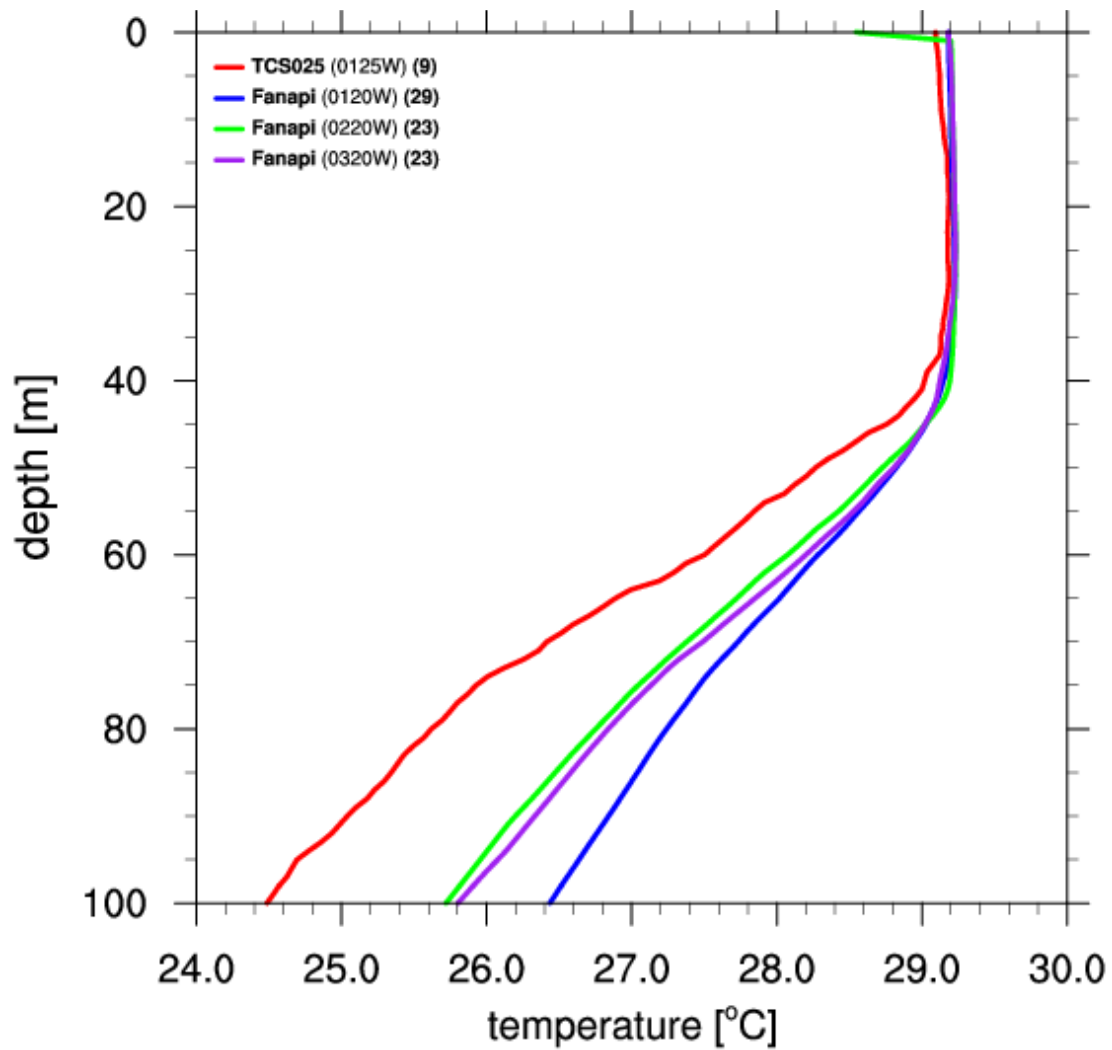


Figure 67 Average oceanic temperature (°C) profiles constructed from AXBT data collected during the first USAF WC-130J mission (0125W) in TCS025 and the first three USAF WC-130J missions for TY Fanapi. The number of AXBTs used to compute each average is shown in the legend.

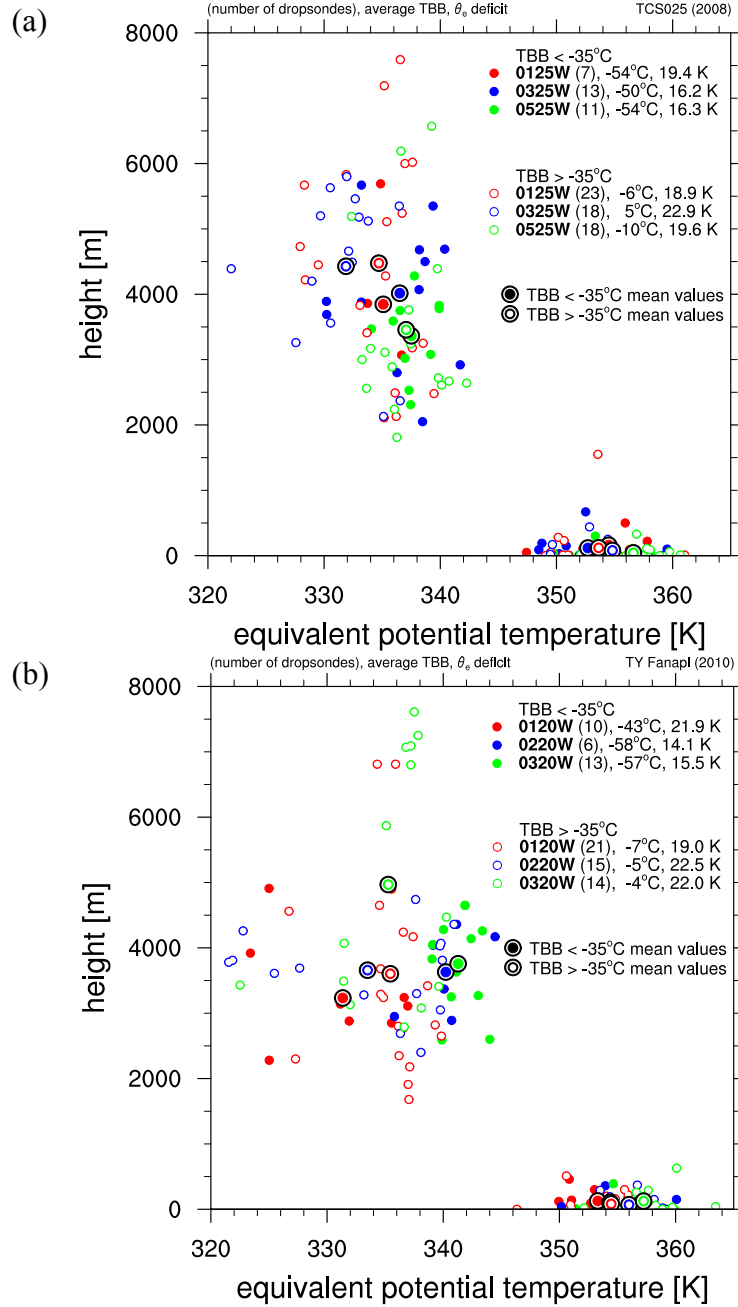


Figure 68 Minimum and maximum  $\theta_e$  (K) for (a) TCS025 and (b) pre-TY Fanapi from individual dropwindsonde profiles during USAF WC-130J missions (shown in inset) for which the MTSAT IR brightness temperatures interpolated to the dropwindsonde time and location were less than  $-35^{\circ}\text{C}$  (filled circles) and greater than  $-35^{\circ}\text{C}$  (open circles). Circles enclosed by thin black circles correspond to the mean  $\theta_e$  extrema of the convective and non-convective environments for each flight. The numbers of dropwindsondes used to compute the average  $\theta_e$  extrema are shown in the inset along with the average IR brightness temperature ( $^{\circ}\text{C}$ ) and average  $\theta_e$  deficit (K) (maximum  $\theta_e$  – minimum  $\theta_e$ ).

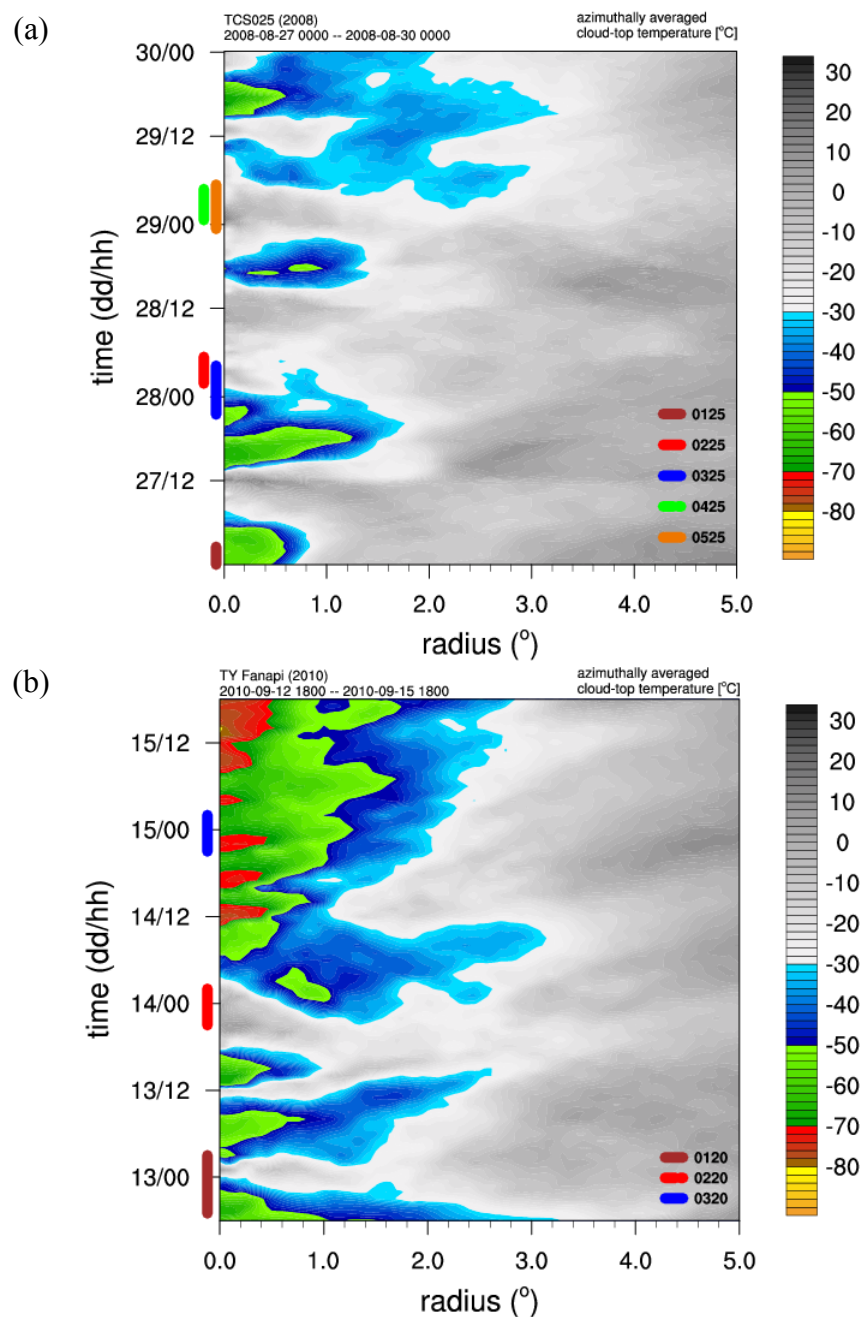


Figure 69 Radially-averaged ( $0^{\circ}$ - $3^{\circ}$ ) MTSAT IR brightness temperature from (a) the ECMWF 850 hPa vorticity maximum position of TCS025 and (b) the modified best-track position of TY Fanapi computed using a combination of JTWC best-track locations and aircraft vortex fixes and were interpolated to 15-minute intervals. Solid colors along the time axis in (a) represent aircraft missions in TCS025 with brown, blue, and orange corresponding to the USAF WC-130J and red and green the NRL P-3 (see inset). Solid colors along the time axis in (b) represent USAF WC-130J pre-TY Fanapi missions.

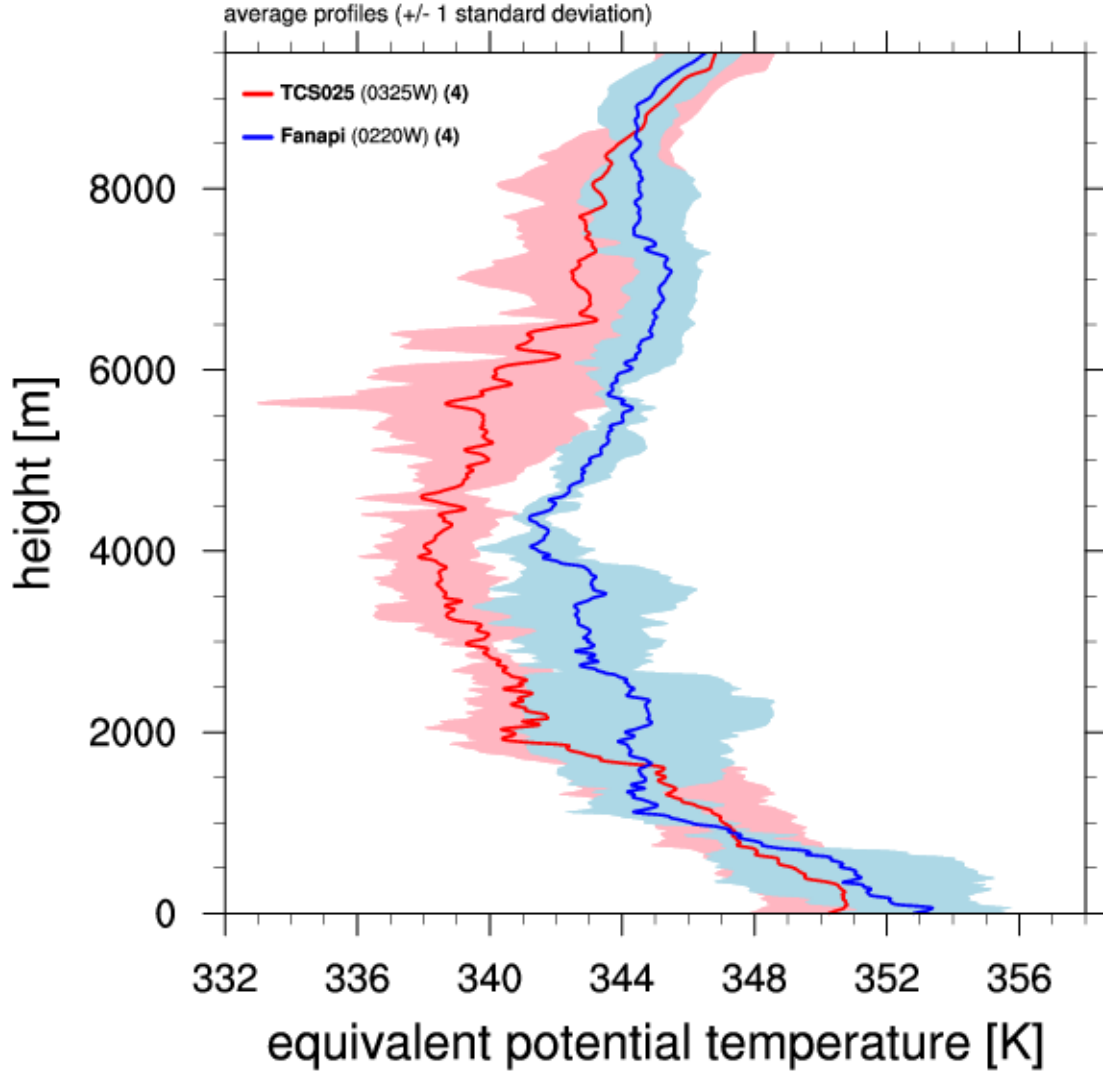


Figure 70 Average profiles of  $\theta_e$  (K) from the four dropwindsondes immediately surrounding the circulations of TCS025 (red line and shading) during the 0325W mission and pre-TY Fanapi (blue line and shading) during the 0220W mission. For TCS025, only dropwindsondes from the USAF WC-130J were used to compute the average. Colored shading surrounding the average profiles denotes  $\pm 1$  standard deviation.

## IV. MULTI-PHYSICS ENSEMBLE

To gain insight into the evolution of the TCS025 disturbance beyond the observation analysis in Chapter III, a multi-physics ensemble was integrated using the WRF-ARW numerical model (see Table 3). Multi-physics ensemble simulations were conducted without data assimilation and were initialized from the ECMWF analysis. The simulations were originally intended to help quantify the physical processes related to the non-development of TCS025. However, as will be described in this chapter, the majority of WRF simulations over-developed the TCS025 disturbance.

For the majority of the WRF multi-physics ensemble simulations (Figure 71a), the predicted minimum sea-level pressures were in good agreement with the ECMWF analysis for the first 24 hours, even including the semi-diurnal oscillations evident in the ECMWF time series. However, most of the simulations exhibited a substantial decline in minimum sea-level pressure shortly after 1200 UTC 28 August. The two simulations (18 and 19 in Table 3) that exhibited the most rapid intensification and lowest sea-level pressure (Figure 71) used unrealistic or overly simplistic physical parameterizations and thus were not a focus in this study. The bulk of the simulations followed a similar storm track defined by minimum sea-level pressure (Figure 72). Simulations that exhibited limited development of the TCS025 disturbance, such as simulation 25 and the ECMWF analysis, had tracks that were to the west of simulations that intensified the disturbance.

Although the majority of the WRF simulations over-developed the TCS025 disturbance, there were notable differences in evolution. This section will analyze and compare two simulations that exhibited different development scenarios for TCS025: simulation 25 that failed to develop the disturbance, and simulation 9, which exhibited moderate development (see bold purple and red lines in Figure 71 and Figure 72). Even though the ECMWF YOTC analysis was shown to have limitations related to its representation of the TCS025 circulation structure based on the ELDORA observations on the mesoscale, it correctly portrayed the non-development of TCS025, and therefore will be used as a point of comparison in evaluating the WRF simulations.

These two simulations chosen in this comparison differed only in their use of microphysics schemes (see Table 3). The non-developing simulation 25 employed the WSM3 microphysics scheme (Hong et al. 2004), which used single variables to account for the mixing ratios of cloud water and cloud ice and the mixing ratios of rain and snow, which precluded mixed phase processes. The over-developing simulation 9 used the Purdue Lin scheme (Lin et al. 1983; Chen and Sun 2002), which accounted for the mixing ratios of liquid cloud water, rain, ice, snow and graupel.

Skamarock et al. (2008) states that “as a general rule, for grid sizes less than 10 km, where updrafts may be resolved, mixed-phase schemes should be used, particularly in convective or icing situations.” However, tropical cyclone simulations that employ microphysics schemes that account for additional hydrometeor species and mixed phase processes have been shown by McFarquhar et al. (2006) to result in more intense storms compared to simulations that use less sophisticated schemes. In the case of TCS025, the additional complexity of the Purdue Lin microphysics scheme in simulation 9 resulted in over-development of the disturbance relative to the more simplistic WSM3 scheme used in simulation 25.

## **A. SYNOPTIC EVOLUTION**

To elucidate why the TCS025 disturbance was consistently over-developed in the majority of multi-physics WRF simulations, the synoptic evolution of the TCS025 disturbance as depicted by WRF simulation 9 (over-development) will be compared to WRF simulation 25 (no development).

Both WRF simulations were initialized at 1200 UTC 27 August, which was between the time of the first and second IOPs (see Figure 18). Based on minimum sea-level pressure (Figure 71), simulation 9 began to intensify the TCS025 disturbance shortly after 1200 UTC 28 August, and by 0000 UTC 28 August (12 h into the simulation), notable differences between the two simulations were readily apparent (Figure 73). Lower geopotential heights were evident close to the low-level circulation near 19°N, 152°E for WRF simulation 9 (Figure 73d), which also had areas of deep convection (not shown). At 200 hPa, a narrow band of northerly winds is evident near



18°N, 157°E (Figure 73b) directly above the eastern periphery of the low-level circulation. A second band of enhanced northerlies is also evident farther to the east near 18°N, 162°E. Both of these bands appear to be outflow channels that turn anticyclonically away from the area above the low-level circulation, and are greatly enhanced in WRF simulation 9 (Figure 73b) relative to simulation 25 (Figure 73a) and the ECMWF analysis (not shown).

Northeast-to-southwest vertical cross sections that extend through the location of the TUTT and the low-level circulation reveal differences in the circulation structure and thermodynamic response to convection after 12 h into the simulation (Figure 74). The vorticity structure associated with the TCS025 circulation in WRF simulation 25 was poorly aligned vertically (Figure 74a). A low-level cyclonic vorticity feature, which was quite shallow, existed north of a mid-level vorticity feature that was strongest near 500 hPa. Relative vorticity was weak and diffuse between the low- and mid-level vorticity features. In contrast, the vorticity depicted by WRF simulation 9 was much stronger than that in simulation 25, and extended from 800 hPa to 400 hPa as a vertically coherent structure (Figure 74b). Similar to simulation 25, a shallow low-level vorticity feature existed to the north of the mid-level vorticity, but less distance separated these two features. Somewhat different from the WRF simulations, the ECMWF analysis depicted a tilted vorticity feature that extended upward from the surface into the mid-troposphere, with maximum vorticity near 700 hPa (see Figure 48b). The positive vorticity associated with the TUTT was slightly weaker in WRF simulation 25 (Figure 74a), and was displaced slightly to the south relative to the position in simulation 9 (Figure 74b).

Vertical cross sections of  $\theta_e$  and virtual temperature ( $T_v$ ) perturbation also reveal striking differences after only 12 hours into the simulations (Figure 74c, d). Although the  $T_v$  perturbations were positive and  $\theta_e$  values were greater relative to the background near ~350 hPa above the low-level circulation in both simulations, the anomalies were somewhat stronger in simulation 9 (Figure 74d) compared to simulation 25 (Figure 74c). In contrast, a comparison of the low-level  $T_v$  perturbations and low-level  $\theta_e$  below the warm upper-level anomalies reveals the largest boundary layer cooling occurred in

simulation 9. This suggests that convectively-generated cold pools were stronger in simulation 9 than in simulation 25.

At the north end of the cross sections in Figure 74c and Figure 74d, low- $\theta_e$  air associated with the TUTT was evident near 600 hPa in both cases. The negative  $T_v$  anomaly associated with the TUTT is strongest in simulation 9 near 350 hPa, which is consistent with the vorticity being slightly stronger in simulation 9. Low- $\theta_e$  air from the TUTT appears to be impinging on the mid-level vorticity feature in both simulations (Figure 74c,d). Near the center of each cross section, a plume of higher- $\theta_e$  air extends upward through the mid-levels near the southern extent of the low- $\theta_e$  air associated with the TUTT. A negative  $T_v$  anomaly is present below this region within the boundary layer, which is indicative of recent convective overturning: boundary layer air (high- $\theta_e$ ) was transported into the mid-levels where mixing occurred with surrounding low- $\theta_e$  air through entrainment processes, and in turn, evaporative downdrafts acted to deplete boundary layer  $\theta_e$ .

By 0000 UTC 29 August (T + 36 h), the low-level circulation in WRF simulation 9 was much stronger compared to simulation 25, and was slightly to the northeast of its position in simulation 25 (Figure 75c, d). The strongest winds were almost exclusively along the eastern side of the circulation. Notable upper-level differences also existed (Figure 75a,b). Although the outflow emanating from the north and south of the system in simulation 25 was relatively weak, the outflow wraps anticyclonically around to the east and south of the ridge above the low-level circulation (Figure 75a). Interestingly, the TCS025 system was actually stronger in the ECMWF analysis than in simulation 25 at 1200 UTC 28 August (see Figure 71a,b). In contrast, upper-level outflow was much stronger in simulation 9 (Figure 75b). A very strong outflow channel is evident near 25°N, 156°E that emanated from northeast of the system, turned anticyclonically toward the south, and merged with an area of strong northerly flow before turning westward near 14°N. A second outflow channel south of the system is also evident, and it followed a similar trajectory away from the TCS025 system toward the southwest. The upper-level

ridge and anticyclonic flow around the periphery of the ridge was much stronger in simulation 9 compared to simulation 25 at this time.

A comparison of vertical cross sections through the low-level circulation valid at 0000 UTC 29 August also reveals striking differences in the circulation structure (Figure 76a,b). The relative vorticity originally associated with the low-level circulation of TCS025 (southern-most vorticity feature in cross section) in simulation 25 continued to appear weak and poorly aligned in the vertical (Figure 76a). The cyclonic vorticity was strongest near 800 hPa, and was much weaker in the mid-levels (~500 hPa) compared to the day before (see Figure 74a). The shallow, lower-tropospheric vorticity feature in the northern part of the cross section had wrapped cyclonically around to the north of the main circulation center. In contrast, relative vorticity associated with the TCS025 circulation in WRF simulation 9 was notably stronger, especially in the low levels, and was well-aligned in the vertical (Figure 76b). A separate lower-tropospheric vorticity feature was also present to the north of the main circulation in simulation 9. It was slightly weaker at the surface, but, similar to the main circulation, appeared better aligned in the vertical than in simulation 25.

Vertical cross sections of  $\theta_e$  and perturbation  $T_v$  valid at 0000 UTC 29 August highlight the ongoing development in WRF simulation 9 (Figure 76c,d). Near the circulation center (to the south of the cross section), the deficit in boundary layer  $\theta_e$  that was present 24 h earlier (see Figure 74d) was no longer evident in simulation 9. Instead, a plume of high- $\theta_e$  air extended through the depth of the troposphere (Figure 76d). Similarly, the magnitude of boundary layer  $\theta_e$  was also elevated in simulation 25 compared to the day before, but mid-level  $\theta_e$  had declined (Figure 76c), perhaps as a result of limited convective activity after the first 12 h in simulation 25.

Although the absolute magnitudes of perturbation  $T_v$  cannot be directly compared at this time due to the different reference profiles resulting from the contrast in development, the following aspects are noteworthy: a positive  $T_v$  anomaly was present in simulation 25 above the low-level circulation, but was much weaker than in simulation 9; and low-level negative  $T_v$  anomalies were still present near the low-level circulation in

both WRF simulations (Figure 76). These anomalies suggest that convective downdrafts were transporting low- $\theta_e$  air into the boundary layer in the WRF simulations.

By 0000 UTC 30 August (T + 60 h), the minimum sea-level pressure in WRF simulation 9 had deepened to 998 hPa and the maximum 10-m wind speed was close to  $23 \text{ m s}^{-1}$ . In contrast, the minimum sea-level pressure and maximum 10-m wind speed in simulation 25 were 1009 hPa and  $13 \text{ m s}^{-1}$ , respectively (see Figure 71). The low-level wind field in simulation 9 (Figure 77d) had become increasingly symmetric about the center compared to the previous day, as the strongest winds were wrapping around the north side of the system. However, winds along the western side of the system were still weak relative to the winds along the eastern side. In contrast, the low-level circulation in simulation 25 was weaker than the day before, and was no longer a closed circulation (Figure 77c). Both simulations exhibited some development farther to the east within the low-level trough (Figure 77c,d), which is inconsistent with the ECMWF analysis (see Figure 34c).

In the upper-levels, both WRF simulations had a band of higher wind speeds that followed an anticyclonic trajectory around the upper-level ridge that was above and to the north of the TCS025 disturbance (Figure 77a,b). The upper-level ridge was much stronger in simulation 9 (Figure 77b), especially to the north of the low-level circulation. Similar to the day before, the northern outflow channel was the most dominant in simulation 9 (Figure 77b). Due to the relatively weak upper-level ridge in simulation 25, the anticyclonic outflow was much weaker (Figure 77a). In fact, the upper-level ridge and anticyclonic flow in simulation 25 were weaker in the ECMWF analysis at this time (see Figure 34b).

A time series of azimuthally-averaged 200 hPa radial velocities indicates the presence of stronger radial outflow at all radii in simulation 9 (Figure 78b) relative to simulation 25 (Figure 78a). At 150 km radius, the azimuthal-mean outflow in simulation 9 was already stronger than in simulation 25 by 1800 UTC 27 August (T + 6 h), and remained stronger throughout the simulation at all radii. In contrast, weak outflow was exhibited by simulation 25 that was similar to the magnitude and structure in the

ECMWF analysis (Figure 78c), with the strongest outflow at large radii from the center. Not surprisingly, the evolution of TCS025 as exhibited by simulation 25 was very similar to the ECMWF analysis.

In summary, the WRF simulations 9 and 25 exhibited discernable differences shortly after the models were initialized. In simulation 9, the low-level geopotential heights decreased in areas where deep convection was occurring. Development of an upper-level ridge and outflow above the TCS025 disturbance were almost immediate and evolved to a much larger magnitude than in simulation 25. The contrasts in synoptic development exhibited by simulations 9 and 25 suggest there were significant differences in how precipitation processes were represented in the two simulations. Rapid pressure (height) falls in the lower troposphere coupled with the development of an upper-level anticyclone and outflow aloft are expected responses to diabatic heating associated with the strong convection in simulation 9. Evidence that strong convective overturning in simulation 9 had redistributed  $\theta_e$  within the atmospheric column was also present; early in the simulation, upper-level  $\theta_e$  was of greater magnitude in simulation 9, while at the same time, the effects of evaporative cooling in the boundary layer were more pronounced (see Figure 74c,d). Thus, despite greater evaporative cooling in the low-level environment, simulation 9 was able to develop a robust, vertically-coherent vortex structure (see Figure 74b) due to strong convective processes. On the other hand, the convective processes were much weaker in simulation 25, and as a result, the circulation remained weak and disorganized.

## **B. CIRCULATION BUDGET ANALYSES**

To analyze the key processes responsible for the formation of the TCS025 disturbance in the WRF simulations, a circulation budget was computed for several boxed regions surrounding the low-level circulation during the early part of the TCS025 evolution. Following the method employed by Davis and Galarneau (2009), the time rate of change in relative vorticity shown in Equation 2 can be rewritten in a form that relates to the circulation tendency within a boxed region by accounting for both eddy and mean contributions as:

$$\frac{\partial C}{\partial t} = -\bar{\eta}\tilde{\delta}A - \oint \eta' \bar{v} \cdot \hat{n} dl + \oint \omega \left( \hat{k} \times \frac{\partial \bar{v}}{\partial p} \right) \cdot \hat{n} dl + \oint (\hat{k} \times \bar{F}) \cdot \hat{n} dl. \quad (10)$$

Here  $C$  represents the circulation,  $\eta$  is the absolute vorticity,  $\tilde{\delta}$  is the mean divergence over the area  $A$  of the box,  $\oint$  represents the line integral around the perimeter of the box,  $\bar{v}$  is the horizontal wind vector,  $\hat{n}$  is the direction normal to the perimeter of the box,  $\omega$  is the vertical velocity in pressure coordinates,  $p$  is pressure, and  $\bar{F}$  represents the frictional force. Overbars correspond with average values around the perimeter of the box, primed quantities denote perturbations from this average, and tildes indicate an average over the area of the box. The terms on the right side in Equation 10 are defined as follows: term one is the contribution from the vertical stretching of vorticity; term two represents the eddy flux of perturbation vorticity into and out of the boxed region via horizontal flow directed normal to the box perimeter; term three represents the tilting of horizontal vorticity into the vertical plane through updrafts along the perimeter of the box. Although neglected in this study, term four represents the frictional force acting along the perimeter of the box. Circulation tendencies due to friction were not explicitly computed, but were accounted for in a residual term along with diabatic effects. Neglecting the friction term was justified based on the analysis by Davis et al. (2013), who found that frictional contribution was generally quite small compared to the other contributions.

To address possible sensitivities with regards to the placement and size of the budget region, budget calculations were performed over different areas using varying box sizes (Figure 79 and Figure 80). Only a few of the budgets in these boxes will be discussed here. An analysis of the impacts that box size, location, and time duration had on the average profiles and budget calculations are provided in Appendix A. As analyzed in Chapter III, the time period leading up to 0000 UTC 28 August was characterized by the strengthening of the L2 circulation at the expense of the L3 circulation to the east (see Figure 31c and Figure 32c). Therefore individual budget boxes were placed to encompass each of these regions from 1800 UTC 27 August to 0600 UTC 28 August. Starting the budget six hours after model initialization time was done to minimize the possibility of

model spin-up issues contaminating the budget results. Since the L2 circulation was the circulation that eventually developed in the WRF simulations, and exhibited some development in the ECMWF analysis, the blue-boxed regions in Figure 79 and Figure 80 will be of primary focus in the following analysis and discussion. To allow for a comparison between budget boxes of different size, the circulation budget was expressed in terms of box-average vorticity by normalizing by the area, and is therefore also referred to as an average vorticity budget in the discussion that follows.

Since the ECMWF analysis correctly depicted the non-development of TCS025, circulation budgets were also computed from the ECMWF operational forecast initialized at 1200 UTC 27 August, and were used as a comparison with the WRF circulation budgets. Since the temporal resolution of the operational forecasts was 3 h and the archived analyses had 6 h resolution, it was more desirable to use the forecasts in the budget calculations.

#### **1. Blue-boxed Region: 1800 UTC 27 August – 0600 UTC 28 August**

The evolution of average vorticity within the blue-boxed regions in Figure 79 and Figure 80 for WRF simulations 25 (Figure 81a) and 9 (Figure 82a) reveal striking differences (Figure 83a). Both simulations were initialized with the strongest relative vorticity in the mid-levels (~500 hPa) and exhibited a steady progression toward increased low-level vorticity. However, the increase in low-level vorticity was far greater in simulation 9, especially after 1800 UTC 27 August (Figure 82a); a stronger circulation can already be identified in simulation 9 by 0000 UTC 28 August, and was much better defined by 1200 UTC 28 August (compare Figure 79 and Figure 80). By 1200 UTC 28 August, the low-level relative vorticity in simulation 25 was beginning to decline (not shown), whereas the low-level vorticity in simulation 9 had continued to increase and was quite strong through a deep layer extending upward from the surface (not shown). In addition, the negative vorticity that developed above 250 hPa after 0000 UTC 28 August was much stronger in simulation 9 (Figure 83a).

The various circulation (vorticity) budget terms for the blue-boxed region illustrate differences in physical processes between the two WRF simulations (Figure 81

and Figure 82). Early in both simulations, the vorticity tendency was positive in the low levels and negative in the upper levels. The vorticity tendency was generally positive in the mid-levels, but periods of negative tendency were also present (Figure 81b and Figure 82b). The positive tendencies in the lower troposphere were largest at the start of this time period and diminished in magnitude by 0600 UTC 28 August. A strong negative tendency was present in the upper levels in simulation 9 from 2100 UTC 27 August until after 0000 UTC 28 August (Figure 82b), which is attributed to the developing upper-level anticyclone (and outflow) identified in the synoptic analysis during this time (see Figure 73a,b and Figure 78a,b). Strong negative upper-level tendencies were also present in simulation 25 (Figure 81b), but did not occur until after 0000 UTC 28 August. Evaluating the difference in vorticity tendency between simulations 9 and 25 (see Figure 83b) reveals that although the two simulations shared a similar time evolution pattern in vorticity tendency, the positive and negative tendencies in simulation 9 were generally of greater magnitude than in simulation 25.

The vertical stretching tendency constituted the largest contribution to the low-level vorticity tendency early in both simulations (Figure 81c and Figure 82c). The largest tendencies occurred primarily between 1800 UTC 27 August and 0000 UTC 28 August with positive tendencies below 500 hPa, and negative tendencies above this level. Thus, the increase in low-level vorticity within the blue-boxed region in the WRF simulations (see Figure 81a and Figure 82a) was primarily due to the stretching of vertical vorticity via deep convection. Positive stretching tendencies were also evident after 0000 UTC 28 August, but were predominantly in the mid-levels in simulation 25 (Figure 81c) and near 700 hPa in simulation 9 (Figure 82c). Comparing the difference in the vorticity tendency due to the stretching term (Figure 83c) reveals that the contribution from stretching was generally much larger in simulation 9, both in the low- and upper-levels, except at 0600 UTC 28 August near 500 hPa when the positive stretching tendency was larger in simulation 25. The largest differences in magnitude corresponded to the negative tendencies in the upper levels at around 0000 UTC 28 August (T + 12 h) when the convection in simulation 9 was quite vigorous.



Tendencies due to horizontal eddy fluxes at the periphery of the blue-boxed region also made up a significant component of the total vorticity tendency (Figure 81d and Figure 82d). The tendency due to eddy fluxes was generally positive in the upper levels and in the lower troposphere near the surface, and negative in the mid-troposphere. Animations of 200 hPa vorticity (not shown) revealed that the positive upper-level tendencies from horizontal eddy fluxes, especially between 1800 UTC 27 August and 2100 UTC 27 August, were due to upper-level negative vorticity anomalies (generated from stretching processes) leaving the boxed region, while in the low- and mid-levels, the negative tendencies were due to outward fluxes of positive vorticity through the eastern boundary of the region.

The differences in vorticity tendency between simulations 9 and 25 due to horizontal eddy fluxes (Figure 83d) did not follow as consistent a pattern as did the differences due to stretching (see Figure 83c). The vorticity anomalies leaving and entering the boxed region were small-scale features. Therefore, it is not surprising that differences in the eddy flux of vorticity failed to delineate a clear trend. However, the contributions due to horizontal eddy fluxes in simulation 9 were greater in magnitude than in simulation 25. This suggests that the positive and negative vorticity anomalies leaving and entering the boxed region were stronger in simulation 9. A visual comparison of Figure 79 and Figure 80 confirms this.

Although not as large as the stretching and eddy flux terms, contributions from the tilting of horizontal vorticity into the vertical plane were positive in the mid- to upper-levels and predominantly negative in the low levels for both simulations (Figure 81e and Figure 82e). Similar to the contributions from stretching and eddy fluxes, vorticity tendencies due to tilting were more pronounced in simulation 9, perhaps as a result of stronger updrafts or larger horizontal vorticity.

Profiles of the circulation budget terms integrated from 1800 UTC 27 August to 0600 UTC 28 August for the blue-boxed region are shown in Figure 81f and Figure 82f for simulations 25 and 9, respectively, and reveal that vertical stretching was the dominant process throughout the entire profile in both simulations. The cumulative effect of horizontal eddy fluxes and tilting were positive in the upper levels and near the

surface, but weakly negative in between. The residual was generally small in magnitude, except near the surface where it is assumed frictional dissipation in the model caused the tendency to be smaller than the sum of the contributions (negative residual).

## **2. Red-boxed Region: 1800 UTC 27 August – 0600 UTC 28 August**

Vorticity budgets in Figure 84 (simulation 25) and Figure 85 (simulation 9) were computed for the red-boxed regions in Figure 79 and Figure 80 from 1800 UTC 27 August to 0600 UTC 28 August. These box regions contained the low-level circulation L3 (see Figure 31c) that decayed in time, and thus the vorticity tendencies were predominantly negative throughout this time period for both simulations. The average vorticity was stronger in the eastern region (red box) compared to the western region (blue box) at the start of the simulations (i.e., the circulation L3 was initially stronger than L2 in the mid-troposphere) (Figure 84a and Figure 85a). However, vorticity quickly decreased in the eastern region while it increased in the western region (see Figure 81a and Figure 82a).

Although contributions to the vorticity tendency from stretching followed a similar pattern to that of the blue-boxed region (positive in the low-levels and negative in the upper-levels) (see Figure 81c and Figure 82c), the magnitude of the stretching term was much smaller over the red-boxed region in both simulations (Figure 84c and Figure 85c); deep convection was much more active in strengthening the low-level circulation in the blue-boxed region to the west. Interestingly, the magnitude of the stretching term was larger in simulation 9 (Figure 86c), which suggests that convective processes were stronger in simulation 9 even away from the developing L2 circulation.

Horizontal eddy fluxes had the largest contributions to the circulation budget for the red-boxed region (Figure 84d and Figure 85d). Aside from short-lived periods of positive tendencies in the mid- and upper-levels, the eddy flux tendency for the red-boxed region was negative in both simulations, especially in the lower troposphere. Perhaps as a result of stronger vorticity anomalies generated by enhanced convective processes, the horizontal eddy fluxes were larger in simulation 9 (Figure 86d).

Between 1800 UTC 27 August to 0000 UTC 28 August in the red-boxed regions, tilting processes were responsible for positive circulation tendencies in the lower troposphere and mostly negative tendencies in the upper levels. After 0000 UTC 28 August and until the end of the budget time period, there were large positive tendencies in the upper-levels from tilting in both simulations.

Profiles of the circulation budget terms integrated from 1800 UTC 27 August to 0600 UTC 28 August for the red-boxed region (Figure 84f and Figure 85f) were quite different from the blue-boxed region for the same time period (see Figure 81f and Figure 82f). Horizontal eddy fluxes had the largest contribution to the circulation tendency in the red-boxed region as the profile was strongly negative below 500 hPa for both simulations. Similar to the blue-boxed region, the cumulative tendency due to stretching was positive near the surface, but the positive tendencies did not extend up as far. In addition, the negative tendencies in the upper levels due to stretching were far weaker compared to in the blue-boxed region. Finally, the contributions from tilting and magnitudes of the residual were similar to those for the blue-boxed regions and were generally small in magnitude.

The circulation budgets for the blue- and red-boxed regions during 1800 UTC 27 August to 0600 UTC 28 August reveal that the circulation tendencies were significantly different. Stretching processes were much weaker in the red-boxed region, while horizontal eddy fluxes were dominant and responsible for negative tendencies throughout the depth of the profile in the red-boxed region. In contrast, stretching processes were dominant in the blue-boxed region.

It is unclear from this circulation budget analysis whether the western L2 circulation (blue-boxed region) developed at the expense of the eastern L3 circulation (red-boxed region). Although the cumulative contribution from horizontal eddy fluxes in the red-boxed region was strongly negative, the eddy flux contribution in the blue-boxed region was also generally negative during this time period. Examining animations of low-level relative vorticity (not shown) reveals that a large amount of vorticity was being fluxed out of the northern boundary of the red-boxed region during this time period, which may have later contributed to the development of the L2 circulation. Therefore,

diagnosing the interaction of the two circulations might have been sensitive to the box locations and the time over which the circulation budget analysis was conducted. That being said, convective processes were much stronger in the blue-boxed region, and based on the circulation budget analysis, this difference appears to be the primary reason why the L2 circulation developed while the L3 circulation did not.

Given the identical initial conditions, it is interesting to observe the stark contrasts in vorticity evolution between simulations 25 and 9 after such a short time. The vorticity budget analysis comparison highlights the dominant role that deep convection had in the evolution of the TCS025 disturbance in the WRF simulation 9. This result is not surprising based on evidence from the synoptic comparison, which also pointed to the role of convection as being pivotal in the over-development of TCS025 in simulation 9 relative to simulation 25.

One question is whether the episode of deep convection and increase in low-level vorticity between 1800 UTC 27 August and 0000 UTC 28 August exhibited by the WRF simulations might be due to model spin-up issues resulting from a “cold start”. However, the evolution of low-level vorticity within the blue-boxed region early in the WRF simulations (see Figure 81a and Figure 82a) followed a similar pattern to that exhibited by the ECMWF operational forecast leading up to 0000 UTC 28 August (Figure 87a). The effects of deep convection were also evident in the ECMWF analysis as positive vorticity tendencies (Figure 87b) due to stretching (Figure 87c) occurred in a similar pattern to that observed in the WRF simulations (see Figure 81b,c and Figure 82b,c). However, the positive and negative vorticity tendencies were not as large as in the WRF simulations, and the negative upper-level vorticity in both WRF simulations after 0000 UTC 28 August (see Figure 81a and Figure 82a) was completely absent from the ECMWF forecast (Figure 87a). Thus, based on similarities to the ECMWF forecast, the presence of deep convection appears to be realistic early in the WRF simulations, however the intensity of the convective processes, especially in simulation 9, appears to be too strong.

### **3. Frictional Spin-down in Simulation 25**

Just as it is insightful to analyze reasons for the spin-up of the circulation in simulation 9, it is also important to examine reasons for the non-development of the circulation in simulation 25. During periods of convective activity (1800 UTC 27 August to 0000 UTC 28 August), simulation 25 exhibited positive circulation tendencies in the low-levels (Figure 81b) that were also primarily due to stretching processes (Figure 81c). The circulation in simulation 25 was intensifying during this time period, except at a slower rate than in simulation 9.

From 0300 UTC to 1200 UTC 28 August, the convective activity in simulations 9 and 25 declined substantially based on the model-derived cloud-top temperature (Figure 88a,c). Unlike the integrated circulation budget profiles from 1800 UTC 27 August to 0600 UTC 28 August (see Figure 81f and Figure 82f), integrated profiles from 0300 UTC to 1200 UTC 28 August for simulations 9 and 25 reveal that vertical stretching of relative vorticity was no longer the dominant low-level process affecting the total circulation tendency (Figure 88b,d). In simulation 25, the stretching tendency was actually slightly negative near the surface, but positive from 850 hPa to 250 hPa (Figure 88b). The tendency from horizontal eddy fluxes in simulation 25 was almost the opposite of the stretching tendency as negative tendencies extended from near the surface up to 250 hPa. The tilting contribution during this period was similar to the contribution during 1800 UTC 27 August to 0600 UTC 28 August with weak positive tendencies extending through most of the troposphere and slightly stronger positive tendencies in the upper troposphere. The negative residual near the surface was most likely due to friction and was larger in magnitude than all other factors. Note that the net circulation tendency from the surface to 750 hPa was negative for simulation 25 (Figure 88b).

The circulation budget for simulation 9 was very similar in structure to simulation 25 except that the negative frictional tendency near the surface was larger in simulation 9 since the low-level winds were already stronger by 0300 UTC 28 August. Nevertheless, the tendency due to stretching in the low-level was slightly positive (Figure 88d). Thus, the total circulation tendency in the low levels for simulation 9 was positive, despite stronger frictional dissipation. This suggests that even during the convective lull, the

convective processes in simulation 9 were still strong enough that the net circulation tendency was positive (i.e., the positive tendencies more than offset friction). In contrast, the convective processes in simulation 25 were essentially absent during this time period since the low-level stretching tendencies actually became negative. As a result, the circulation in simulation 25 experienced a spin-down in the low levels during this time period (Figure 88b).

Interestingly, both simulations exhibited the largest tendencies from stretching in the mid-levels during this time (Figure 88b,d). The fact that the stretching tendency near the surface was negative following the convectively active period in simulation 25 suggests that stratiform precipitation processes were becoming increasingly important; mid-level convergence was contributing to spin up the mid-level circulation while low-level divergence was tending to spin down the circulation near the surface. Stratiform precipitation processes also appear to have been active in simulation 9 during this time. However, the mid-level convergence maximum was at a lower level than in simulation 25 (Figure 88d), and with positive stretching tendencies near the surface, the total circulation tendency was positive in the low- and mid-levels in simulation 9.

### **C. COMPARISON OF CONVECTIVE INTENSITY**

Due to the vorticity budget analysis and synoptic comparison of WRF simulations 9 and 25, which suggest differences were primarily related to the representation of precipitation (convective) processes, this section will provide a closer examination of the differences in convective intensity and suggest possible reasons for these differences.

Since the WRF model simulations 9 and 25 quickly diverged, the convective structure and intensity at a particular time and location varied substantially between simulations. This made a direct comparison of individual convective elements impractical. Instead, a comparison of time- and space-averaged quantities was used to illuminate differences related to convection in the WRF simulations; dynamic and thermodynamic quantities were averaged within the blue-boxed region in Figure 79 and Figure 80 from 1200 UTC 27 August to 1200 UTC 28 August and used in the comparison.

# **1. Differenced Quantities: Blue-boxed Region: 1200 UTC 27 August - 1200 UTC 28 August**

Differences in the average vertical velocity over the blue-boxed regions as a function of pressure (Figure 89a) confirms that the upward vertical velocity in simulation 9 was stronger compared to simulation 25, especially in the upper levels between 300 hPa and 250 hPa. Likewise, differences in average divergence (Figure 89c) are also striking and reaffirm that the convective processes in simulation 9 were much stronger and were associated with a somewhat larger low-level convergence and much larger upper-level divergence than in simulation 25. Not surprisingly, the areal-averaged divergence differences match up well with the differences in vorticity tendency over this area resulting from the stretching term (see Figure 83c). Low-level convergence in the WRF simulations led to the vertical stretching of relative vorticity, which dominated the positive vorticity tendency in the lower troposphere. Likewise, strong upper-level divergence, which was also identified in the synoptic analysis as regions of enhanced upper-level outflow (see Figure 73a,b and Figure 75a,b), resulted in negative vorticity tendencies in the upper-levels. It is worth noting that due to the relatively coarse temporal resolution (30 minute output), it is not clear from this study whether the divergence profile was driving the vertical velocity, or vice versa.

Above the surface layer, the differences in areal-average diabatic heating rates (Figure 89b) (simulation 9 – simulation 25) were almost entirely positive with the maximum difference ( $\sim 1 \text{ K h}^{-1}$ ) near the 350 hPa level. As expected, the vertical structure and temporal evolution of the diabatic heating rate differences closely resembled differences in vertical velocity; larger upward vertical velocities in simulation 9 corresponded to larger diabatic heating rates. Interestingly, the largest differences in the heating rates occurred immediately below the level where vertical velocity differences were largest.

The reason for the smaller difference in diabatic heating rates near  $\sim 650$  hPa is not entirely clear. However, this level appears to be near the melting level where the representation of microphysical processes in simulation 9 would be different from simulation 25; mixed-phase processes were accounted for in simulation 9, but not in simulation 25.

Near the surface, simulation 9 exhibited greater diabatic cooling rates relative to simulation 25. This may seem surprising given the rapid development of simulation 9 relative to simulation 25, and various studies (e.g., Bister and Emanuel 1997) have surmised that the impact of evaporative downdrafts should diminish as a system progresses towards development. The largest differences in low-level cooling rates tended to occur when the updraft (Figure 89a) and upper-level diabatic heating rate (Figure 89b) differences were also largest.

Positive areal-average differences (simulation 9 – simulation 25) in upper-level  $\theta_e$  (Figure 89d) began to occur near 350 hPa at the same time when the updraft strength in simulation 9 increased relative to simulation 25. Interestingly, there was a progression of increased  $\theta_e$  from the upper-levels toward the surface with time, while the near-surface  $\theta_e$  anomaly (relative to simulation 25) was largely negative for simulation 9. However, the largest magnitude difference in  $\theta_e$  at ~300 hPa occurred after the negative boundary layer  $\theta_e$  difference anomaly disappeared around 0600 UTC 28 August, which was when the sea-level pressure falls began in simulation 9 (see Figure 71).

## **2. Average Convective/non-convective Profiles: Blue-boxed Region: 1800 UTC 27 August – 0600 UTC 28 August**

Being that the only difference between simulations 9 and 25 was in the representation of microphysical processes, the average dynamic and thermodynamic structures were examined in light of these differences in an attempt to explain the contrasts in convective intensity that were related to the differing development outcomes. To narrow the focus of the comparison on the convective processes, averages of convective-related quantities were computed for grid points within the blue-boxed regions of Figure 79 and Figure 80 where the model-derived cloud-top brightness temperature values were  $< -35^{\circ}\text{C}$  and  $> -35^{\circ}\text{C}$  (similar to the dropwindsonde thermodynamic analysis in Chapter III). Additional averages based on positive and negative vertical velocity were computed at these convective ( $< -35^{\circ}\text{C}$ ) and non-convective ( $> -35^{\circ}\text{C}$ ) grid points. To assist in this examination, simulation 12 was also included in the comparison. The TCS025 disturbance in simulation 12 developed more



than in simulation 25, but did not reach the same intensity as in simulation 9 (see bold green lines in Figure 71 and Figure 72). Simulation 12 was configured similarly to simulations 9 and 25, except it employed the WSM6 double moment (WSM6 DM) bulk microphysics scheme (Lim and Hong 2010), which also accounted for the number concentrations of cloud condensation nuclei, cloud liquid water, and rain in addition to the mixing ratios accounted for in the Purdue Lin scheme.

As might be expected based on the large differences in vertical velocity from simulation 9 relative to simulation 25 from 1800 UTC 27 August to 0600 UTC 28 August (see Figure 89), the updraft magnitude averaged over all grid points where the model-derived cloud-top brightness temperature was  $< -35^{\circ}\text{C}$  was the largest in simulation 9 (Figure 90a). Perhaps somewhat surprisingly, the average downdraft magnitude was also largest in simulation 9 (Figure 90a). The strongest updrafts in simulations 9 and 12 occurred near 250 hPa with a secondary maximum near 700 hPa, whereas a distinct minimum in updraft strength was present at the  $\sim 500$  hPa level. In contrast, the strongest updrafts in simulation 25 were located near 600 hPa, and the updrafts in the upper levels were much weaker than those in simulations 9 and 12. Updrafts in simulations 12 and 25 were quite similar in magnitude below 500 hPa, but above this, the updrafts in simulation 12 were stronger. Simulation 9 possessed the strongest average downdrafts at all levels (Figure 90a). The downdrafts in simulations 12 and 25 were similar in magnitude between 300 hPa and 600 hPa, but stronger in simulation 12 above and below this level.

In the non-convective environment (model-derived cloud-top brightness temperature  $> -35^{\circ}\text{C}$ ), updrafts and downdrafts were much weaker (Figure 90a) and the mean vertical velocity was positive (not shown). It is interesting that the development of the TCS025 disturbance in simulation 9 did not simultaneously result in a weakening of the downdrafts as previous studies have suggested (e.g., Bister and Emanuel 1997). Instead, the two simulations that developed the disturbance (9 and 12) possessed stronger downdrafts than the non-developing simulation (25).

Examining the total precipitating (hydrometeor) mixing ratio, which included the mixing ratios of rain, snow, and graupel (graupel for simulations 9 and 12 only), revealed

that simulation 25 possessed the largest concentration of hydrometeors above 500 hPa in the convective environment (Figure 90d). This was due to an abundance of snow in simulation 25 (not shown). Simulation 12 contained the second highest precipitating mixing ratio above 550 hPa, and from 550 hPa to 850 hPa, it had the largest precipitating mixing ratio, which was primarily due to rain (not shown). Simulation 9 possessed the largest precipitating mixing ratio (rain) near the surface, but it was significantly less in the mid- and upper-levels than in simulations 12 and 25. Although the precipitating mixing ratio in simulation 9 was less than that in simulation 12 above 800 hPa, and less than that in simulation 25 above 600 hPa, it exhibited the largest precipitation rate by a large margin (Figure 90e). In addition, despite having the smallest precipitating mixing ratio, the non-precipitating mixing ratio (cloud water and cloud ice mixing ratio) below 500 hPa was largest in simulation 9 relative to the other two simulations (Figure 90c).

A comparison of average diabatic heating rates for grid points with positive vertical velocity within the convective environment (Figure 90b) reveals that simulation 9 possessed larger heating rates almost throughout the column, especially in the upper levels. The diabatic heating rates of simulations 12 and 25 were very similar, but were slightly larger in simulation 12 near 700 hPa and above 300 hPa and slightly less near 550 hPa. All simulations exhibited a shallow layer of diabatic cooling near the surface. The prominent maximum in the diabatic heating rate near 500 hPa was evident in all three simulations and appears to be related to microphysical processes near the melting level. Updrafts in the non-convective environment still exhibited positive diabatic heating rates, although of much smaller magnitude than in the convective environment.

For grid points where the vertical velocity was negative, diabatic cooling generally prevailed (Figure 90b). The largest diabatic cooling in the convective environment occurred slightly below 600 hPa in all simulations, which is near the level at which melting was occurring. Below 800 hPa, the largest diabatic cooling occurred in simulation 9 and was likely related to the fact that simulation 9 exhibited the strongest downdrafts in the lower troposphere. Note that the spread among the diabatic heating profiles appears to be closely related to the pattern in vertical velocity. At levels where the diabatic heating in simulation 9 was much larger than in simulations 12 and 25, the

differences in updraft strength were also quite large, which suggests that the strength of the average vertical velocity was closely tied to the diabatic heating.

Profiles of average CAPE (Figure 90f) also reflect differences in the convective nature among the WRF simulations. In both the convective and non-convective environments, simulation 9 possessed the smallest average CAPE, while simulation 25 had the largest. Low values of CAPE in simulation 9 are not necessarily indicative of convective inhibition since model fields were only output every 30 minutes, which is nearly equivalent to the typical convective timescale. Rather, combined with the fact that the average vertical velocity was greatest in simulation 9, the low values of CAPE suggest that convective overturning in the atmosphere was ongoing. One interpretation is that as CAPE became available in simulation 9, it was almost immediately consumed through convection. The fact that the release of CAPE in simulation 9 occurred more quickly compared to other simulations may be due to the level of development of the TCS025 system, or a result of positive feedbacks stemming from differences in the representation of the microphysics; stronger updrafts are consistent with enhanced low-level convergence, which could have then contributed to the generation of new convection and the continued release of CAPE. In addition, it is possible that due to differences in the vertical distribution of precipitating and non-precipitating mixing ratios, cloud-radiative feedbacks played a role in the continued development of convection in simulation 9, while acting to inhibit strong convection in simulation 25.

### **3. Additional Numerical Simulations Examining Sensitivities to Microphysical Precipitation Processes**

Since the minimum in updraft strength (Figure 90a) appears to occur at nearly the same level as the precipitating mixing ratio maximum (Figure 90d), hydrometeor mass loading may be responsible for the reduction in updraft velocity. For example, simulations 12 and 25, which exhibited larger mixing ratios in the mid- and upper-levels, experienced a reduction in updraft strength relative to simulation 9.

Therefore, to test the hypothesis that hydrometeor mass loading resulting from the WSM3 scheme contributed to the reduction in vertical velocity and ultimately inhibited

development, an additional simulation was conducted in which the gravity drag term in the vertical momentum equation was reduced by 50% to reduce the drag due to hydrometeor mass loading. However, the evolution of minimum sea-level pressure reveals that the change made little difference in the development for this case (Figure 91).

Although hydrometeor mass loading does not appear to have been a significant factor in determining the strength of convection, there were most likely secondary effects related to the hydrometeor distributions that may have also impacted convective intensity. The fact that the upper-level precipitating mixing ratio was largest in simulation 25 in both the convective and non-convective environments suggests that the areal coverage of snow lofted into the upper-levels via updrafts (i.e., “anvil spreading”) was more pronounced in simulation 25. This lofting of snow might have been caused by a slower sedimentation rate for snow in the WSM3 scheme relative to the other schemes, which would have allowed for longer residence times for snow in the upper levels in simulation 25. Fovell et al. (2009) found that radiative interactions with the hydrometeor distribution played an important role in determining modeled storm track by modifying the large-scale thermodynamic field, and hence, the radial pressure gradient and winds. Although difficult to diagnose from this analysis, it is possible that secondary effects due to hydrometeor profile distributions might have similarly affected the intensity of convection in the simulations after a period of time.

Also worthy of further investigation was the fact that simulation 9 had the largest precipitation rate despite having the smallest precipitating mixing ratio in the mid- and upper-levels. This might be explained by differences relating to the formulation of terminal fall speeds for various hydrometeor species in the microphysics schemes. In their modeling study of an idealized storm and a heavy precipitation event over Korea, Hong et al. (2009) noted that the sedimentation rate (terminal fall speed) of graupel in the Purdue Lin scheme (used here in simulation 9) was about twice as large as in the WSM6 scheme (similar formulation to that in simulation 12). They suggested that due to the faster sedimentation rate of graupel, a reduction of hydrometeors occurs as graupel acts to “sweep out” other hydrometeors as it falls. Hong et al. (2009) suggested that a faster sedimentation rate for graupel would reduce the amount of time available for

sublimation, which would contribute to an increase the diabatic heating rate above the freezing level. Hong et al. (2009) concluded that the slower sedimentation rate delayed development and reduced the intensity of the idealized storm in their study.

To test the hypothesis that excessive graupel fall speed might have contributed to the over-development of TCS025 in simulation 9, an additional simulation was integrated in which the graupel fall speed was reduced in magnitude to match the formulation used in the WSM6 scheme. Similar to the experiment in which the hydrometeor drag was reduced in the WSM3 scheme, the changes made little difference to limit development for this case (Figure 91).

It is perhaps not surprising that a single parameter such as graupel fall speed or hydrometeor drag failed to significantly impact the modeled evolution of the TCS025 disturbance. The microphysics schemes used in the multi-physics ensemble are quite complex. Undoubtedly the interactions with other physical processes are highly non-linear, and as such it is difficult to clearly identify the key physical processes in each scheme responsible for the different model outcomes. However, a consistent finding based on the average profiles is that the developing cases tended to exhibit stronger vertical velocities and enhanced diabatic heating rates (Figure 90a,b). Thus, instead of looking for a direct relationship between the physical processes represented by the various microphysics schemes and the modeled evolution of the TCS025 system, it was decided to examine the net diabatic heating resulting from these processes. Several additional experiments (Figure 92) were conducted using the Purdue Lin microphysics scheme in which the diabatic heating was multiplied by a factor that ranged from 0.5 – 1.1 throughout the simulations. Interestingly, experiments with a diabatic factor of 0.9 and less failed to develop, while factors of 0.95 and greater yielded development. In addition, the magnitude of the development matched up closely with the magnitude of the multiplication factors, which indicates that the diabatic heating rates were important in modulating storm development.

Differences in development in Figure 92 for the diabatic factors of 0.9 and 0.95 is perhaps surprising in that such a small change in diabatic heating could lead to vastly different model outcomes. Profiles of average diabatic heating rates within the blue-

boxed region for the 1800 UTC 27 August to 0600 UTC 28 August time period reveal the 0.95 case had a magnitude between that of simulation 9 (diabatic factor of 1.0) and the non-developing simulation 12 (Figure 93). Interestingly, the small reduction in the diabatic heating factor from 0.95 to 0.90 resulted in a substantial reduction in the heating profile above 500 hPa such that the diabatic heating magnitude was less than in the non-developing simulation 12. Below 500 hPa, the diabatic heating profiles of factor-0.90 simulation and simulation 12 were very similar.

These experiments confirm the utmost importance of diabatic heating on the evolution of the TCS025 system. It suggests that the representation of microphysical processes are extremely important, especially for systems similar to the TCS025 disturbance that were close to developing.

In summary, the characteristics of convection differed substantially between the three WRF simulations examined due to differences in the representation of the microphysics. Rogers et al. (2007) compared the microphysical quantities from mesoscale models with observations within the tropical cyclone environment. They found that the correlation between hydrometeor mixing ratio and vertical motion was much higher in the models (i.e., microphysical processes were playing too large a role in determining vertical velocity in the model simulations). Therefore, given the diversity among the microphysics schemes, it is not surprising that there were significant differences in model solutions, especially considering that the TCS025 disturbance at times appeared to be near the threshold of some development.

Simulation 9 possessed the strongest vertical velocity and the largest diabatic heating and precipitation rates (see Figure 90). As a result of stronger updrafts in simulation 9, the precipitation cycle was enhanced. The diabatic heating rate was larger as a result of the accelerated precipitation cycle, and this led to pressure falls and ultimately to the development of the TCS025 disturbance. The additional experiments suggest that the excessive diabatic heating rates in simulation 9 were vital in the rapid development of the TCS025 disturbance relative to the other simulations.

## **D. OBSERVATIONAL VERIFICATION: CONVECTIVE INTENSITY**

To investigate the assumption that convective processes were over represented in the WRF simulations, proxies for deep convection (MTSAT IR brightness temperature and radar reflectivity), and the thermodynamic structure ( $\theta_e$  deficit) were examined and compared with model-derived equivalents.

### **1. MTSAT IR/model-derived Cloud-top Temperature**

To compare model output with MTSAT IR brightness temperature, model-derived cloud-top brightness temperatures were computed following the method employed by Stoelinga (2009), whereby the optical depth, whose contributions include effects from cloud ice and cloud water mixing ratios, was integrated downward from the model top (50 hPa) to the level equal to one optical depth. The zenith angle was assumed to be zero, and the cloud absorption coefficient was held constant. The temperature at the level of one optical depth into the cloud was defined to represent the cloud-top brightness temperature.

Although model-derived cloud-top brightness temperature may be sensitive to the microphysics scheme employed by the model, it is useful in that it can be compared with observations, and it provides an assessment of the convective intensity that does not change as quickly in time or space as vertical velocity (i.e., it effectively allows for a comparison over greater spatial and temporal scales).

Comparing the MTSAT IR brightness temperature valid at 2345 UTC 27 August (Figure 94a) with the model-derived cloud-top brightness temperatures of simulations 9 and 25 valid at 0000 UTC 28 August (Figure 94c,e) reveals a lack of intermediate cloud-top temperature values ( $-30^{\circ}\text{C}$  to  $10^{\circ}\text{C}$ , blue and white colors) in the WRF simulations, which are more prevalent in the MTSAT IR and are often associated with stratiform precipitation processes. In addition, the clear-sky brightness temperature values in the WRF simulation were higher compared to the MTSAT IR, which is most likely an artifact of the simplistic nature whereby the model-derived brightness temperatures were calculated.

Histograms of MTSAT IR brightness temperature were computed by binning values within  $\pm 3^\circ$  of the 850 hPa ECMWF circulation center position and histograms of model-derived cloud-top brightness temperature were computed by binning values within  $\pm 3^\circ$  of the 850 hPa PV-weighted center position from model output (Figure 94b,d,f). The MTSAT IR histograms for TCS025 (Figure 94b) contain a wide range of brightness temperature values, however brightness temperature values for WRF simulation 9 (Figure 94f) were either very low (deep convection) or relatively high (representative of near cloud-free conditions). As observed in Figure 69, TCS025 and TY Fanapi both experienced pulses of deep convection followed by periods when convection subsided early in their evolution. However, simulation 9 did not exhibit the same pattern. Rather, very low cloud-top brightness temperatures characteristic of deep convection were evident throughout the simulation and appeared to increase with time. On the other hand, the nature of deep convection exhibited by simulation 25 (Figure 94d) appeared to more closely match MTSAT IR observations; after an initial period characterized by low brightness temperature values, deep convection became increasingly intermittent in nature. In addition, simulation 25 exhibited a wider range of brightness temperature values compared to simulation 9, which was more consistent with the MTSAT observations.

## **2. ELDORA and Model-derived Reflectivity**

Model-derived reflectivity was also computed following the method outlined by Stoelinga (2009). Equivalent reflectivity factors were computed based on the rain, snow, and graupel mixing ratios by assuming spherical particles of constant density, exponential size distributions, and constant intercept parameters.

A comparison of ELDORA and model-derived reflectivity also reveals striking differences between how convection was represented in the model and the nature of convection in reality (Figure 95). Areas exhibiting enhanced reflectivity in WRF simulations 9 and 25 appeared cellular in nature (Figure 95c,d), whereas regions with stronger reflectivity in the ELDORA radar observations, such as the broad feature near  $18.5^\circ\text{N}$  and  $150.5^\circ\text{E}$  (Figure 95a), were much weaker in magnitude and diffuse.



A vertical cross section of ELDORA radar reflectivity through the circulation center and area of maximum reflectivity at 4 km altitude suggests stratiform precipitation processes were most common at the time of the second IOP (Figure 95b). However, a similar cross section through model-derived reflectivity reveals that convective hot towers were common in simulation 9 at this time (Figure 95f) as areas with reflectivity greater than 35 dBZ were evident above 10 km altitude. The vertical cross of simulation 25 indicates that reflectivity was closer in magnitude to the ELDORA observations (Figure 95d), but, similar to simulation 9, the precipitation structure appeared convective in nature. Areas of reflectivity in simulation 25 extended higher into the upper levels, perhaps as a result of the abundance of snow (see Figure 90d).

While previous studies have shown that the magnitude of model-derived reflectivity is usually too large when compared to observations (Lang et al. 2011), the differences in reflectivity noted in Figure 95 were not limited to magnitude alone; the structure of reflectivity in the WRF simulations was characteristic of deep convection, especially in simulation 9, whereas stratiform precipitation was more prevalent in the ELDORA radar observations.

The comparisons of MTSAT IR brightness temperature with model-derived cloud-top brightness temperature and ELDORA radar reflectivity with model-derived reflectivity suggest that the convective processes modeled by the WRF simulations were too strong relative to stratiform processes when compared with observations. This conclusion is in agreement with the multi-physics ensemble intercomparison that revealed the strength of the convective processes to be a key factor responsible for the over-development of the TCS025 disturbance.

The thermodynamic profile of the ECMWF analysis (used to initialize the multi-physics WRF ensemble) was compared with dropwindsonde data (see Appendix B) to determine whether deep convection in the WRF simulations might have been a result of errors in the initial thermodynamic profile. However, this appears not to have been the case as there was good agreement between the thermodynamic profiles of the ECMWF analysis and dropwindsonde data.

### 3. Equivalent Potential Temperature Deficit

The average  $\theta_e$  deficit for the blue-boxed region used in the circulation budget comparison (see Figure 79 and Figure 80) was also computed for several of the multi-physics ensemble cases from 1200 UTC 27 August to 1200 UTC 28 August (Figure 96). The deficit was computed by differencing the mid-tropospheric  $\theta_e$  minimum value from the  $\theta_e$  maximum value near the surface.

After a maximum  $\theta_e$  deficit of  $\sim 17$  K near 1500 UTC 27 August, the  $\theta_e$  deficit declined for each case (Figure 96a). The smallest  $\theta_e$  deficit occurred in the moderate developing simulation 12 as the  $\theta_e$  deficit declined to about 13 K shortly after 0000 UTC 28 August. The non-developing simulation 25 possessed the largest  $\theta_e$  deficit throughout the time period. Interestingly, the non-developing simulation 25 possessed the largest low-level  $\theta_e$  maximum (Figure 96c) until 0600 UTC 28 August, but also had the smallest mid-tropospheric minimum (Figure 96b). This indicates that convective processes were not as active in simulation 25 to redistribute  $\theta_e$  within the column. The reduction in the  $\theta_e$  deficit for simulations 9 and 12 relative to 25 suggests that deep convection was not only acting to redistribute  $\theta_e$  within the column, but  $\theta_e$  was also increasing in the column as the system organized and developed.

The  $\theta_e$  deficits computed from WRF simulations 9, 12, and 25 were much lower than that computed from dropwindsonde data. The largest  $\theta_e$  deficit in the model simulations was about 17 K (Figure 96a), and by 0000 UTC 28 August at the time of the second IOP, the  $\theta_e$  deficit ranged from about 13-15 K. In contrast, the  $\theta_e$  deficit computed from dropwindsonde data in the convective environment (MTSAT IR brightness temperature  $< -35^\circ\text{C}$ ) during the second IOP was 16.2 K (see Figure 68). The average  $\theta_e$  deficit for dropwindsondes in the non-convective environment (MTSAT IR brightness temperature  $> -35^\circ\text{C}$ ) was 22.9 K. The fact that the average  $\theta_e$  deficit in the model simulations was smaller than the average  $\theta_e$  deficit computed from dropwindsondes in the convective environment suggest that the  $\theta_e$  deficits in the model simulations were too small.

The average dropwindsonde mid-tropospheric  $\theta_e$  minimum for the second IOP was 337 K for the convective environment and 332 K for the non-convective environment (see Figure 68), which was less than the blue-boxed average in the model simulations that was closer to 338 K (Figure 96b). The average near-surface maximum  $\theta_e$  from dropwindsondes during the second IOP was about 353 K in the convective environment and 355 K in the non-convective environment (see Figure 68), whereas the average low-level  $\theta_e$  maximum in the model simulations was between 352 and 353 K (Figure 96c). After only 12 h of model simulation time, the average thermodynamic characteristics of the blue-boxed region were similar to the thermodynamic characteristics of dropwindsondes within the convective environment, albeit with a stronger convective signature. This also suggests the representation of convective processes in the model simulations was too strong.

## **E. IMPACTS OF DEEP CONVECTION**

### **1. Circulation Alignment and Thermodynamic Response**

To examine the effect that deep convection had on the structure and evolution of the TCS025 circulation in the WRF simulations, circulation alignment was examined in light of the convective intensity exhibited by simulations 9 and 25. Circulation alignment was diagnosed by computing PV centroid (PV-weighted) positions at 900 hPa and 500 hPa as a function of time within a  $\pm 3^\circ$  box of the subjectively determined 900 hPa and 500 hPa circulation center positions. Various box sizes and exponential weighting factors were tested and it was found that a  $\pm 3^\circ$  box with an exponential weighting factor of 2 worked best. For a brief discussion of the impact that box size and weighting factor had on the diagnosed PV center, see Appendix C. The 900 hPa and 500 hPa PV centroid positions (Figure 97) were analyzed in conjunction with their separation distance and displacement angle (Figure 98a and Figure 99a) relative to the environmental vertical wind shear vector computed from the CFSR dataset (see Figure 35). Diagnostics of the circulation alignment were then compared with the level of development (minimum sea-level pressure, maximum 10-m wind speed, and average 900 hPa and 500 hPa relative vorticity) and the convective intensity associated with the simulated TCS025 disturbance;

model-derived cloud-top temperature was averaged within 100-km radius of the 900 hPa PV centroid position as a function of time (Figure 98b,c and Figure 99b,c).

Both simulations began with the 500 hPa center position southeast of the 900 hPa center position (Figure 97). Near 0000 UTC 28 August, the translation speed of the TCS025 system slowed significantly (Figure 97) and the distance between the low- and mid-level centers reached a temporary minimum in both simulations (Figure 98a and Figure 99a). The average model-derived cloud-top brightness temperature leading up to 0000 UTC 28 August suggested deep convection was present close to the low-level PV center in both simulations (Figure 98b and Figure 99b). Shortly before 1200 UTC 28 August, the convective intensity weakened in simulation 9, but low brightness temperature values persisted in simulation 25 past this time.

By 1200 UTC 28 August, the environmental vertical wind shear had weakened, and based on the PV center positions, the TCS025 disturbance was beginning to move toward the northeast (Figure 97). The separation distance between the 900 hPa and 500 hPa positions in simulation 25 had increased significantly relative to 0000 UTC 28 August (Figure 99a), whereas the separation distance in simulation 9 had only increased slightly (Figure 99b). The intensity of the TCS025 disturbance in each simulation remained similar until about 1200 UTC 28 August when a decline in minimum sea-level pressure and an increase in the maximum 10-m wind speed occurred in simulation 9 (Figure 99b). Although fluctuations in the average 900 hPa relative vorticity were of greater amplitude in simulation 9 prior to 1200 UTC 28 August, it was not until after 1800 UTC 28 August when differences in low-level vorticity became significant (Figure 98c and Figure 99c).

The separation distance in simulation 25 decreased again shortly after 1200 UTC 28 August for a short period of time as the low-level PV center accelerated relative to the mid-level center and became positioned northwest of the mid-level center (Figure 97a and Figure 98a). The separation distance decreased in simulation 9, but not until 0000 UTC 29 August, and the improvement in alignment was much more pronounced, but equally short lived (compare Figure 97b and Figure 99a). The convective intensity

exhibited by simulation 9 at 0000 UTC 29 August was beginning to increase again (Figure 99b), while deep convection was altogether absent from simulation 25 during this time (Figure 98b).

The low- and mid-level PV centers in simulation 25 began to move apart after 1200 UTC 29 August when the environmental vertical wind shear was beginning to increase in strength (Figure 97a); the mid-level center stayed on a northward trajectory while the low-level center moved toward the northwest (Figure 97a and Figure 98a). Based on cloud-top brightness temperature, convection was almost nonexistent near the center during this time and the system did not exhibit any signs of development (Figure 98b). As the separation distance dramatically increased, the separation angle relative to the vertical wind shear remained near  $40^\circ$ . However, it could be argued that the interaction between the mid-level and low-level circulation was minimal due to the large separation distance and limited intensity of the system.

After the initial burst of deep convection near the low-level PV center in simulation 9 prior to 0000 UTC 28 August, convection remained weak until after 0000 UTC 29 August (Figure 99b). Pulses of deep convection occurred between 0000 UTC 29 August and 0000 UTC 30 August when the average model-derived cloud-top temperature declined below  $-40^\circ\text{C}$ . Following the decline in separation distance at 0000 UTC 29 August, a second sharp decline occurred near 1200 UTC 29 August before the low- and mid-level PV centers temporarily moved farther apart shortly thereafter (Figure 99a). This increase in separation distance occurred as the mid-level center rotated around to the northwest of the low-level center. After 0000 UTC 30 August, the mid- and low-level centers co-located and alignment significantly improved as the separation distance decreased to less than 10 km by the end of the simulation while the average cloud-top brightness temperature fluctuated between  $-30^\circ\text{C}$  and  $-40^\circ\text{C}$  (Figure 99b).

Although the initial decline in separation distance prior to 0000 UTC 28 August was accompanied by a burst of deep convection, the correlation between separation distance and convective intensity from this point onward was poor. After 0000 UTC 29 August when the convective intensity increased somewhat, the circulation did experience

sort-lived periods of improved alignment. However, the dramatic increase in the separation distance after 1200 UTC 29 August was not marked by a cessation of convective activity (Figure 99a). This suggests that the environmental influences (i.e., vertical wind shear and changes in the synoptic wind and pressure patterns) were more important than convection during this time in determining alignment. The connection between alignment and convective activity might also be a function of the intensity and organization of the system. Vigh and Schubert (2009) found that if diabatic heating occurred within the RMW, the intensification of a system would proceed far more efficiently, indicating there may be times when deep convection is more effective at increasing the intensity of the low-level circulation below the mid-level circulation through stretching processes (see Figure 81c and Figure 82c), which would improve vertical alignment of the circulation.

Thus there are many factors to consider that might explain why the correlation between alignment and convective intensity was lacking. That being said, the integrated convective activity exhibited by simulation 9 was much larger than in simulation 25. This allowed the circulation in simulation 9 to become better aligned in the vertical while the low- and mid-level circulation centers in simulation 25 moved farther apart. In addition, it is likely that the weaker circulation in simulation 25 was more susceptible to environmental influences (i.e., vertical wind shear). This was evident after 1800 UTC 29 August when the separation distance in simulation 25 suddenly increased at the same time when the environmental vertical wind shear strengthened (Figure 97a).

In their study of tropical cyclogenesis and vertical wind shear orientation, Rappin and Nolan (2012) found that for weak systems where the tilt became significant, the rate at which the low- and mid-level circulations precessed about each other slowed due to weaker coupling between the low- and mid-level circulations. In the idealized simulations analyzed by Rappin and Nolan (2012), a slow precession rate inhibited storm-scale moisture saturation and intensification. In addition, Raymond and Carrillo (2011) argued that a down-shear left alignment would act to oppose system-relative flow caused by vertical wind shear, which would help to minimize some of the negative impacts of vertical wind shear. The orientation of circulation tilt relative to the vertical wind shear

vector in simulation 9 remained close to  $0^\circ$  (down-shear) until 0000 UTC 29 August (Figure 99a). By 0000 UTC 29 August, when simulation 9 was beginning to exhibit signs of development, the tilt vector became oriented left of the shear vector (Figure 99a), but this orientation only lasted until 1200 UTC 29 August when the orientation became right of shear. The fact that the tilt orientation in simulation 25 remained nearly constant at  $40^\circ$  throughout the simulation while the separation distance between the low- and mid-level centers increased (Figure 98a), suggests this orientation was primarily due to environmental influences rather than the interaction between the mid- and low-level circulations. Similarly, since the circulation in simulation 9 did not precess into a left-of-shear orientation while it intensified and became better aligned also supports the idea that environmental influences were dominating the vortex-shear relationship at this time. In addition, it is possible that the environmental vertical wind shear computed from CFSR data did not adequately represent the vertical wind shear experienced by the low- and mid-level circulations during this time.

A possible limitation of this alignment analysis arises from the use of model-derived cloud-top temperature to quantify and compare the convective intensity of the WRF simulations. The WSM3 microphysics scheme (simulation 25) generated an abundance of upper-level ice and snow (Figure 90d,e) that remained suspended in the upper levels for relatively long periods of time (not shown). As previously discussed in this chapter, this might have been a result of sedimentation rates that were too slow, or due to the omission of graupel, which has been argued to play a significant role in removing hydrometeors in the Purdue Lin scheme (Hong et al. 2009). As a result of condensate and hydrometeor mass being suspended in the upper levels, model-derived cloud-top temperature values in simulation 25 remained relatively low well after deep convection appears to have subsided. Re-examining the vorticity tendency due to stretching (see Figure 81c and Figure 82c) suggests that deep convection was beginning to dissipate near 0000 UTC 28 August in both simulations. However, low brightness temperature values extended well past this time in simulation 25 (Figure 98b), and were likely the result of remnant upper-level cloud and hydrometeor mass rather than an indication of active deep convection. This suggests that caution must be used when

model-derived brightness temperature is used as a proxy for deep convection due to its sensitivity to the representation of microphysical processes.

Analyses of dropwindsonde data (see Figure 51) and back trajectories (see Figure 60) revealed that during the second IOP, low- $\theta_e$  air associated with the TUTT north of the TCS025 system was beginning to impinge upon the mid-level circulation and had caused a reduction in boundary layer  $\theta_e$  relative to before and after this time (see Figure 58). It was hypothesized that the impact of low- $\theta_e$  air inhibited subsequent convection. The vertical cross sections of  $\theta_e$  from simulation 9 and 25 valid at 0000 UTC 28 August (Figure 74c,d) also revealed low- $\theta_e$  air associated with the TUTT, but it is a question of whether differences in circulation intensity and alignment modulated the impact of the low- $\theta_e$  air in the simulations. To examine whether low- $\theta_e$  air associated with the TUTT might have impinged upon the TCS025 system in the different WRF simulations, the radial advection of  $\theta_e$  from simulations 25, 12, and 9 were compared.

To compute the radial advection of  $\theta_e$  ( $-u_r \partial \theta_e / \partial r$ , where  $u_r$  is the radial wind component and  $r$  is the radius from the center), the 900 hPa PV centroid position was used to interpolate  $\theta_e$  to cylindrical coordinates and to determine the radial component of the wind. Plots of  $\theta_e$  and radial wind speed at 500 hPa for simulations 25 and 9 that were interpolated to cylindrical coordinate grids reveal that low- $\theta_e$  air was present in both simulations north of the TCS025 system (Figure 100a,b) where the radial wind speed (Figure 100c,d) was predominantly negative (inflow) to the north. The 500 hPa level was close to the mid-tropospheric  $\theta_e$  minimum level diagnosed from the dropwindsonde analysis (see Figure 68a).

To facilitate the comparison between WRF simulations 9 and 25, the radial advection of  $\theta_e$  was azimuthally averaged between the 850 hPa and 400 hPa pressure surfaces from 100 – 200 km radius of the low-level PV center for the first 24 h of simulation time (Figure 101a). The radial advection of  $\theta_e$  was compared with azimuthally averaged inertial stability (see Equation 6), which is directly related to the strength of the tangential wind and is an indicator of the resistance to radial displacements within the flow (Figure 101b).



Just prior to 1800 UTC 27 August, the average radial  $\theta_e$  advection became increasingly negative between 850 hPa and 400 hPa in both simulations (Figure 101a), indicating low- $\theta_e$  air was being advected radially inward. This time corresponded to when the TUTT was in close proximity to the north of the TCS205 system. The advection of low- $\theta_e$  air in simulation 9 became began after 1800 UTC 27 August, whereas the advection of low- $\theta_e$  air began slightly later in simulation 25. The strongest advection of low- $\theta_e$  air occurred around 2000 UTC 27 August in both simulations, and was slightly larger in magnitude in simulation 9. Although the magnitude fluctuated somewhat, the advection of low- $\theta_e$  air into the TCS025 system became less pronounced after 0000 UTC 28 August (Figure 101).

Interestingly, azimuthally-averaged  $\theta_e$  (Figure 101c) increased in all simulations during the time when negative  $\theta_e$  advection was occurring. An inspection of model-derived cloud-top brightness temperature indicates this was when deep convection was active in simulations 9 and 25 (see Figure 98b and Figure 99b), which suggests that deep convection caused  $\theta_e$  to increase in the column despite the negative environmental influence of the TUTT north of the TCS025 system. By 0000 UTC 28 August, the average  $\theta_e$  in simulation 25 had risen to be slightly greater than 340 K, however, it remained nearly constant from this point onward. In contrast, the average  $\theta_e$  in simulation 9 continued to increase throughout the time period, and was greater than 342 K by 1200 UTC 28 August. The increase in  $\theta_e$  after 0000 UTC 28 August was most likely aided by the enhanced surface heat fluxes (latent and sensible) in simulation 9 compared to simulation 25. The surface heat fluxes in simulation 9 began to increase relative to simulation 25 shortly after 1800 UTC 27 August when the inertial stability began to increase (i.e., surface fluxes increased as the low-level circulation strengthened). The enhanced fluxes and deep convection caused  $\theta_e$  to steadily increase within the atmospheric column at a much greater rate than in simulation 25.

The differences in circulation alignment between simulations 9 and 25 only became significant after 0000 UTC 28 August, which was past the peak time when low-

$\theta_e$  air from the TUTT was impacting the system (see Figure 98a and Figure 99a). In addition, the analysis of inertial stability (Figure 101b) indicates the circulation in simulation 9 was at nearly the same intensity as the circulation in simulation 25 during the time when low- $\theta_e$  air from the TUTT was present. Thus at this point there was little difference between the simulations with regards to the circulations being able to resist radial displacements within the flow. It wasn't until after the low- $\theta_e$  air associated with the TUTT moved away from the immediate vicinity of the TCS025 disturbance that the inertial stability in simulation 9 began to increase significantly relative to simulation 25.

Since there was little difference in the alignment and strength of the circulations in simulations 9 and 25 during the time when the low- $\theta_e$  air from the TUTT was present near the TCS025 circulation, it is not surprising that the radial advection of low- $\theta_e$  air was similar for the two WRF simulations. There had not been an adequate amount of time for the model solutions to diverge by the time the low- $\theta_e$  air from the TUTT impacted the system. In addition, amidst active convection and significant heat and moisture fluxes from the surface, it might have been challenging to attribute contrasts in development of the TCS025 system to small differences in  $\theta_e$  advection. Within the simulated environment, especially in simulation 9, the convective processes tended to dominate the solution. However, observations suggest the impact of low- $\theta_e$  air from the TUTT was more significant in reality (see Figure 51, Figure 58, Figure 59, Figure 60, and Figure 61) within an environment that was characterized by weak convection and poor vertical alignment of the circulation.

## **2. Vertical Wind Shear**

In addition to vortex alignment, the interaction between deep convection and vertical wind shear was also analyzed. In a modeling study that examined sensitivities related to the intensification of Hurricane Emily (2005), Li and Pu (2008) found that simulated hurricane intensity did not correlate well with the magnitude of the environmental vertical wind shear. It was therefore a question of whether the environmental vertical wind shear computed from the CFSR analysis dataset (see Figure

35) was characteristic of the vertical wind shear experienced more locally over the convective scale in the WRF simulations, and whether the presence of deep convection might have modulated the vertical wind shear magnitude.

Early in the simulated evolution of TCS025 (2000 UTC 27 August), deep convective updrafts greater than  $5 \text{ m s}^{-1}$  associated with the TCS025 disturbance were surrounded by areas of weak upper-level wind speed relative to the background environmental flow in simulations 25 and 9 (Figure 102a,b). Some of the reduction in upper-level flow was undoubtedly related to synoptic changes as the TUTT was moving westward to the north of the low-level circulation where convection was prevalent. However, in the high temporal and spatial resolution animations of 200 hPa wind speed from WRF simulation 20 (not shown), strong convective updrafts can be identified penetrating and weakening the upper-level environmental flow.

Immediately apparent from Figure 102a,b is that there was a larger number of updrafts greater than  $5 \text{ m s}^{-1}$  in simulation 9 compared to simulation 25 at 2000 UTC 27 August. The updrafts were generally located within a band of reduced wind speed at 200 hPa that was oriented northwest to southeast, south of the TUTT. The area of reduced upper-level wind speed in simulation 9 appeared to extend over a larger area than in simulation 25, while wind speed magnitudes were much higher to the north and south of this region in simulation 9. The stronger wind speed at 200 hPa coincided with a much stronger pressure gradient to the north and south of the low wind speed area in simulation 9, which was a result of increased geopotential height over the convective area (Figure 102a,b) (i.e., stronger upper-level wind speed relative to simulation 25 was an indication of enhanced upper-level outflow emanating from the convective area (see Figure 78)).

As a result of the stronger outflow, vertical wind shear (200 hPa – 850 hPa) to the south and north of the convective area was much stronger in simulation 9 compared to simulation 25 (Figure 102c,d). The average vertical wind shear and the vertical wind shear of the average wind were computed within the white-boxed regions shown in Figure 102 that roughly encompassed the areas of convection associated with the simulated TCS025 disturbance. The vertical wind shear of the average wind was calculated by first averaging the U and V wind components within the boxed region at

200 hPa and 850 hPa before differencing, while the U and V components were differenced first in the average vertical wind shear computation (Table 4). At 1800 UTC and 2000 UTC 27 August, the average vertical wind shear within the boxed region was strongest in simulation 9, while the vertical wind shear of the mean wind was strongest in simulation 25 (Table 4). Early in the simulations, differences in the low-level flow appear to have been smaller than the upper-level differences (see Figure 73), thus the contrasts in vertical wind shear between simulation 9 and 25 were predominantly a result of contrasts in upper-level flow. The fact that the vertical wind shear of the mean wind was less in simulation 9 suggests there was a greater percentage of cancellation when averaging the U and V wind components over the boxed area. Even though the average vertical wind shear within the white-boxed region was stronger in simulation 9, it was mostly due to enhanced convective outflow, which is predominantly divergent in nature, and this caused the vertical wind shear of the mean wind to be less for simulation 9.

Park et al. (2012) found that the vertical wind shear experienced by a non-uniform, asymmetric, and time-varying system may be quite different from the vertical wind shear calculated by averaging over an area symmetric from the storm center position. Likewise, there appears to be a difference between the vertical wind shear characteristic of the background environment and that experienced within the convectively active region in the WRF simulations. The environmental vertical wind shear for this time period, which was computed from the CFSR dataset by removing the irrotational and non-divergent component of the shear associated with the TCS025 disturbance, was about 15 kt from the north-northwest (see Figure 35). The fact that the vertical wind shear of the mean wind over the convective area was less than the CFSR value for both simulations and was weakest in simulation 9, which experienced the strongest convection and outflow, suggests that convection impacted the magnitude of vertical wind shear over this region. However, the effect that differences in vertical wind shear had on convection is less clear, as is the spatial scale over which convection and system organization responded to vertical wind shear.

Interestingly, updrafts greater than  $5 \text{ m s}^{-1}$  at 200 hPa appear to be along the southern boundary of the low wind speed area (Figure 102a,b), which was very close to

where the vertical wind shear was quite strong (Figure 102c,d). The environmental CFSR vertical wind shear was northerly at this time (see Figure 35) and might have caused convective updrafts to tilt southward with height. The fact that convection did not seem to form closer to the middle of where vertical wind shear was weakest suggests that low-level convective forcing was either stronger to the south, or that deep convection was being favorably influenced by the presence of vertical wind shear to some degree.

In summary, stronger convective processes in WRF simulation 9 resulted in the intensification of the circulation relative to simulation 25 (see Figure 74). As Davis and Ahijevych (2012) suggest, deep convection is likely to help improve the vertical alignment of a system's circulation. Deep convective towers, and the associated latent heat release, would cause rapid pressure falls and development of a low-level circulation below a pre-existing mid-level circulation, creating a vertically coherent circulation structure. Although not immediate, the circulation alignment steadily improved in simulation 9, but failed to do so in simulation 25 (see Figure 97a and Figure 98a). In addition, as deep convection acted to disrupt and reduce the magnitude of the upper-level background flow, the vertical wind shear over the convective area was effectively reduced relative to the magnitude of the environmental vertical wind shear. Therefore, beyond improving the vertical alignment of the circulation structure directly, areas of deep convection can also act to shield an incipient disturbance from the negative effects of vertical wind shear by reducing the magnitude of the upper-level flow. It is possible that both of these processes were acting in simulation 9 to allow the circulation structure to become better vertically aligned relative to the circulation depicted by simulation

## **F. MULTI-PHYSICS ENSEMBLE DISCUSSION AND SUMMARY**

To complement the observational analysis and gain further insight into the evolution of the non-developing TCS025 disturbance, a multi-physics ensemble was employed using the WRF-ARW numerical model. However, the majority of the simulations over-intensified the disturbance (see Figure 71a). Simulation 9, which used the Purdue Lin microphysics scheme, exhibited strong development, while simulation 25, which used the simplistic WSM3 microphysics scheme, more closely matched the

ECMWF analysis and failed to develop the disturbance. A detailed comparison of simulations 9 and 25 was conducted to identify key differences between the two simulations.

Differences between simulation 9 and 25 were evident after only 12 h of simulation time: simulation 9 exhibited a reduction in low-level geopotential height near convective areas and enhanced upper-level outflow relative to simulation 25 (see Figure 73). Vertical cross sections of relative vorticity (see Figure 74a,b) suggest the circulation was stronger in simulation 9 and more vertically aligned; vertical cross sections of  $\theta_e$  indicated convection was more active in simulation 9 (see Figure 74c,d). These trends continued, and by the end of the simulations (72 h of integration), simulation 9 had developed TCS025 significantly (see Figure 77d), whereas the disturbance had weakened to an open wave in simulation 25 (see Figure 77c).

It is interesting that simulation 25 produced the most “correct” result with regards to the evolution of TCS025 despite the use of a simple microphysics scheme (WSM3). The omission of graupel and mixed phase processes from the WSM3 scheme are obvious limitations, and often it is difficult to identify when the omission of these processes may be justified. However, for TCS025, the extra complication of the 6-class schemes degraded the solution. This suggests that additional observation-based validation needs to be done with respect to the microphysical processes represented in numerical models. In addition, with the known limitations of the WSM3 scheme, one could argue that simulation 25 produced the most realistic result for the wrong reasons. This perhaps serves as a good reminder that there may be times when the model outcome appears to be correct, but the physical processes responsible for storm development in the model simulation differ from those in reality.

Although the multi-physics ensemble was constructed primarily by varying the microphysics schemes, it is important to note that the differences in the development of TCS025 were just as large for two simulations that used different boundary layer schemes. Simulations 14 and 24 both employed the WSM6 microphysics scheme, but the YSU boundary layer scheme was used in simulation 14, and simulation 24 used the MYJ

boundary layer scheme (see Table 3). While only weak development occurred in simulation 24 (MYJ), over-development occurred in simulation 14 (YSU) and the evolution of minimum sea-level pressure was very similar to that of simulation 9 (see Figure 71). The sensitivity to the parameterization of boundary layer processes is consistent with the modeling study by Bao et al. (2012) that found that different boundary layer parameterization schemes led to large differences in the intensity evolution and structural characteristics of the simulated tropical cyclone.

Circulation budgets of simulations 9 and 25 were conducted for the blue-boxed regions in Figure 79 and Figure 80 for the time period from 1800 UTC 27 August to 0600 UTC 28 August. Within the blue-boxed region, average vorticity was initially strongest in the mid-levels but increased in the lower troposphere. While the circulation tendency due to the stretching of vertical vorticity was the dominant process in both simulations (see Figure 81f and Figure 82f), the stretching tendencies (both negative and positive) were larger in simulation 9, which indicates that convective activity was stronger in simulation 9.

A vorticity budget analysis and inspection of the low-level vorticity evolution (see Figure 109) suggest simulation 9 developed as a result of the aggregation of positive low-level vorticity produced primarily through the vertical stretching of vorticity via deep convection. This pathway toward storm formation matches that described by Hendricks et al. (2004) and Montgomery et al. (2006). However, since the modeled outcome did not match reality, it is not clear whether the evolution depicted by the model might be a legitimate route to storm formation. The analysis of the formation of TCS025 in simulation 9 can perhaps better serve to help identify model deficiencies with respect to observations.

Between 0300 UTC and 1200 UTC 28 August, convection was waning in both simulations (see Figure 88a,c), however, convective processes in simulation 9 were still active enough such that the integrated circulation tendency due to stretching in the low-levels was still positive (see Figure 88d). This allowed low-level spin-up to continue in simulation 9. In contrast, the integrated stretching tendency was negative during this time period in simulation 25 (Figure 88b) allowing frictional dissipation to spin down the low-

level circulation. The stretching tendency (and total tendency) was positive in the mid-levels for simulation 25 during this time, which indicates that stratiform precipitation processes (mid-level convergence and low-level divergence) were dominant.

Examining averaged quantities from the blue-boxed region (see Figure 89) confirms that the convective processes were stronger in simulation 9. Vertical velocity, diabatic heating, low-level convergence, and upper-level divergence were all stronger in simulation 9 than in simulation 25. In addition, mid- and upper-level  $\theta_e$  were greater in simulation 9 but smaller in magnitude near the surface, which indicates that convective overturning was more active in simulation 9. Average profiles of various quantities were also constructed according to model-derived cloud-top brightness temperature (see Figure 90). The same pattern held in that the magnitude of vertical velocity, diabatic heating rate, and precipitation rate were generally greatest for the developing simulation 9 and smallest for the non-developing simulation 25 in both the convective and non-convective environments. Profiles of average CAPE were smaller in magnitude in simulation 9 compared to simulation 25. Combined with the fact that vertical velocity was largest in simulation 9, this indicates that CAPE was readily consumed as it became available, offering another indication of stronger convective processes in simulation 9.

Several model-derived diagnostics that might serve as proxies for convective intensity (cloud-top temperature, reflectivity) were computed and compared with similar observational diagnostics. Based on these comparisons, convective processes represented by the model simulations were generally much stronger in intensity than observations suggested. Model-derived cloud-top brightness temperature and reflectivity revealed a predominantly convective structure, whereas observations suggested stratiform precipitation was more common. Furthermore, histograms of model-derived cloud-top temperature, especially for simulation 9, failed to indicate the presence of intermediate cloud-top temperature values (see Figure 94) that were far more prevalent in observations (i.e., the stratiform-convective spectrum of cloud-top temperature values was not well represented by the model simulations). These differences indicate the model simulations were producing too much convective precipitation and not enough stratiform precipitation, even in simulation 25 that failed to develop. The strong convective



signature evident in model-derived cloud-top temperature and reflectivity in simulation 9 agreed with the VHT-pathway to formation. The prevalence of convective-type precipitation in the model simulations, and the general lack of stratiform precipitation regions (including MCSs) did not allow for a comparison of MCS characteristics between model output and observations.

The average  $\theta_e$  deficit within the blue-boxed region of the model simulations (see Figure 96a) was generally less than the  $\theta_e$  deficit computed from dropwindsonde data, even when only considering dropwindsondes from the convective environment (see Figure 68a). Thus, the processes responsible for increasing mid-level  $\theta_e$  and reducing low-level  $\theta_e$  (i.e., convective processes) were too strong in the model simulations exhibiting development, which is in agreement with other aspects of the multi-physics ensemble analysis.

Based on the circulation budget and average profile comparison, it was evident that the convective processes were much stronger in simulation 9 compared to simulation 25. In order to assess the impact that the difference in convective intensity had on circulation structure, an analysis of the vertical alignment was conducted based on the 900 hPa and 500 hPa PV-weighted center positions (see Figure 97). Although the correlation between model-derived cloud-top temperature and the PV-weighted center separation distance was poor (see Figure 98 and Figure 99), the separation distance tended to decrease over time in simulation 9, whereas the separation distance became larger in simulation 25. This suggests that while the alignment of the circulation was most likely affected by outside environmental factors in both simulations, it was ultimately the nature of convection (i.e., strength, duration, and spatial coverage) in simulation 9 that caused the vertical alignment of the circulation to improve.

The presence of low- $\theta_e$  air associated with the TUTT was evident up-shear of the low-level circulation during the second IOP (see Figure 51). A comparison of average 850 hPa - 400 hPa radial  $\theta_e$  advection (see Figure 101) indicated the presence of low- $\theta_e$  air from the TUTT, but active convection and positive heat fluxes from the surface allowed  $\theta_e$  to increase during this time in both simulations. In the adjoint sensitivity

analysis by Doyle et al. (2012), it was concluded that the TUTT located to the northwest of TCS025 negatively impacted the low-level circulation via dry air intrusion along the western side of the circulation. Therefore, it is possible that if the convective processes in the WRF model simulations had been weaker (in better agreement with observations), the impact of the low- $\theta_e$  air from the TUTT would have more effectively limited development in the simulations.

Park et al. (2013) suggested that the vertical wind shear experienced by an asymmetric system similar to TCS025 might be significantly different from the shear computed over a symmetric area from the storm center. Likewise, Li and Pu (2008) found that there was a poor correlation between the environmental vertical wind shear and the intensity of simulated storms. Throughout the evolution of TCS025, vertical wind shear was an important environmental influence. However, a careful analysis of upper-level wind structure revealed that deep convection was also affecting the magnitude of vertical wind shear (see Figure 102). As updrafts reached the upper-troposphere, the upper-level flow was disrupted and the wind speed magnitude was reduced. This had the effect of reducing vertical wind shear over the convective area. Therefore not only did deep convection lead to improved vertical alignment of the circulation in simulation 9, it also helped to maintain and protect the circulation alignment by reducing the magnitude of vertical wind shear.

Due to the prevalence of deep convection that was evident early in the model simulations, the model initial conditions (ECMWF analysis) were compared with observations to determine if the thermodynamic profile was unrealistically unstable to support deep convection (see Appendix B). However, there was good agreement between the ECMWF analysis and dropwindsonde data, which indicates that the propensity for deep convection in the WRF model simulations was not due to erroneously unstable initial conditions. In an attempt to explain the differences in convective intensity exhibited by simulations 9 and 25, additional numerical simulations were conducted: the effect of hydrometeor mass loading was made smaller in simulation 25 and the graupel fall speed was reduced in simulation 9. Both experiments failed to yield different results

from their respective control simulations, which indicates these factors had a negligible impact on the simulations.

Since Park et al. (2013) concluded that the modeled latent heating rates for TCS025 were greater than suggested by ELDORA observations and that the latent cooling rates were too small, another set of simulations was conducted using identical parameters to simulation 9 (Purdue Lin microphysics scheme) except the diabatic heating rate was adjusted by a multiplication factor throughout the simulations. It was found that the development and intensification of the TCS025 disturbance was extremely sensitive to the diabatic heating rate (see Figure 92). Multiplication factors of 0.95 and greater allowed the disturbance to develop, while factors of 0.9 or less inhibited development. This spread of solutions in the additional diabatic heating experiments highlights the importance of correctly representing microphysical processes and their relation to diabatic heating. In addition, it is perhaps also important to consider the vertical profile of latent heating and cooling, as Park et al. (2013) suggested low-level heating is most effective at inducing low-level convergence and storm spin-up.

Doyle et al. (2012) conducted a sensitivity analysis and comparison of a developing (TY Nuri) and non-developing (TCS025) tropical disturbance using the adjoint and tangent linear models for the Coupled Ocean–Atmosphere Mesoscale Prediction System (COAMPS), in which the COAMPS model correctly depicted the non-development of TCS025. Based on wind, temperature, and moisture perturbation experiments that failed to yield significant differences in the development of the TCS025 disturbance, Doyle et al. (2012) concluded that TCS025 was not close to the critical development threshold. Here, both the multi-physics ensemble, and the additional WRF simulations in which the diabatic heating was slightly increased or decreased, revealed a stronger sensitivity. This suggests the sensitivity to microphysical processes and latent heating was much larger than the wind, temperature, and moisture sensitivities. This is perhaps due to the fact that changing the diabatic heating rate or using a different microphysics scheme alters the nature of convection throughout the duration of the simulation. Development of TCS025 was sensitive to the strength of convection and its

associated latent heating rate, such that the cumulative effect of small changes in the latent heating rate had a large impact on the development outcome.

The second hypothesis of this study suggested the reason that the majority of high-resolution simulations consistently over-developed TCS025 was due to the prevalence of intense convective precipitation processes. The analyses of simulations 9 (developing) and 25 (non-developing) and comparison with observations confirms this hypothesis. Strong convective processes in simulation 9 contributed to positive vorticity generation in the lower troposphere and the development of an anticyclone and outflow aloft. Latent heating associated with deep convection induced strong low-level convergence and spin-up of the disturbance. The continued development of deep convection helped strengthen the circulation and improve the circulation alignment in the vertical. In turn, this helped protect the developing system from negative environmental influences. Although convective processes were present early in simulation 25, they were much weaker in intensity. Stratiform precipitation processes became increasingly dominant during lulls in convective activity, much more so than in simulation 9. The stratiform precipitation processes caused a net spin-down of the low-level circulation in simulation 25. A comparison with observations suggests the model simulations, especially simulation 9, were dominated by convective precipitation processes, whereas in reality, stratiform precipitation was more common.

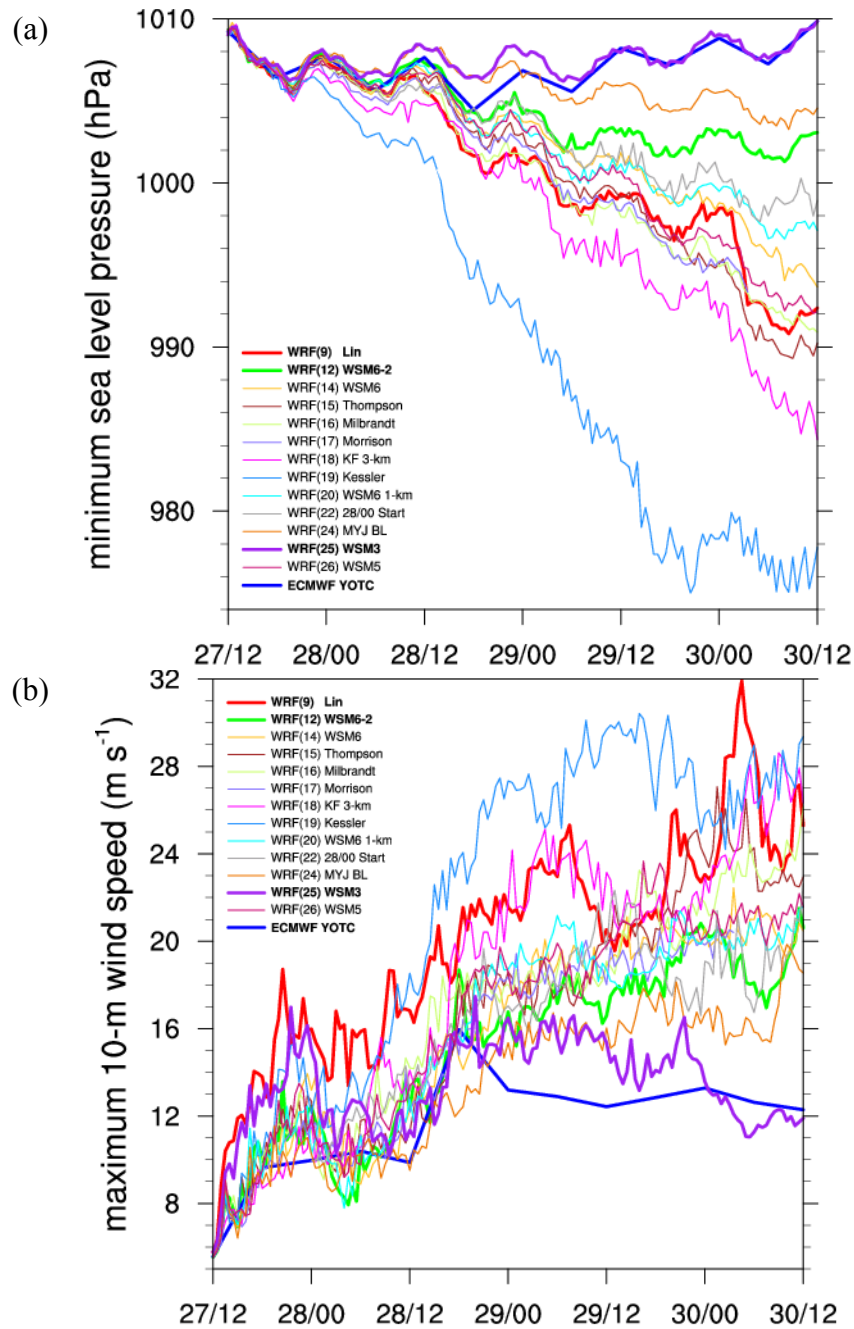


Figure 71 (a) Minimum sea-level pressure (hPa) and (b) maximum 10-m wind speed ( $\text{m s}^{-1}$ ) from 1200 UTC 27 August to 1200 UTC 30 August for the multi-physics WRF-ARW ensemble as indicated in the inset and described in Table 3 plus the ECMWF YOTC analysis. Bold lines denote simulations that are extensively compared in this chapter.

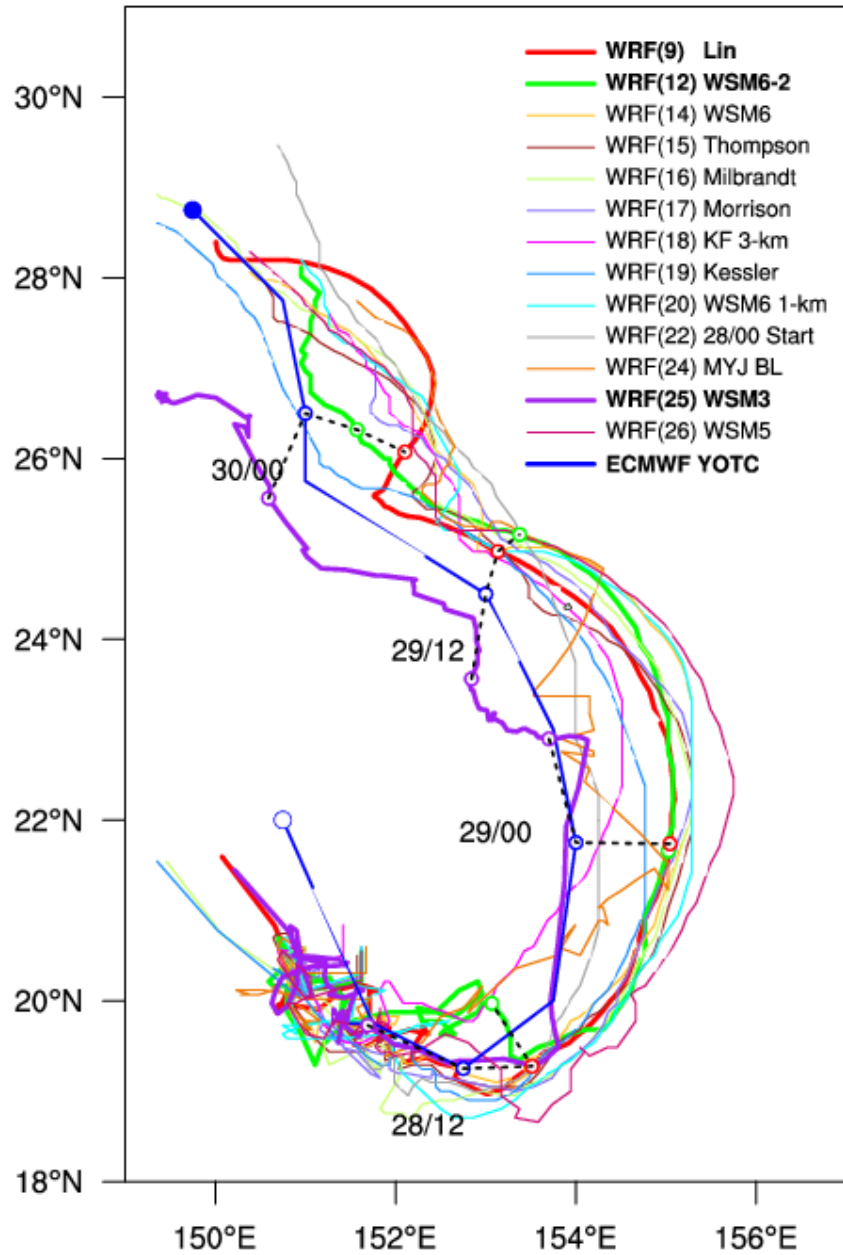


Figure 72 As in Figure 71, except the tracks based on minimum sea-level positions from WRF simulations and the ECMWF YOTC analysis from 1200 UTC 27 August to 1200 UTC 30 August. Large open and filled blue circles mark the starting and ending positions, respectively, of the ECMWF YOTC analysis. Small circles connected by dashed lines denote center positions from simulations of focus in this study (bold lines) at times annotated in figure. Latitude and longitude positions from the WRF simulations were smoothed using a 5-point running average.

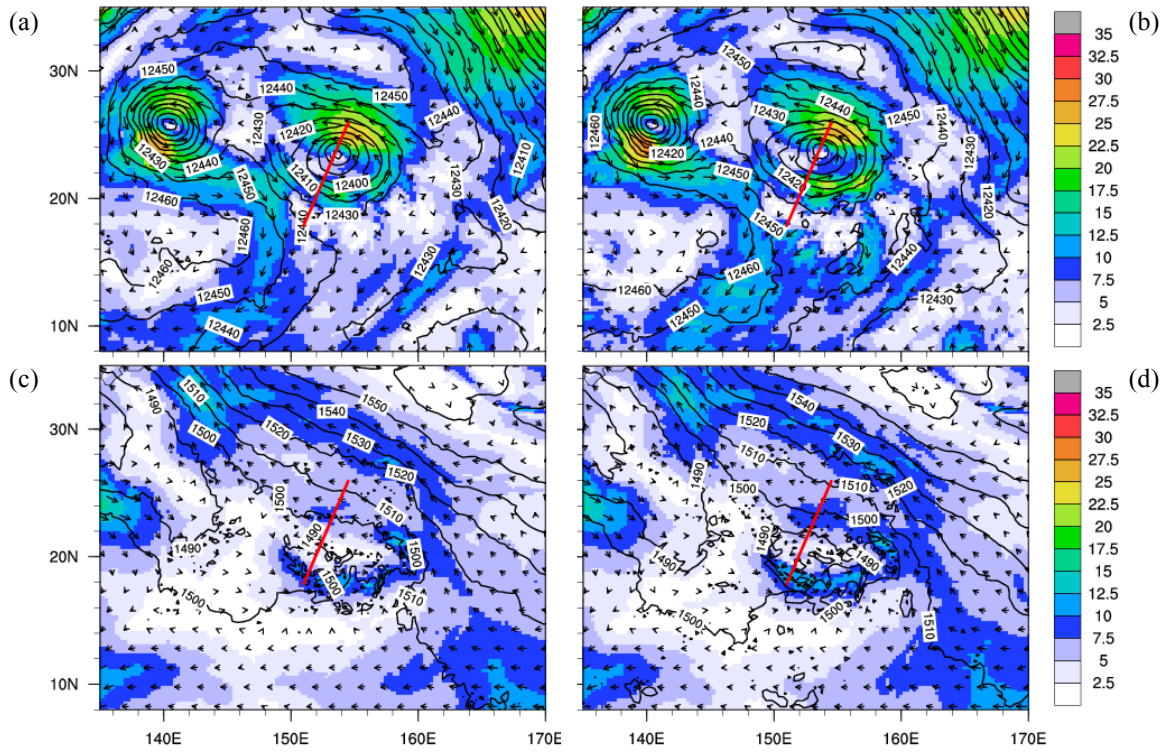


Figure 73 Wind speed ( $\text{m s}^{-1}$ , shading) and geopotential height (m, contoured) at 200 hPa (top) and 850 hPa (bottom) valid at 0000 UTC 28 August (T + 12 h) for (a, c) WRF simulation 25 and (b, d) WRF simulation 9. The red lines indicate the location of the vertical cross-sections in Figure 74.

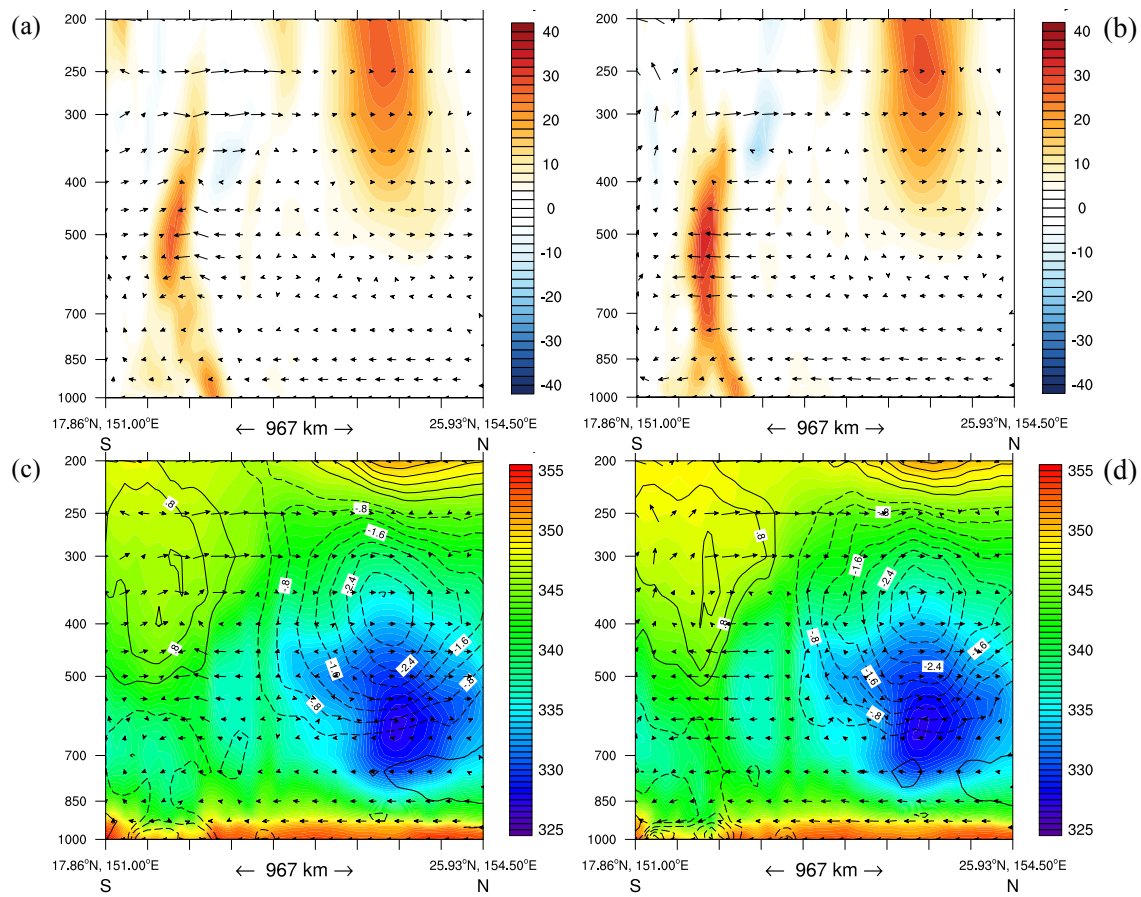


Figure 74 Vertical cross sections along the red lines in Figure 73 of (top) relative vorticity ( $10^{-5} \text{ s}^{-1}$ , shading) and (bottom) equivalent potential temperature (K, shading) and virtual temperature perturbation (K, contours) valid at 0000 UTC 28 August for (a, c) WRF simulation 25 and (b, d) WRF simulation 9. The ordinate axis is in pressure (hPa). Vectors represent wind speeds in the plane of the cross section, and vertical velocity has been rescaled by multiplying by a factor of 10. The average virtual temperature out to  $6^\circ$  radius from the circulation center position was used as the reference state to determine the virtual temperature perturbations in (c) and (d).



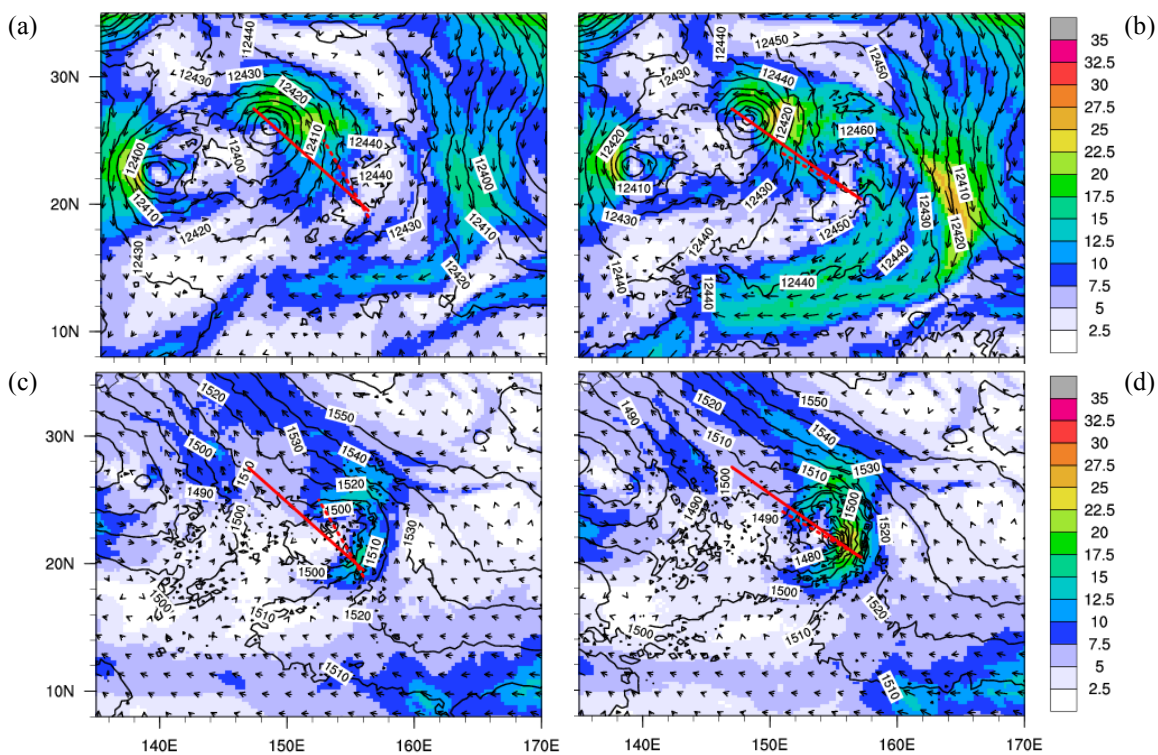


Figure 75 As in Figure 73, except valid at 0000 UTC 29 August (T + 36 h) and the red lines indicate the locations of the cross sections in Figure 76.

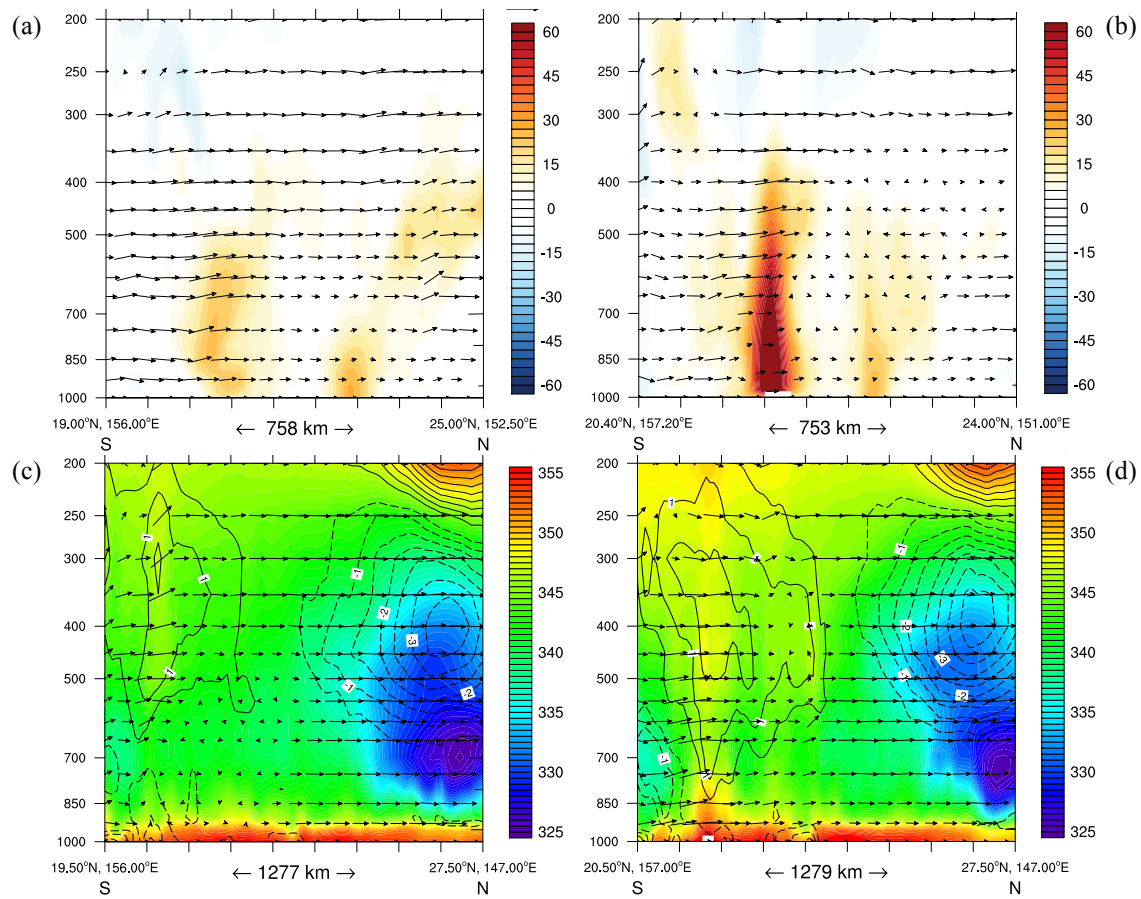


Figure 76 As in Figure 74, except for 0000 UTC 29 August ( $T + 36$  h). The locations of the vertical cross sections in (a) and (b) correspond to the short, dashed red lines in Figure 75 (a, c) and (b, d), respectively. The locations of the vertical cross sections in (c) and (d) correspond to the longer solid red lines in Figure 75 (a, c) and (b, d), respectively. Note that the horizontal scaling in (a) and (b) is different from Figure 74a,b.

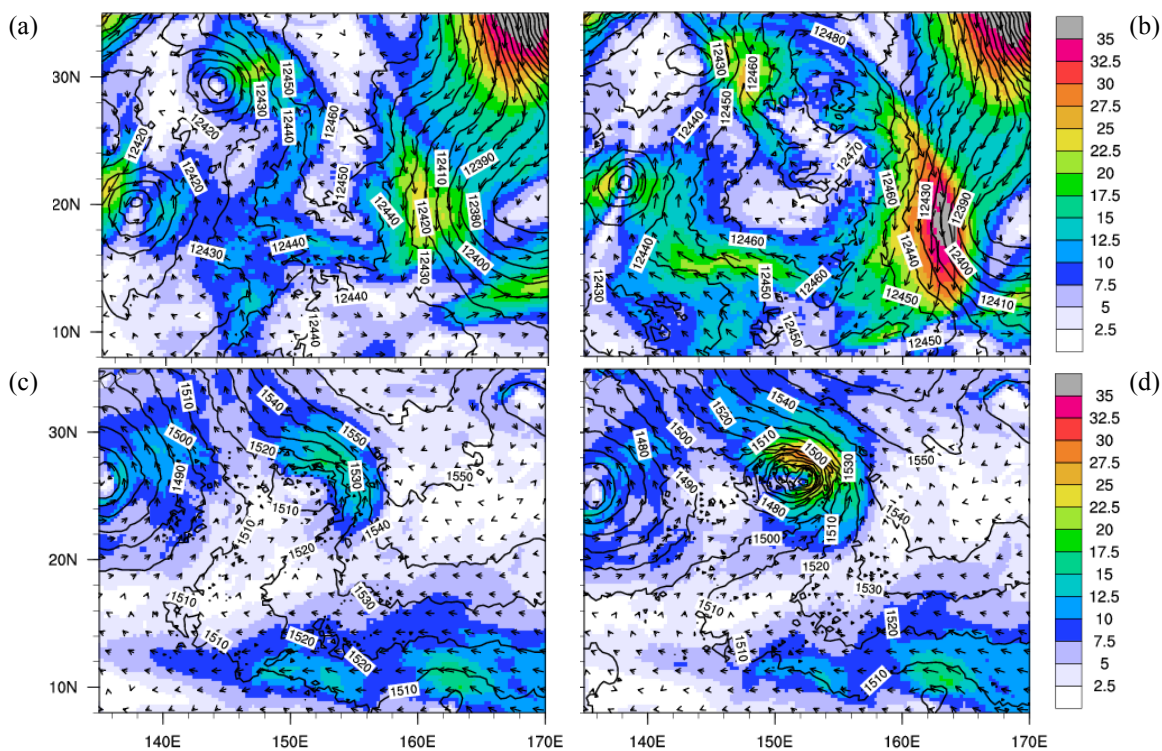


Figure 77 As in Figure 73, except valid at 0000 UTC 30 August (T + 60 h) without red lines indicating cross section locations.

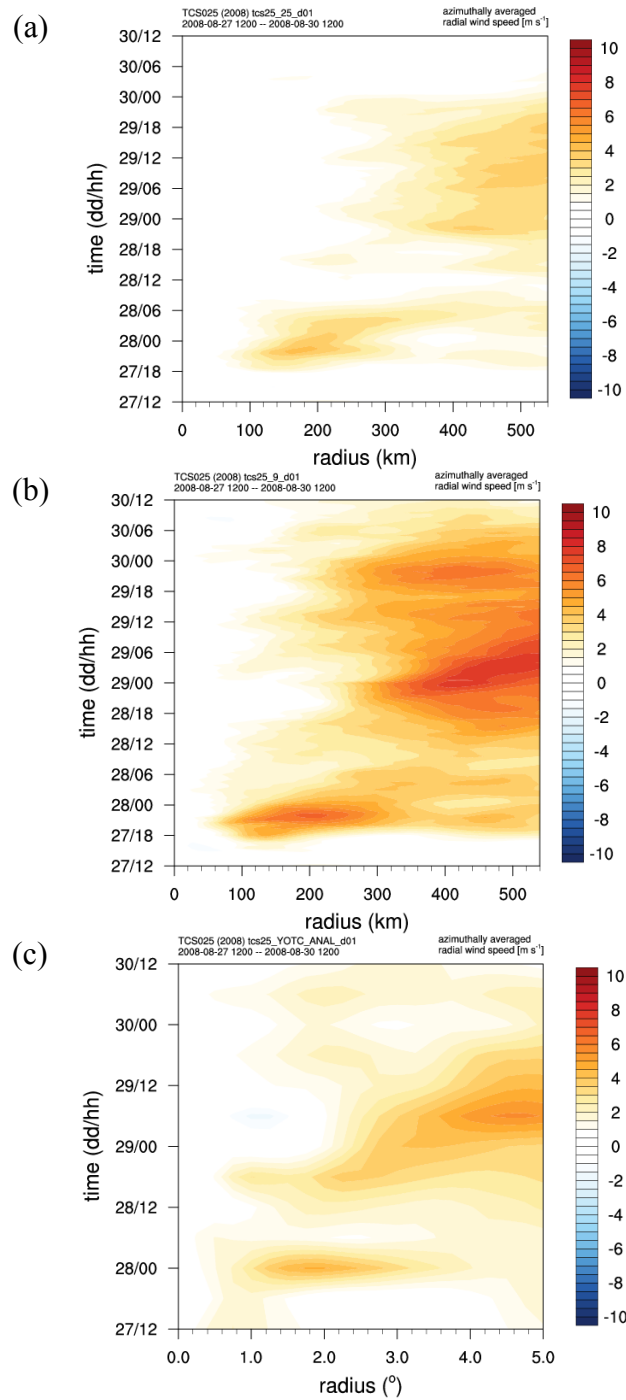


Figure 78 Time series of azimuthally-averaged 200 hPa radial wind speeds ( $\text{m s}^{-1}$ ) as a function of radius from (a) WRF simulation 25, (b) WRF simulation 9, and (c) the ECMWF analysis. Values were first transformed to cylindrical coordinates before azimuthal averaging using center positions determined from the 900 hPa PV centroid.

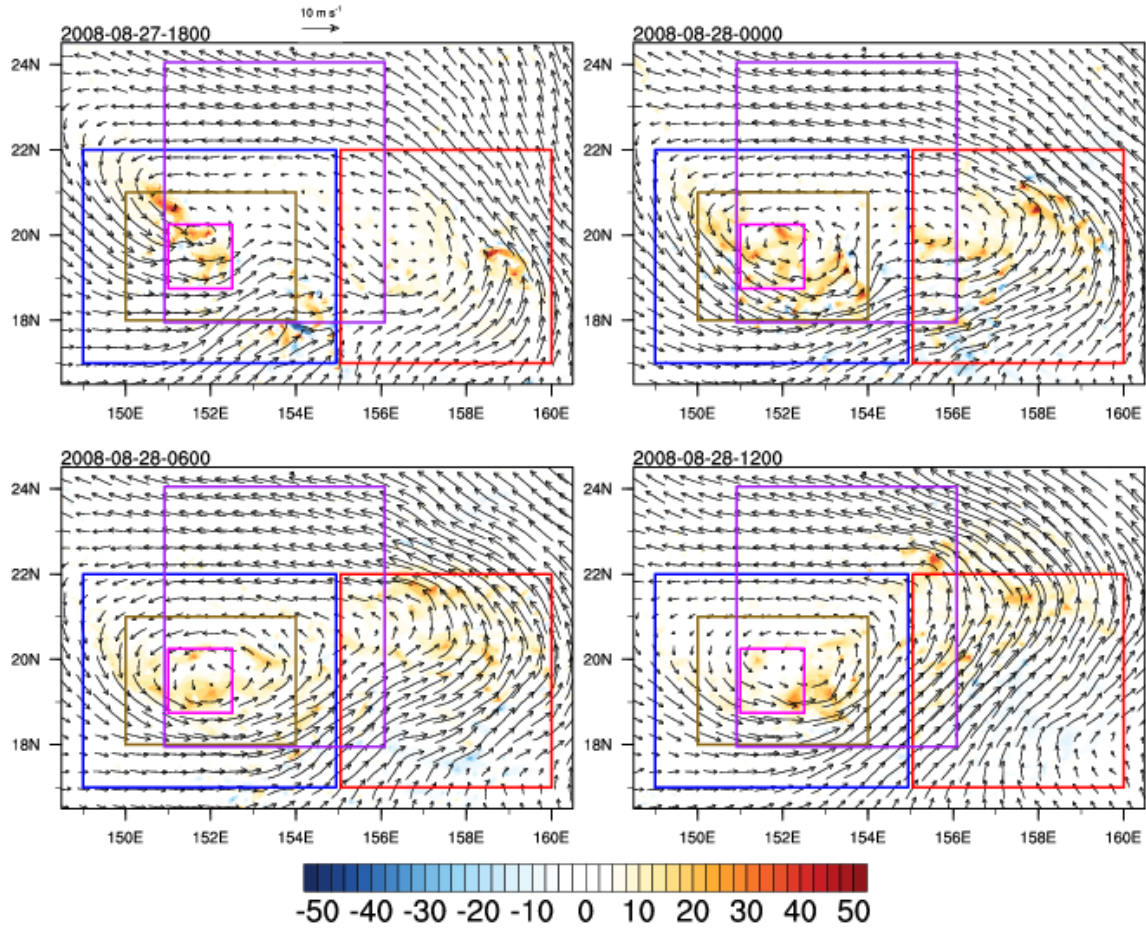


Figure 79 850 hPa wind vectors ( $\text{m s}^{-1}$ , with  $10 \text{ m s}^{-1}$  reference vector indicated at top) and 950-700 hPa average relative vorticity ( $10^{-5} \text{ s}^{-1}$ , color shading) from WRF simulation 25 at 6-h intervals from 1800 UTC 27 August to 1200 UTC 28 August. Boxed regions of various colors correspond to areas over which circulation budgets and averages were computed.



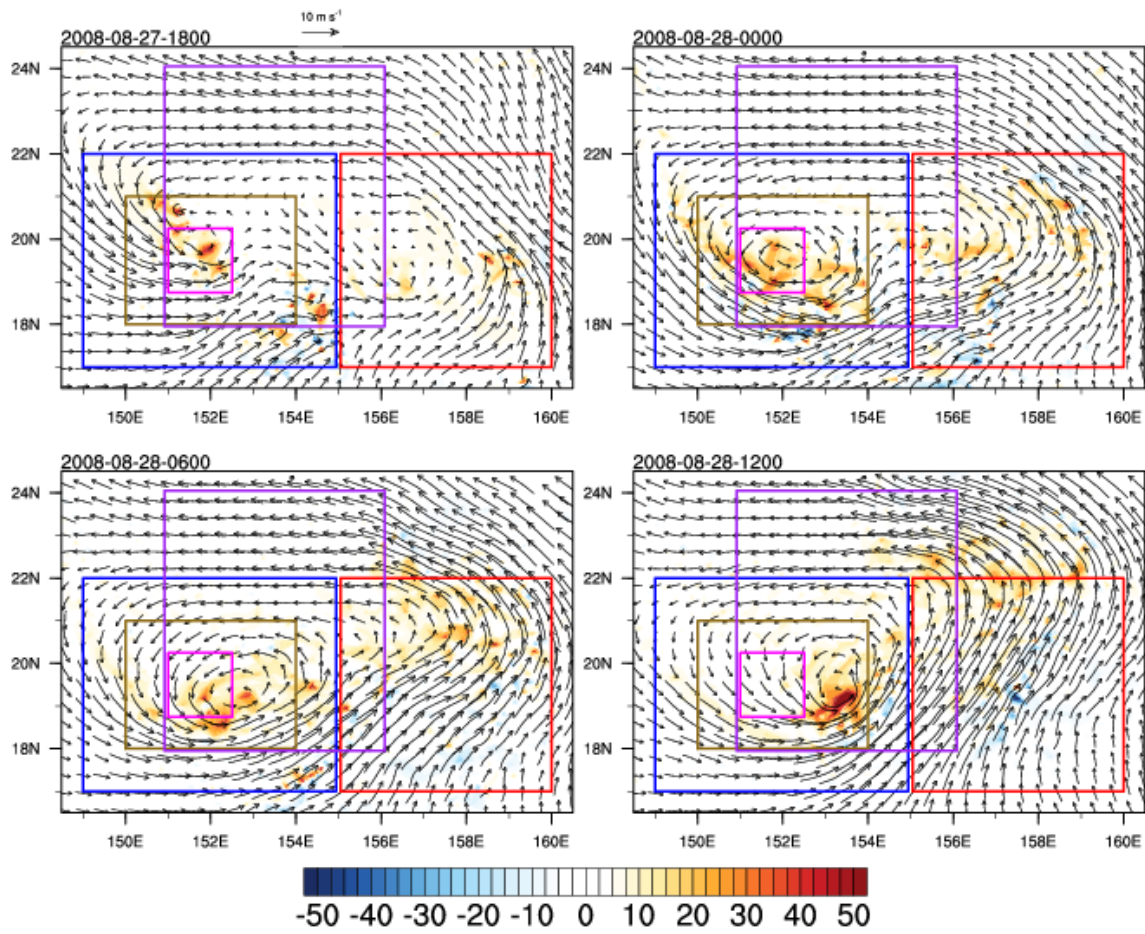


Figure 80 As in Figure 79, except for WRF simulation 9.

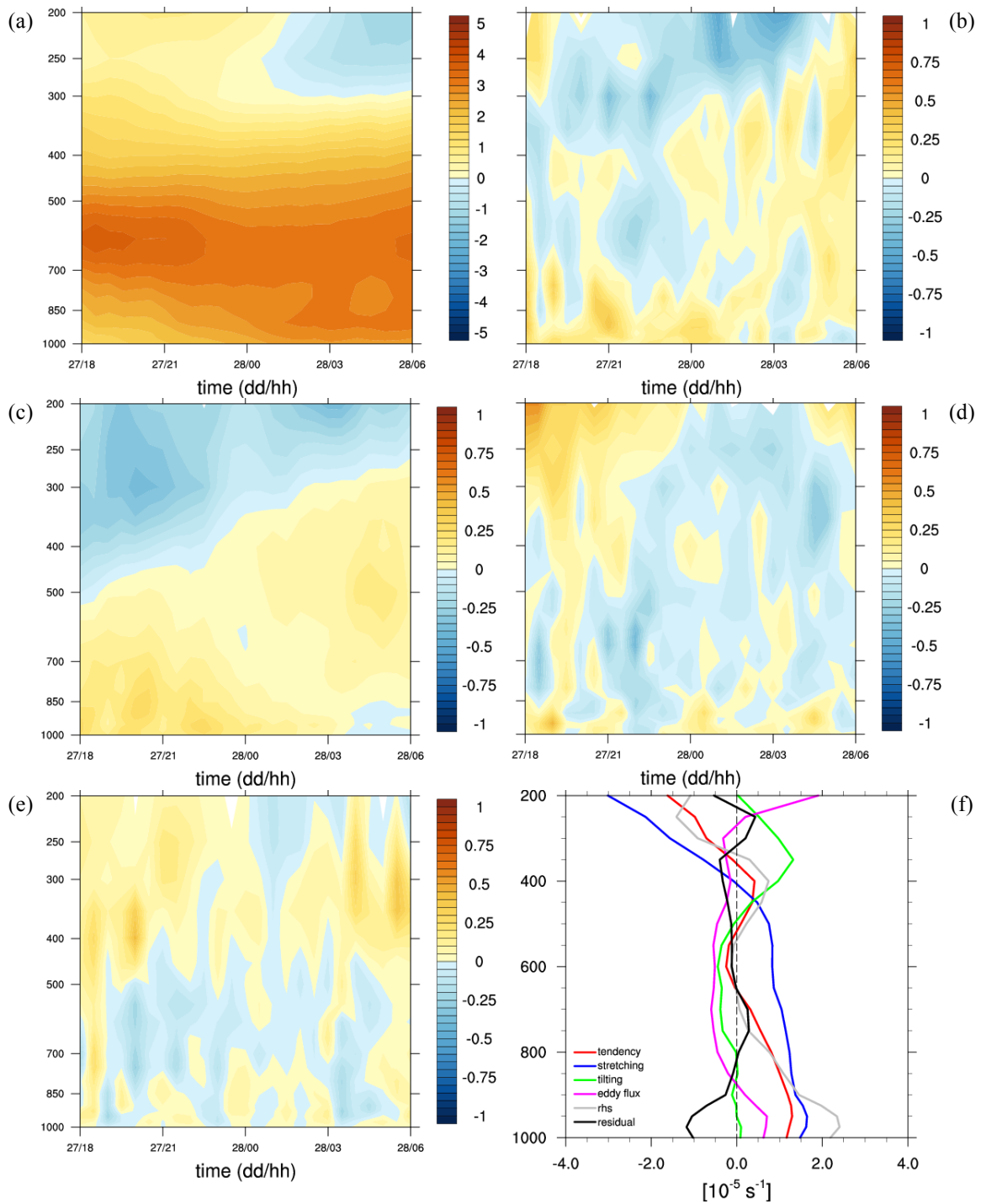


Figure 81 Time evolution from WRF simulation 25 from 1800 UTC 27 August to 0600 UTC 28 August for the blue-boxed region in Figure 79 of (a) relative vorticity ( $10^{-5} \text{ s}^{-1}$ ), (b) total circulation tendency ( $10^{-5} \text{ s}^{-1} \text{ h}^{-1}$ ), (c) circulation tendency due to stretching ( $10^{-5} \text{ s}^{-1} \text{ h}^{-1}$ ), (d) circulation tendency due to horizontal eddy fluxes ( $10^{-5} \text{ s}^{-1} \text{ h}^{-1}$ ), (e) circulation tendency due to tilting ( $10^{-5} \text{ s}^{-1} \text{ h}^{-1}$ ), and (f) integrated circulation budget contributions. Ordinate axes are in pressure (hPa).

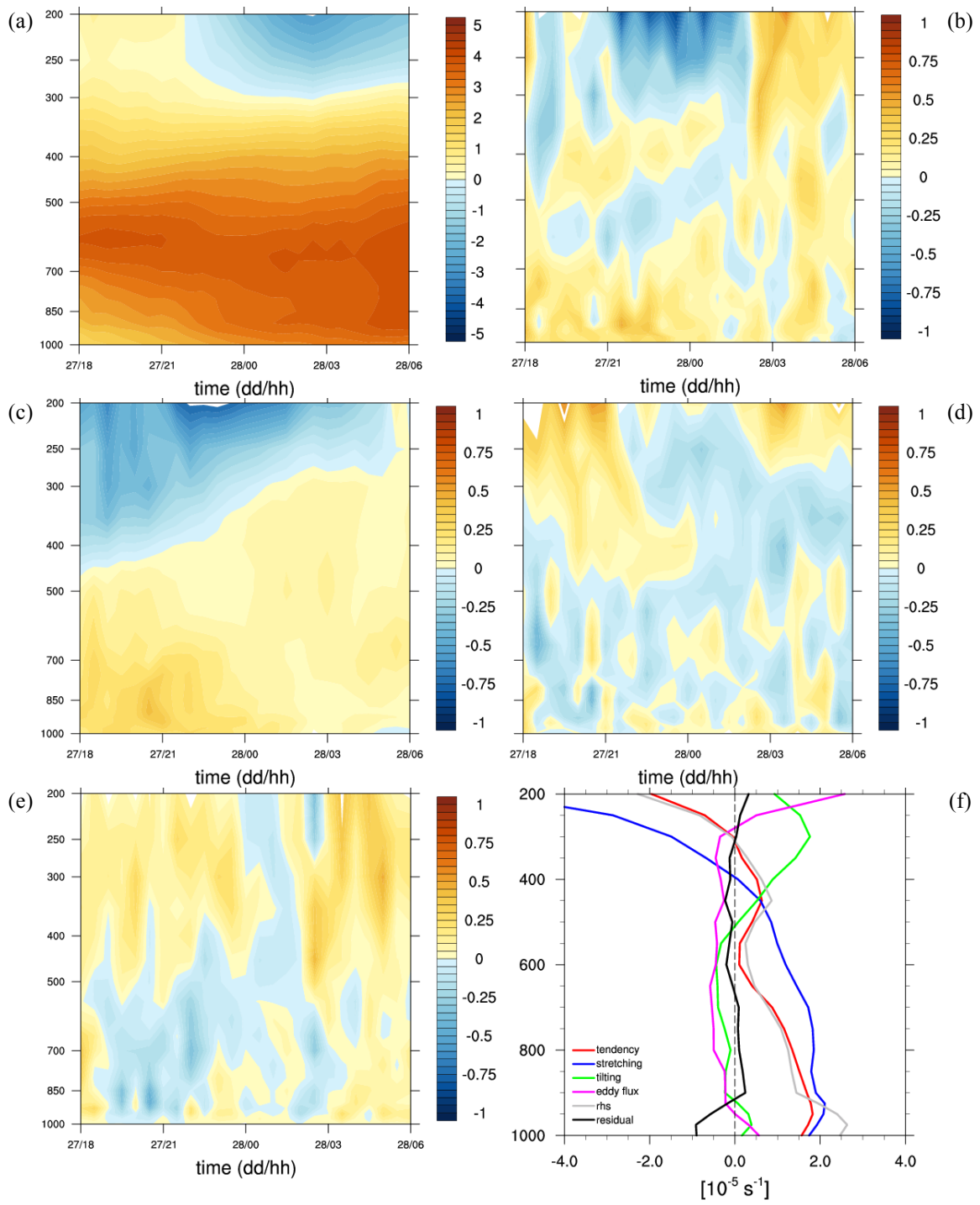


Figure 82 As in Figure 81, except for WRF simulation 9 for the blue-boxed region in Figure 80.



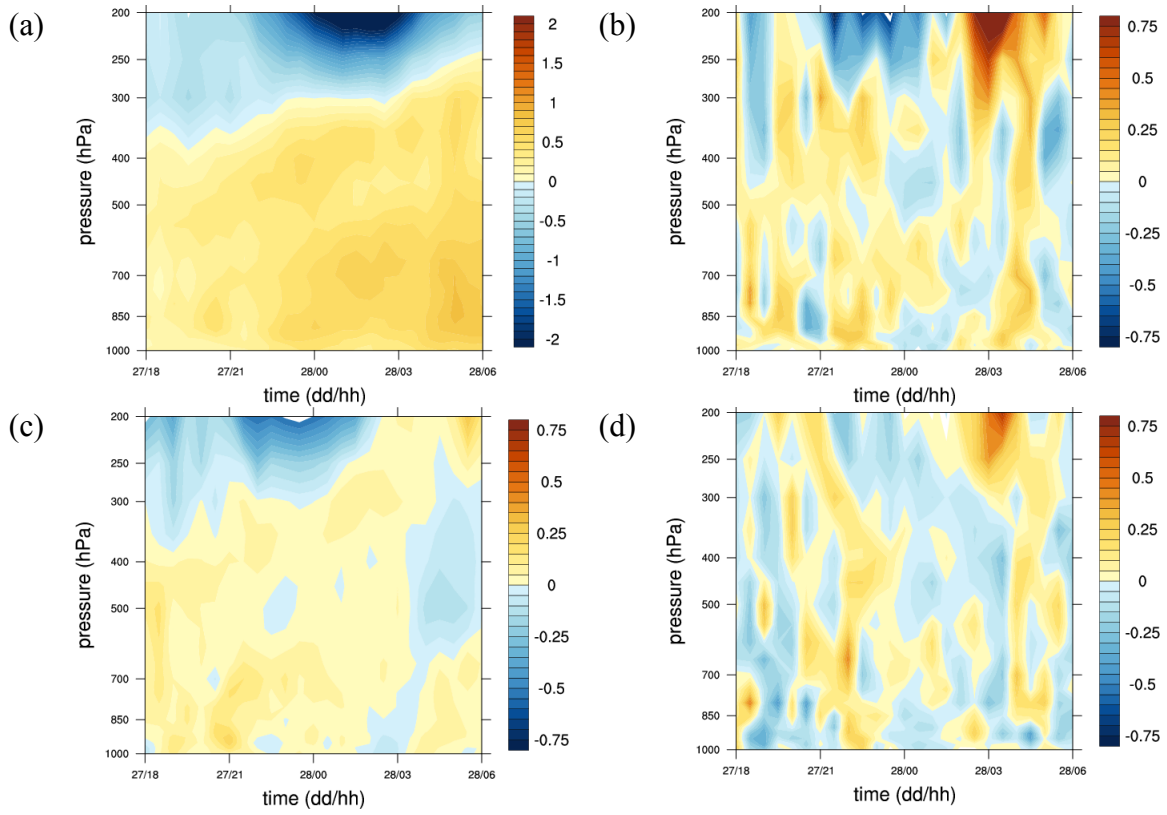


Figure 83 Differences between WRF simulations 9 and 25 (9-25) averaged over the blue-boxed regions in Figure 79 and Figure 80 for (a) relative vorticity ( $10^{-5} \text{ s}^{-1}$ ), (b) total circulation tendency ( $10^{-5} \text{ s}^{-1} \text{ h}^{-1}$ ), (c) circulation tendency due to stretching ( $10^{-5} \text{ s}^{-1} \text{ h}^{-1}$ ), and the circulation tendency due to horizontal eddy fluxes ( $10^{-5} \text{ s}^{-1} \text{ h}^{-1}$ ) Note that the color scales in this figure are different from those used in Figure 81 and Figure 82.

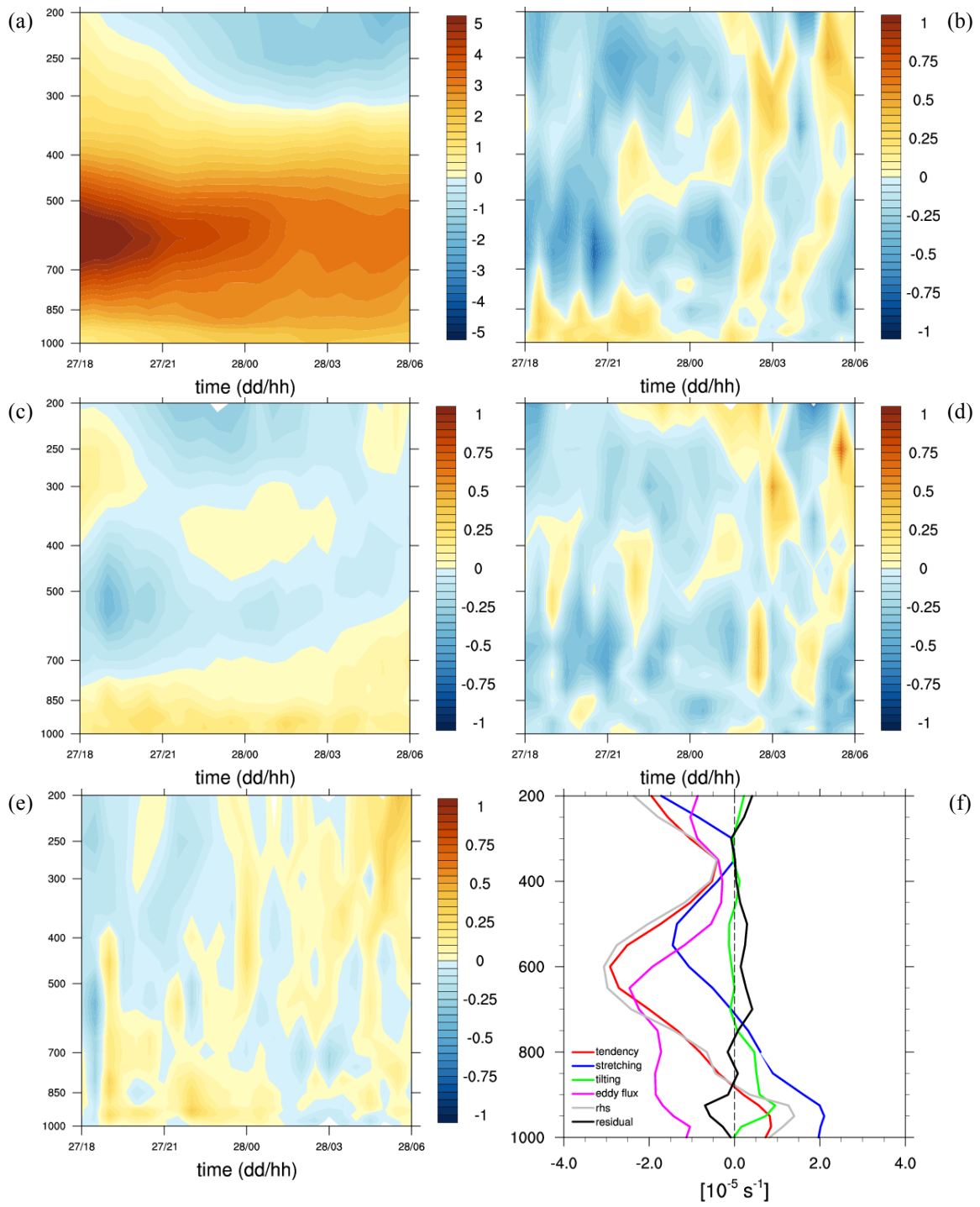


Figure 84 As in Figure 81, except for simulation 25 in the red-boxed region in Figure 79.

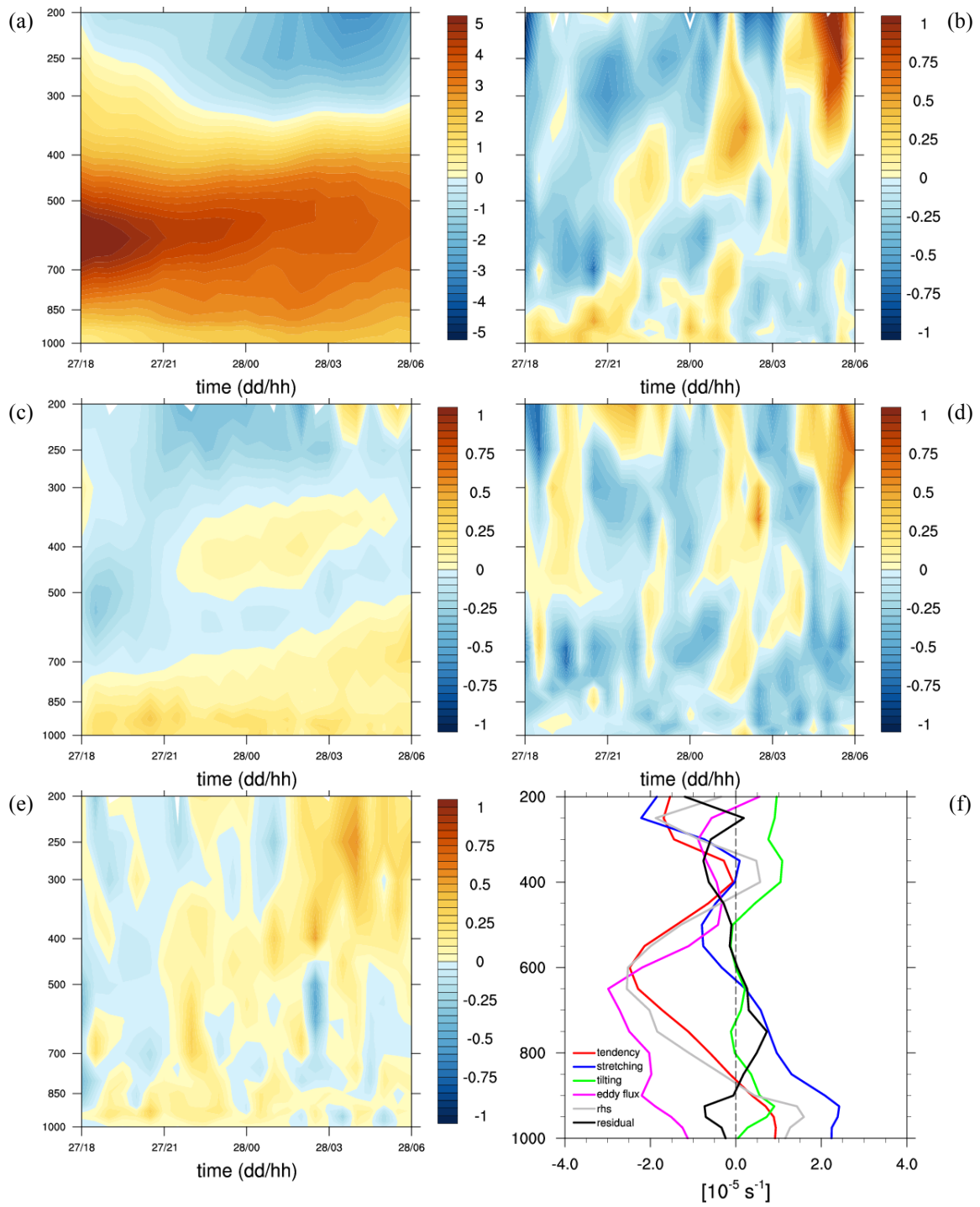


Figure 85 As in Figure 81, except for simulation 9 in the red-boxed region in Figure 80.

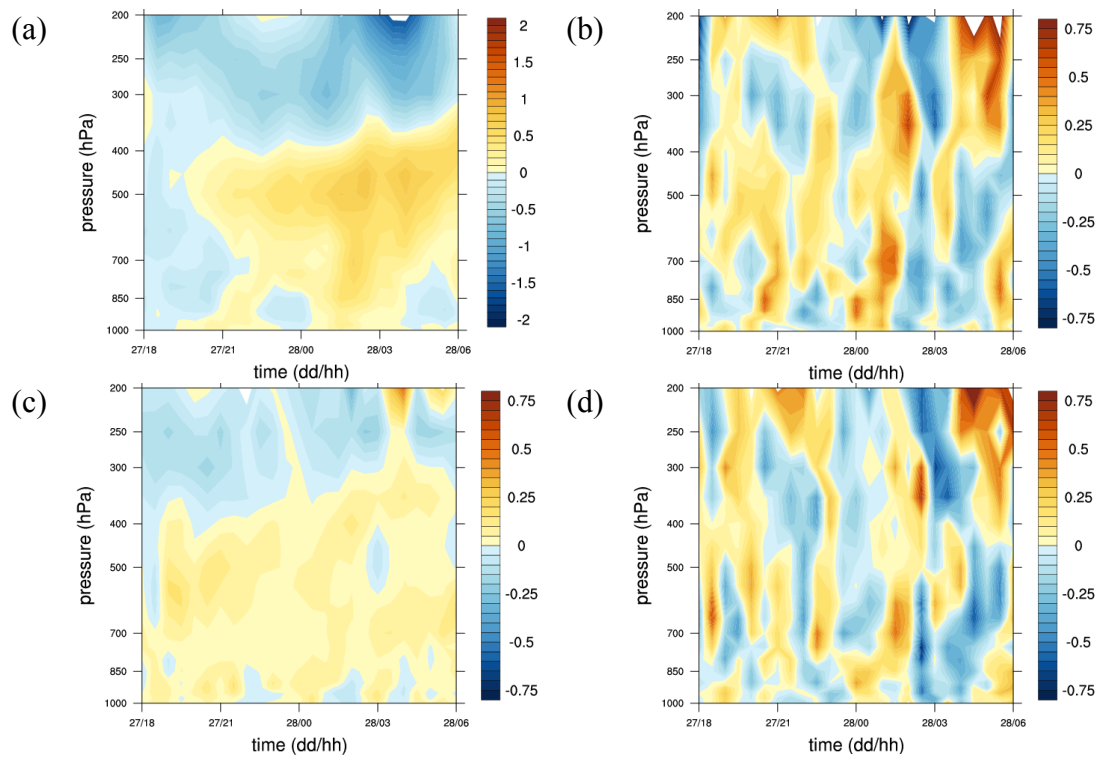


Figure 86 As in Figure 83, except for the red-boxed regions in Figure 79 and Figure 80.

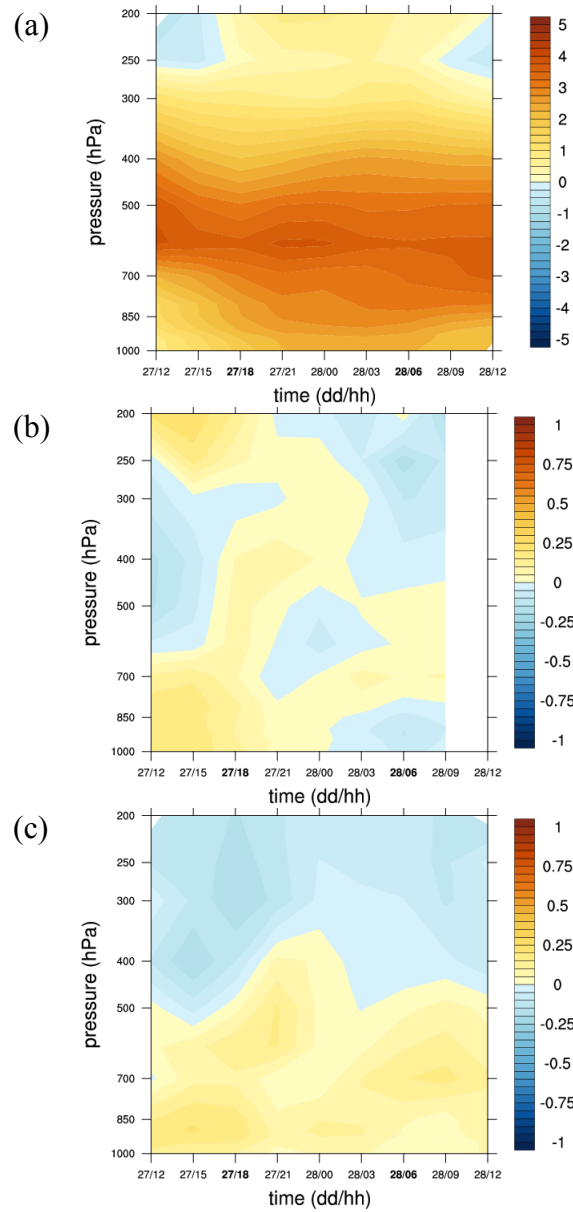


Figure 87 Time evolution from the ECMWF operational forecast from 1200 UTC 27 August to 1200 UTC 28 August averaged over the blue-boxed region in Figure 79 of (a) relative vorticity ( $10^{-5} \text{ s}^{-1}$ ), (b) total circulation tendency ( $10^{-5} \text{ s}^{-1} \text{ h}^{-1}$ ), and (c) circulation tendency due to stretching ( $10^{-5} \text{ s}^{-1} \text{ h}^{-1}$ ). Note that the scales used in this figure are different from those in Figure 81 and Figure 82.

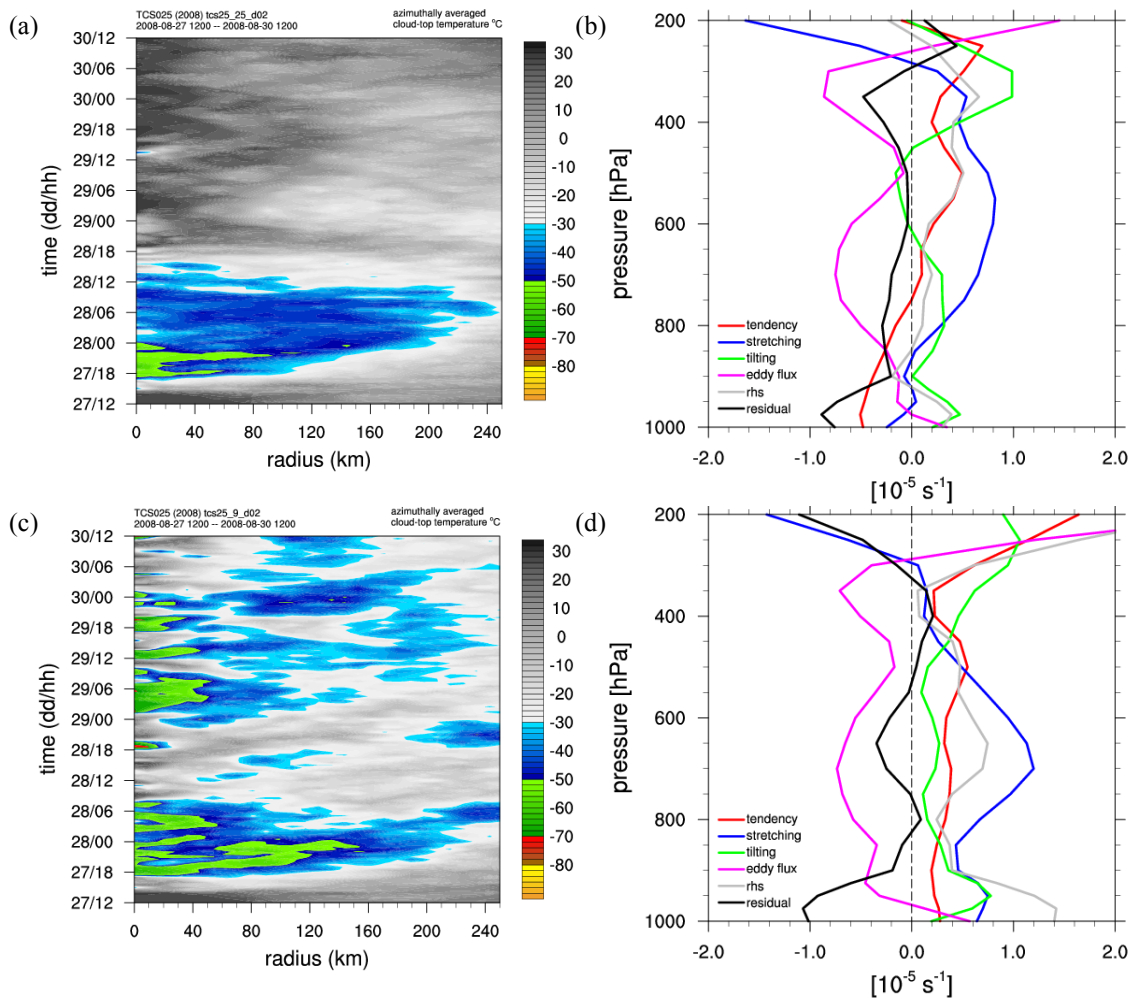


Figure 88 (a, c) Azimuthally-averaged cloud-top brightness temperatures (°C) and (b, d) integrated circulation budget contributions for the time period 0300-1200 UTC 28 August for the blue-boxed region in Figure 79 for WRF simulations (a, b) 25 and (c, d) 9.

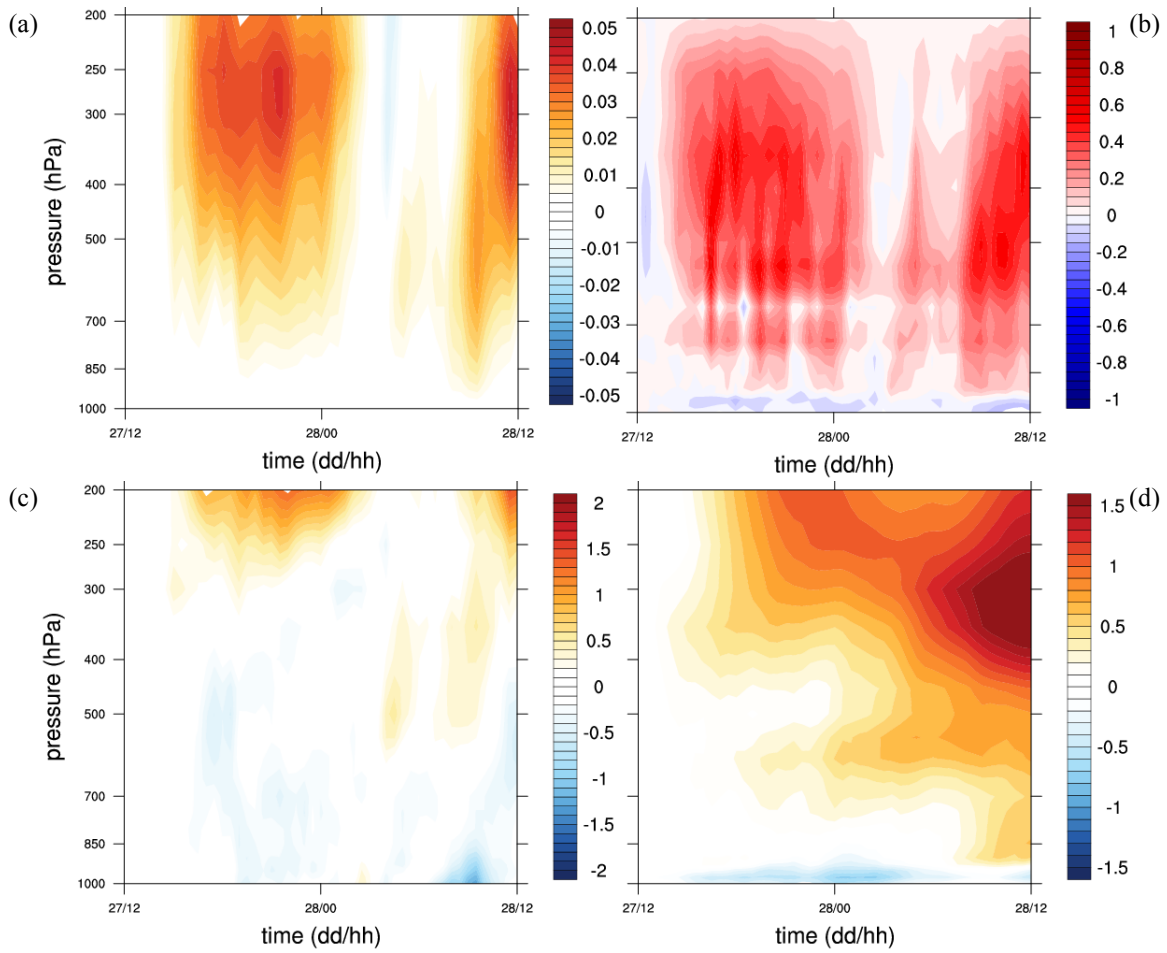


Figure 89 Differences between WRF simulations 9 and 25 (9-25) averaged over the blue-boxed regions in Figure 79 and Figure 80 from 1200 UTC 27 August to 1200 UTC 28 August for (a) vertical velocity ( $\text{m s}^{-1}$ ), (b) diabatic heating rate ( $\text{K h}^{-1}$ ), (c) divergence ( $10^{-5} \text{ s}^{-1}$ ), and (d) equivalent potential temperature (K).



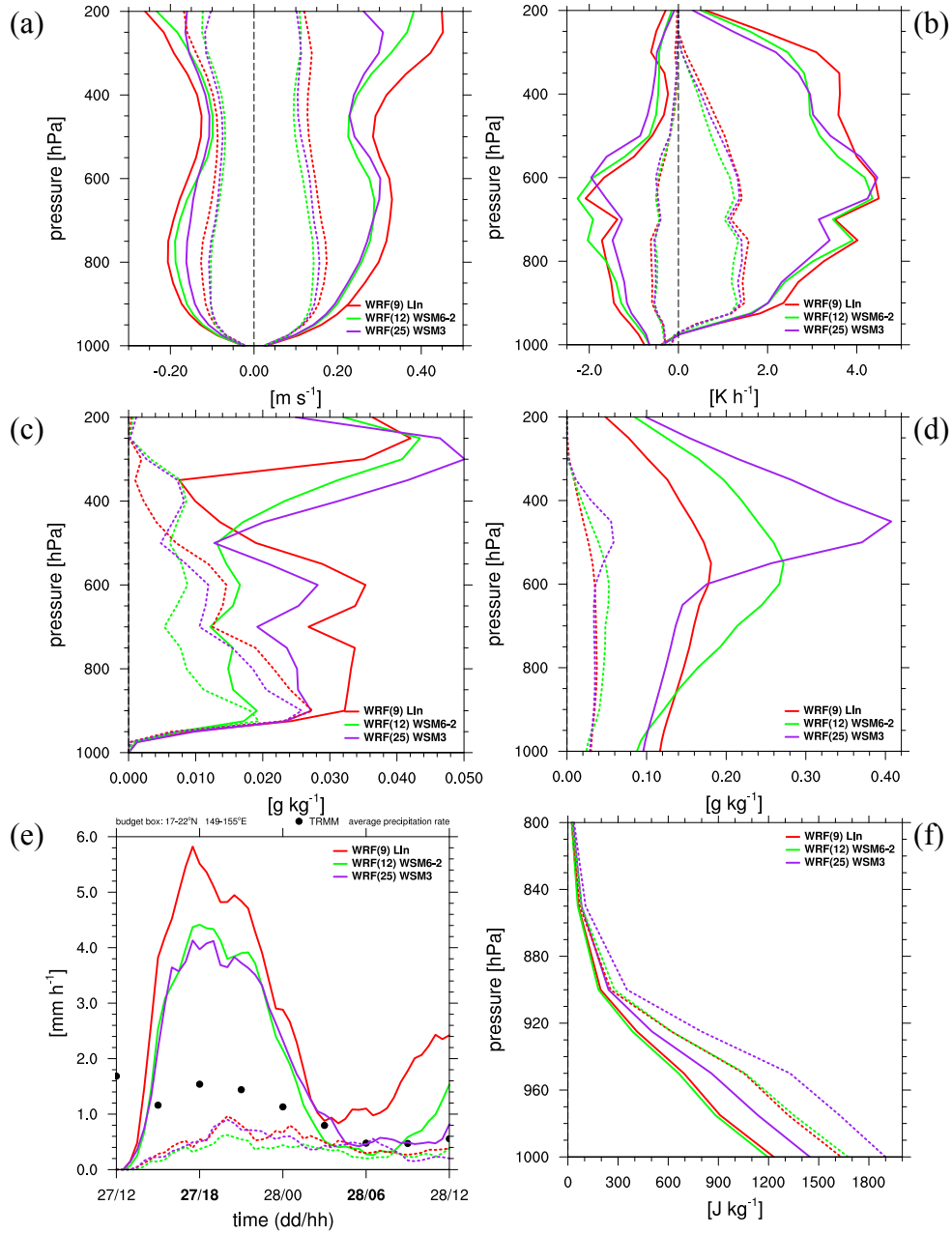


Figure 90 Vertical profiles from the WRF simulations 9 (red), 12 (green), and 25 (purple) for grid points where the model-derived cloud-top brightness temperatures were  $< -35^{\circ}\text{C}$  (solid lines) and  $> -35^{\circ}\text{C}$  (dashed lines) averaged within the blue-boxed region in Figure 79 from 1800 UTC 27 August to 0600 UTC 28 August of (a) positive and negative vertical velocity ( $\text{m s}^{-1}$ ), and (b) diabatic heating rate ( $\text{K h}^{-1}$ ) corresponding with the positive and negative vertical velocities. (c) Total non-precipitating mixing ratio ( $\text{g kg}^{-1}$ ), (d) total precipitating mixing ratio ( $\text{g kg}^{-1}$ ), (e) average precipitation rate ( $\text{mm h}^{-1}$ ) as a function of time, and (f) CAPE ( $\text{J kg}^{-1}$ ). Black dots in (e) denote the average TRMM precipitation rate estimates for the blue-boxed region at the corresponding times.



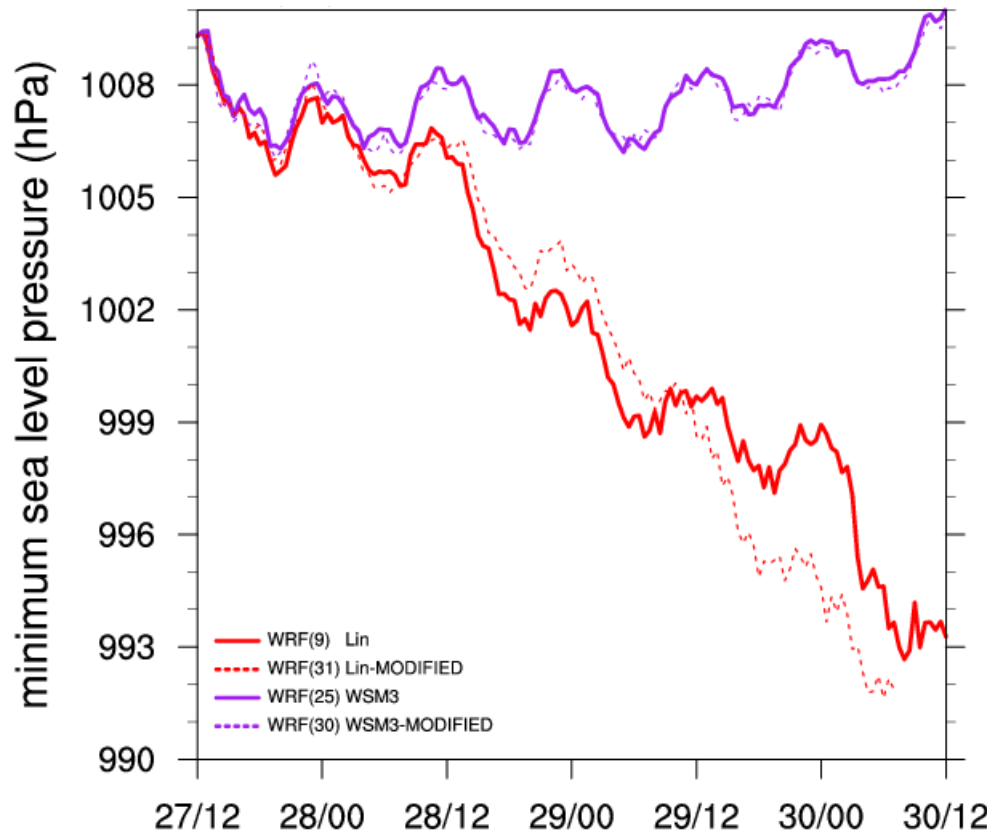


Figure 91 Minimum sea-level pressure (hPa) from simulation 25 (solid purple), simulation 25 except hydrometeor drag was reduced by 50% (dashed purple), simulation 9 (solid red), and simulation 9 except the graupel fall speed was reduced to match the WSM6 formulation (dashed red).

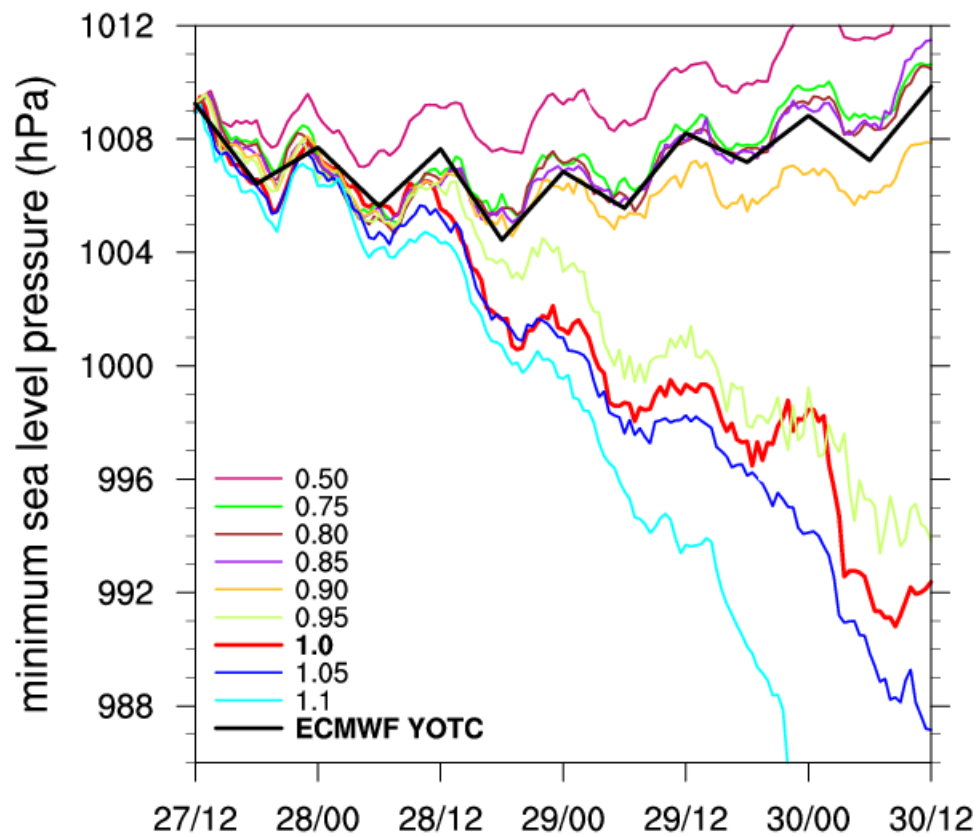


Figure 92 Minimum sea-level pressure (hPa) for simulations that used the Purdue Lin microphysics scheme in which the diabatic heating rate was multiplied by a factor ranging from 0.5 to 1.1. The minimum sea-level pressure from the ECMWF analysis (black) is shown for reference.

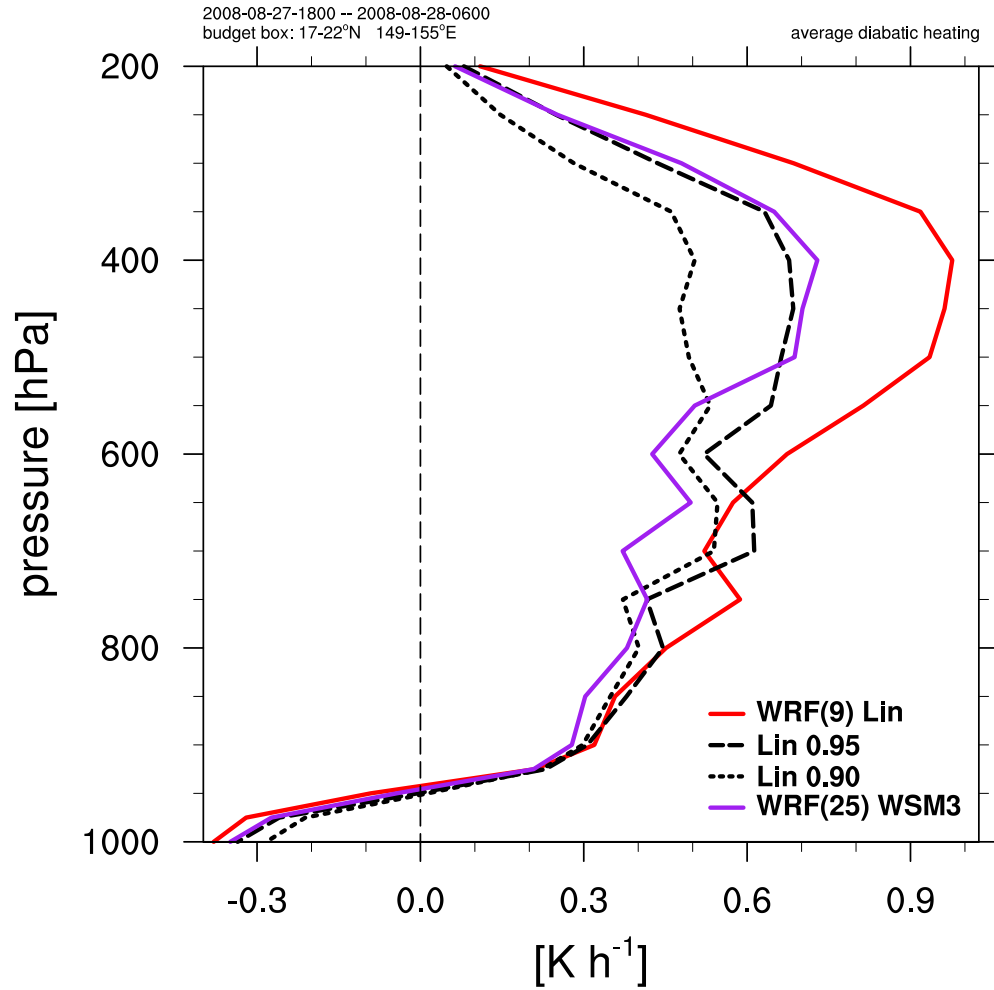


Figure 93 Vertical profiles of diabatic heating rate ( $\text{K h}^{-1}$ ) for simulation 9 (red line), simulation 25 (purple line), and for simulations that used the Purdue Lin microphysics scheme in which the diabatic heating rates were multiplied by a factor of 0.95 (long dashed line) and 0.90 (short dashed line).

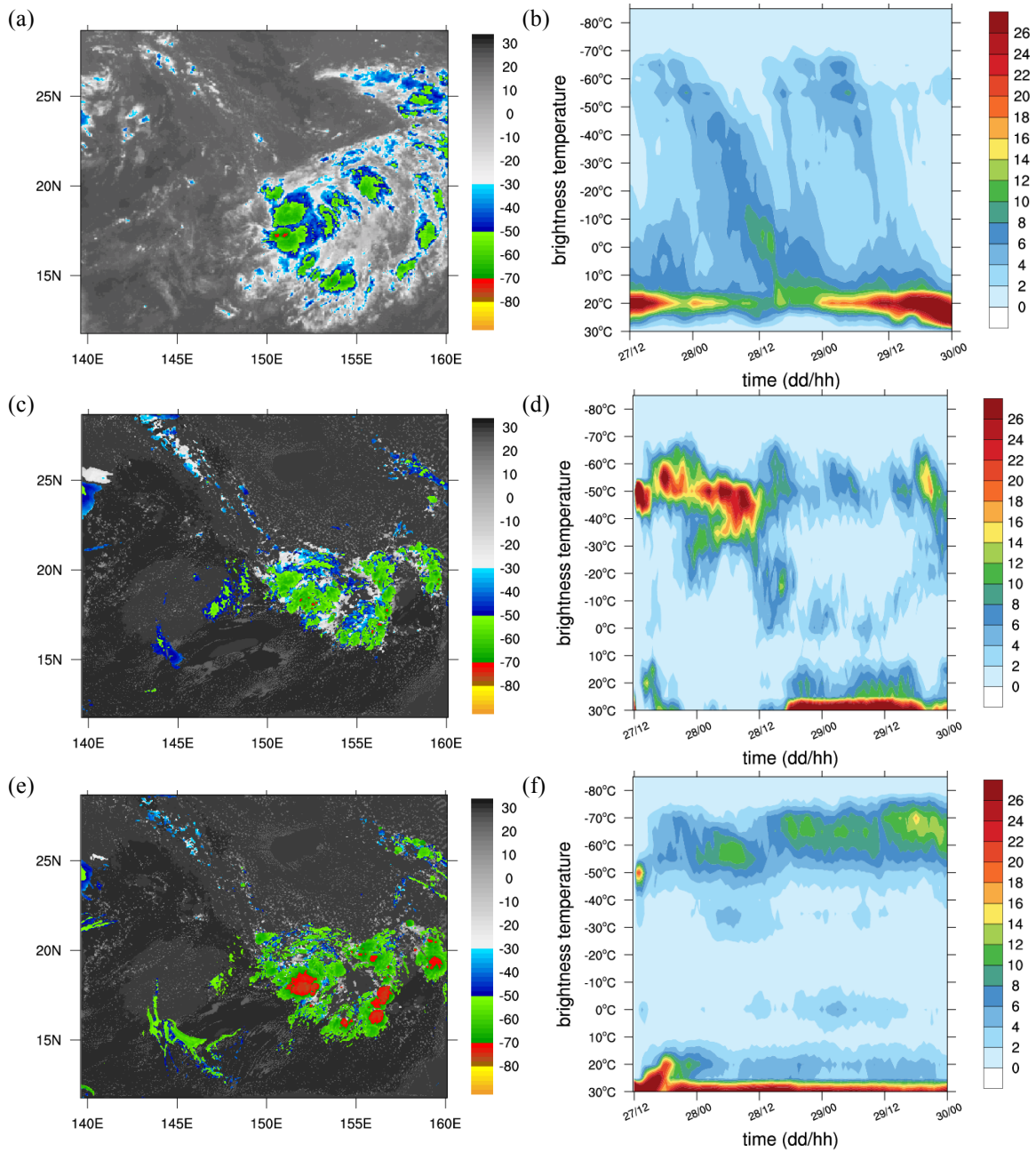


Figure 94 (a) MTSAT-IR brightness temperature (°C) at 2345 UTC 27 August and model-derived cloud-top brightness temperature at 0000 UTC 28 August from WRF simulations (c) 25 and (e) 9. Histograms as a function of time during the evolution of TCS025 of (b) MTSAT IR brightness temperature (°C) and of model-derived cloud-top brightness temperature (°C) from (d) WRF simulation 25 and (f) WRF simulation 9. Histograms were created by binning brightness temperature values within a  $\pm 3^\circ$  box of the respective center position for each case (see text).

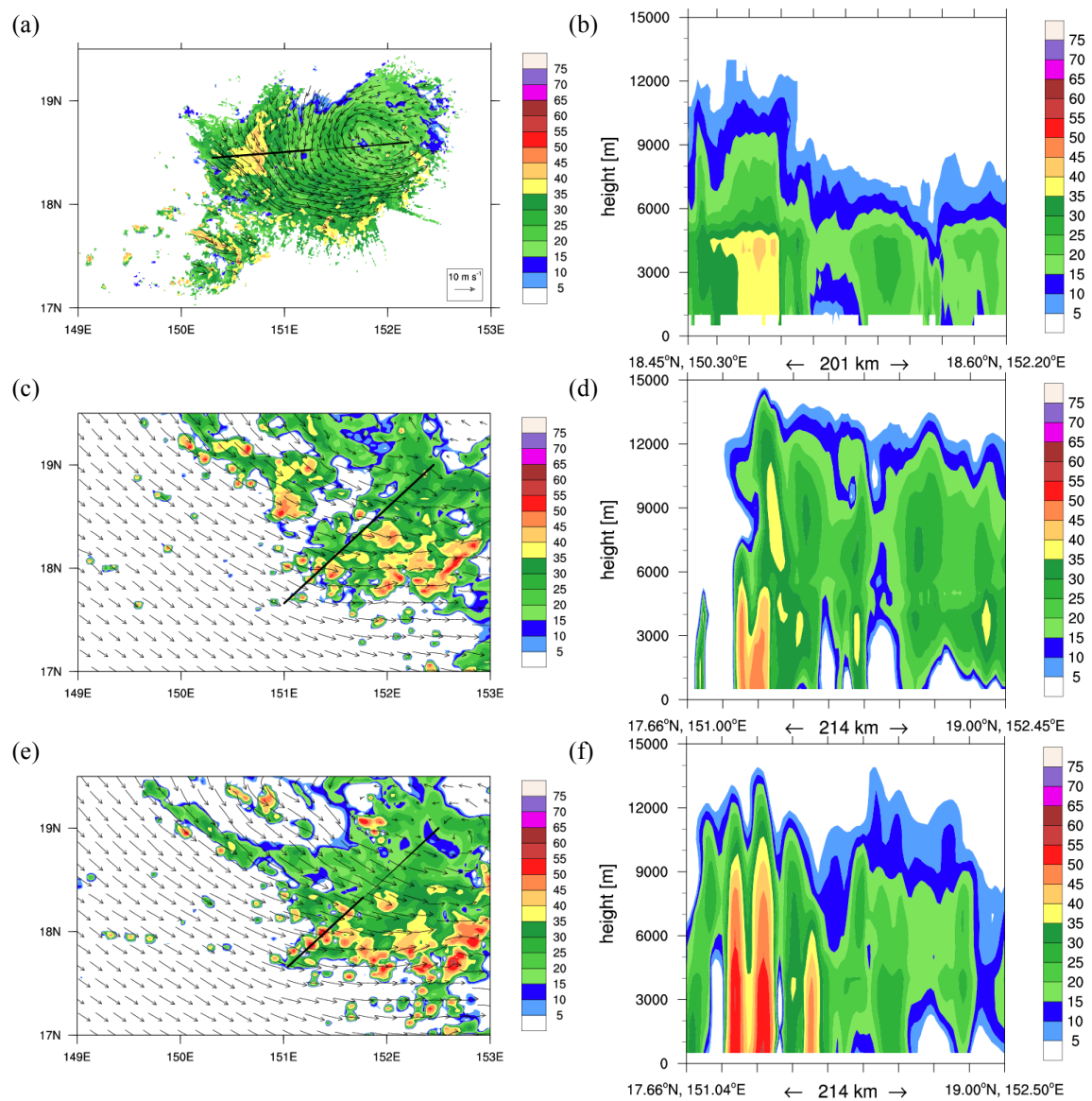


Figure 95 Left panels: reflectivity (dBZ, shading) and horizontal wind vectors ( $\text{m s}^{-1}$ ) at 4-km height from (a) the NRL P-3 ELDORA dual Doppler radar, (c) WRF simulation 25, and (e) WRF simulation 9 valid at 0000 UTC 28 August. Right panels: vertical cross-sections of reflectivity (dBZ, shading) for (b) the NRL P-3 ELDORA dual Doppler radar, (d) WRF simulation 25, and (f) WRF simulation 9. Cross-section locations for (b, d, and f) correspond to the black lines in (a, c, and e), respectively.

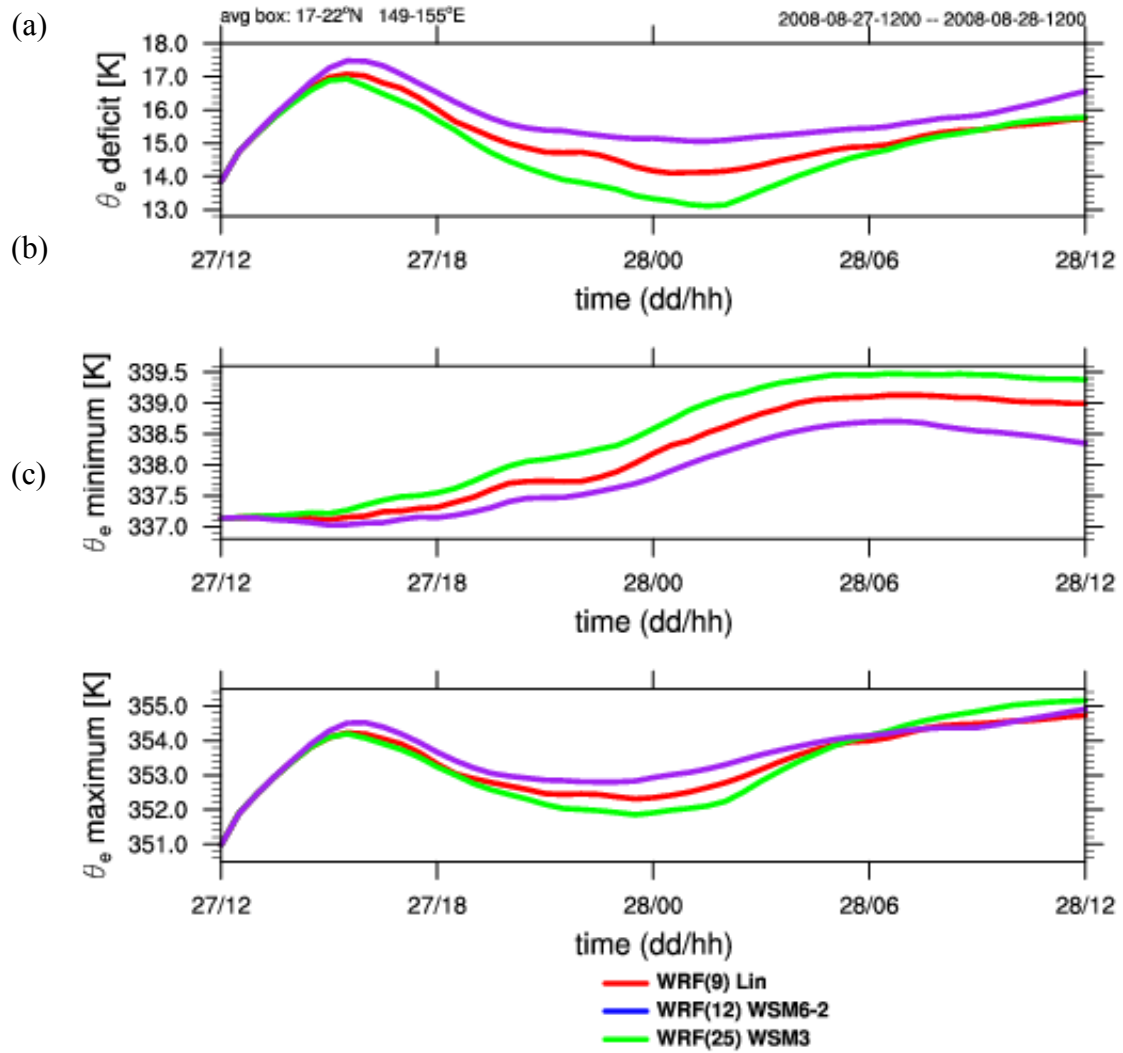


Figure 96 Average (a)  $\theta_e$  deficit (K), (b) mid-tropospheric  $\theta_e$  minimum, and (c) lower-tropospheric  $\theta_e$  maximum for the blue-boxed region in Figure 79 for WRF simulations 9 (red), 12 (green), and 25 (purple).

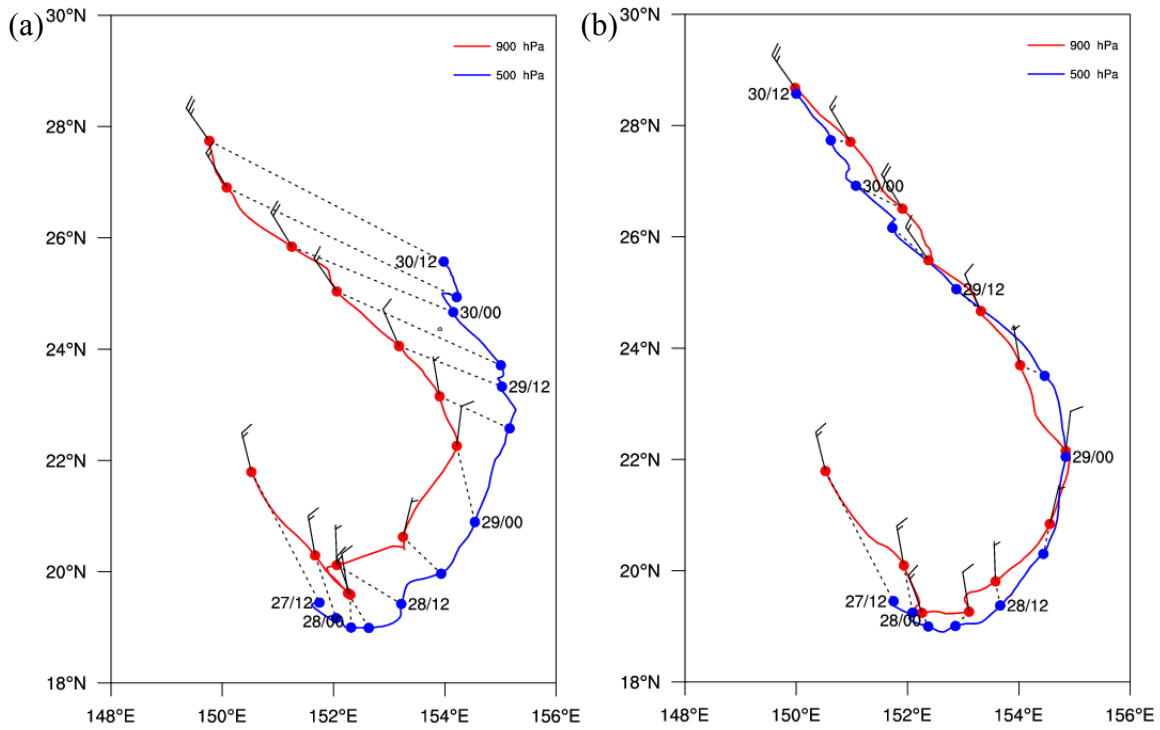


Figure 97 Potential vorticity centroid positions at 900 hPa (red) and 500 hPa (blue) for (a) WRF simulation 25 and (b) WRF simulation 9 from 1200 UTC 27 August to 1200 UTC 30 August. Red and blue dots indicate the PV centroid positions at 6 h intervals and are connected by dashed lines. Wind barbs correspond to the environmental vertical wind shear computed using the CFSR dataset (see Figure 35) (1 full barb = 10 kt).

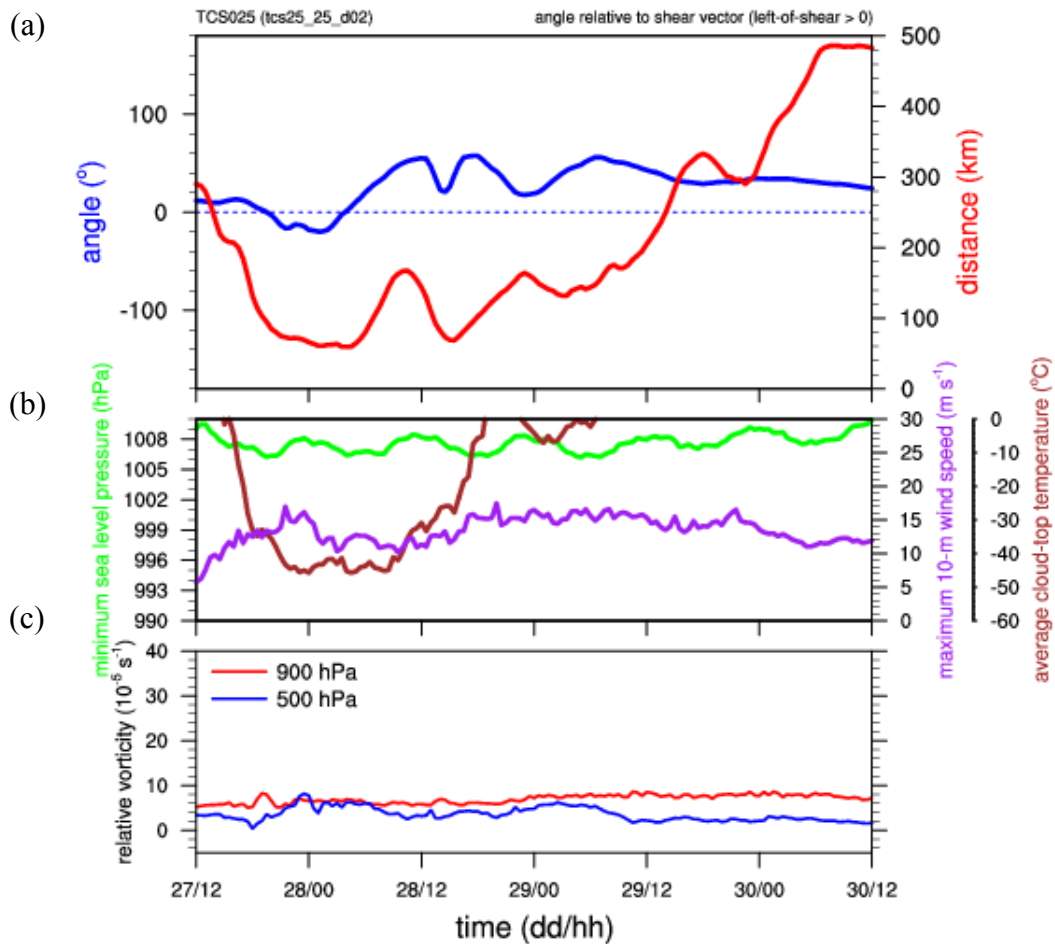


Figure 98 (a) Separation distance (km, red line) between the 900 hPa and 500 hPa PV centroid positions and the direction of vortex tilt (°, blue line) relative to the environmental vertical wind shear direction for WRF simulation 25. Positive angles correspond to a vortex tilt that is left of the shear vector. (b) Minimum sea-level pressure (hPa, green line), maximum 10-m wind speed (m s<sup>-1</sup>, purple line), and radially averaged (0-100 km) model-derived cloud-top brightness temperature (°C, brown line) for WRF simulation 25. (c) Radially averaged (0-100 km) relative vorticity (10<sup>-5</sup> s<sup>-1</sup>) at 900 hPa (red line) and 500 hPa (blue line) for WRF simulation 25.



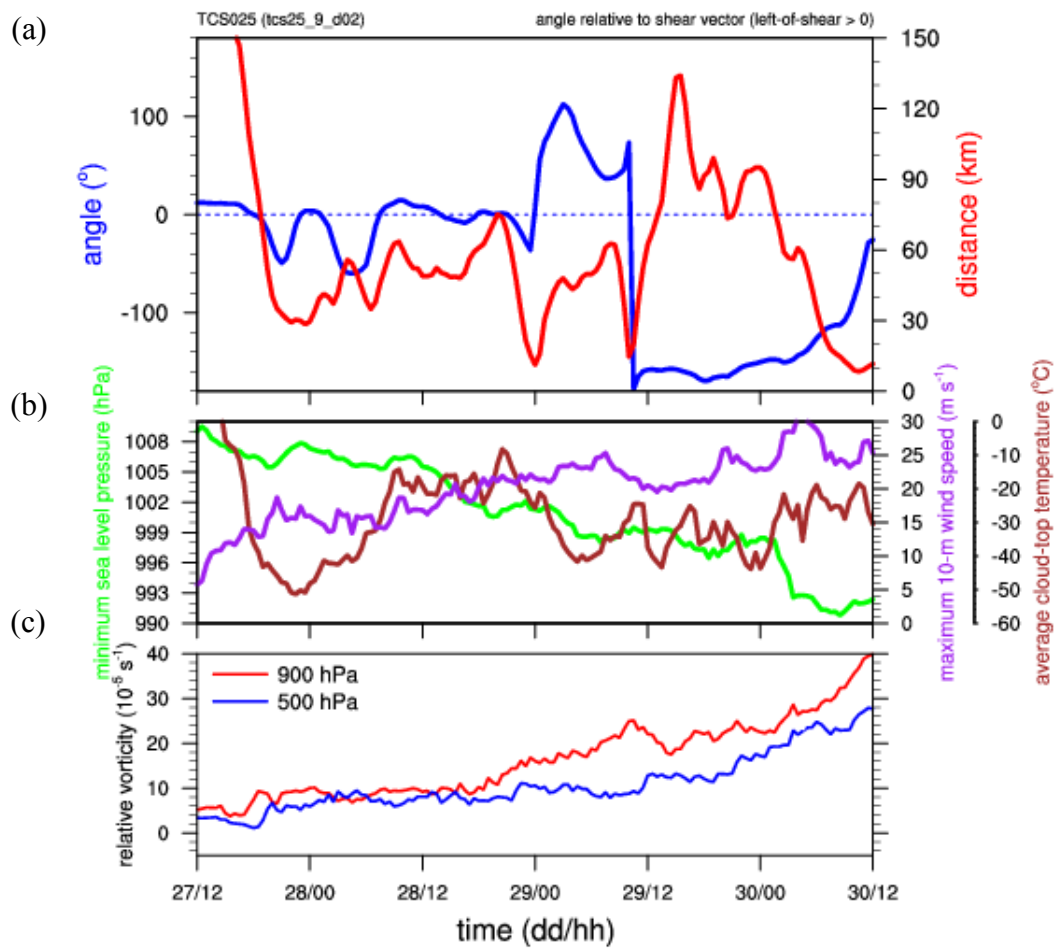


Figure 99 As in Figure 98, except for WRF simulation 9.

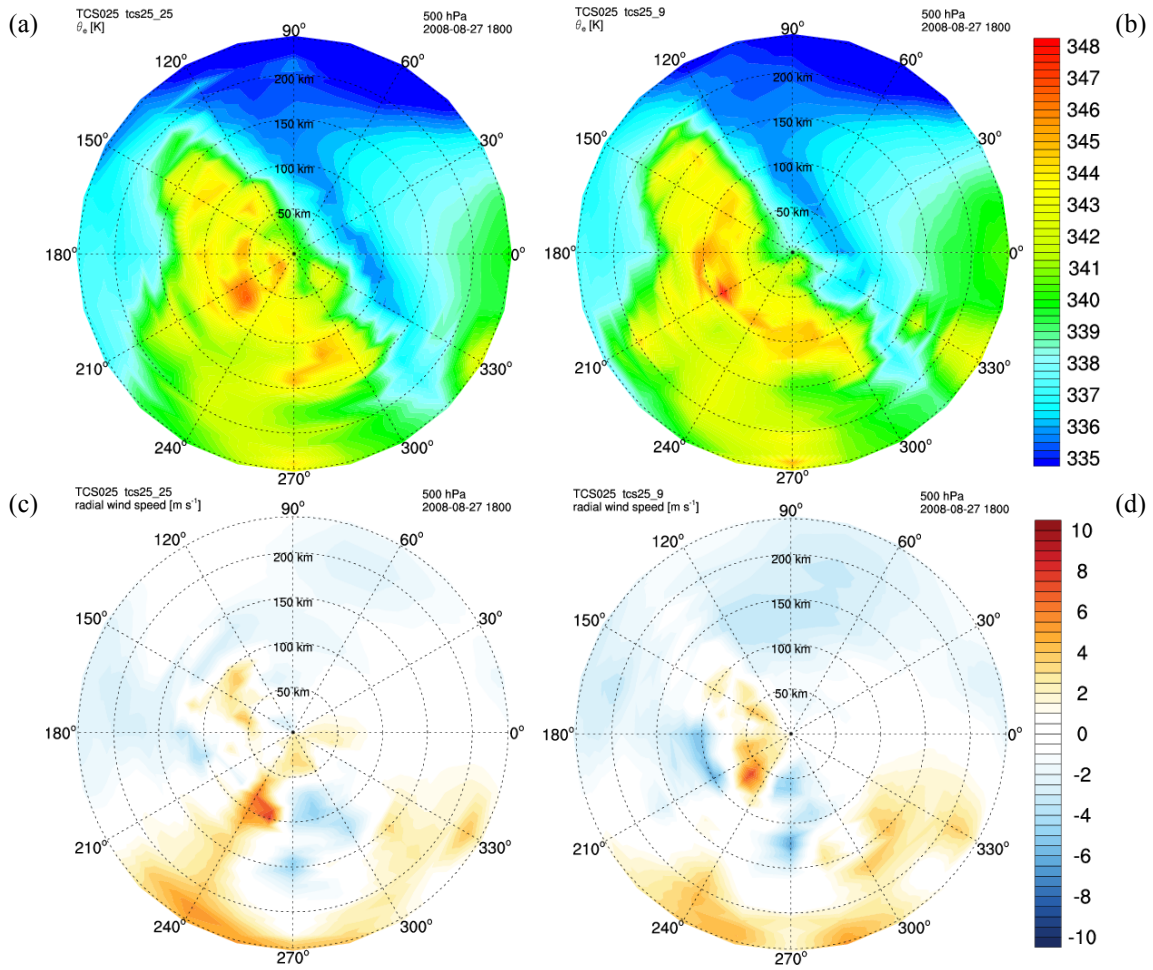


Figure 100 (a, b) Equivalent potential temperature (K) and (c, d) radial wind speed ( $\text{m s}^{-1}$ ) at 500 hPa in cylindrical coordinate form from (a, c) WRF simulation 25 and (b, d) WRF simulation 9 at 1800 UTC 27 August. Data were interpolated to cylindrical coordinates using the 900 hPa PV centroid positions. North corresponds to the azimuth of 90°, and dashed circles indicate range (km) from the center position.

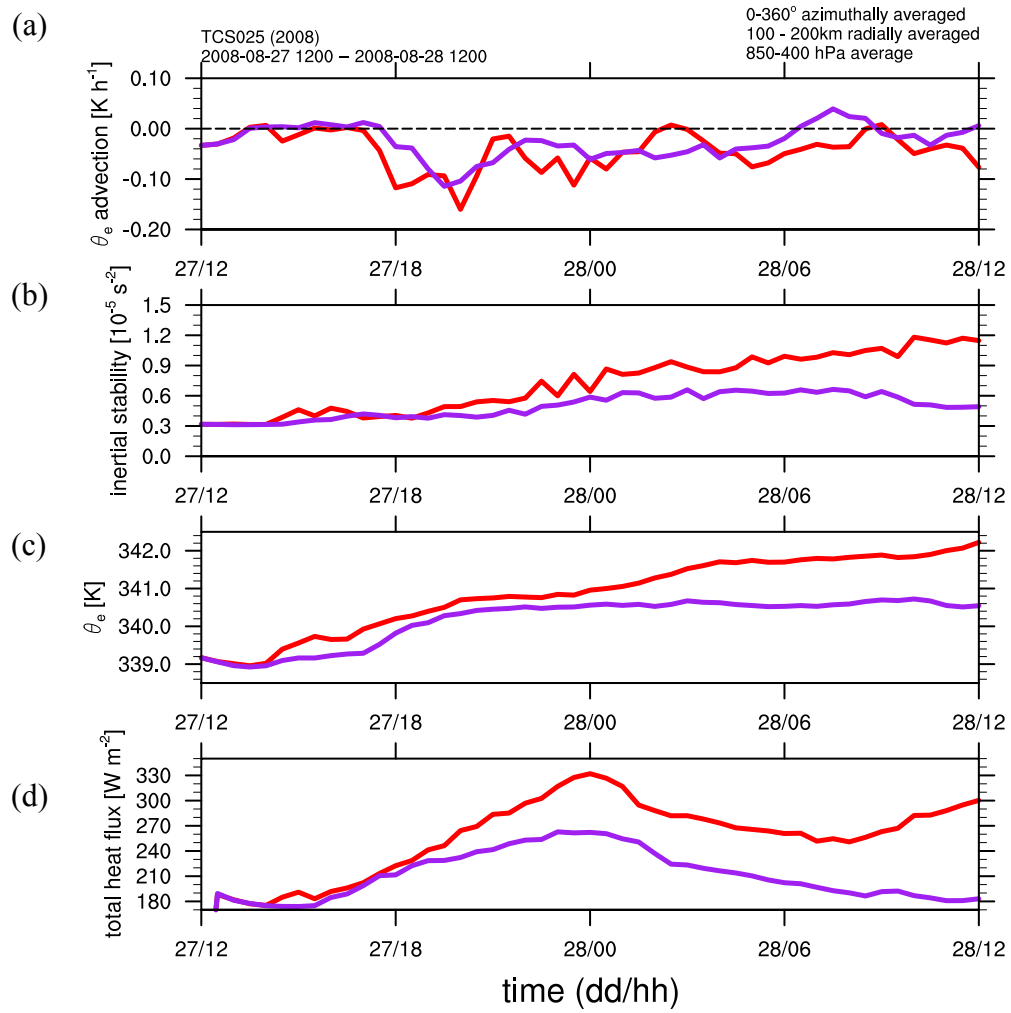


Figure 101 Time series of averaged (a)  $\theta_e$  advection by the radial wind ( $\text{K h}^{-1}$ ), (b) inertial stability ( $10^{-5} \text{ s}^{-2}$ ), (c)  $\theta_e$  (K), and (d) total heat flux (latent and sensible) from the surface ( $\text{W m}^{-2}$ ) for simulations 9 (red) and 25 (purple). Quantities were averaged azimuthally ( $0^\circ$ - $360^\circ$ ) and radially (100-200 km) from the 900 hPa PV centroid positions between the 850 hPa and 400 hPa isobaric surfaces.

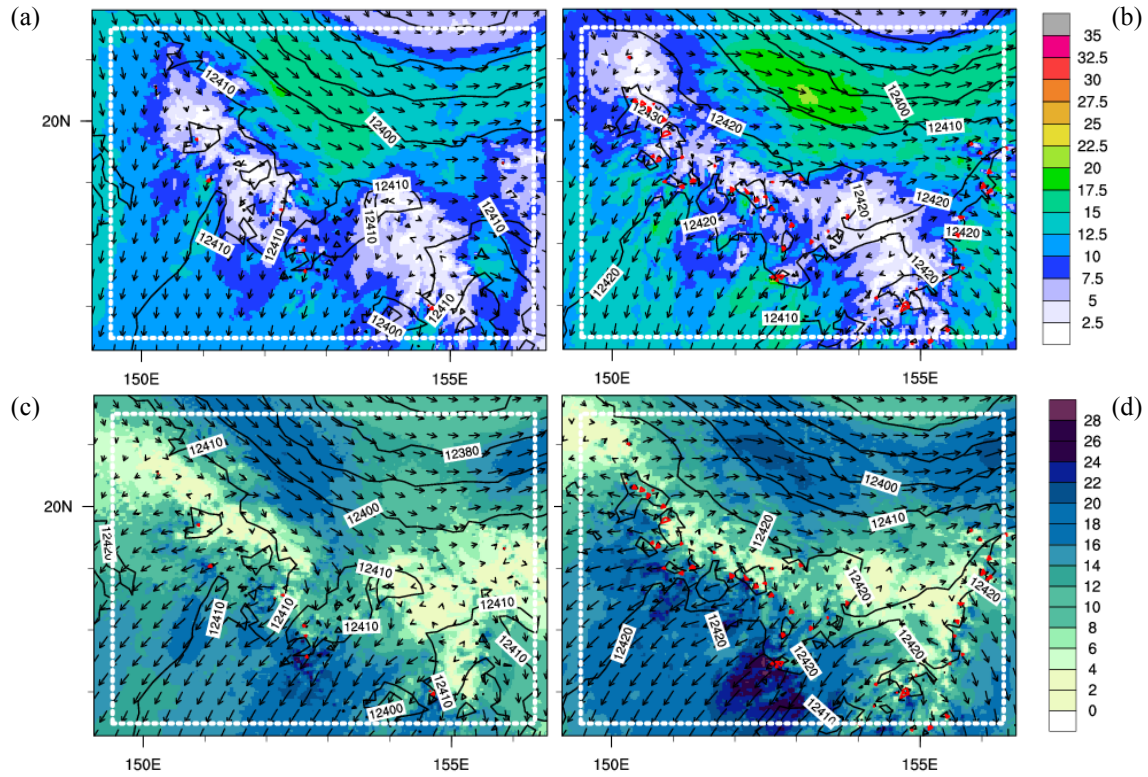


Figure 102 (a, b): Wind speed ( $\text{m s}^{-1}$ , shading), geopotential height (m, black contours), and vertical velocity ( $\text{m s}^{-1}$ , red contours with a  $5 \text{ m s}^{-1}$  contour interval) at 200 hPa at 2000 UTC 27 August for (a) WRF simulation 9 and (b) WRF simulation 25. (c, d): As in (a, b), except color shading represents the 200-850 hPa vertical wind shear ( $\text{m s}^{-1}$ ). The white-boxed area corresponds to the region where vertical wind shear was computed in Table 4 (see discussion in text).

	vertical wind shear of the average wind		average vertical wind shear	
	1800 UTC	2000 UTC	1800 UTC	2000 UTC
<b>simulation 25</b>	7.4 m s <sup>-1</sup> (14.3 kt)	6.5 m s <sup>-1</sup> (12.6 kt)	11.5 m s <sup>-1</sup> (22.4 kt)	11.8 m s <sup>-1</sup> (22.9 kt)
<b>simulation 9</b>	6.4 m s <sup>-1</sup> (12.4 kt)	5.0 m s <sup>-1</sup> (9.8 kt)	12.9 m s <sup>-1</sup> (25.2 kt)	14.0 m s <sup>-1</sup> (27.2 kt)

Table 4 Vertical wind shear values (200 hPa – 850 hPa) corresponding to the white-boxed regions in Figure 102 for WRF simulations 25 and 9 at 1800 UTC and 2000 UTC 27 August (see text for details).

THIS PAGE INTENTIONALLY LEFT BLANK

## V. DATA ASSIMILATION

Based on the operational analysis in Chapter III, it was concluded that misalignment of the circulation structure in the vertical in the presence of northerly vertical wind shear (see Figure 35) prevented the development of the TCS025 disturbance. Although episodes of deep convection were observed (see Figure 37 and Figure 38), the strength of the convective processes was not adequate to improve alignment and lead to formation. The WRF simulations initialized from the ECMWF analysis that over-developed the TCS025 disturbance exhibited stronger convective processes than observations suggested (see Figure 94 and Figure 95). Notable differences in circulation structure were evident between the SAMURAI analysis, which incorporated ELDORA dual-Doppler airborne radial velocities, and the ECMWF analysis that was used to initialize the multi-physics WRF simulations (see Figure 45 and Figure 48). Given these differences between the ECMWF and SAMURAI analyses, a possible explanation for the overly strong convective processes and their subsequent impacts on over-development in the WRF simulations was the aligned circulation structure present in the ECMWF analysis used as initial conditions. As a result, it was desirable to examine the impact of assimilating ELDORA radial velocity data. Therefore, the WRF-DART data assimilation system was used in addition to the multi-physics ensemble to gain further insight into the non-development of the TCS025 disturbance. A detailed description of the WRF-DART data assimilation system and the procedure used for this study is given in Chapter II.

Since the TCS025 circulation as observed by the ELDORA radar exhibited poor vertical alignment, the goal of the DART-WRF experiments was to examine whether data assimilation of ELDORA winds would reduce alignment, and whether a misaligned circulation would limit the intensity of the simulated convective precipitation processes and ultimately inhibit development of the TCS025 disturbance. It was hypothesized that the assimilation of ELDORA radial velocity data, which depicted a more realistic circulation structure, would reduce the intensity of the precipitation processes and result in a model solution that was more in line with observations.

## **A. ELDORA RADIAL VELOCITIES IMPACT ON CIRCULATION STRUCTURE**

During the first phase of the DART-WRF data assimilation (1200 UTC 27 – 0600 UTC 28 August), the majority of ensemble members exhibited the same oscillatory pattern in minimum sea-level pressure (Figure 103) as in the multi-physics ensemble and the ECMWF analysis (see Figure 71a). Perhaps due to smoothing in the DART-WRF ensemble mean (DWEM), the minimum sea-level pressure was slightly higher than the mean minimum sea-level pressure exhibited by the 96 ensemble members.

Since the DART-WRF ensemble employed the same microphysics scheme (Purdue Lin) as WRF simulation 9, simulation 9 was used as a point of comparison and is referred to as the control simulation in this section. At 0600 UTC 28 August, the minimum sea-level pressure of the DWEM and the control simulation were very similar (~1006 hPa) (Figure 103). However, there were notable differences in circulation structure. Whereas a well-developed circulation was evident at 5-km altitude in the control simulation and the DWEM (Figure 104 a,b), the vorticity in the control simulation was stronger and displaced northward relative to the DWEM. Perhaps most importantly, low-level vorticity in the DWEM was much weaker and the circulation did not appear to be closed as in the control simulation (Figure 104c,d).

Vertical cross sections of relative vorticity reveal a strong, vertically-aligned circulation was already present in the control simulation by 0600 UTC 28 August (Figure 105a). In contrast, the circulation structure depicted in the DWEM was misaligned in the vertical (Figure 105b). While the maximum relative vorticity in the DWEM was near 5-km altitude, a separate and much weaker low-level vorticity feature was displaced to the north (Figure 105b).

Qualitatively, the circulation structure in the DWEM was very similar to that exhibited by the SAMURAI analysis (see Figure 51b), but the vorticity magnitude was less in the DWEM due to smoothing associated with the ensemble mean (Figure 105b). In addition, the mid-level vorticity maximum in the SAMURAI analysis was at a higher altitude and the low-level vorticity feature was not displaced as far to the north as in the DWEM (see Figure 51b).



## B. DART-WRF ENSEMBLE MEAN FORECAST

To evaluate the impacts of the misaligned circulation structure in the DWEM, the WRF model was initialized from the DWEM and integrated from 0600 UTC 28 August to 1200 UTC 30 August without further data assimilation. This simulation was designated as the DART-WRF ensemble mean forecast (DWEMF) and the setup parameters for this simulation were identical to the control simulation. Similar to the control simulation, the DWEMF over-developed the TCS025 disturbance (Figure 103). However, development was delayed by about 24 h relative to the control simulation, and the storm was not as intense by the end of the simulation.

The large-scale synoptic features (Figure 106) in the DWEMF at initialization time (0600 UTC 28 August) were very similar to the conditions in the control simulation (see Figure 73b,d). The wind speed magnitude was largest along the eastern side of the low-level trough (Figure 106b) and weak anticyclonic flow was present at 200 hPa to the southeast of the TUTT near 152°E, 22°N (Figure 106a). The position of the TUTT was slightly to the west of the 0000 UTC 28 August position in the control simulation (see Figure 73b).

A limitation of initializing the DWEMF from the DWEM was that the ensemble mean appeared much smoother than individual ensemble members or the control simulation. In addition, the mean state of the ensemble was not necessarily a physical or balanced state, so there was some concern that there would be a model adjustment period. However, this did not seem to be an issue as there were no noticeable numerical artifacts early in the DWEMF.

As previously shown, the mid-level vorticity feature associated with the TCS025 disturbance in the DWEMF was weaker and more diffuse at 0600 UTC 28 August than that exhibited by the control simulation, and the vorticity below 850 hPa was exceptionally weak (Figure 106c). One can infer from the vertical cross section of  $\theta_e$  (Figure 106d) that the convective processes had not been as active during the DART-WRF data assimilation compared to the control simulation (see Figure 74d), as there was less high- $\theta_e$  air present in the mid- and upper-levels and less low- $\theta_e$  air near the surface

in the DWEMF. Additionally, the magnitudes of the virtual temperature perturbations in the surface layer were larger in the DWEMF (Figure 106d), which indicates that there had been less evaporative cooling.

After 18 h (0000 UTC 29 August), some similarities with the control simulation were evident. The wind speeds along the eastern side of the low-level circulation had increased considerably (Figure 107b) and the upper-level outflow emanating from the convective area had strengthened (Figure 107a). However, both the low-level circulation and upper-level outflow were much stronger in the control simulation at 0000 UTC 29 August (see Figure 75b, d). Relative vorticity (Figure 107c) had increased near the surface and mid- and upper-level  $\theta_e$  (Figure 107d) had also increased relative to 18 h earlier.

By 0000 UTC 30 August, the low-level circulation was beginning to form a closed circulation (Figure 108b) and the upper-level outflow had continued to strengthen (Figure 108a). The structure of the upper- and low-level flow appeared qualitatively very similar to the control simulation at 0000 UTC 30 August (see Figure 77b,d). However, the vertical cross-section of relative vorticity from the DWEMF at 0000 UTC 30 August (Figure 108c) reveals that relative vorticity associated with the TCS025 disturbance was relatively disorganized and much weaker than in the control simulation even 24 h earlier at 0000 UTC 29 August (see Figure 76b). This suggests the circulation had not fully consolidated into a single vertically-coherent structure by this time. The cross section of  $\theta_e$  (Figure 108d) reveals that  $\theta_e$  had increased throughout the column and that a positive virtual temperature anomaly dominated the mid-troposphere. However, similar to the vorticity, the plume of high- $\theta_e$  air was sharply tilted toward the north with height. An analysis of the low- and mid-level PV-weighted center positions reveals that the mid-level vorticity rotated around to the north of the low-level vorticity center after 1200 UTC 29 August (see Figure 112).

The synoptic comparison between the DWEMF and the control simulation indicates that almost immediately after the DWEMF was initialized from the improved initial conditions provided by the DWEM, the model solution followed the same pathway

of development that was exhibited by the control simulation. The low-level wind field and upper-level outflow became progressively stronger while the vorticity associated with the TCS025 disturbance increased in intensity, especially in the low-levels. By 0000 UTC 30 August, the minimum sea-level pressure had declined considerably, but was not as low as in the control simulation (see Figure 103). The fact that the vertical structure of vorticity in the DWEMF was still disorganized at 0000 UTC 30 August suggests that initializing the WRF model with the misaligned circulation structure derived from the airborne ELDORA radar data helped to delay and ultimately limit development.

### **C. VORTICITY EVOLUTION COMPARISON**

To provide context for the following circulation budget comparison of the DWEMF and the control simulation, a sequence of low-level relative vorticity figures were constructed for the DWEMF (Figure 110) and the control simulation (Figure 109) that highlight the consolidation and development of the low-level circulation in each case. An additional set of figures was constructed for the non-developing WRF simulation 25 to provide for another source of comparison (Figure 111).

At 1200 UTC 28 August, the control simulation (Figure 109) possessed a tighter circulation and stronger vorticity near the main low-level circulation center near 19°N, 153°E than in the DWEMF and simulation 25. In addition, the vorticity was also much stronger to the northeast of the main circulation center. This area of vorticity eventually wrapped around the main circulation and was absorbed by 1200 UTC 29 August. In general, the evolution of the low-level flow and spin-up in the DWEMF was similar to that exhibited by the control simulation, but development did not occur as quickly.

The low-level vorticity for the non-developing WRF simulation 25 (Figure 111) appeared to reach its best stage of organization between 1200 UTC 29 August and 0000 UTC 30 August, however the individual vorticity elements were noticeably weaker than in the control simulation and the DWEMF. By 1200 UTC 30 August, the low-level circulation in the non-developing simulation was no longer closed but instead was an open wave. Although the magnitude of low-level vorticity and circulation structure in the non-developing simulation 25 were similar to those in the DWEMF at 1200 UTC 28

August, the intensity and number of low-level vorticity anomalies along the eastern side of the low-level circulation were considerably less in simulation 25 than in the DWEMF by 0000 UTC 29 August. This indicates that the vorticity generation processes were much stronger in the DWEMF compared to the non-developing WRF simulation 25, both near and away from the low-level circulation center.

#### **D. CIRCULATION RE-ALIGNMENT IN THE DWEMF**

The 900 hPa and 500 hPa PV-weighted center positions (Figure 112), separation distance, and tilt orientation with respect to the environmental vertical wind shear vector (Figure 113) were also computed for the DWEMF in a similar manner to that employed for simulation 9 (control simulation) and simulation 25 (see Figure 97, Figure 98, and Figure 99).

Not surprisingly, there was a large separation distance between the 900 hPa and 500 hPa PV center positions at the initialization time (0600 UTC 28 August) (Figure 112 and Figure 113a). The initial separation distance in the DWEMF was greater than might be expected from Figure 104b,d and Figure 105b as a result of the method by which the PV-weighted centers were computed (see Appendix C). By 1800 UTC 28 August, the separation distance declined temporarily (Figure 113a), but increased again as the low- and mid-level circulations translated rapidly to the northwest (Figure 112). The separation distance between the low- and mid-level PV centers in the control simulation was not as large during the time when the TCS025 system began translating to the northwest (Figure 97b), perhaps as a result of the stronger coupling between the low- and mid-level circulations. Shortly after 1200 UTC 29 August and continuing to the end of the simulation, the separation distance in the DWEMF began to decline when the 500 hPa center became positioned to the north of the 900 hPa center. Although alignment in the DWEMF improved by the end of the simulation, the circulation in the DWEMF did not reach the same degree of alignment as in the control simulation.

The orientation of the tilt angle relative to the environmental vertical wind shear vector (Figure 113a) followed a similar evolution as in the control simulation. Early in the DWEMF, the orientation angle was generally close to  $0^\circ$  (down-shear), but as the

circulation intensified, the tilt angle orientation became increasingly left-of-shear. By the end of the simulation the mid-level circulation had rotated to the north of the low-level circulation such that the tilt orientation was up-shear before becoming slightly right-of-shear.

Based on the average model-derived cloud-top temperature for the DWEMF (Figure 113b), the intensity of the convection in the DWEMF was less than that exhibited by the control simulation (see Figure 99b). Other measures such as the box-averaged quantities to be discussed in Figure 116 imply the convection in the DWEMF was just as strong as in the control simulation, if not stronger. This is perhaps an example of a limitation of using model-derived cloud-top temperature to characterize convective intensity. As in the control simulation, the immediate correlation between average model-derived cloud-top temperature (Figure 113b) and separation distance (Figure 113a) for the DWEMF was poor. Although there was not an immediate response of increased alignment during periods of active deep convection and substantial fluctuations in the separation distance occurred, there was an overall trend of increasing alignment in the DWEMF throughout the course of the simulation.

Based on the conclusions from the alignment comparison between simulations 9 and 25 and the alignment analysis of the DWEMF, the presence of convection was important for circulation alignment. These comparisons as in Figure 112 and Figure 113 indicate the alignment process was complex and other factors such as environmental influences and the strength and organization of the disturbance at the time of the convective episodes also likely impacted the alignment response.

#### **E. CIRCULATION BUDGET: PURPLE-BOXED REGION: 1200 UTC 28 AUGUST – 1800 UTC 28 AUGUST**

Circulation budgets were calculated from 1200 UTC 28 August to 1800 UTC August (see purple-boxed regions in Figure 109 and Figure 110) for the control simulation (Figure 114) and the DWEMF (Figure 115). Commencing the circulation budget six hours after the DWEMF was initialized was done to minimize any spin-up issues that might have been caused by imbalances in the DWEM fields. During this

period, the main vorticity feature associated with the low-level circulation was translating to the northeast while additional vorticity elements were being advected into the eastern side of the box (see Figure 109 and Figure 110). Due to the increasing translation speed of the TCS025 disturbance, the advection of vorticity into and out of the boxed area caused the horizontal eddy fluxes to become increasingly large such that the contributions from other processes were obscured as the circulation consolidated. As a result, the circulation budget was limited in duration to six hours ending at 1800 UTC 28 August. Eddy fluxes became overly dominant after this time such that the effect of the other processes was obscured.

In the control simulation, the box-average vorticity was a maximum just above 700 hPa (Figure 114a), whereas in the DWEMF, the box-average vorticity maximum was slightly below 700 hPa (Figure 115a). Between 1200 UTC 28 August and 1800 UTC 28 August, the vorticity tendency was predominantly positive below 500 hPa in the control simulation (Figure 114b) and in the DWEMF (Figure 115b), but was negative in the upper-levels. The magnitudes of the positive vorticity tendencies below 500 hPa were larger in the control simulation, while the negative upper-levels tendencies were larger in the DWEMF.

The circulation tendency due to stretching was very similar in the DWEMF (Figure 115c) and control simulation (Figure 114c). Positive tendencies dominated the low- and mid-levels while negative tendencies were present above this. Note that the positive tendencies due to stretching extended up to a higher level in the control simulation and the negative tendencies in the upper-levels were slightly stronger.

The largest differences in circulation tendency appear to have been due to the contribution from eddy fluxes. In general, the horizontal eddy fluxes contributed negatively to the circulation tendency in the DWEMF (Figure 115d), whereas the horizontal eddy fluxes were mostly a positive factor in the control simulation (Figure 114d), except for a portion of the profile near 350 hPa.

Both simulations had a similar vertical and temporal distribution of the tilting contribution to the circulation tendency (Figure 114e and Figure 115e). Positive

contributions were present near the surface and above 550 hPa, with a shallow region of negative tendencies centered near 700 hPa.

Vertical profiles of the integrated circulation budget tendencies for the purple-boxed region from 1200 UTC 28 August to 1800 UTC 28 August are shown in Figure 114f and Figure 115f. For the control simulation, the largest positive contribution in the low-levels was due to vertical stretching (Figure 114f). The integrated effect of stretching was strongly positive below 400 hPa, but negative above this level. Between 500 hPa and 900 hPa, positive contributions from the horizontal eddy fluxes were even larger than stretching, primarily because of positive vorticity anomalies being advected into the eastern side of the box (see Figure 109). While the contribution from tilting was positive above 600 hPa, below this level, the tilting contribution was negligible. There was a larger residual component below 900 hPa than was calculated for the blue-boxed circulation budget (see Figure 82f) since the low-level wind speeds were stronger by this time, which resulted in greater friction spin-down. In summary, the integrated circulation tendency over this time period in the control simulation was a maximum near 600 hPa due to the combination of stretching and eddy fluxes.

In the DWEMF, the positive contribution from stretching was larger near the surface than in the control simulation (Figure 115f), but this stretching contribution did not extend as high into the troposphere as it did in the control simulation. The most striking difference in the DWEMF during this time was the slightly negative contribution from horizontal eddy fluxes, which was due to differences in the orientation of the low-level circulation relative to the budget box. Whereas vorticity was being primarily advected out of the eastern side of the box in the DWEMF, the low-level circulation in the control simulation was undergoing more consolidation during this period (see Figure 109 and Figure 110). In addition, the vorticity anomalies entering the budget region in the control simulation were much stronger. The reason for the fairly large positive residual above 900 hPa in the circulation budget for the DWEMF is not immediately evident.

The circulation budget comparison between the DWEMF and the control simulation reveals that the processes contributing to vorticity generation were generally similar. Since the contribution from the vertical stretching of relative vorticity was

consistently positive in the low- and mid-troposphere within the boxed-region, the vorticity anomalies along the periphery of the budget box were most likely generated or amplified through vertical stretching processes outside of the budget box area. Thus, it is reasonable to conclude that the vertical stretching of relative vorticity was the most consistent factor modulating the strength of the low-level circulation for the two cases. Even though the mid- and low-level circulations were misaligned in the initial conditions for the DWEMF, the overall circulation evolved similarly to the control simulation, which suggests that strong convective processes were a major factor in both simulations.

**F. AVERAGE PROFILES: PURPLE-BOXED REGION: 1200 UTC 28 AUGUST – 1800 UTC 28 AUGUST**

A comparison of averaged quantities within the purple-boxed region for the time period from 1200 UTC 28 August to 1800 UTC 28 August (Figure 116) also suggests the nature of the precipitation processes in the DWEMF were very similar to that in the control simulation. Similar calculations are provided for the moderate developing WRF simulation 12, the non-developing WRF simulation 25, and the DWEM, which was still undergoing data assimilation during this period.

Below 500 hPa, the magnitude of average vertical velocity (Figure 116a) was largest in the DWEMF compared to the other cases, and the vertical velocity profile in the DWEMF was most similar to the control simulation, which possessed the strongest average vertical velocity near 300 hPa. The average vertical velocity magnitude in the DWEM was less than in WRF simulation 12, but greater than in the non-developing WRF simulation 25.

The box-average diabatic heating rate (Figure 116b) was slightly larger in the DWEMF compared to the control simulation. Based on these diabatic heating and vertical velocity profiles, one can infer that convection was slightly stronger during this period in the DWEMF than in the control simulation.

The relative magnitudes of the average precipitation rates within the purple-boxed region (Figure 116c) are consistent with the vertical velocity and diabatic heating rates. Specifically, the precipitation rates in the control simulation and in the DWEMF were very



similar. The control simulation exhibited the largest average precipitation rates until about 1500 UTC 28 August, and then the largest rates were in the DWEMF. As expected from the vertical velocity and diabatic heating rates, the precipitation rates were smaller for the WRF simulations 12 and 25. Box-average precipitation rate estimates from TRMM indicate that the precipitation rates in the model simulations were generally too large within this region during the first 12 h, however, the model precipitation rates were in better agreement with the TRMM values from 1800 UTC 28 August to 0600 UTC 29 August.

Low-level convergence was slightly larger in the DWEMF compared to the control simulation (Figure 116d). The control simulation and simulations 12 and 25 all exhibited a secondary convergence maximum near 600 hPa. This secondary maximum was also evident in the DWEM and DWEMF, but was not as prominent. Divergence was present above 400 hPa in all profiles, with the largest divergence in the control simulation and WRF simulation 12.

As expected, box-average relative vorticity (Figure 116e) was largest in the control simulation below 600 hPa. Between 600 hPa and 400 hPa, the control simulation and WRF simulation 12 had very similar vorticity magnitudes that were larger than in the other simulations. The non-developing simulation 25 exhibited the smallest box-average vorticity below 600 hPa, but had a very similar profile to the DWEM and DWEMF cases above this level. The DWEM and DWEMF vorticity profiles were almost identical except the average vorticity in the DWEMF was slightly stronger below 800 hPa. As was inferred from the circulation budget analysis, the convective precipitation processes in the DWEMF likely contributed to the amplification of low-level relative vorticity relative to the DWEM.

The magnitude of mid-level ( $\sim 500$  hPa)  $\theta_e$  (Figure 116f) was largest for WRF simulation 12, followed by the control simulation, DWEMF, DWEM, and the non-developing simulation 25. Although the convective processes in simulation 12 were not as strong as in the control simulation, the microphysical processes were evidently more effective at increasing mid-level  $\theta_e$  in simulation 12. The highest values of low-level  $\theta_e$  were in the DWEM, but the differences among the various cases in  $\theta_e$  near the surface

were not nearly as large as they were in the mid-levels. While convective processes were most effective at increasing mid-level  $\theta_e$  in simulation 12 and the control simulation, these simulations had the smallest  $\theta_e$  values near the surface, which is an indication of convective overturning redistributing  $\theta_e$  within the atmospheric column.

## **G. ENSEMBLE FORECASTS**

### **1. 0600 UTC 28 August – 1200 UTC 30 August**

In addition to the DWEMF, the full WRF ensemble was also integrated in forecast mode (no data assimilation) for two initial times; 0600 UTC 28 August (after the first ELDORA flight), and 0600 UTC 29 August (after the second ELDORA flight). Based on minimum sea-level pressure (Figure 117), the majority of the ensemble members exhibited some development of the TCS025 system, however the average minimum sea-level pressure of the ensemble did not decline as much as in the control simulation.

There was a large spread in the tracks based on the minimum sea-level pressure positions of the ensemble forecast members (Figure 118). The mean track was offset to the west of the control simulation track. The colors of the ensemble member tracks are grouped according to the minimum sea-level pressure at 1200 UTC 30 August (Figure 118). Ensemble member forecasts that exhibited development of the TCS025 disturbance had tracks that were generally to the east of the members that only experienced moderate or no development. The same pattern was observed in the multi-physics ensemble (see Figure 72).

For the cases in which very little development occurred, it was common for the circulation associated with the TCS025 disturbance to be absorbed by the large-scale trough to the west (not shown). As a result, these ensemble members followed tracks farther to the west. Based on the strong interaction with this trough for ensemble members with weak circulations, it may indicate that the tracks were predominantly determined by the strength of the modeled TCS025 circulations rather than the environmental conditions along the track. However, further study is needed to clarify the reasons for the ensemble track differences.

This suggests that the ensemble members that followed a trajectory farther to the east were stronger, and as a result, less likely to be absorbed by the trough to the west. In general, the ensemble forecast tracks were quite similar, so it's unlikely that the environmental conditions along the eastern tracks were more favorable for development (i.e., rather than the track modulating intensity, the strength of the modeled TCS025 disturbance tended to determine the track).

## **2. 0600 UTC 29 August – 1200 UTC 30 August**

The second ensemble forecast initiated after the second ELDORA flight at 0600 UTC 29 August was integrated to 1200 UTC 30 August (Figure 119). Two modes of intensity change existed: while the majority of the ensemble members did not develop the TCS025 disturbance, a few members experienced significant development. For those members that had already developed by this time, the tendency was to weaken somewhat during this period. The mean of the ensemble minimum sea-level pressure remained relatively unchanged through the end of the forecast.

## **H. DATA ASSIMILATION DISCUSSION AND SUMMARY**

Based on the observational analysis, and specifically the ELDORA radar radial velocities that were used to construct a SAMURAI analysis, it was determined that the circulation structure of the TCS025 disturbance was not vertically aligned (see Figure 48a). However, the ECMWF analysis, which was used to initialize the multi-physics ensemble, possessed an unrealistically strong low-level circulation that was well aligned vertically with the mid-level circulation (see Figure 48b). Additionally, the representation of convective precipitation processes in the high-resolution simulation 9 (Purdue Lin microphysics scheme) led to vertical alignment and intensification of TCS025. Therefore, the DART-WRF system was employed to assimilate data collected during the second and third IOPs, specifically ELDORA Doppler radar data, with the objective of improving initial conditions and assessing the role of vertical alignment in the non-development of TCS025.

The analyzed minimum sea-level pressure of the DART-WRF ensemble mean (DWEM) closely matched the minimum sea-level pressure of the ECMWF analysis (see

Figure 103) until near the end of the data assimilation period (0600 UTC 29 August). After the first ELDORA-equipped NRL P-3 flight at 0600 UTC 28 August, the circulation structure in the DWEM was similar to the SAMURAI analysis (see Figure 104 and Figure 105), except that the vorticity field was much smoother in the DWEM, which is expected of the ensemble mean. Relative to the control simulation (WRF simulation 9), the mid-level vorticity maximum was displaced farther south of the low-level vorticity maximum, which was also much weaker and diffuse.

The DART-WRF ensemble mean forecast (DWEMF) was integrated to 1200 UTC 30 August starting from the state of the DWEM at 0600 UTC 28 August. Similar to the control simulation, the DWEMF also over-developed the TCS025 disturbance, however development was delayed by about 24 h relative to the control simulation (see Figure 103). This over-development occurred even though the low-level vorticity in the DWEMF (see Figure 110) was very similar in magnitude to that exhibited by the non-developing simulation 25 (see Figure 111) at 1200 UTC 28 August (6 h after initialization of the DWEMF).

Similar to the evolution in the control simulation, the DWEMF exhibited a decrease in the 850 hPa geopotential height and a strengthening of the upper-level anticyclone and outflow near areas of active deep convection. However, vertical cross sections of vorticity and  $\theta_e$  at 0000 UTC 30 August (see Figure 108c,d) reveal that the circulation in the DWEMF was relatively disorganized and still misaligned in the vertical relative to the circulation in the control simulation, which was already vertically aligned from the surface to high in the troposphere by 0000 UTC 29 August.

A circulation budget calculated from 1200 UTC to 1800 UTC 28 August for the DWEMF and control simulation revealed that the vertical stretching of vorticity was the primary mechanism by which low-level vorticity increased in both simulations. The low-level positive circulation tendency due to stretching was actually stronger in the DWEMF. Due to the increasing translation speed of the TCS025 disturbance at this time, positive contributions from horizontal eddy fluxes became increasingly important in the control simulation, but were small and negative in the DWEMF. This difference appears

to have been due to differences in the orientation of the circulations with respect to the budget box. As the circulation in the control simulation consolidated, areas of positive vorticity entered the boxed region and contributed to low-level spin-up (see Figure 109). This process also occurred for the DWEMF, but was slightly delayed. This indicates that areas of convectively-generated low-level vorticity, which were initially displaced away from the center, later consolidated with the low-level circulation and contributed to spin-up.

Although the misalignment of the circulation in the DWEMF was initially large and the separation distance between the low- and mid-level centers fluctuated as the system evolved (Figure 113a), there was nearly continuous convection present near the low-level circulation, and this resulted in an overall trend of increasing alignment. However, the separation distance between the 900 hPa and 500 hPa PV-weighted center positions at the end of the simulation was considerably larger than in the control simulation due to the delay in the development of the DWEMF.

A comparison of averaged quantities over the purple-boxed region (see Figure 116) indicates that the nature of convection in the DWEMF was similar to the control simulation. Average profiles of the vertical velocity, diabatic heating rate, and precipitation rate were very close in magnitude. The average vorticity profile of the DWEMF was most similar to the DWEM, except that the magnitude of vorticity in the lower-troposphere was slightly greater. Thus, the low-level vorticity generation caused by strong convective processes in the DWEMF was moving the model solution away from that of the DWEM.

In order to further examine the propensity for the model to develop the TCS025 disturbance when initialized at 0600 UTC 28 August (after the first NRL P-3 flight), each ensemble member was integrated from its state at 0600 UTC 28 August to 1200 UTC 30 August without further data assimilation. The majority of the ensemble members over-developed the TCS025 disturbance (see Figure 117). Specifically, ensemble members that tended to have increased rates of development followed tracks east of mean ensemble track (see Figure 118). By contrast, ensemble members with less development followed tracks that were farther to the west. The over-development in the ensemble

forecasts indicates that without data assimilation to constrain the model solution, strong convective processes in the model tended to dominate the solution leading to development.

Another ensemble forecast from initial conditions at 0600 UTC 29 August (after the second ELDORA-equipped NRL P-3 flight) resulted in two types of solutions (see Figure 119): the majority of forecasts had an increase in the minimum sea-level pressure through 1200 UTC 30 August, and only a small number of the ensemble forecasts experienced strong development. As a result, the mean minimum sea-level pressure existed somewhere between these two sets of solutions.

It is noteworthy that despite initializing the DWEMF with a weak circulation that exhibited poor vertical alignment, deep convection was still able to develop. The presence of deep convection helped the circulation align and strengthen, and ultimately allowed the TCS025 disturbance to develop. Based on the boxed average quantities, the intensity of convection early in the DWEMF was similar to the control simulation. This suggests that the circulation alignment did not have an obvious impact on the nature of convection. Given deep convection with ample latent heating, the unfavorable large-scale environmental conditions (i.e., vertical wind shear) did not prevent over-development of TCS025 despite the initial misalignment of the circulation.

Since the assimilation of observations prevented development of TCS025 in the DWEM until the initialization of the DWEMF, it might appear as though the difference in final intensity between the control simulation and the DWEMF was simply a result of the control simulation having more time to develop. However, the fact that the circulation in the DWEMF was relatively weak and disorganized at 0000 UTC 30 August, which was 24 h after the circulation in the control simulation was already strong and vertically well-aligned, suggests the delay in development resulted from other factors. Despite the presence of strong convective processes in the DWEMF that somewhat reduced the circulation misalignment, it is concluded the delay in development did not allow adequate time for the circulation to align and strengthen sufficiently before being negatively impacted by the deteriorating large-scale environmental conditions. Although vertical wind shear remained weak until shortly after 0000 UTC 29 August (see Figure 35), the low-level circulation was beginning to move more rapidly to the north (see Figure 112) due to changes in the large-scale environmental flow. While deep convection in the

control simulation had sufficient time to eliminate the circulation misalignment before the translation speed of TCS025 increased, this was not the case for the DWEMF. The increase in translation speed slowed the circulation alignment process in the DWEMF, and by 0000 UTC 30 August, vertical wind shear had increased significantly. This kept the circulation in the DWEMF from achieving the same degree of alignment and organization as in the control simulation.

Similar to the DWEMF initialized at 0600 UTC 28 August, a second DWEMF was initialized at 0600 UTC 29 August (after the second NRL P-3 flight equipped with ELDORA radar) and integrated for thirty hours until 1200 UTC 30 August. Although an in-depth analysis of this forecast was not conducted, the minimum sea-level pressure for the second DWEMF appeared to be trending downward near the end of the simulation (see Figure 117). It is not clear whether the forecast would have experienced continued development had the simulation time been extended. Regardless, the first DWEMF initialized at 0600 UTC 28 August exhibited greater development over the first thirty hours of its integration. This suggests that the environmental conditions had continued to deteriorate (i.e., increasing vertical wind shear), which limited development of the DWEMF initialized at 0600 UTC 29 August.

While the third hypothesis of this study suggested the intensity of the precipitation processes in the model simulations would be limited by a more realistic vortex structure, an analysis of the DWEMF proved this was not the case. Although the initial vortex structure was more representative of observations due to the DART-WRF data assimilation, the impact of the misaligned vortex structure had on the nature of the precipitation processes was negligible. Therefore, it appears that initializing the DWEMF with a circulation that was poorly aligned in the vertical only delayed development. However, the delay in development was significant in that it did not allow the convective processes sufficient time to improve alignment before the large-scale environment became less favorable. This caused the circulation in the DWEMF to remain disorganized, which limited the final intensity of TCS025 in the simulation.

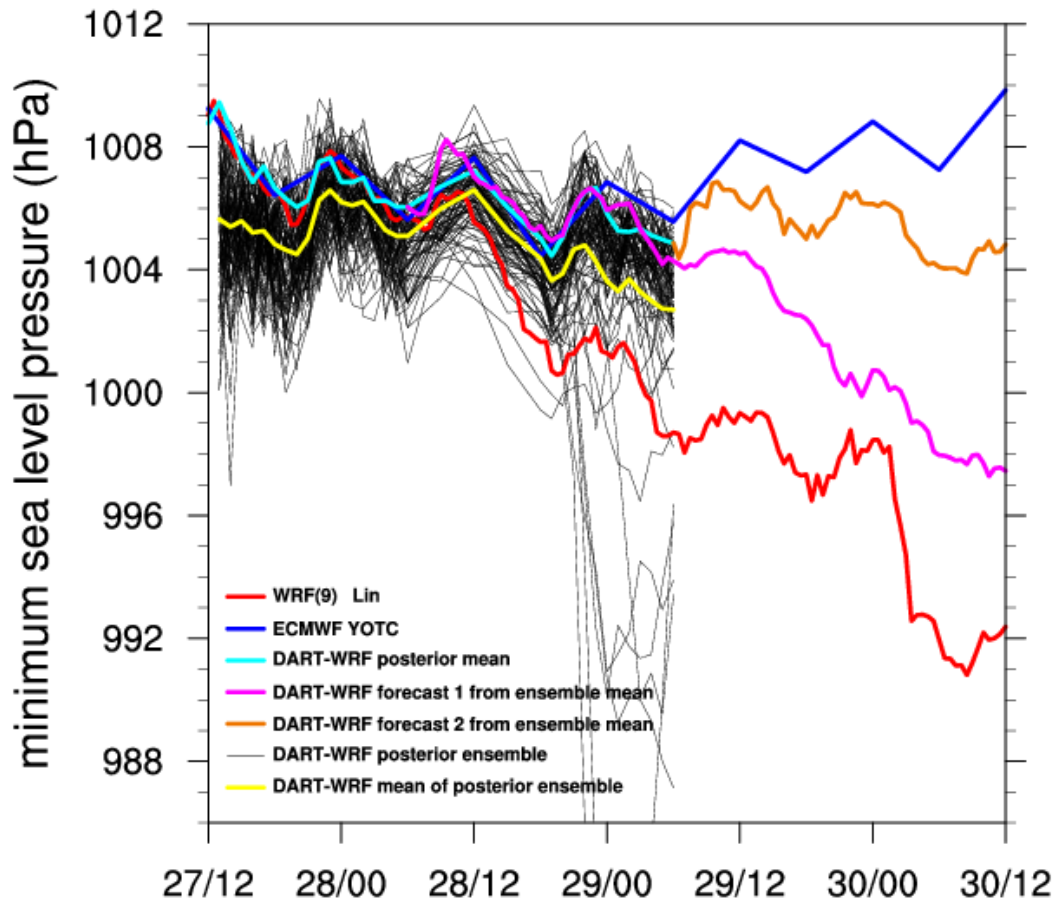


Figure 103 Minimum sea-level pressure (hPa) from the control simulation (red), ECMWF analysis (blue), DART-WRF posterior ensemble mean (cyan), DART-WRF ensemble mean forecast-1 (magenta), DART-WRF ensemble mean forecast-2 (orange), DART-WRF posterior ensemble (ninety-six members, black), and the mean of the DART-WRF posterior ensemble (yellow).



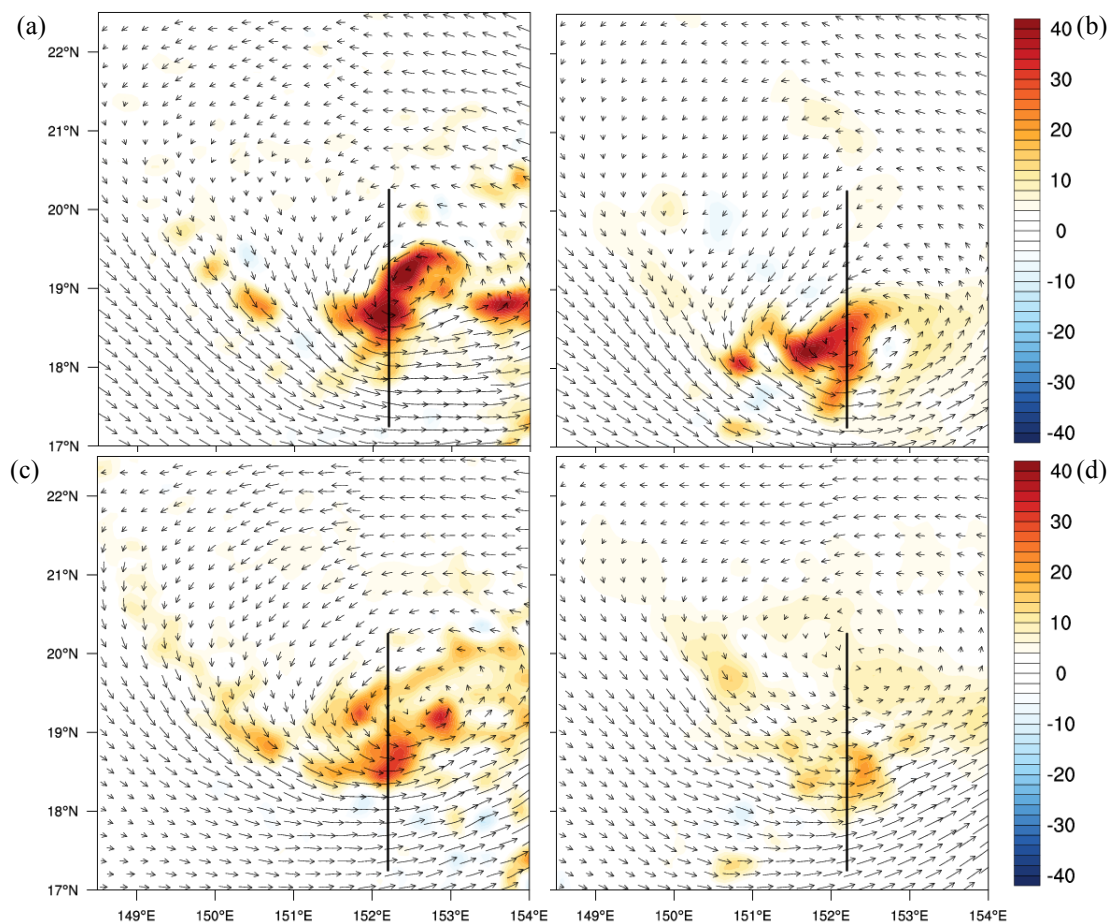


Figure 104 Relative vorticity ( $10^{-5} \text{ s}^{-1}$ , shaded) at (a, b) 5- and (c, d) 1.5-km altitude for (a, c) WRF simulation 9 (control simulation) and (b, d) the DART-WRF ensemble mean at 0600 UTC 28 August (after the first ELDORA flight). The black lines denote the location of the vertical cross section shown in Figure 105.

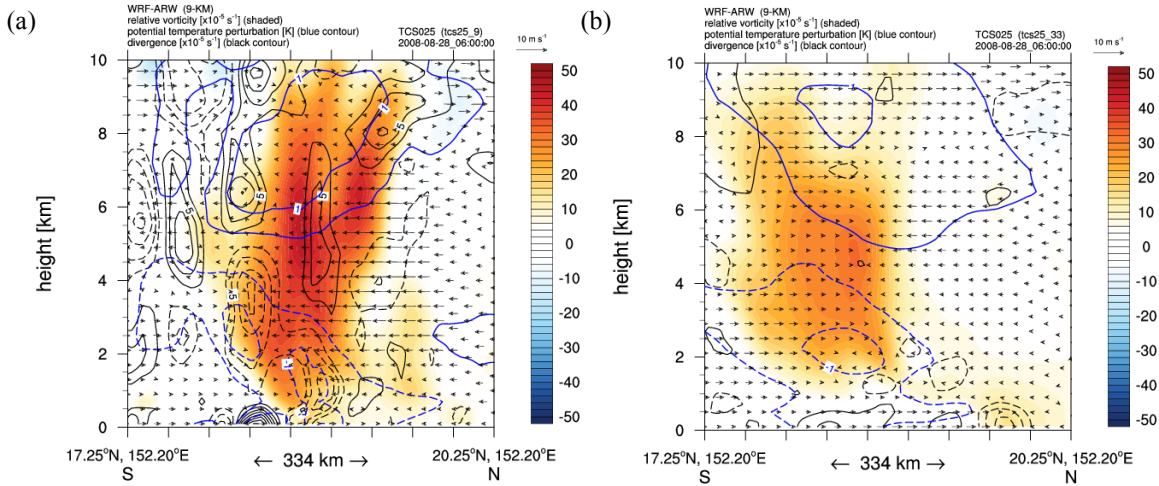


Figure 105 South-to-north vertical cross sections of relative vorticity ( $10^{-5} \text{ s}^{-1}$ , shaded), potential temperature anomaly (K, blue contours every 0.25 K), divergence ( $10^{-5} \text{ s}^{-1}$ , black contours every  $2.0 \times 10^{-5} \text{ s}^{-1}$ ), and in-plane wind vectors ( $\text{m s}^{-1}$ , with  $10 \text{ m s}^{-1}$  reference vector indicated at the top right in each panel) from (a) WRF simulation 9 (control simulation) and (b) the DART-WRF ensemble mean at 0600 UTC 28 August. Dashed contours indicate negative values. The locations of the cross sections correspond to the solid black lines in Figure 104.

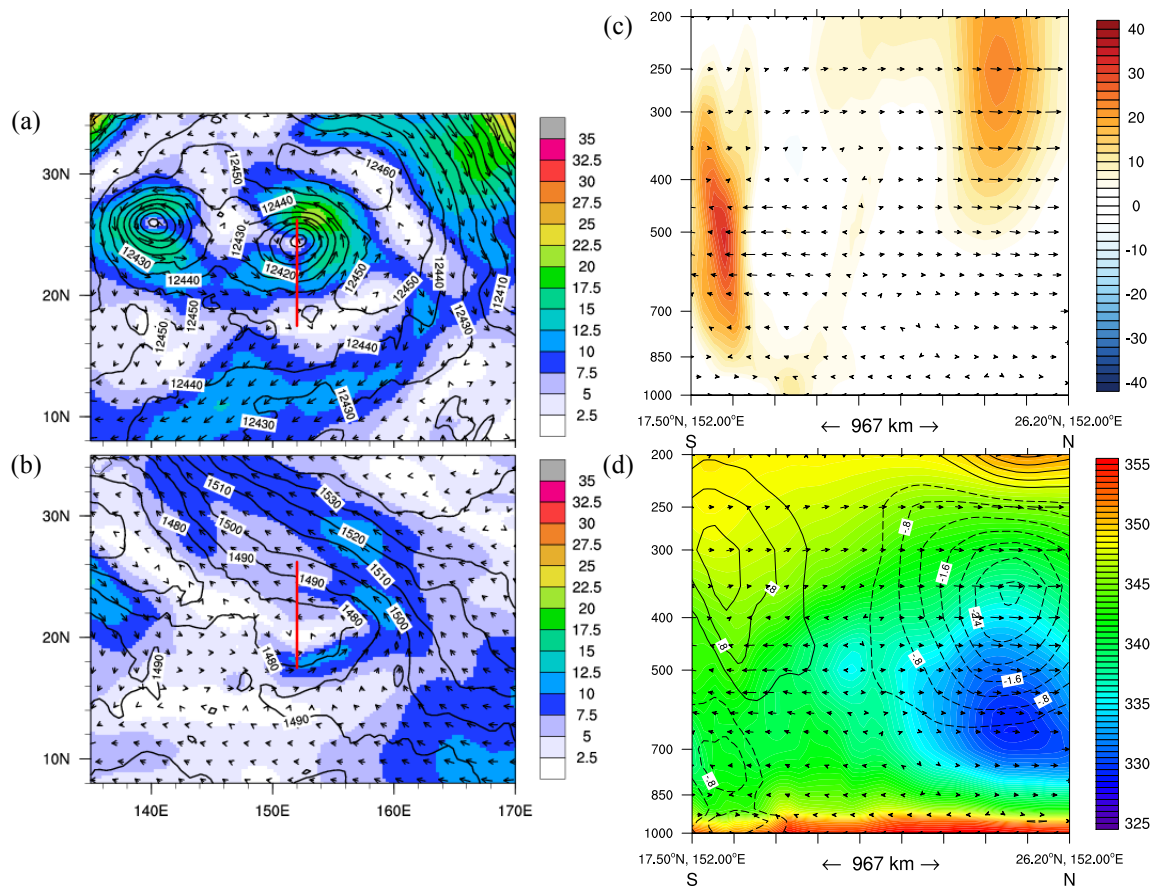


Figure 106 Wind speed ( $\text{m s}^{-1}$ , shaded) and geopotential height (m, contoured) at (a) 200 hPa and (b) 850 hPa, and south-to-north vertical cross sections of (c) relative vorticity ( $10^{-5} \text{ s}^{-1}$ , shading), and (d)  $\theta_e$  (K, shading) and virtual temperature perturbation (K, contours) at the initial time of 0600 UTC 28 August for the DWEMF. The ordinate axis in (c) and (d) is in pressure (hPa). Vectors in (c) and (d) represent wind speeds in the plane of the cross sections, and vertical velocity has been rescaled by multiplying by a factor of 10. The average virtual temperature out to  $6^\circ$  radius from the circulation center position was used as the reference state to determine the virtual temperature perturbation in (d). The red lines in (a) and (b) mark the location used for the vertical cross sections in (c) and (d). The vorticity cross section in (c) is similar to that in Figure 105b, except with different horizontal scaling.

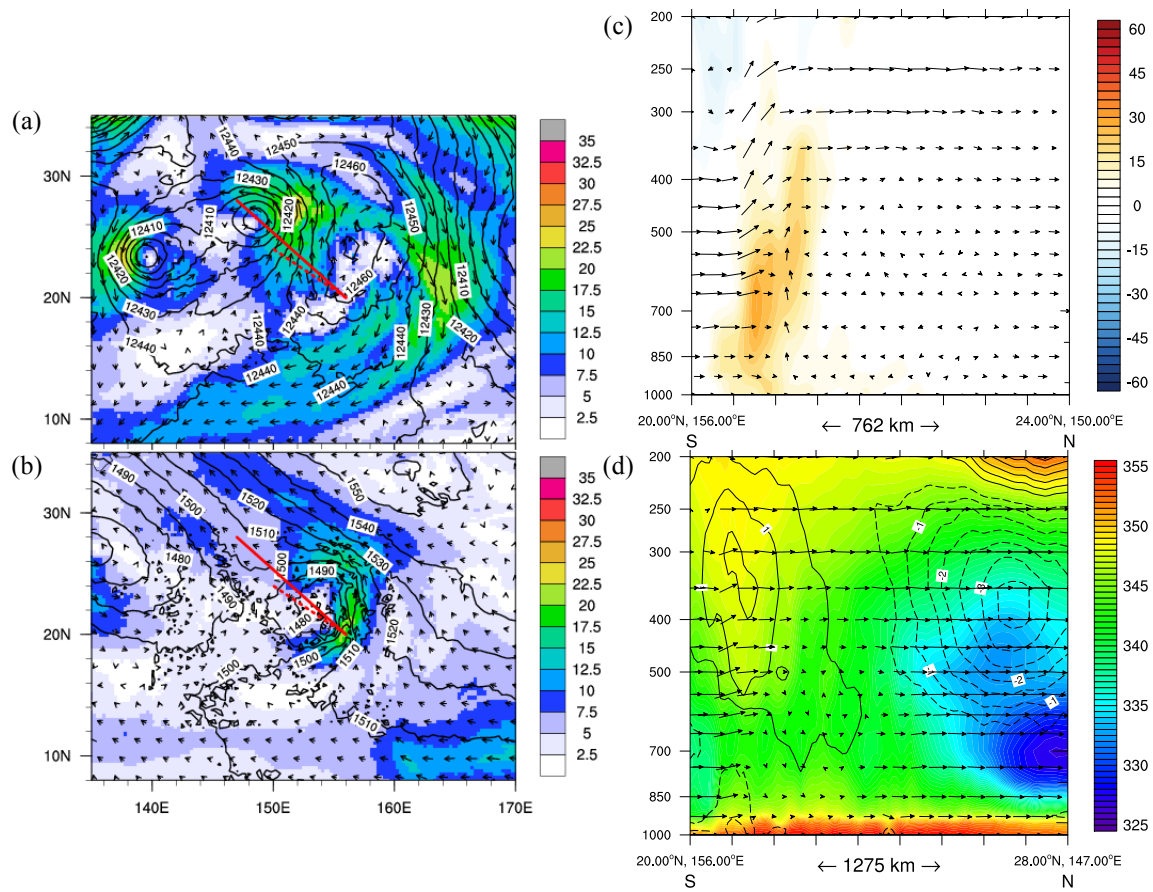


Figure 107 As in Figure 106, except at 0000 UTC 29 August ( $T + 18$  h). The dashed and longer solid red lines in (a) and (b) denote the locations used for the vertical cross sections in (c) and (d), respectively. Note that the cross-section location and horizontal scaling in (c) is different from (d).

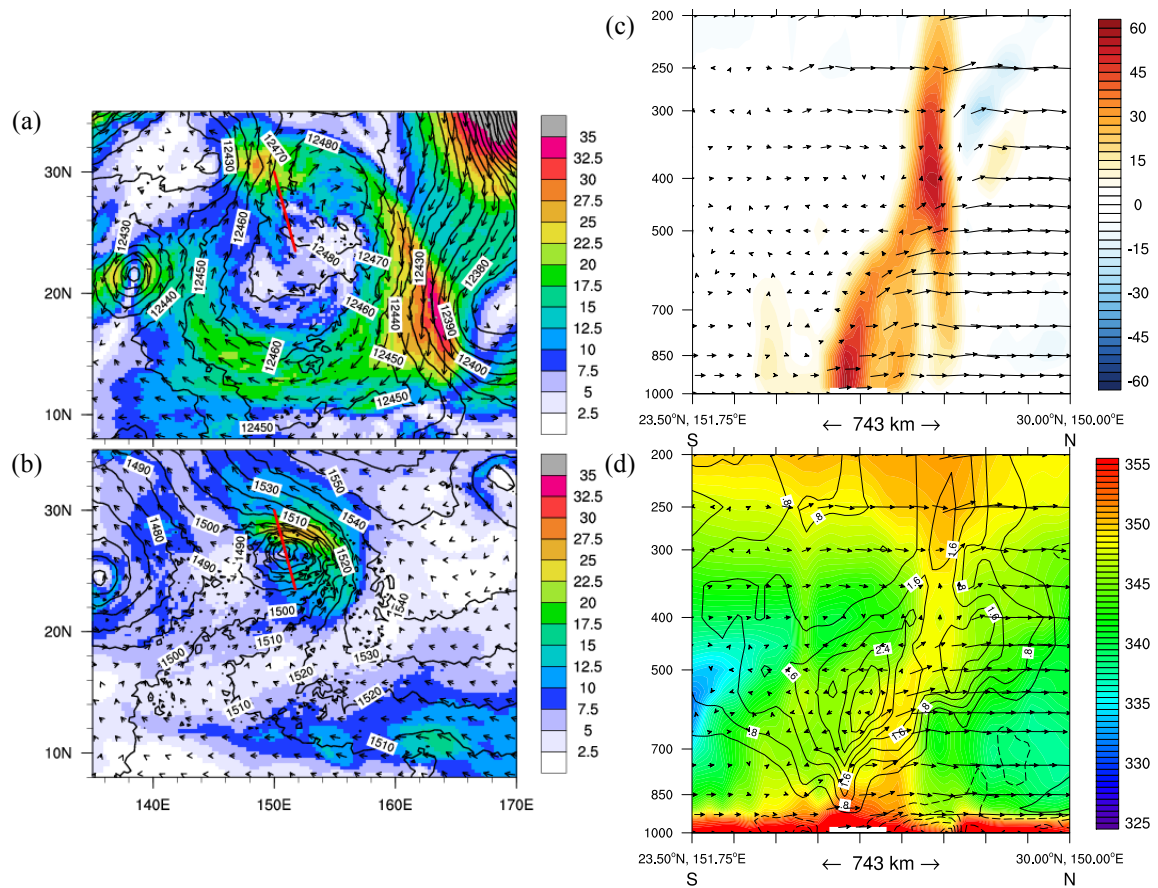


Figure 108 As in Figure 106, except at 0000 UTC 30 August (T + 42 h). The solid red line in (a) and (b) denotes the location used for the vertical cross sections in (c) and (d).



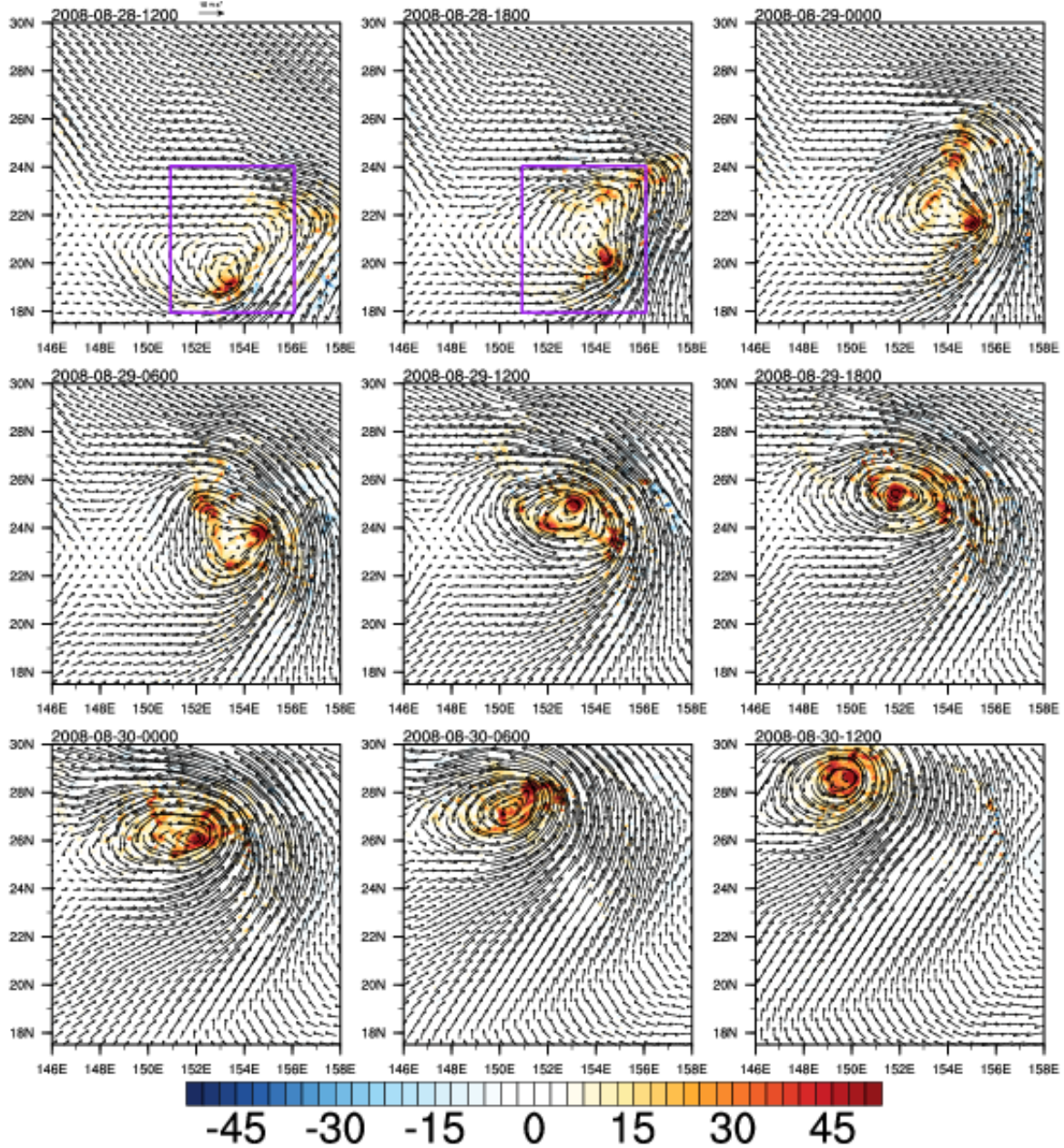


Figure 109 950-700 hPa average relative vorticity, ( $10^{-5} \text{ s}^{-1}$ , shaded) and 850 hPa wind vectors ( $\text{m s}^{-1}$ , with a  $10 \text{ m s}^{-1}$  reference vector indicated above the top left panel) at 6 h intervals from 1200 UTC 28 August to 1200 UTC 30 August for WRF simulation 9 (control simulation). The purple boxed-region in the top panels corresponds to the area over which a circulation budget (see Figure 114) and averages (see Figure 116) were computed from 1200–1800 UTC 28 August.



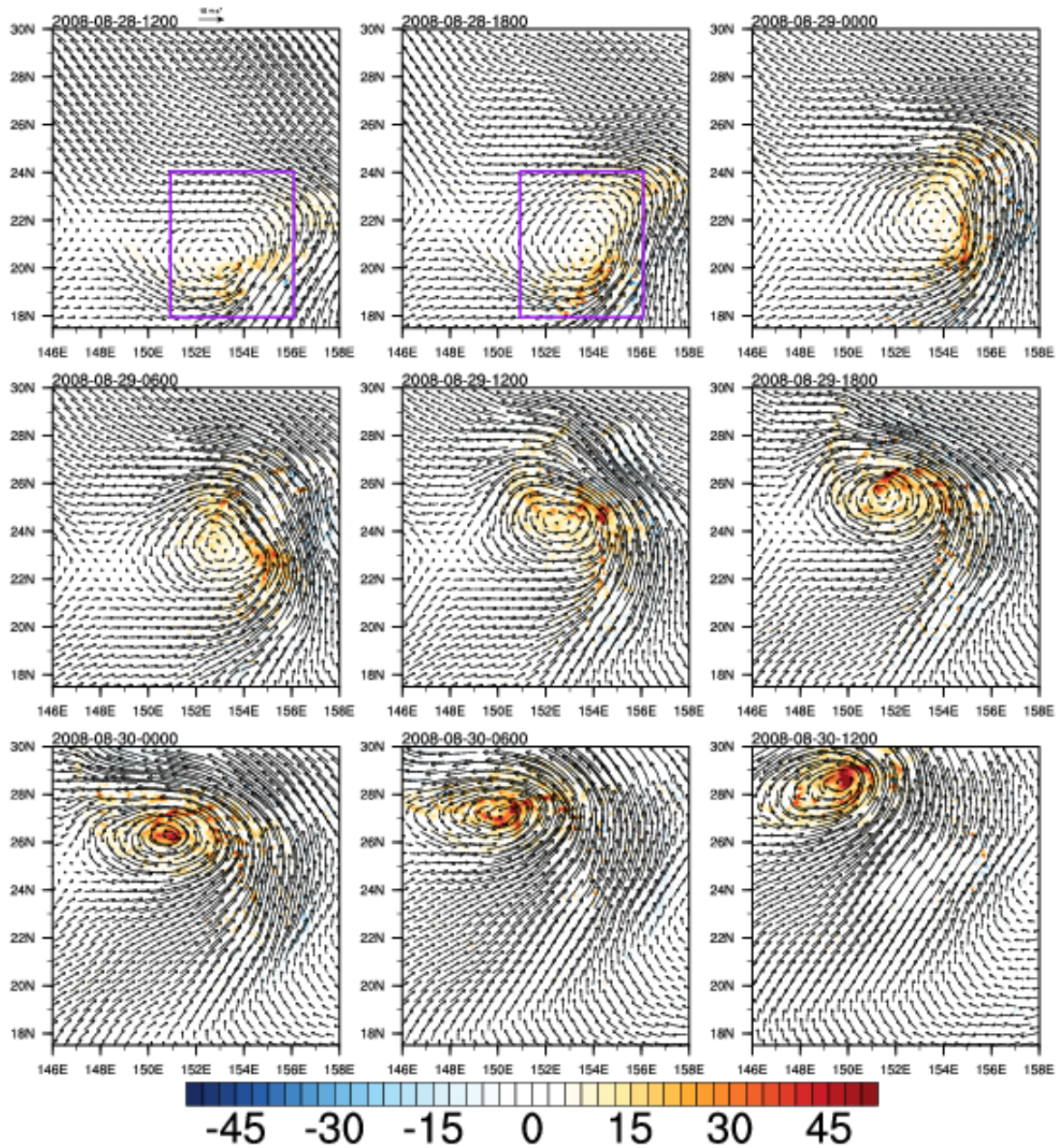


Figure 110 As in Figure 109, except for the DART-WRF ensemble mean forecast (DWEMF). The purple boxed-region in the top panels corresponds to the area over which a circulation budget (see Figure 115) and averages (see Figure 116) were computed from 1200–1800 UTC 28 August.

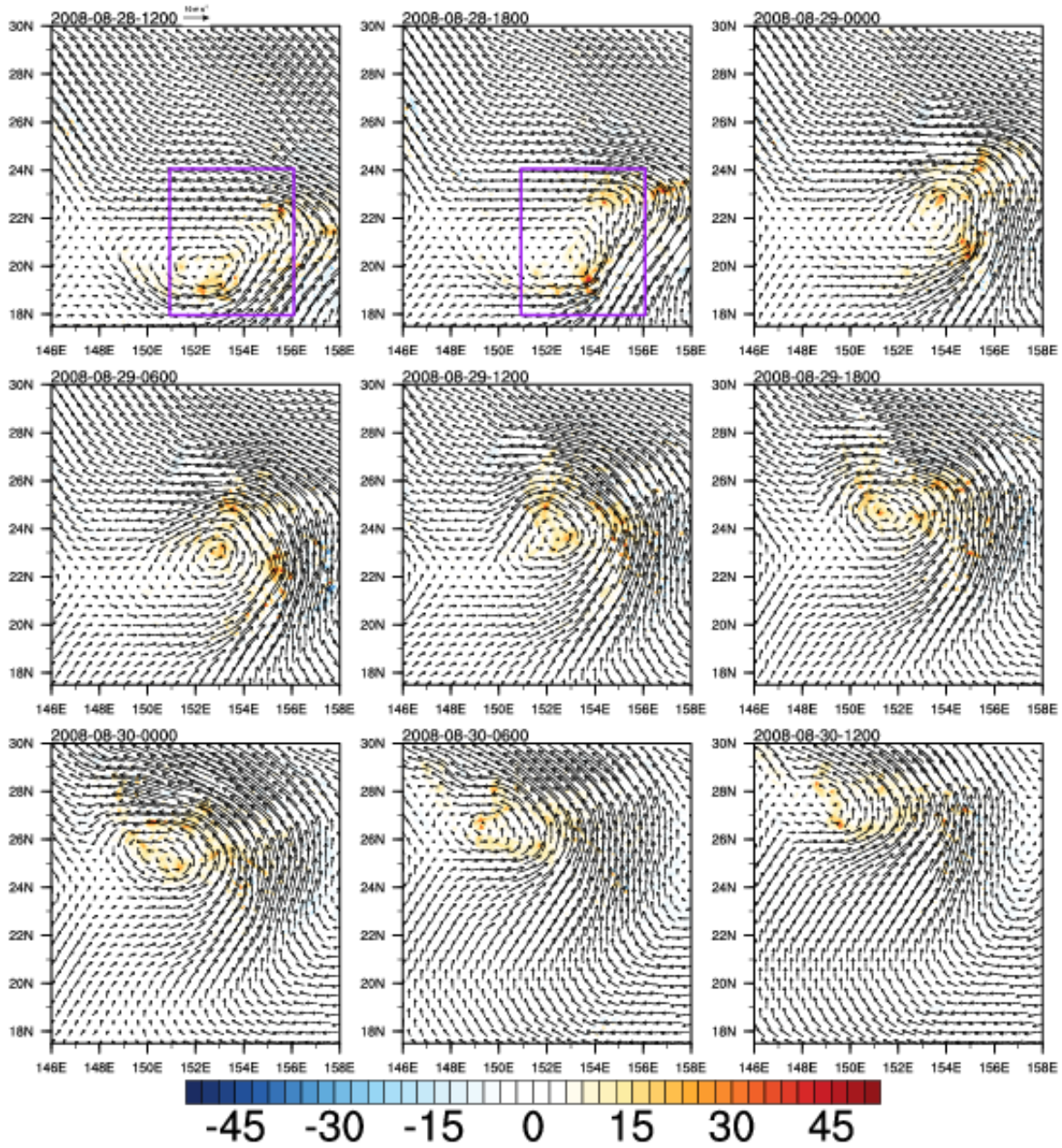


Figure 111 As in Figure 109, except for the non-developing WRF simulation 25. The purple boxed-region in the top panels corresponds to the area over which averages (see Figure 116) were computed from 1200–1800 UTC 28 August.



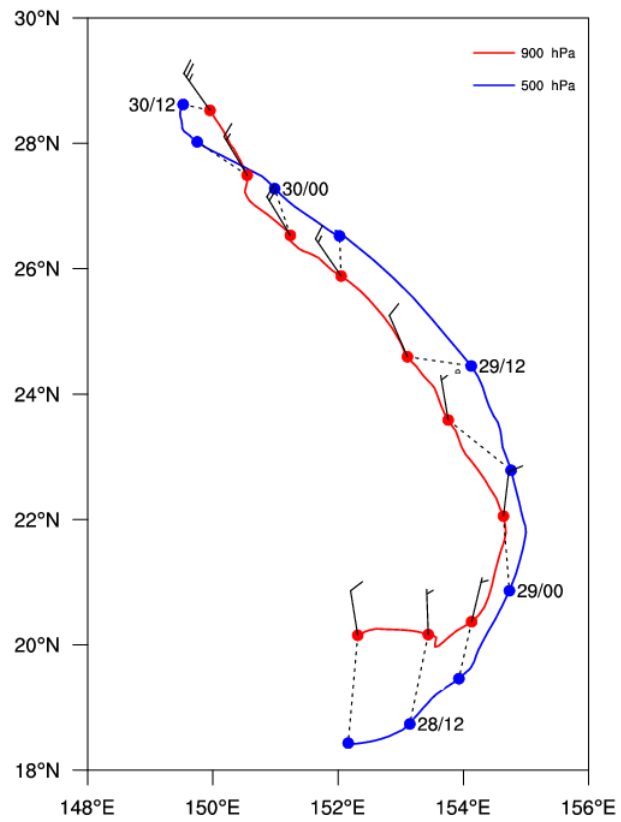


Figure 112 As in Figure 97, except for the DWEMF.

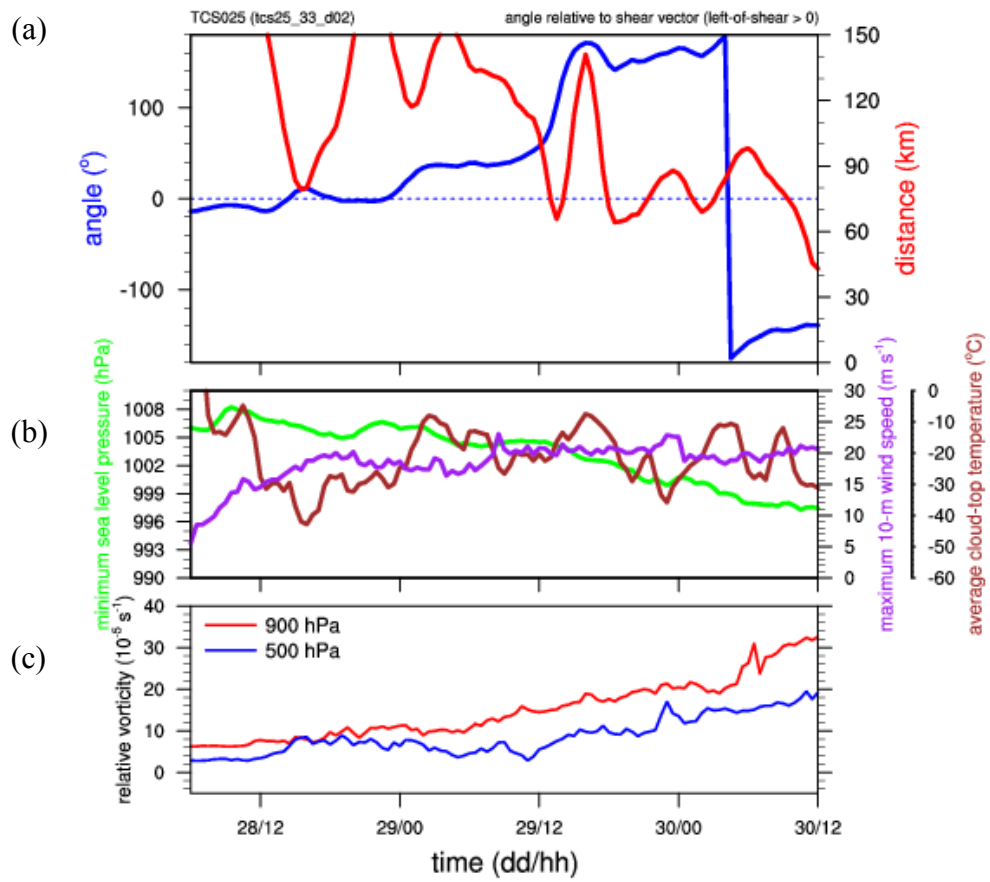


Figure 113 As in Figure 98, except for the DWEMF.

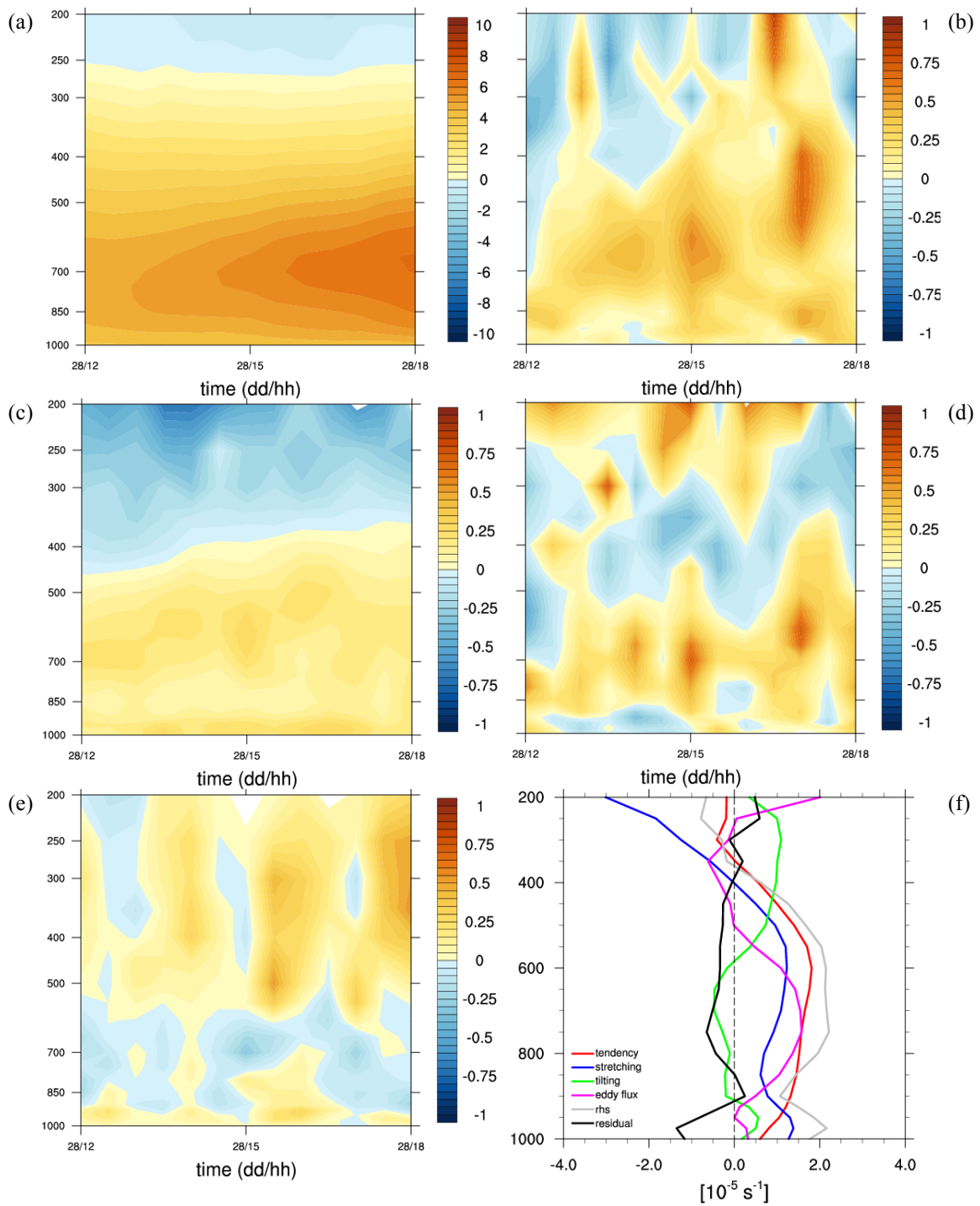


Figure 114 Circulation budget tendencies as in Figure 81, except for the purple-boxed region in Figure 109 from 1200 UTC 28 August to 1800 UTC 28 August for WRF simulation 9 (control simulation).

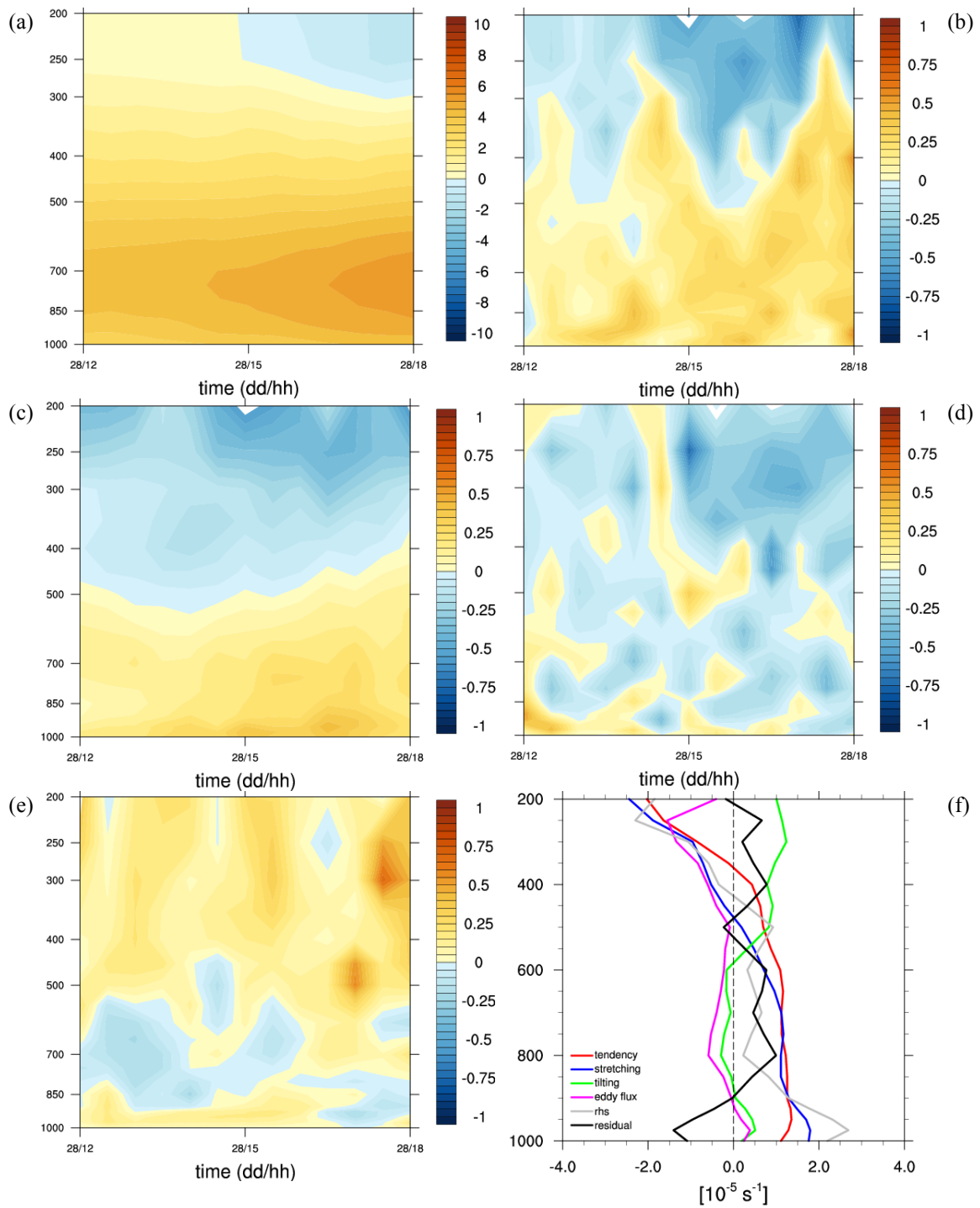


Figure 115 Circulation budget tendencies as in Figure 81, except for the purple-boxed region in Figure 110 from 1200 UTC 28 August to 1800 UTC 28 August for the DART-WRF ensemble mean forecast (DWEMF).

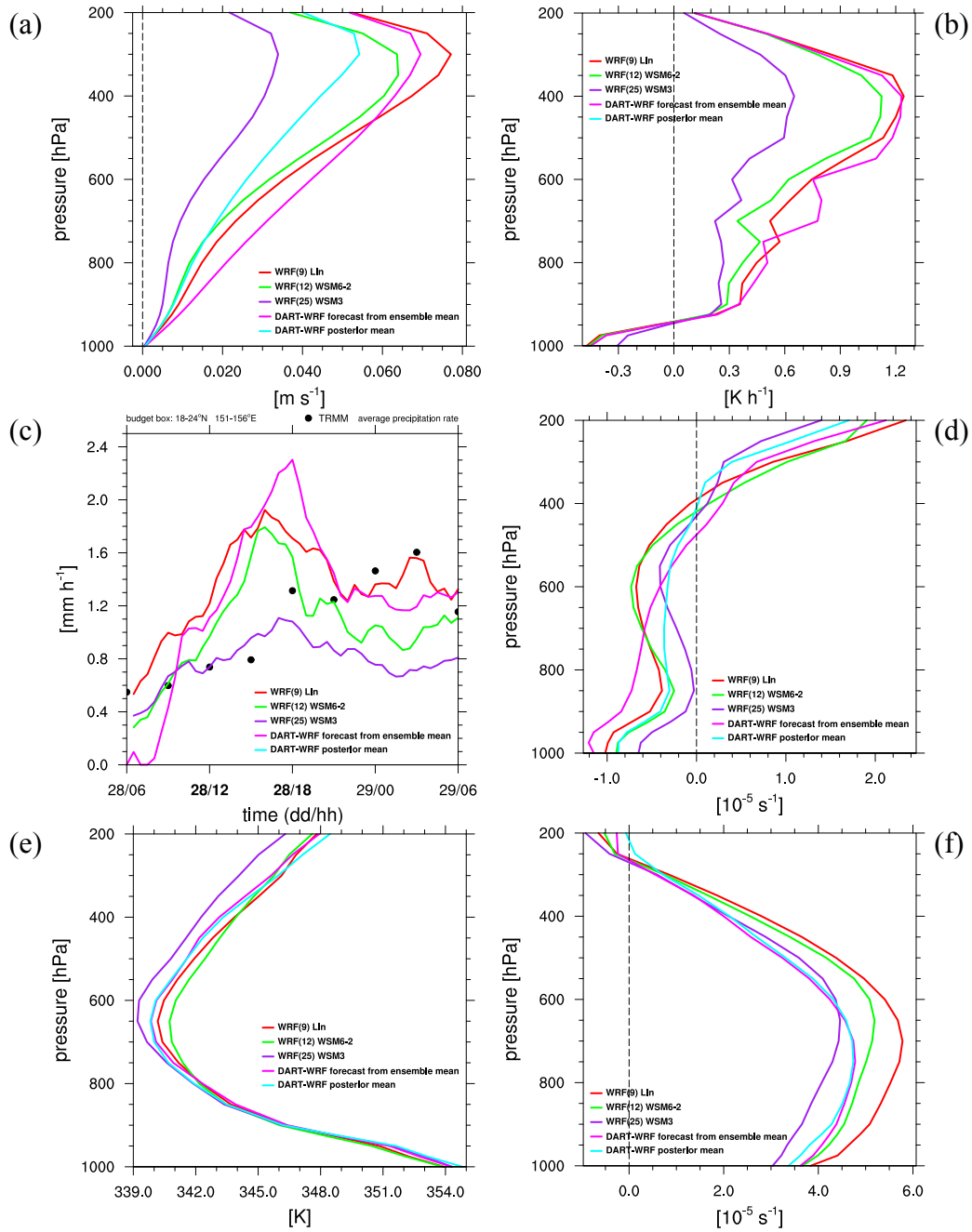


Figure 116 Average profiles of (a) vertical velocity ( $\text{m s}^{-1}$ ), (b) diabatic heating rate ( $\text{K h}^{-1}$ ), (c) precipitation rate ( $\text{mm h}^{-1}$ ), (d) divergence ( $10^{-5} \text{ s}^{-1}$ ), (e)  $\theta_e$  (K), and relative vorticity ( $10^{-5} \text{ s}^{-1}$ ) for the WRF simulation 9 (control simulation, red), WRF simulation 12 (green), WRF simulation 25 (purple), DART-WRF ensemble mean forecast (magenta), and the DART-WRF posterior mean (cyan). Quantities were averaged within the purple-boxed region in Figure 72, and averaged in time for (a, b, d, e, f) from 1200 UTC 28 August to 1800 UTC 28 August. Black dots in (c) denote the average TRMM precipitation estimate for the purple-boxed region at the corresponding times.

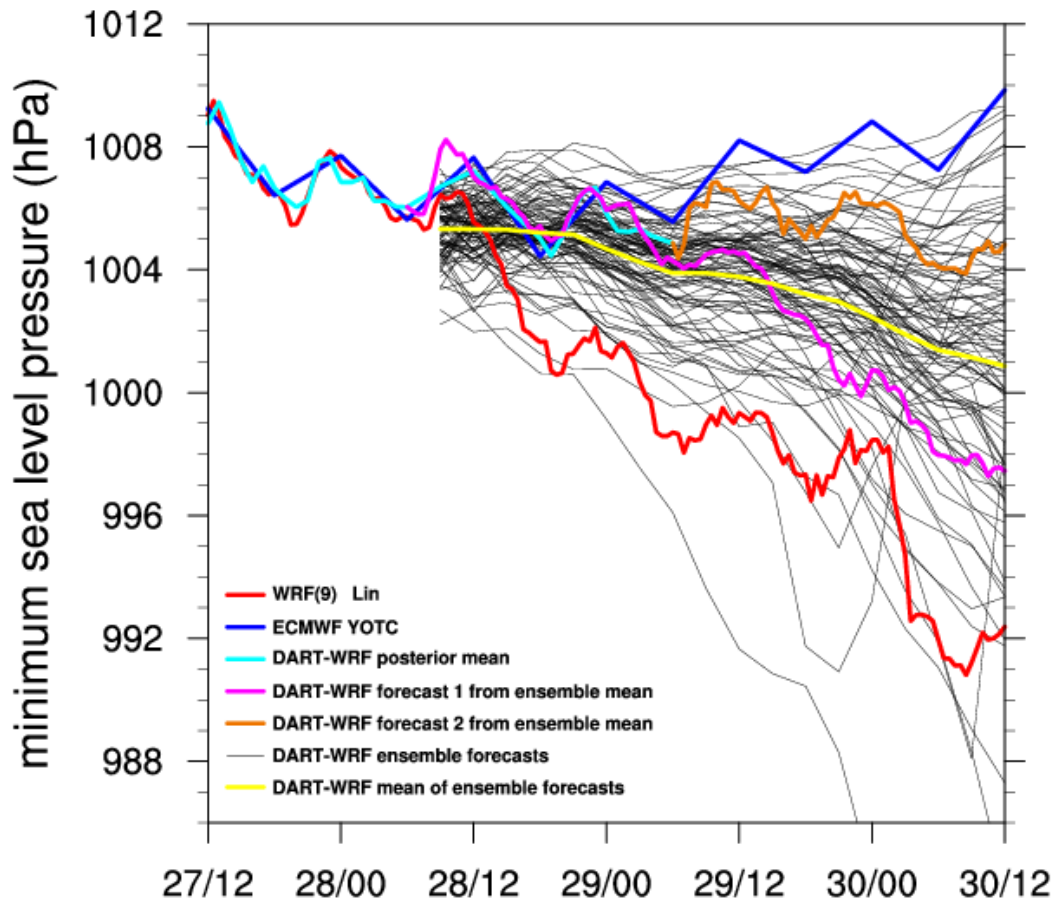


Figure 117 Minimum sea-level pressure (hPa) from the control simulation (red), ECMWF analysis (blue), DART-WRF posterior ensemble mean (cyan), DART-WRF ensemble mean forecast-1 (magenta), DART-WRF ensemble mean forecast-2 (orange), DART-WRF ensemble initialized at 0600 UTC 28 August and integrated in forecast mode (no further data assimilation) (ninety-six members, black), and the mean of the DART-WRF ensemble integrated in forecast mode (yellow).

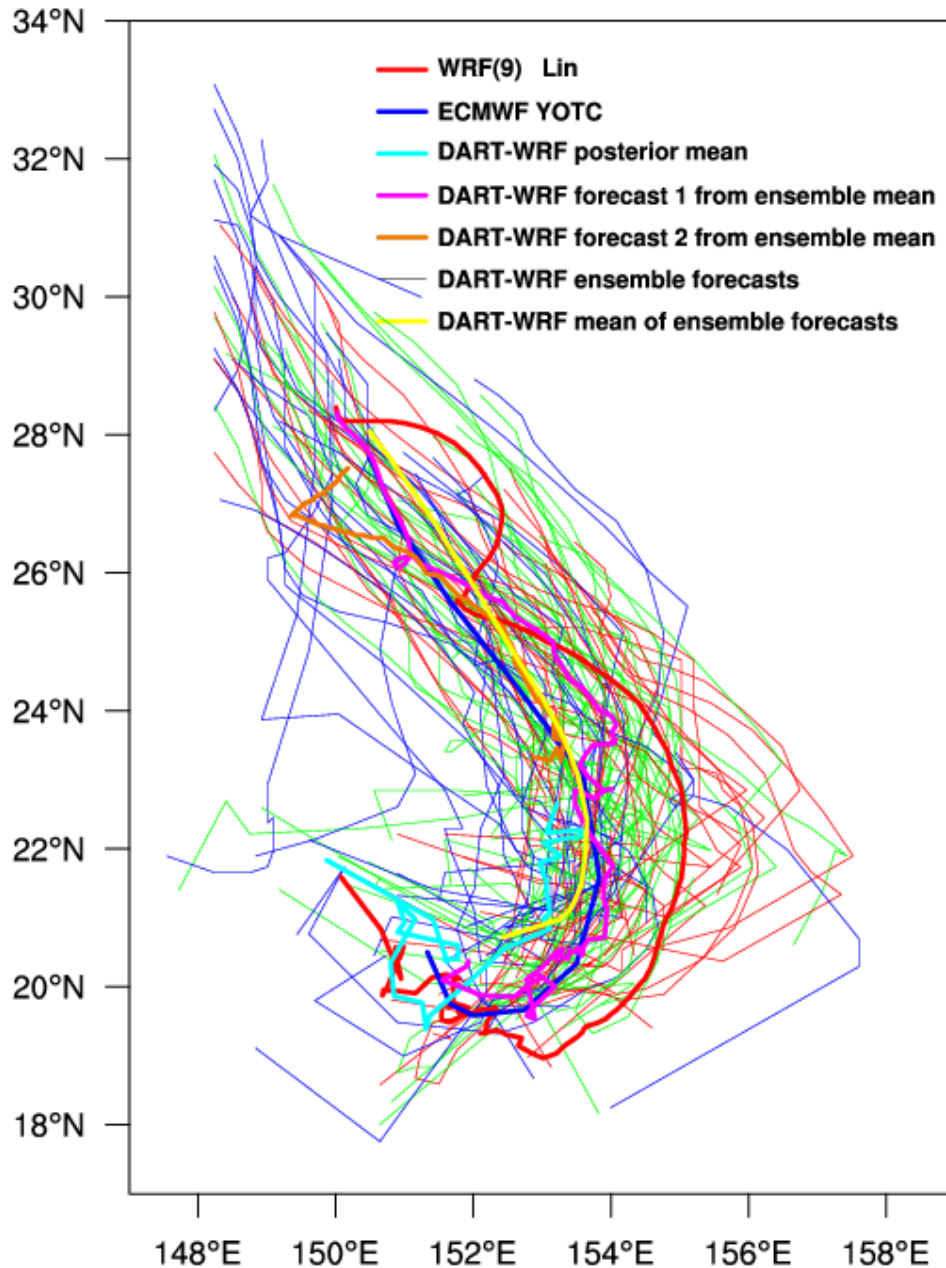


Figure 118 Minimum sea-level pressure tracks for the control simulation (red), ECMWF analysis (blue), DART-WRF posterior ensemble mean (cyan), DART-WRF ensemble mean forecast-1 (magenta), DART-WRF ensemble mean forecast-2 (orange), DART-WRF ensemble initialized at 0600 UTC 28 August and integrated in forecast mode (no further data assimilation) (96 members, thin red, green and blue lines), and the mean of the DART-WRF ensemble integrated in forecast mode (yellow). Tracks for ensemble members with a minimum sea-level pressure at 1200 UTC 30 August  $> 1004$  hPa are colored blue, between 1000 hPa and 1004 hPa are colored green, and  $< 1000$  hPa are colored red. Latitude and longitude positions were smoothed using a 3-point running average.

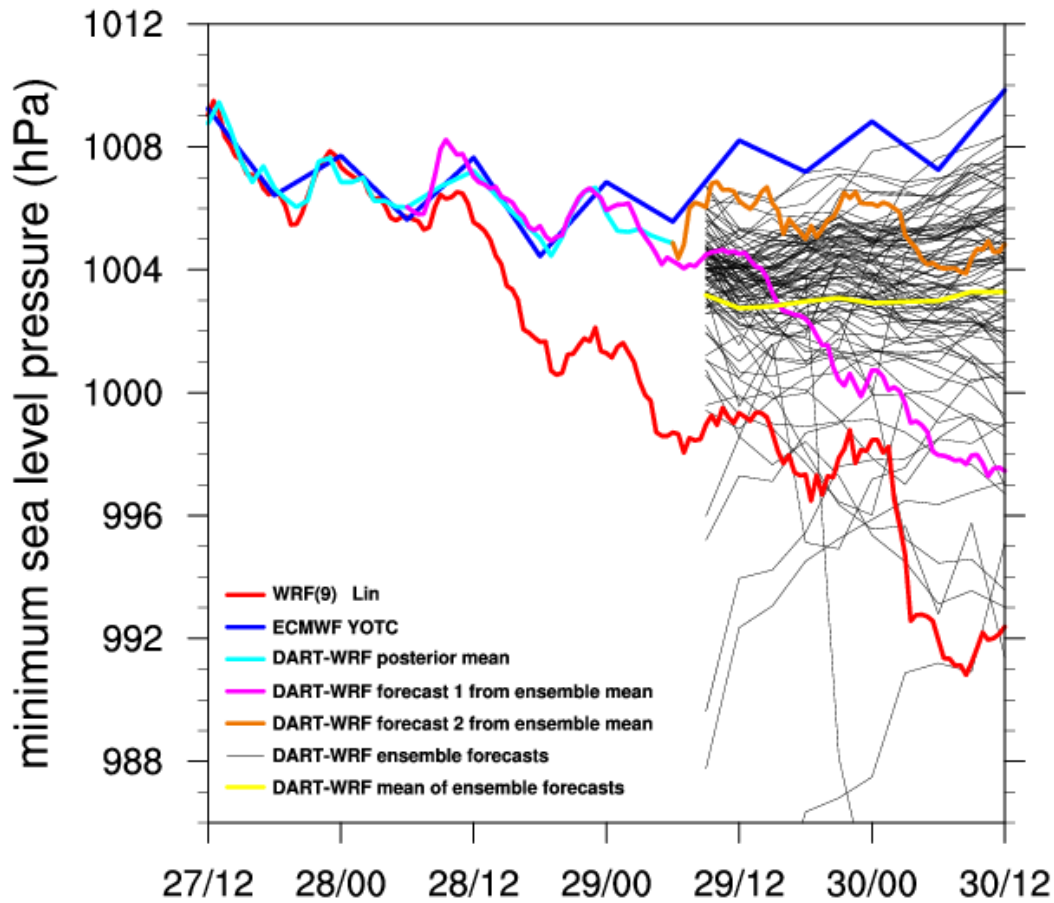


Figure 119 As in Figure 117, except minimum sea-level pressure (hPa) for the DART-WRF ensemble initialized at 0600 UTC 29 August and integrated in forecast mode (ninety-six members, black), and the mean of the DART-WRF ensemble integrated in forecast mode (yellow).



## **VI. SUMMARY AND CONCLUSIONS**

The in-situ dataset collected during the evolution of TCS025 provided a unique opportunity to examine a non-developing tropical disturbance. Since there remains many unanswered questions related to tropical storm formation, an in-depth analysis of a “null case” is perhaps just as important as documenting storm formation, since the vast majority of tropical disturbances fail to develop and intensify. Often, there exists a great amount of uncertainty with respect to the likelihood of formation. In the case of TCS025, global forecast models suggested further development was likely (see Figure 1), but the system failed to develop.

### **A. HYPOTHESIS #1 EVALUATION – OBSERVATIONS**

From the observational analysis it was evident that the circulation of the TCS025 system was weak, asymmetric, and misaligned in the vertical. Dropwindsonde-derived circulation center positions indicated that there was significant misalignment in the vertical during the second IOP (see Figure 44), and despite sampling biases, it appeared as though the alignment during the first and third IOPs was also poor. In addition, a SAMURAI analysis during the second IOP, which combined dropwindsonde, flight-level, and ELDORA dual Doppler radar data with the ECMWF analysis, indicated the mid-level circulation was located a significant distance south (down-shear) of a much weaker low-level circulation (see Figure 45 and Figure 48). The system-relative flow for TCS025 was stronger as a result of the circulation misalignment in the vertical (see Figure 47).

An analysis of MTSAT IR brightness temperature revealed that the environment surrounding TCS025 was marked by intermittent periods of convection. The reflectivity from ELDORA (see Figure 50) indicated that convection organized into MCSs that consisted of large stratiform precipitation regions. MCS activity followed the convective diurnal cycle to peak in intensity near 1800 UTC (see Figure 37). MCSs formed south of the TCS025 circulation and moved southward under the presence of northerly vertical wind shear. Davis and Ahijevych (2012) suggested that the circulation alignment of a

tropical disturbance would improve if strong, deep convection could persist in the vicinity of the mid-level circulation. However, convection associated with TCS025 remained relatively weak, as MCSs were generally not able to persist past the diurnal convective minimum. In addition, stratiform precipitation appears to have been more prevalent than deep convection.

The large-scale environment of TCS025 was modulated primarily by an upper-level TUTT cell that came into close proximity to the disturbance during the second IOP near 0000 UTC 28 August (see Figure 32b). As the TUTT cell approached TCS025, northerly vertical wind shear over the system was strong and a thermodynamic profile comparison based on an average of dropwindsonde data revealed that mid-tropospheric  $\theta_e$  was lowest during the second IOP (see Figure 58b). Vertical cross sections of  $\theta_e$  constructed from dropwindsonde data (see Figure 51) revealed the presence of mid-level low- $\theta_e$  air to the north (up-shear) of the TCS025 circulation that originated from the TUTT cell to the east (see Figure 60). A large area of low- $\theta_e$  air was present in the boundary layer near regions of recent convection. Because the circulation of TCS025 was weak, asymmetric, and misaligned in the vertical, the system-relative flow was large and mid-level low- $\theta_e$  air was able to infiltrate areas of convection near the circulation (Riemer et al. 2010) before being transported into the boundary layer through convective downdrafts. Based on longitudinally averaged MTSAT IR brightness temperature (see Figure 61), there was a lull in deep convection after the dissipation of MCS-G when low- $\theta_e$  air impacted TCS025. The next round of deep convection did not form until the system had moved a significant distance to the north.

A comparison with TY Fanapi (2010) during the early stages of its development, when the intensity was similar to that exhibited by TCS025, helped to identify differences in structure that would affect the outcome of each disturbance. TY Fanapi shared a similar thermodynamic environment to TCS025. In fact, air to the northwest of the low-level circulation center was of lower  $\theta_e$  than that during the second IOP for TCS025 (see Figure 66) and the average  $\theta_e$  deficits (see Figure 68) and AXBT profiles (see Figure 67) were similar to TCS025. However, vertical wind shear was much weaker for TY Fanapi

(see Figure 64b), and this allowed the circulation of TY Fanapi to remain better vertically aligned (see Figure 65). System-relative flow is less for a vertically-aligned circulation and this kept the inner-core of Fanapi somewhat protected from the impacts of the low- $\theta_e$  air (see Figure 70), whereas the inner-core of TCS025 was more exposed. Although both TY Fanapi and TCS025 experienced intermittent periods of convection (see Figure 69), a lull in convective activity occurred after the encounter with low- $\theta_e$  air. Convection was able to redevelop for TY Fanapi, but failed to rebound in intensity for TCS025. This suggests that the alignment of TY Fanapi protected it from the full impact of low- $\theta_e$  air, whereas the poor circulation structure of TCS025 allowed low- $\theta_e$  air to disrupt convection near the circulation, and this ultimately inhibited further development.

In summary, the convective intensity of TCS025 was not sufficient to improve alignment of the circulation while in the presence of strong vertical wind shear. The weak, asymmetric, and misaligned circulation structure resulted in increased system-relative flow that allowed low- $\theta_e$  air to infiltrate and negatively impact the thermodynamic environment of TCS025. Despite a reduction in vertical wind shear following the second IOP, convection remained weak in the presence of the low- $\theta_e$  air. Without deep convection, alignment of the TCS025 circulation was not able to improve and this kept the TCS025 disturbance from developing further. Thus, the observational analysis supports the first hypothesis of this study: TCS025 failed to develop in part due to poor vertical alignment of the vortex structure that prevented enhancement and organization of deep convection.

## **B. HYPOTHESIS #2 EVALUATION – MULTI-PHYSICS ENSEMBLE**

To extend the observational analysis of TCS025 and quantify the processes responsible for its non-development, a multi-physics ensemble was used that employed the WRF-ARW numerical model. However, finding a model solution that correctly depicted the evolution of TCS025 proved problematic as the majority of simulations over-developed the disturbance (see Figure 71a). Two simulations were chosen for further examination and comparison: simulation 9 that exhibited development of the TCS025 disturbance, and simulation 25 that correctly forecast non-development.

Simulations 9 and 25 were only different in their representation of microphysical processes. By comparing two model solutions that spanned the development spectrum, it was hoped that the key processes responsible for the non-development of TCS025 could be identified and explored further.

Differences in the evolution of the two simulations were evident shortly after model initialization time: the TCS025 disturbance in simulation 9 exhibited a larger decline in low-level geopotential height and the anticyclone and outflow above the convection associated with the disturbance increased in intensity (see Figure 73). Thirty-six hours after model initialization, vertical cross sections revealed the rapid development in simulation 9 of a coherent low-level vortex in the presence of deep moist convection (see Figure 76b,d), whereas the vortex in simulation 25 remained weak and disorganized. Evidence of convective overturning in simulation 25 was not as pronounced (see Figure 76a,c) as in simulation 9.

Circulation budgets from 1800 UTC 27 August to 0600 UTC 28 August for simulations 9 and 25 reveal that the circulation was initially strongest in the mid-levels, but that positive low-level tendencies quickly formed and were stronger in simulation 9 (see Figure 81f and Figure 82f). The stretching of vertical vorticity through low-level convergence and convection was the dominant mechanism by which the low-level circulation increased during this time. At the same time, negative circulation tendencies due to stretching processes were present in the upper-levels, and corresponded to the increase in the upper-level anticyclone over the convective area. This suggests that convective precipitation processes were active and causing a spin-up of the low-level circulation, especially in simulation 9. This was further confirmed by larger magnitudes of the average vertical velocity, diabatic heating rate, and precipitation rate in simulation 9 for both convective and non-convective environments (see Figure 90).

After 0000 UTC 28 August, the convective intensity began to decline in both simulations (see Figure 88a,c). For simulation 25, the stretching tendency in the low-levels became negative while it remained positive in the mid-levels (see Figure 88b). This suggests stratiform precipitation processes (mid-level convergence and low-level divergence) were most active during this time, which contributed to a net spin-down of

the low-level circulation. In contrast, simulation 9 continued to intensify during the lull in convection as there was sufficient convective activity and low-level convergence (positive low-level stretching tendency) to offset frictional dissipation (see Figure 88d).

To investigate why the nature of convection was so different amongst the model solutions, additional numerical simulations were conducted in which convective-related parameters were altered. It was found that the final intensity and rate of development of TCS025 was extremely sensitive to the diabatic heating rate. A small reduction in the diabatic heating rate could prevent development in a simulation otherwise identical to simulation 9 (see Figure 92). The additional diabatic heating experiments along with the multi-physics ensemble illustrate that the development scenario for TCS025 was very sensitive to the representation of microphysical processes and their impact on the strength of convection and diabatic heating rate.

A comparison of the characteristics of convection as exhibited by the model solutions and observations (IR brightness temperature, reflectivity,  $\theta_e$  deficit) suggests the intensity of the convective processes was over-exaggerated in the model solutions while stratiform precipitation processes appear to have been underrepresented (see Figure 94) (i.e., based on observations, the model simulations did a poor job of representing the spectrum of precipitation processes).

To assess the impact that the convective processes had on circulation alignment, the evolution of the separation distance between the 900 hPa and 500 hPa PV-weighted center positions was examined (see Figure 97, Figure 98, and Figure 99). It was found that the alignment in simulation 9 steadily improved while in the presence of convection whereas deep convection was generally absent from simulation 25 and the mid- and low-level circulations moved farther apart. Without improved alignment, the circulation in simulation 25 was left exposed to environmental influences that caused the separation distance between the low- and mid-level circulations to increase over time. In addition, it was found that deep convective updrafts disrupted the upper-level flow, which in turn caused a reduction in the magnitude of vertical wind shear. Therefore, the presence of deep convection in the model simulations not only promoted vortex alignment directly

through convective precipitation processes, it also protected the circulation and its alignment by reducing the magnitude of vertical wind shear over the convective area.

The impact of low- $\theta_e$  air associated with the TUTT cell to the north of the TCS025 system was also investigated. Although the presence of the low- $\theta_e$  air can be identified (see Figure 101), it had little impact on the inner-core thermodynamics; positive influences from convection and surface fluxes were much larger and this led to an increase of  $\theta_e$  during this time. Had convection and overall system organization been weaker, as observations suggest, the negative impact of low- $\theta_e$  air on the inner-core thermodynamic structure might have been greater.

A goal of the multi-physics ensemble was to evaluate why the high-resolution model simulations consistently over-developed the TCS025 disturbance. It was hypothesized that the non-development of TCS025 was a result of convective precipitation processes that were over represented in the model simulations. The multi-physics ensemble intercomparison confirms this. Simulation 9 exhibited intense convective precipitation processes that were characterized by strong low-level convergence, upper-level divergence, and large diabatic heating rates. The low-level circulation increased primarily through the stretching of vertical vorticity. Deep moist convection improved the vertical alignment of the circulation and reduced the impact of vertical wind shear. On the other hand, the convective intensity exhibited by simulation 25 was far less, and this ultimately inhibited development. Weak convection limited low-level spin-up and kept the low- and mid-level circulations from becoming better vertically aligned, which left the circulation in simulation 25 more susceptible to outside environmental influences. A comparison with observations, which depict weak convection and a greater amount of stratiform precipitation, suggests the modeled processes exhibited by simulation 25 were more realistic.

### **C. HYPOTHESIS #3 EVALUATION – DATA ASSIMILATION**

The circulation structure of TCS025 observed by ELDORA radar during the second IOP appeared weak, asymmetric, and exhibited poor vertical alignment (see Figure 45). In contrast, the ECMWF analysis, which was used to initialize the multi-

physics ensemble, depicted a stronger low-level circulation that was better aligned in the vertical with the mid-level circulation. Given that the majority of the multi-physics ensemble simulations incorrectly forecast the development of TCS025 (see Figure 71a), it became a question of whether the unrealistic circulation structure exhibited by the ECMWF analysis, and present in the initial conditions, might have had a favorable impact on development. To examine this further, the DART-WRF data assimilation system was employed to assimilate data collected during the second and third IOPs, with specific emphasis on the ELDORA radial velocity data, to assess the impact of circulation alignment in the evolution of TCS025.

After assimilation of the first set of ELDORA data, the DART-WRF ensemble mean (DWEM) at 0600 UTC 28 August was used to initialize the DART-WRF ensemble mean forecast (DWEMF). The circulation structure of TCS025 initially in the DWEMF looked very similar to the SAMURAI analysis (see Figure 48a and Figure 105b); the low-level circulation was relatively weak and displaced a significant distance to the north of a stronger mid-level circulation. Despite poor vertical alignment of the circulation, the DWEMF over-intensified the TCS025 disturbance, but development was delayed relative to the control simulation (simulation 9) by about 24 h (see Figure 117).

The large-scale structural changes exhibited by the DWEMF appeared very similar to those evident in the control simulation, albeit slightly delayed in timing: a reduction in low-level geopotential height and a strengthening of the upper-level anticyclone and outflow aloft (see Figure 108a). However, by 0000 UTC 30 August, the vortex structure still appeared relatively weak and disorganized (see Figure 108b) compared to the state of the control simulation 24 h earlier (see Figure 76b). Although the separation distance between the low- and mid-level circulations in the DWEMF decreased over time (see Figure 112), the separation distance was significantly greater than that exhibited by the control simulation at the end of the simulation. Thus the convective precipitation processes did not have adequate time to improve alignment to the same degree experienced by the control simulation. The differences in the circulation structure and final intensity suggests that although the DWEMF followed a similar development pathway to that of the control simulation, the delay in development made the circulation in the DWEMF somewhat more susceptible to the deteriorating environmental conditions.

The structure of low-level vorticity at the start of the DWEMF (see Figure 110) appeared very similar in intensity and spatial coverage to that exhibited by the non-developing WRF simulation 25 (see Figure 111). However, not long into the simulation, the appearance of low-level vorticity in the DWEMF more closely matched the structure and intensity exhibited by the control simulation. This suggested the processes responsible for the amplification of low-level vorticity in the DWEMF were similar to those of the control simulation. A circulation budget comparison confirmed this to be the case (see Figure 114 and Figure 115). Positive low-level circulation tendencies were primarily due to stretching processes for both the DWEMF and the control simulation.

The circulation budget analysis suggested the nature of convection was very similar in the DWEMF and the control simulation. Boxed averaged quantities revealed that the vertical velocity, low-level convergence, diabatic heating rate, and precipitation rate were generally largest in the DWEMF, and that the DWEMF profiles were most similar to those of the control simulation (see Figure 116). The third hypothesis of this study proposed that if high-resolution model simulations were initialized with a more realistic vortex structure, the nature of the precipitation processes would be affected, with the implication that this would limit development of TCS025 in the model simulations. However, the analysis of the low-level spin-up of the DWEMF and comparison of the convective characteristics revealed this hypothesis to be invalid. Despite initializing the DWEMF with a misaligned circulation structure, convective precipitation processes were quite strong and were responsible for the low-level spin-up of the circulation within an environment that was still favorable for development.

To examine whether the TCS025 disturbance was likely to develop from slightly different initial conditions, each ensemble member was initialized from its state at 0600 UTC 28 August and integrated forward in forecast mode (no further data assimilation). Although there was a large spread in solutions, the majority of the ensemble members exhibited development of the TCS025 system (see Figure 117). This suggests that without data assimilation to constrain the model solution, the strong convective precipitation processes present in the model tended to dictate the outcome: development of TCS025.



## **D. CONCLUSIONS**

In summary, based on the observational analysis, the TCS025 disturbance failed to develop in part due to misalignment of the vortex structure in the vertical. This increased the system-relative flow and allowed outside environmental influences to negatively impact the inner-core thermodynamic structure of TCS025, which weakened subsequent convection. Observations suggested stratiform precipitation processes were more prevalent than convective processes. Without deep convection, spin-up of the low-level circulation was limited and circulation alignment remained poor. It was concluded that the negative feedback between limited convection and poor vertical alignment of the circulation while in the presence of deteriorating environmental conditions inhibited development of the TCS025 disturbance.

The multi-physics ensemble revealed that in simulations that exhibited strong convective precipitation processes, the low-level circulation intensified and TCS025 developed. To assess whether the propensity for strong convection and over-development might have been due to an unrealistically aligned vortex structure present in the initial conditions, data assimilation experiments were conducted to improve the initial conditions. The assimilation of all observations, including ELDORA radar observations, provided initial conditions that were more representative of the observed structure of TCS025, which was not aligned in the vertical. Strong convective precipitation processes also occurred in the DART-WRF ensemble mean forecast, and ultimately this led to the development of the TCS025 disturbance. However, the development was delayed relative to the control simulation. This indicates that the misalignment of the vortex structure in the DWEMF was overcome by convective precipitation processes that eventually led to alignment of the vortex and intensification.

At the time of the TCS-08 field experiment, it was uncertain whether the TCS025 disturbance would experience development. The numerical experiments presented in this study suggest that the proper representation of microphysical processes (and boundary layer processes) in numerical models is critical if storm development or non-development is to be forecast accurately, especially for systems similar to TCS025 that are sensitive to the nature of the precipitation processes.

THIS PAGE INTENTIONALLY LEFT BLANK

## VII. FUTURE WORK AND RECOMMENDATIONS

The in-situ observational dataset collected during TCS025 provided a unique opportunity to examine the evolution of a non-developing tropical disturbance. Although many details of the non-development of TCS025 were examined in this observational and modeling study, there are aspects that could be expanded upon and several findings worthy of further examination.

The DART-WRF data assimilation system was used to assimilate all available data collected during the second and third IOPs to provide a more realistic circulation structure of the TCS025 disturbance. As an extension to this study, additional data assimilation experiments could be conducted to examine the impact that individual observational data sets (e.g., dropwindsondes, flight-level data, ELDORA radial velocity) had on the structure and evolution of TCS025.

Data thinning was necessary in the implementation of the DART-WRF ensemble system due to computational limitations and numerical issues. Due to time constraints, the amount of data was reduced by omitting observations to achieve an observational spacing that roughly matched the grid spacing of the analysis. This approach could be improved upon by employing a more sophisticated averaging technique for the various datasets.

The numerical modeling component of this study revealed that the development of TCS025 in the model simulations was extremely sensitive to the diabatic heating rate. This points to the importance of adequately representing precipitation processes if forecasts of storm formation are to be improved. While recent studies have compared differences in the latent heating profiles of developing and non-developing systems (e.g., Park and Elsberry 2013), more work is needed to further explore these differences and their causes. Additional high-resolution numerical simulations that focus on the precipitation structure in both developing and non-developing environments are needed in combination with verifying airborne Doppler radar observations. Furthermore, it is

recommended that a flight track consisting of a limited number of turns be used during operation of the Doppler radar to reduce uncertainty in the vertical velocity observations.

The majority of observations collected during TCS025 were centered on 0000 UTC, which is after the diurnal convective maximum time, so that observations could be made available in near-real time for global forecast data assimilation systems. Although improving short- to mid-range forecasts is of unquestioned importance, it would also be beneficial to sample the storm structure at other times during the convective cycle, especially leading up to the diurnal convective maximum time.

Vertical wind shear was an important factor in the misalignment and non-development of TCS025. Interestingly, high-resolution simulations indicated that deep convection impacted the upper-level flow and reduced the magnitude of vertical wind shear (see Davis and Bosart 2004; Hendricks and Montgomery 2006). More study is needed to better understand the relationship between deep convection and vertical wind shear. Additional numerical simulations with high temporal resolution might be used to examine the interaction between strong updrafts and the upper-level flow structure. In addition, since the computed environmental vertical wind shear may be different than the shear experienced over a small-scale area of convection or for an asymmetric system like TCS025, it remains an open question of how to best quantify vertical wind shear with respect to its impact on storm formation.

## **APPENDIX A. BUDGET BOX SENSITIVITY ANALYSIS**

The time over which pertinent vorticity features and areas of deep convection remained within a particular boxed region decreased as box size was reduced. Therefore, using larger budget boxes allowed for budget and average computations to be extended over a longer period of time. In addition, since the intensity of the convective areas and vorticity features often varied in time and location between simulations, using a larger box also allowed for comparisons amongst simulations despite these differences. It was therefore a question of whether box size, location, and time span over which averages were computed impacted circulation budgets and box-average profiles. To facilitate a comparison, circulation budgets and box-average profiles were computed and compared for several different box configurations.

### **A. MAGENTA: 1200 UTC 27 AUGUST – 1800 UTC 27 AUGUST**

Average profiles and a circulation budget were computed for the magenta box (see Figure 79) from 1200 UTC 27 August to 1800 UTC 27 August. A small area of convection and increased vorticity were present within this region during this time. Although the magnitudes of quantities were generally larger than for the other boxed regions, the general patterns appeared very similar. The upper-level vertical velocity (Figure 120a) was strongest in the simulation 9 (control simulation), and weakest in the non-developing simulation 25. The diabatic heating profiles (Figure 120b) for the moderate developing simulation 12 were very similar to those from simulation 9, except near 400 hPa where the diabatic heating was slightly stronger in simulation 9.

Perhaps the most notable aspect of the magenta box was that the average vorticity was notably weaker near the surface compared to in the mid-troposphere (Figure 120c). The mid-level maximum in vorticity was not uncommon among other boxed regions, but low-level vorticity was relatively weak in the magenta box. This appears to have been a result of computing the circulation budget during the first six hours of simulation time, rather than for a period of time later in the simulation, as the average vorticity within the larger blue-boxed region was initially strongest in the mid-troposphere (see Figure 82a).

Vertical velocity (Figure 120a), diabatic heating rate (Figure 120b), low- and mid-level vorticity (Figure 120c), low-level convergence, and upper-level divergence (Figure 120d) were strongest in simulations 9 and 12, but there was not much spread between profiles as very little time had passed since the start of the simulations to allow for significant differences in model solutions.

The time series of the average precipitation rate (Figure 120e) appeared very similar to that of the blue- and brown-boxed regions. The largest precipitation rates occurred in simulation 9, followed by simulations 12 and 25. Interestingly, all three cases exhibited precipitation rates that exceeded the TRMM average for this area and time period.

The integrated circulation budget tendencies within the magenta-boxed region for simulation 9 (Figure 120f) indicates positive tendencies from eddy fluxes and stretching processes were dominant in the lower-troposphere. The stretching tendency profile matched that from other boxed regions, but the eddy flux contribution within the magenta box was larger than in other boxed regions. This was a result of the small box size as vorticity features were likely to enter or leave the box during the six hour budget time. The contribution from eddy fluxes became less important for larger boxed areas (see Figure 121f and Figure 122f).

## **B. BROWN: 1800 UTC 27 AUGUST – 0000 UTC 28 AUGUST**

A circulation budget and average profile analysis was also conducted for the brown-boxed region (see Figure 79), which was slightly larger than the magenta box, and extended from 1800 UTC 27 August to 0000 UTC 28 August. Most of the average profiles appeared very similar to those from the magenta-boxed region, but were of smaller magnitude.

Similar to the magenta-boxed region, the precipitation rate (Figure 121e) was largest in simulation 9, and smallest in simulation 25. The average low-level vorticity (Figure 121c) was stronger in the brown-boxed region compared to the magenta box (see Figure 120c), but mid-level vorticity was weaker within the brown box. In addition, there was a greater difference in the magnitude of diabatic heating (Figure 121b), low-level

convergence (Figure 121d), low-level vorticity (Figure 121c), and upper-level vertical velocity (Figure 121a) between simulations 9 and 12 compared to the magenta box. The increase in spread between the profiles of simulations 9 and 12 relative to the magenta-boxed region was a result of using a budget time period that was later in the simulation, which allowed the solutions of the two simulations to diverge somewhat. Similar to the magenta boxed-region, average profiles from the non-developing simulation 25 were noticeably smaller in magnitude compared to the other two simulations, which indicates that the convective precipitation processes in simulation 25 were much weaker.

The integrated circulation budget profiles (Figure 121f) for simulation 9 within the brown-boxed region indicate that positive stretching processes were also the most important in the lower troposphere. The contribution from eddy fluxes was smaller in the low-levels relative to the magenta-boxed region. Perhaps most different were the contributions from the tilting tendencies; the tilting tendencies within the magenta box were negative and large in magnitude below 600 hPa, whereas the tendencies from tilting within the brown-boxed region were positive throughout the profile, especially near the surface and in the upper-levels.

### **C. BLUE: 1800 UTC 27 AUGUST – 0600 UTC 28 AUGUST**

Average profiles and a circulation budget were also computed for the larger blue-boxed region (see Figure 79) for the twelve hour period extending from 1800 UTC 27 August to 0600 UTC 28 August. Aside from smaller magnitudes compared to the magenta- and brown-boxed regions, qualitatively there were no significant differences. Vertical velocity (Figure 122a), low-level convergence, upper-level divergence (Figure 122d), low- and mid-level vorticity (Figure 122c), diabatic heating rate (Figure 122b), and precipitation rate (Figure 122e) were generally largest in simulation 9 and smallest in simulation 25.

The integrated circulation budget profiles (Figure 122f) for the blue-boxed region of simulation 9 were most similar in structure to those of the brown-boxed region. The largest contribution to the circulation tendency profile in the low- and upper-levels was from the stretching tendency.

Therefore, based on the qualitative comparison of averaged quantities and integrated circulation budget profiles of the various boxed regions, it was concluded that there was little sensitivity to the location and size of the region during the early part of the simulations. Although magnitudes of averaged quantities were larger for smaller regions, the relative difference between profiles remained the same: the magnitude of vertical velocity, diabatic heating, low-level convergence, upper-level divergence, low- and mid-level vorticity was largest in the developing simulation 9, and smallest in the non-developing simulation 25. Thus, to allow for differences amongst the simulations relating to the position and timing of convection and vorticity features of interest, the blue-boxed region was used for the detailed comparison.



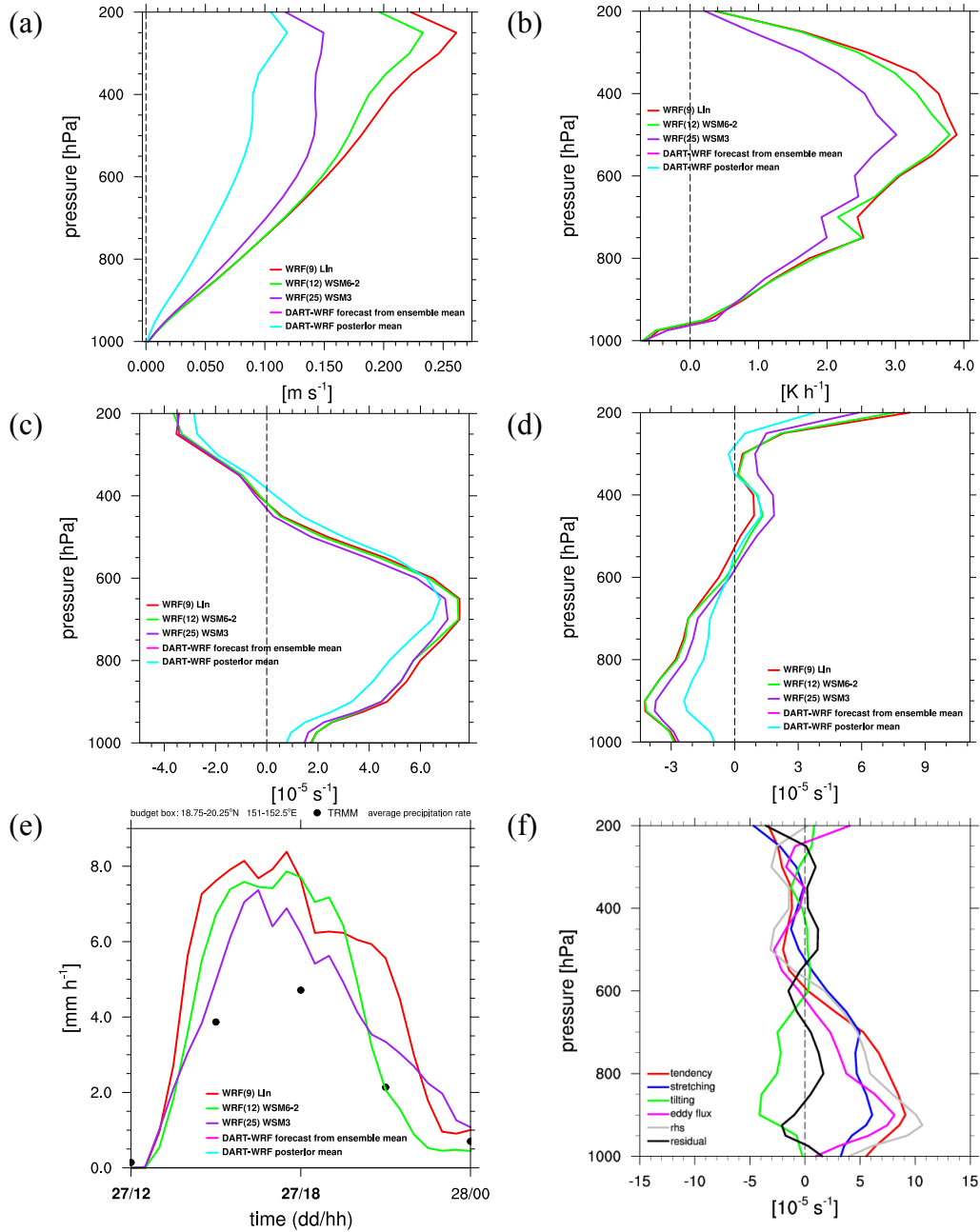


Figure 120 Average profiles of (a) vertical velocity ( $\text{m s}^{-1}$ ), (b) diabatic heating rate ( $\text{K h}^{-1}$ ), (c) relative vorticity ( $10^{-5} \text{ s}^{-1}$ ), (d) divergence ( $10^{-5} \text{ s}^{-1}$ ), and (e) precipitation rate ( $\text{mm h}^{-1}$ ) for WRF simulations 9 (red), 12 (green), 25 (purple), DART-WRF ensemble mean forecast (magenta), and the DART-WRF posterior mean (cyan). Quantities were averaged within the **magenta**-boxed region in Figure 72, and averaged in time for (a, b, c, d) from 1200 UTC 27 August to 1800 UTC 27 August. (f) Profiles of integrated circulation budget contributions for WRF simulation 9 for the time period from 1200 UTC 27 August to 1800 UTC 27 August. Black dots in (e) denote the average TRMM precipitation estimate for the magenta-boxed region at corresponding times.

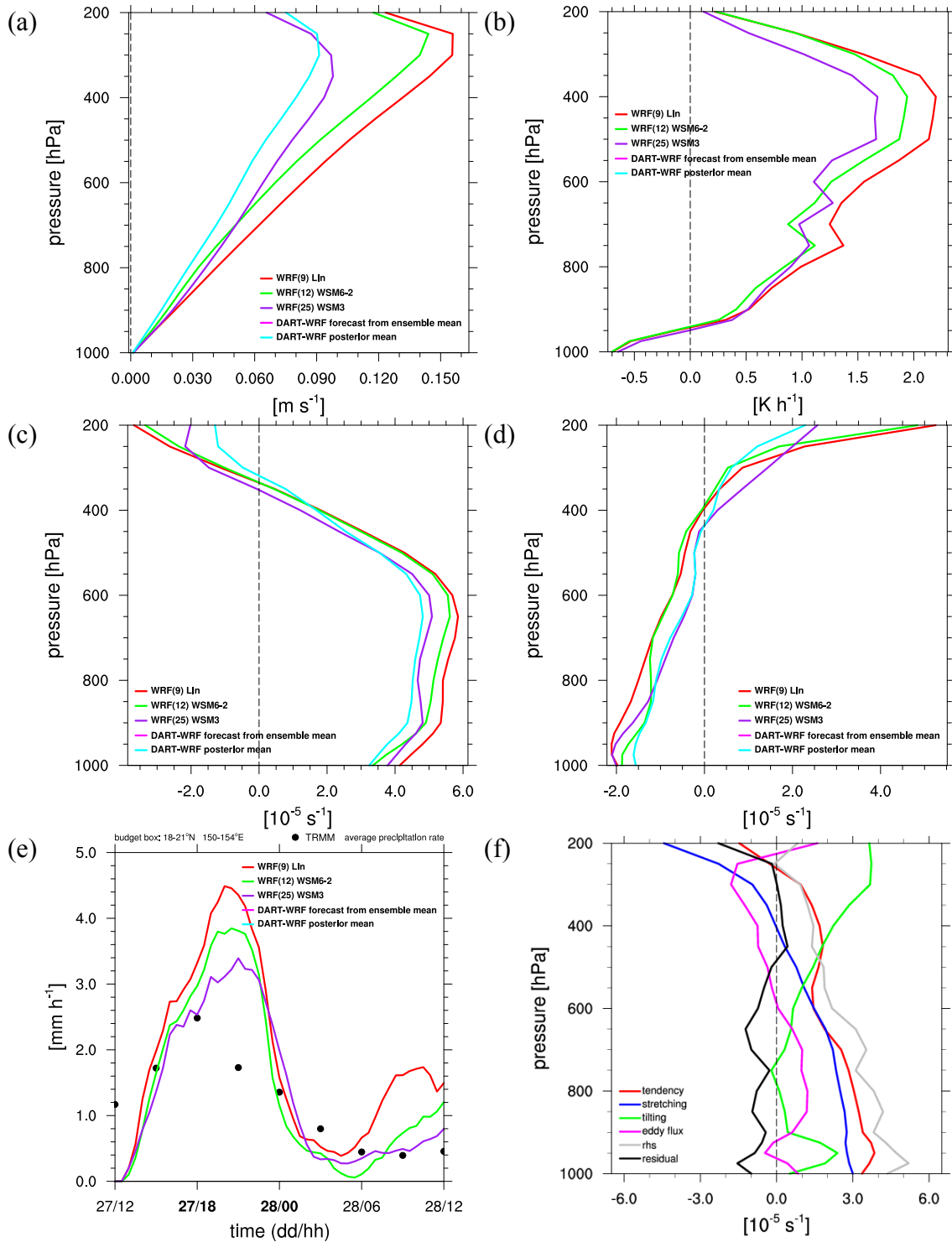


Figure 121 Same as Figure 120, except quantities were averaged within the **brown**-boxed region in Figure 72, and averaged in time for (a, b, c, d) from 1800 UTC 27 August to 0000 UTC 28 August. (f) Profiles of integrated circulation budget contributions for WRF simulation 9 for the time period from 1800 UTC 27 August to 0000 UTC 28 August.

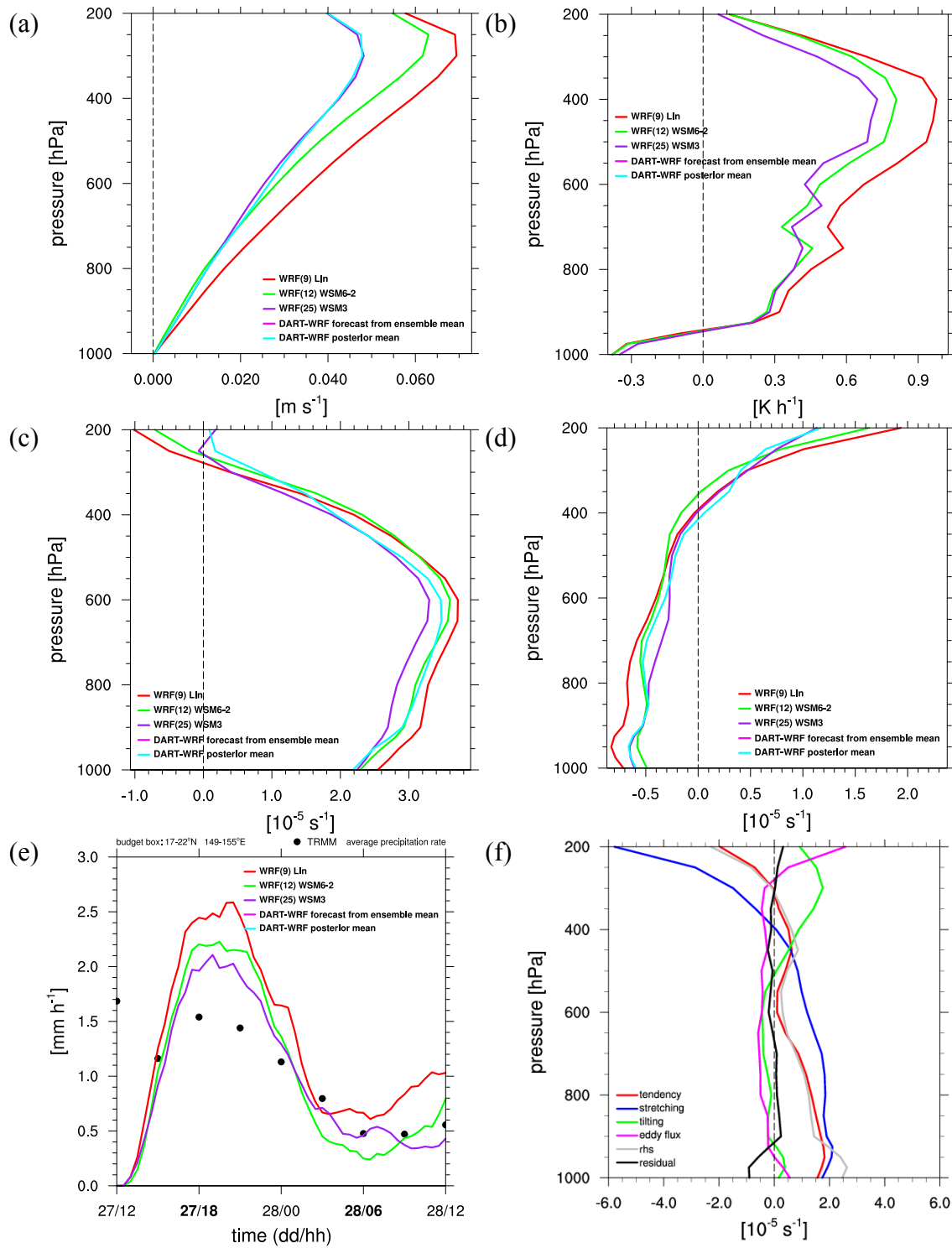


Figure 122 Same as Figure 120, except quantities were averaged within the **blue**-boxed region in Figure 72, and averaged in time for (a, b, c, d) from 1800 UTC 27 August to 0600 UTC 28 August. (f) Profiles of integrated circulation budget contributions for WRF simulation 9 for the time period from 1800 UTC 27 August to 0600 UTC 28 August.

THIS PAGE INTENTIONALLY LEFT BLANK

## **APPENDIX B. ECMWF-DROPWINDSONDE THERMODYNAMIC COMPARISON**

To examine why the convective response in the WRF simulations was so strong relative to observations, the thermodynamic conditions in the ECMWF analysis, which were used to initialize the WRF simulations, were compared with dropwindsonde data to determine if they were representative of actual conditions. Since the majority of the WRF simulations began to diverge from reality by the time of the second IOP (~0000 UTC 28 August), a direct comparison of WRF simulation output with observations was not attempted.

In agreement with MTSAT IR observations, convection exhibited by the ECMWF analysis was relatively weak (not shown). However, since the WRF model was initialized from the ECMWF analysis, and generally exhibited a much stronger convective response, it was not clear whether the lack of convective activity in the ECMWF analysis was the result of model deficiencies (i.e., the correct response for the wrong reasons). If the strong convection in the WRF simulations was due to initial and lateral boundary conditions that were incorrectly “primed” to support deep convection, it is possible that the lack of adequate horizontal resolution in the ECMWF analysis limited convection in the ECMWF model for the wrong reasons. The high-resolution WRF simulations had the ability to resolve small scale features (i.e., convection was explicitly resolved), whereas the resolution of the ECMWF was relatively coarse, and necessitated the use of a convective parameterization scheme. It is therefore worthwhile to examine whether the thermodynamic environment depicted by the ECMWF analysis matched observations.

The dropwindsonde comparison was conducted using data collected during the second IOP, which was twelve hours after the WRF simulations were initialized. As stated in section II, the WRF simulations were initialized after the first IOP to take advantage of data-improved initial conditions.

Individual dropwindsonde profiles (screw-T log-P diagrams) from convective and non-convective regions were examined (two example profiles are displayed in Figure 123), and it was found that the profiles agreed quite closely with the ECMWF analysis.

This was not surprising given that the dropwindsonde data were available for assimilation by the ECMWF data assimilation system in near real-time during the T-PARC/TCS-08 field experiment.

Average profiles of thermodynamic quantities were also examined from the second USAF WC-130J mission (0325W) during the second IOP, and compared with the ECMWF thermodynamic fields. MTSAT IR brightness temperature was interpolated to the location and time of each dropwindsonde such that averages could be created for convective environments (IR brightness temperature less than  $-35^{\circ}\text{C}$ ) and non-convective environments (IR brightness temperature greater than  $-35^{\circ}\text{C}$ ).

The average profiles of relative humidity (Figure 124a,c) reveal good agreement between the ECMWF analysis and dropwindsonde data, especially below 7 km. Deviations above this level are not surprising as small changes in specific humidity at such low temperatures can have a large impact on the relative humidity. Small deviations in relative humidity are present between 1 km and 4 km for both the convective and non-convective environments, but are generally small (less than 5% difference). Most importantly, the relative humidity values were in close agreement near the surface, which is where deviations might have caused a large convective response similar to that exhibited by the WRF model.

The average dropwindsonde profiles of  $\theta_e$  also agree quite closely with the ECMWF analysis in both the convective and non-convective environments (Figure 124b), however there was a low-bias in the ECMWF analysis below 2 km and a high bias within a very shallow layer near the surface. Differences in average  $\theta_e$  reveal the low bias in the ECMWF analysis below 2 km to be between 2 K and 3 K and the high bias near the surface to be about 3 K in the convective environment profiles (Figure 124d). This suggests there were shallow regions of low-level cooling not resolved by the ECMWF, which were most likely due to evaporative downdrafts in the real atmosphere. Reasons why the ECMWF failed to resolve the low-level cooling in the convective regions are not clear. Since the low- and mid-level thermodynamic dropwindsonde data

appear to have been assimilated by the ECMWF, it is likely that the convectively-generated cold pools were too shallow to be adequately resolved by the ECMWF model.

In general, the thermodynamic conditions in the ECMWF analysis closely matched those observed from dropwindsonde data. Notable ECMWF biases included a low- $\theta_e$  bias below 2 km, and a high- $\theta_e$  bias in the convective environment within a shallow layer adjacent to the surface. It is therefore concluded that the thermodynamic conditions within the ECMWF analysis were representative of the actual conditions based on dropwindsonde observations. It is unlikely that the lack of an extremely shallow near-surface cold pool in the ECMWF analysis would have led to a greater propensity for deep convection in the WRF simulations.

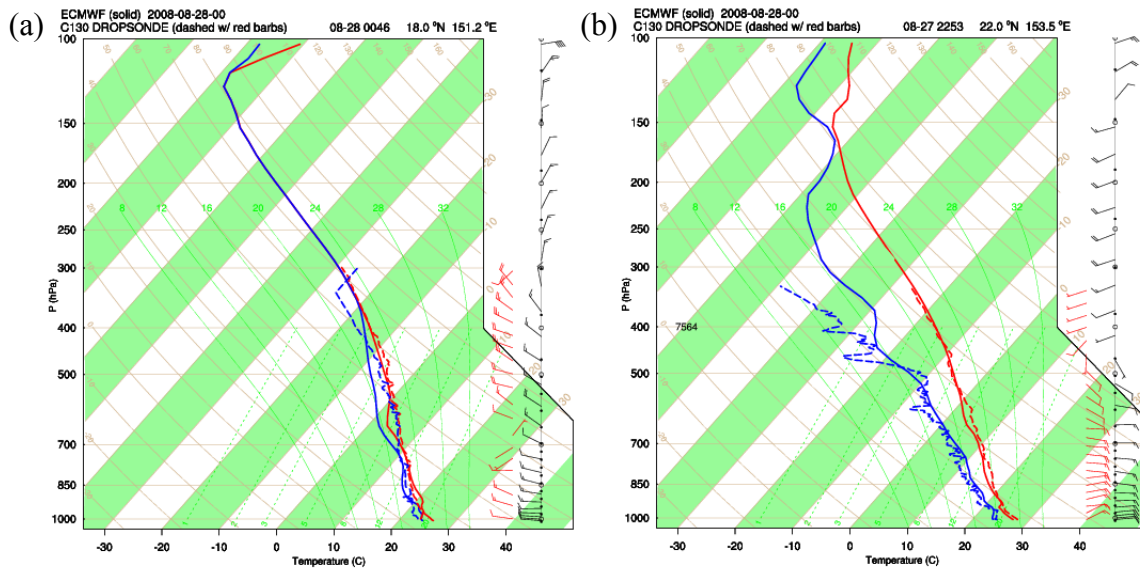


Figure 123 Skew-T log-P comparisons in (a) and (b) constructed from dropwindsondes “A” and “B” in Figure 43, respectively, (dashed colors), and the ECMWF analysis at the same locations (solid colors), valid at 0000 UTC 28 August. Red and blue profiles correspond to temperature and dewpoint, respectively. Black wind barbs represent winds from the ECMWF analysis, and red wind barbs are for dropwindsonde winds (1 full barb = 10 kt).



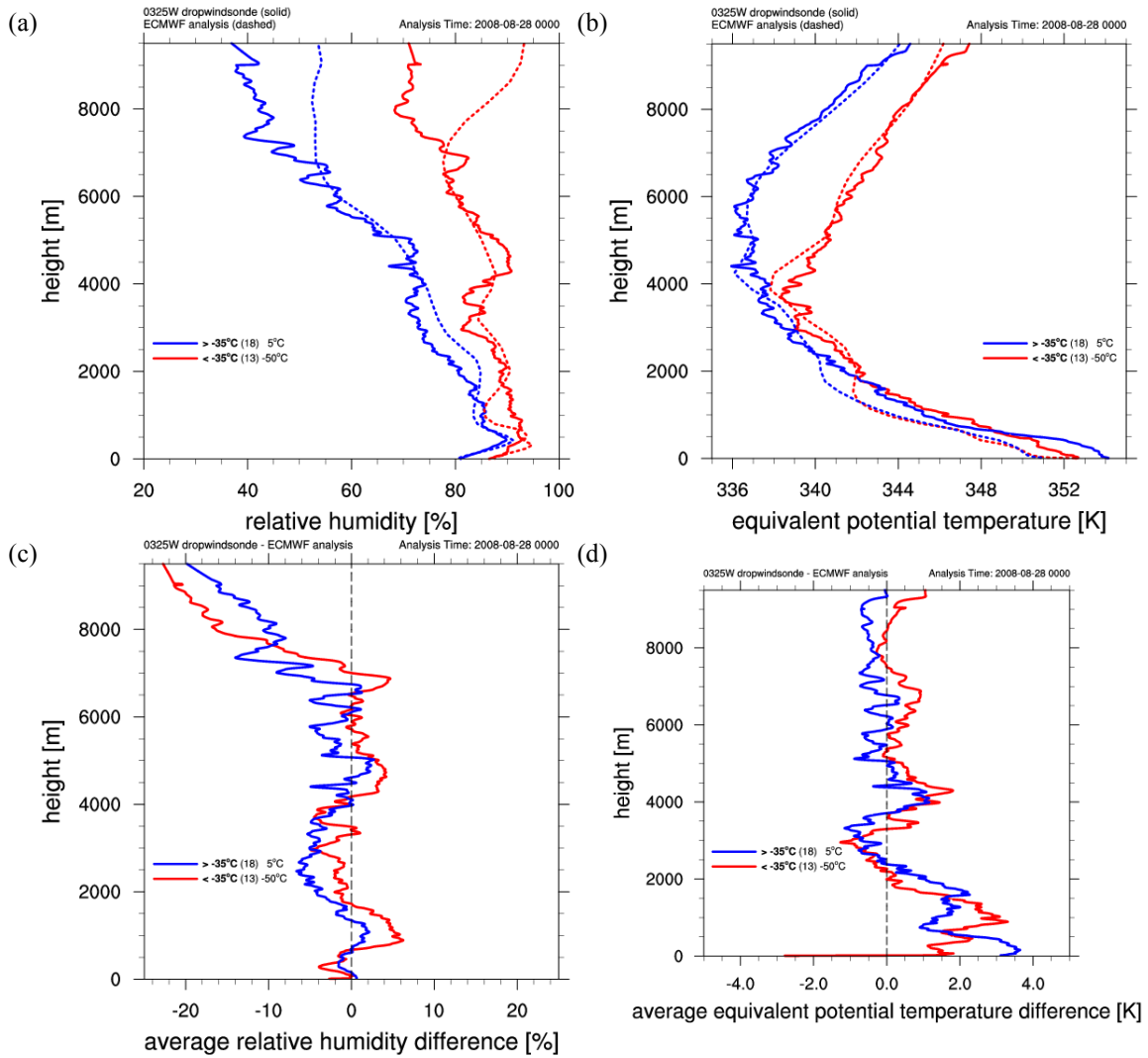


Figure 124 Vertical profiles of (a) average relative humidity (%), (b) average  $\theta_e$  (K), (c) average relative humidity difference (%), and (d) average  $\theta_e$  difference (K) from dropwindsonde data collected during the second USAF WC-130J mission (0325W), and the ECMWF analysis at the same locations, valid at 0000 UTC 28 August. Red and blue profiles correspond to dropwindsondes for which the MTSAT IR brightness temperature (interpolated to the dropwindsonde time and location) was less than  $-35^{\circ}\text{C}$  and greater than  $-35^{\circ}\text{C}$ , respectively.

THIS PAGE INTENTIONALLY LEFT BLANK

## APPENDIX C. PV-WEIGHTED CENTER POSITIONS

To analyze the vertical alignment of the circulation for the various multi-physics ensemble cases and the DART-WRF ensemble mean forecast, the PV-weighted center positions at 900 hPa and 500 hPa were computed based on a method described by Davis et al. (2008a).

Due to the relative weakness of the TCS025 system, objectively identifying the pertinent PV features associated with the TCS025 disturbance proved problematic at times. In order to provide continuity in time, and constrain the center to be within the region of interest, the PV-weighted center position was computed within a boxed region surrounding subjectively determined 900 hPa and 500 hPa circulation center positions that were smoothed in time using a 5-point running average ( $\pm 1$  hour). Sensitivity experiments were conducted to examine the impact of box size and the use of an exponential weighting factor. Each set of parameters tested had strengths and weaknesses, but after a configuration was chosen that appeared to work best, it was kept consistent for all analyses.

A box size of  $\pm 3^\circ$  was found to work best as this was generally large enough to encompass the majority of the PV features associated with the low- and mid-level circulations. Larger boxes tended to result in center positions that were biased toward the box center. An example of 900 hPa and 500 hPa PV-weighted center positions that were identified within a  $\pm 3^\circ$  box of the subjectively identified circulation centers are shown in Figure 125.

In addition, it was determined that an exponential weighting factor of 2 seemed to work best. This allowed the center positions to track more closely to the stronger PV features within the box and also helped reduce biases toward the center of the box. Figure 126 compares the effect of using exponential weighting factors of 1 and 2 at a time when the PV was asymmetrically distributed relative to the circulation center.

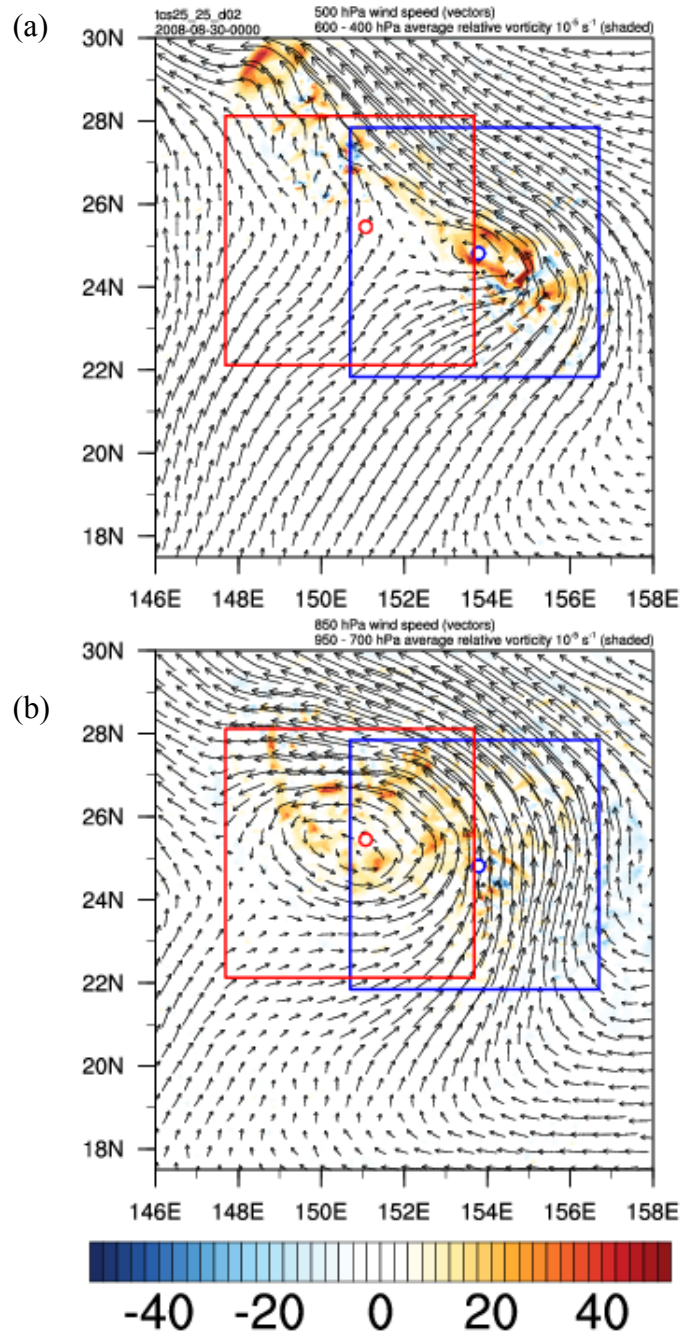


Figure 125 Relative vorticity (shaded,  $10^{-5} \text{ s}^{-1}$ ) averaged between (a) 600-400 hPa and (b) 950-700 hPa and wind speed at (a) 500 hPa and (b) 850 hPa (vectors) for the non-developing WRF simulation 25 at 0000 UTC 30 August. The blue and red open circles correspond to the diagnosed PV-weighted center positions at 500 hPa and 900 hPa, respectively. The blue- and red-boxed regions correspond to the area over which the PV-weighted center positions were calculated.

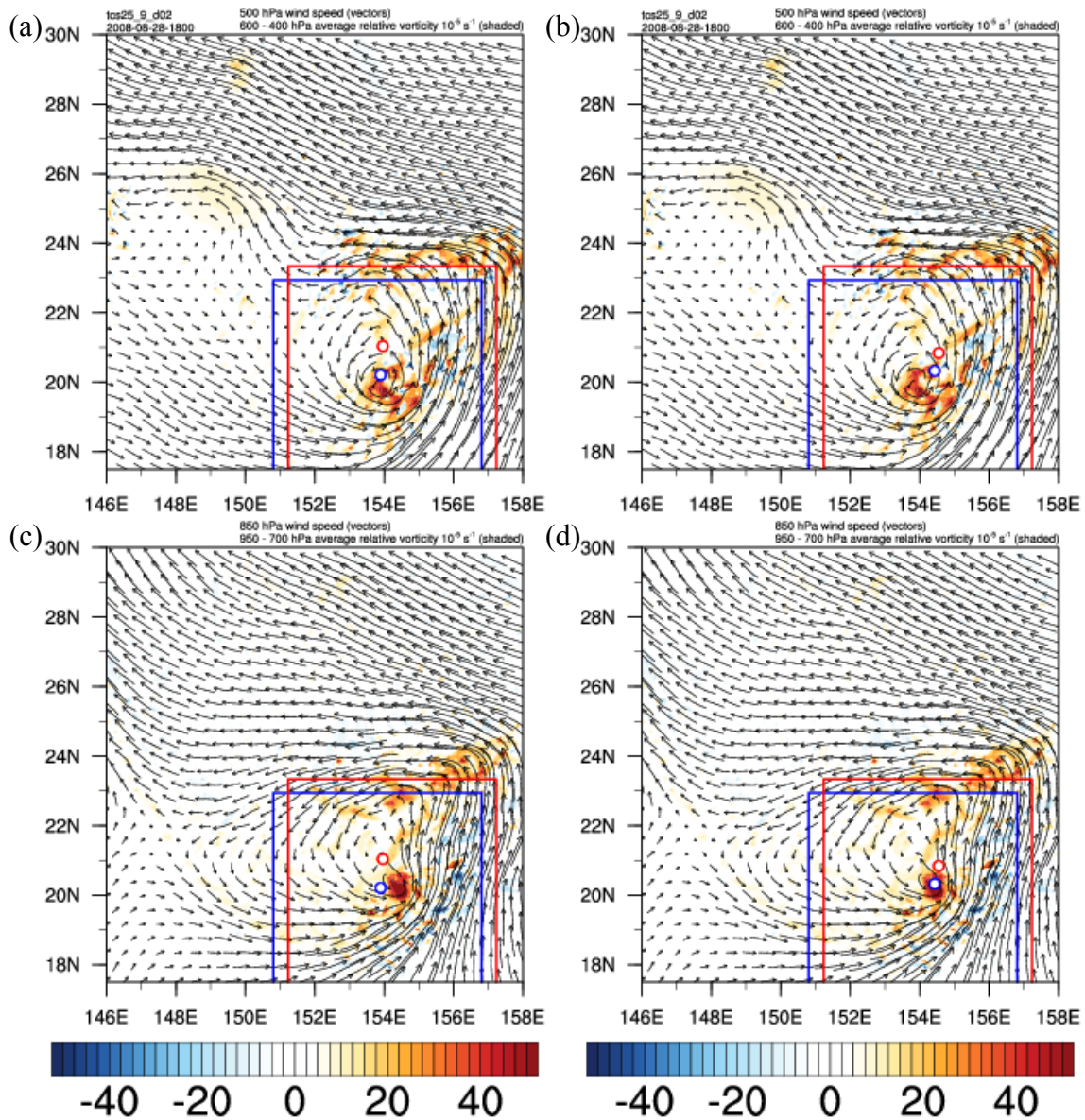


Figure 126 Relative vorticity (shaded,  $10^{-5} \text{ s}^{-1}$ ) averaged between (a, b) 600-400 hPa and (c, d) 950-700 hPa and wind speed at (a, b) 500 hPa and (c, d) 850 hPa (vectors) for the WRF control simulation 9 at 1800 UTC 28 August. The blue and red open circles correspond to the diagnosed PV-weighted center positions at 500 hPa and 900 hPa, respectively. The blue- and red-boxed regions correspond to the area over which the PV-weighted center positions were calculated. PV center positions were determined using exponential weighting factors of 1 in (a, c) and 2 in (b, d).

THIS PAGE INTENTIONALLY LEFT BLANK

## LIST OF REFERENCES

- Anderson, J. L., 2001: An ensemble adjustment Kalman filter for data assimilation. *Mon. Wea. Rev.*, **129**, 2884–2903.
- Anderson, J. L., 2003: A local least squares framework for ensemble filtering. *Mon. Wea. Rev.*, **131**, 634–642.
- Anderson, J., T. Hoar, K. Raeder, H. Liu, N. Collins, R. Torn, and A. Avellano, 2009: The data assimilation research testbed: A community facility. *Bull. Amer. Meteor. Soc.*, **90**, 1283–1296.
- Bartels, D. L., and R. A. Maddox, 1991: Midlevel cyclonic vortices generated by mesoscale convective systems. *Mon. Wea. Rev.*, **119**, 104–118.
- Bell, M. M., and M. T. Montgomery, 2010: Sheared deep vortical convection in pre-depression Hagupit during TCS08. *Geophys. Res. Lett.*, **37**, L06802, doi:10.1029/2009GL042313.
- Bell, M. M., M. T. Montgomery, and K. A. Emanuel, 2012: Air-sea enthalpy and momentum exchange at major hurricane wind speeds observed during CBLAST. *J. Atmos. Sci.*, **69**, 3197–3222.
- Bell, M. M., W.-C. Lee, C. A. Wolff, and H. Cai, 2013: A Solo-based automated quality control algorithm for airborne tail Doppler radar data. *J. Appl. Meteor. Climatol.*, in press.
- Bister, M., and K. A. Emanuel, 1997: The genesis of Hurricane Guillermo: TEXMEX analyses and a modeling study. *Mon. Wea. Rev.*, **125**, 2662–2682.
- Chen, S. S., and W. M. Frank, 1993: A numerical study of the genesis of extratropical convective mesovortices. Part I: Evolution and dynamics. *J. Atmos. Sci.*, **50**, 2401–2426.
- Chen, S.-H., and W.-Y. Sun, 2002: A one-dimensional time dependent cloud model. *J. Meteor. Soc. Japan*, **80**, 99–118.
- Davis, C. A., and L. F. Bosart, 2004: The TT problem: Forecasting the tropical transition of cyclones. *Bull. Amer. Meteor. Soc.*, **85**, 1657–1662.
- Davis, C. A., S. C. Jones, and M. Riemer, 2008a: Hurricane vortex dynamics during Atlantic extratropical transition. *J. Atmos. Sci.*, **65**, 714–736.
- Davis, C., C. Snyder, and A. C. Didlake, 2008b: A vortex-based perspective of eastern Pacific tropical cyclone formation. *Mon. Wea. Rev.*, **136**, 2461–2477.

- Davis, C. A., and T. J. Galarneau, 2009: The vertical structure of mesoscale convective vortices. *J. Atmos. Sci.*, **66**, 686–704.
- Davis, C. A., and D. A. Ahijevych, 2012: Mesoscale structural evolution of three tropical weather systems observed during PREDICT. *J. Atmos. Sci.*, **69**, 1284–1305.
- Davis, C. A., S. C. Jones, D. Anwender, J. Badey, and L. Scheck, 2013: Mesoscale cyclogenesis over the western North Pacific Ocean during TPARC. *Tellus A*, **65**, 18621, <http://dx.doi.org/10.3402/tellusa.v65i0.18621>.
- Davis, C. A., and D. A. Ahijevych, 2013: Thermodynamic environments of deep convection in Atlantic tropical disturbances. *J. Atmos. Sci.*, **70**, 1912–1928.
- DeMaria, M., 1996: The effect of vertical shear on tropical cyclone intensity change. *J. Atmos. Sci.*, **53**, 2076–2088.
- Dolling, K. P., and G. M. Barnes, 2012a: The creation of a high equivalent potential temperature reservoir in Tropical Storm Humberto (2001) and its possible role in storm deepening. *Mon. Wea. Rev.*, **140**, 492–505.
- Dolling, K., and G. M. Barnes, 2012b: Warm-core formation in Tropical Storm Humberto (2001). *Mon. Wea. Rev.*, **140**, 1177–1190.
- Doyle, J. D., C. A. Reynolds, C. Amerault, and J. Moskaitis, 2012: Adjoint sensitivity and predictability of tropical cyclogenesis. *J. Atmos. Sci.*, **69**, 3535–3557.
- Dudhia, J., 1989: Numerical study of convection observed during the winter monsoon experiment using a mesoscale two-dimensional model. *J. Atmos. Sci.*, **46**, 3077–3107.
- Dudhia, J., 1996: A multi-layer soil temperature model for MM5. Preprints, *Sixth PSU/NCAR Mesoscale Model Users' Workshop*, Boulder, CO, NCAR, 3 pp. [Available online at <http://www.mmm.ucar.edu/mm5/lsm/soil.pdf>.]
- Dunkerton, T. J., M. T. Montgomery, and Z. Wang, 2009: Tropical cyclogenesis in a tropical wave critical layer: Easterly waves. *Atmos. Chem. Phys.*, **9**, 5587–5646.
- Elsberry, R. L., and P. A. Harr, 2008: Tropical cyclone structure (TCS08) field experiment science basis, observational platforms, and strategy. *Asia-Pacific J. Atmos. Sci.*, **44**, 209–231.
- Emanuel, K. A., 1986: An air-sea interaction theory for tropical cyclones. Part I: Steady-state maintenance. *J. Atmos. Sci.*, **43**, 585–605.
- Fovell, R. G., K. L. Corbosiero, and H.-C. Kuo, 2009: Cloud microphysics impact on hurricane track as revealed in idealized experiments. *J. Atmos. Sci.*, **66**, 1764–1778.



- Frank, W. M., and E. A. Ritchie, 1999: Effects of environmental flow upon tropical cyclone structure. *Mon. Wea. Rev.*, **127**, 2044–2061.
- Frank, W. M., and E. A. Ritchie, 2001: Effects of vertical wind shear on the intensity and structure of numerically simulated hurricanes. *Mon. Wea. Rev.*, **129**, 2249–2269.
- Fritsch, J. M., and J. S. Kain, 1993: Convective parameterization for mesoscale models: The Fritsch–Chappell scheme. *The Representation of Cumulus Convection in Numerical Models, Meteor. Monogr.*, No. 46, Amer. Meteor. Soc., 159–164.
- Fritsch, J. M., J. D. Murphy, and J. S. Kain, 1994: Warm core vortex amplification over land. *J. Atmos. Sci.*, **51**, 1780–1807.
- Fu, B., M. S. Peng, T. Li, and D. E. Stevens, 2011: Developing versus nondeveloping disturbances for tropical cyclone formation. Part II: Western North Pacific\*. *Mon. Wea. Rev.*, **140**, 1067–1080.
- Gray, W. M., 1975: Tropical cyclone genesis. Dept. of Atmos. Sci. Paper No. 234, Colo. State Univ., Ft. Collins, CO, 121 pp.
- Gray, W. M., 1982: Tropical cyclone genesis and intensification. Topics in Atmospheric and Oceanographic Sciences, Intense Atmospheric Vortices, L. Bengtsson and J. Lighthill, Eds., Springer-Verlag 3-20. [ISBN 3-540-11657-5.]
- Gray, W. M., 1998: The formation of tropical cyclones. *Meteorol. Atmos. Phys.*, **67**, 37–69.
- Harr, P. A., and R. L. Elsberry, 1996: Structure of a mesoscale convective system embedded in Typhoon Robyn during TCM-93. *Mon. Wea. Rev.*, **124**, 634–652.
- Harr, P. A., R. L. Elsberry, and J. C. L. Chan, 1996: Transformation of a large monsoon depression to a tropical storm during TCM-93. *Mon. Wea. Rev.*, **124**, 2625–2643.
- Harr, P. A., M. S. Kalafsky, and R. L. Elsberry, 1996: Environmental conditions prior to formation of a midget tropical cyclone during TCM-93. *Mon. Wea. Rev.*, **124**, 1693–1710.
- Hendricks, E. A., M. T. Montgomery, and C. A. Davis, 2004: The role of "vortical" hot towers in the formation of tropical cyclone Diana (1984). *J. Atmos. Sci.*, **61**, 1209–1232.
- Hendricks, E. A., and M. T. Montgomery, 2006: Rapid scan views of convectively generated mesovortices in sheared Tropical Cyclone Gustav (2002). *Wea. Forecasting*, **21**, 1041–1050.

- Hildebrand, P. H., W.-C. Lee, C. A. Walther, C. Frush, M. Randall, E. Loew, R. Neitzel, R. Parsons, J. Testud, F. Baudin, and A. LeCornec, 1996: The ELDORA/ASTRAIA airborne Doppler weather radar: High-resolution observations from TOGA COARE. *Bull. Amer. Meteor. Soc.*, **77**, 213–232.
- Hock, T. F., and J. L. Franklin, 1999: The NCAR GPS dropwindsonde. *Bull. Amer. Meteor. Soc.*, **80**, 407–420.
- Holland, G. J., 1987: Mature structure and structure change. *A Global View of Tropical Cyclones*, R. L. Elsberry, Ed., Naval Postgraduate School, 13–52.
- Holton, J. R., 2004: *An Introduction to Dynamic Meteorology*. 4th ed., Elsevier Academic Press, 529 pp.
- Hong, S.-Y., J. Dudhia, and S.-H. Chen, 2004: A revised approach to ice microphysical processes for the bulk parameterization of clouds and precipitation. *Mon. Wea. Rev.*, **132**, 103–120.
- Hong, S.-Y., Y. Noh, and J. Dudhia, 2006: A new vertical diffusion package with an explicit treatment of entrainment processes. *Mon. Wea. Rev.*, **134**, 2318–2341.
- Hong, S.-Y., K.-S. Sunny Lim, J.-H. Kim, J.-O. Jade Lim, and J. Dudhia, 2009: Sensitivity study of cloud-resolving convective simulations with WRF using two bulk microphysical parameterizations: ice-phase microphysics versus sedimentation effects. *J. Appl. Meteor. Climatol.*, **48**, 61–76.
- Houze, R. A., Jr., W.-C. Lee, and M. M. Bell, 2009: Convective contribution to the genesis of Hurricane Ophelia (2005). *Mon. Wea. Rev.*, **137**, 2778–2800.
- Houze, R. A., Jr., 2004: Mesoscale convective systems. *Rev. Geophys.*, **42**, RG4003, doi:10.1029/2004RG000150.
- Janjic, Z. I., 1990: The step-mountain coordinate: physical package, *Mon. Wea. Rev.*, **118**, 1429–1443.
- Janjic, Z. I., 1996: The surface layer in the NCEP Eta Model, *Eleventh Conference on Numerical Weather Prediction*, Norfolk, VA, 19–23 August; Amer. Meteor. Soc., Boston, MA, 354–355.
- Janjic, Z. I., 2002: Nonsingular Implementation of the Mellor–Yamada Level 2.5 Scheme in the NCEP Meso model, *NCEP Office Note*, **No. 437**, 61 pp.
- Jensen, J., 2009: Project managers quality report, Jorgen Jensen – TPARC. NCAR/Earth Observing Laboratory, 15 pp.
- Jones, S. C., 1995: The evolution of vortices in vertical shear. I: Initially barotropic vortices. *Q. J. R. Meteorol. Soc.*, **121**, 821–851.

- Jorgensen, D. P., P. H. Hildebrand and C. L. Frush, 1983: Feasibility test of an airborne pulse-Doppler meteorological radar. *J. Climate Appl. Meteor.*, **22**, 744–757.
- Kain, J. S., 2004: The Kain–Fritsch convective parameterization: An update. *J. Appl. Meteor.*, **43**, 170–181.
- Kalman, R. E., and R. S. Bucy, 1961: New results in linear filtering and prediction theory. *J. Basic Eng.*, **83D**, 95–108.
- Kerns, B. W., and S. S. Chen, 2013: Cloud clusters and tropical cyclogenesis: developing and non-developing systems and their large-scale environment. *Mon. Wea. Rev.*, **141**, 192–210.
- Lang, S. E., W.-K. Tao, X. Zeng, and Y. Li, 2011: Reducing the biases in simulated radar reflectivities from a bulk microphysics scheme: Tropical convective systems. *J. Atmos. Sci.*, **68**, 2306–2320.
- Lee, C. S., 1989a: Observational analysis of tropical cyclogenesis in the western North Pacific. Part I: Structural evolution of cloud clusters. *J. Atmos. Sci.*, **46**, 2580–2598.
- Lee, C. S., 1989b: Observational analysis of tropical cyclogenesis in the western North Pacific. Part II: Budget analysis. *J. Atmos. Sci.*, **46**, 2599–2616.
- Lee, W.C., M. Bell, C. Wolff, E. Loew, and M. Donovan, 2009: THORPEX Pacific Asian Regional Campaign (TPARC) and Tropical Cyclone Structure (TCS08) ELDORA data quality report. NCAR/Earth Observing Laboratory, 9 pp.
- Li, X., and Z. Pu, 2008: Sensitivity of numerical simulation of early rapid intensification of Hurricane Emily (2005) to cloud microphysical and planetary boundary layer parameterizations. *Mon. Wea. Rev.*, **136**, 4819–4838.
- Lim, K.-S. S., and S.-Y. Hong, 2010: Development of an effective double-moment cloud microphysics scheme with prognostic cloud condensation nuclei (CCN) for weather and climate models. *Mon. Wea. Rev.*, **138**, 1587–1612.
- Lin, Y.-L., R. D. Farley, and H. D. Orville, 1983: Bulk parameterization of the snow field in a cloud model. *J. Climate Appl. Meteor.*, **22**, 1065–1092.
- Malvig, S. C., 2009: Analysis of a non-developing tropical circulation system during the tropical cyclone structure (TCS08) field experiment. M.S. thesis, Dept. of Meteorology, Naval Postgraduate School, Monterey, CA, USA, 98 pp.
- McBride, J. L., 1981: Observational analysis of tropical cyclone formation. Part I: Basic description of data sets. *J. Atmos. Sci.*, **38**, 1117–1131.

- McBride, J. L., and R. Zehr, 1981: Observational analysis of tropical cyclone formation. Part II: Comparison of non-developing versus developing systems. *J. Atmos. Sci.*, **38**, 1132–1151.
- McFarquhar, G. M., H. Zhang, G. Heymsfield, J. B. Halverson, R. Hood, J. Dudhia, and F. Marks, 2006: Factors affecting the evolution of Hurricane Erin (2001) and the distributions of hydrometeors: Role of microphysical processes. *J. Atmos. Sci.*, **63**, 127–150.
- Mellor, G. L., and T. Yamada, 1982: Development of a turbulence closure model for geophysical fluid problems. *Rev. Geophys. Space Phys.*, **20**, 851–875.
- Mlawer, E. J., S. J. Taubman, P. D. Brown, M. J. Iacono, and S. A. Clough, 1997: Radiative transfer for inhomogeneous atmospheres: RRTM, a validated correlated-k model for the longwave. *J. Geophys. Res.*, (D14), 16663–16682.
- Molinari, J., J. Frank, and D. Vollaro, 2012: Convective bursts, downdraft cooling, and boundary layer recovery in a sheared tropical storm. *Mon. Wea. Rev.*, **141**, 1048–1060.
- Montgomery, M. T., L. L. Lussier III, R. W. Moore, and Z. Wang, 2010: The genesis of Typhoon Nuri as observed during the tropical cyclone structure 2008 (TCS-08) field experiment - Part 1: The role of the easterly wave critical layer. *Atmos. Chem. Phys.*, **10**, 9879–9900.
- Montgomery, M. T., M. E. Nicholls, T. A. Cram, and A. B. Saunders, 2006: A vortical hot tower route to tropical cyclogenesis. *J. Atmos. Sci.*, **63**, 355–386.
- Montgomery, M. T., and R. K. Smith, 2012: The genesis of Typhoon Nuri as observed during the Tropical Cyclone Structure 2008 (TCS08) field experiment - Part 2: Observations of the convective environment. *Atmos. Chem. Phys.*, **12**, 4001–4009.
- Musgrave, K. D., C. A. Davis, and M. T. Montgomery, 2008: Numerical simulations of the formation of Hurricane Gabrielle (2001). *Mon. Wea. Rev.*, **136**, 3151–3167.
- National Aeronautics and Space Administration (NASA), cited 2013: [Retrieved 7/16/2013 from: [http://disc.sci.gsfc.nasa.gov/precipitation/documentation/TRMM\\_README/TRMM\\_3B42\\_readme.shtml](http://disc.sci.gsfc.nasa.gov/precipitation/documentation/TRMM_README/TRMM_3B42_readme.shtml)].
- National Hurricane Center (NHC), cited 2012: [Retrieved 1/8/2013 from: <http://www.nhc.noaa.gov/aboutgloss.shtml#TROPCYC>].
- Nguyen, L. T., and J. Molinari, 2012: Rapid intensification of a sheared, fast-moving hurricane over the Gulf Stream. *Mon. Wea. Rev.*, **140**, 3361–3378.
- Nolan, D. S., 2007: What is the trigger for tropical cyclogenesis? *Aust. Met. Mag.*, **56**, 241–266.

- Nolan, D. S., Y. Moon, D. P. Stern, 2007: Tropical cyclone intensification from asymmetric convection: Energetics and efficiency. *J. Atmos. Sci.*, **64**, 3377–3405.
- Nolan, D. S., and M. G. McGauley, 2012: Tropical cyclogenesis in wind shear: Climatological relationships and physical processes. To appear in *Cyclones: Formation, Triggers, and Control*. K. Oouchi and H. Fudeyasu, eds., Nova Science Publishers, Hapauge, New York.
- Park, M.-S., C.-H. Ho, J. Kim, and R. Elsberry, 2011: Diurnal circulations and their multi-scale interaction leading to rainfall over the South China Sea upstream of the Philippines during intraseasonal monsoon westerly wind bursts. *Climate Dynam.*, **37**, 1483–1499.
- Park, M.-S., R. L. Elsberry, and P. A. Harr, 2012: Vertical wind shear and ocean heat content as environmental modulators of western North Pacific tropical cyclone intensification and decay. *Tropical Cyclone Research and Review*, **1**, 448–457.
- Park, M.-S., and R. L. Elsberry, 2013: Latent heating and cooling rates in developing and nondeveloping tropical disturbances during TCS-08: TRMM PR versus ELDORA retrievals. *J. Atmos. Sci.*, **70**, 15–35.
- Park, M.-S., A. B. Penny, R. L. Elsberry, B. J. Billings, J. D. Doyle, 2013: Latent heating and cooling rates in developing and nondeveloping tropical disturbances during TCS-08: Radar-equivalent retrievals from mesoscale numerical models and ELDORA. *J. Atmos. Sci.*, **70**, 37–55.
- Peng, M. S., B. Fu, T. Li, and D. E. Stevens, 2011: Developing versus nondeveloping disturbances for tropical cyclone formation. Part I: North Atlantic. *Mon. Wea. Rev.*, **140**, 1047–1066.
- Penny, A. B., S. C. Malvig, and Patrick A. Harr, 2010: The role of multiple mesoscale convective systems in a non-developing tropical disturbance observed during the Tropical Cyclone Structure-2008 (TCS-08) field experiment. 29th Conference on Hurricanes and Tropical Meteorology, Tucson AZ, *Amer. Meteorol. Soc.*, 10–14 May.
- Rappin, E. D., and D. S. Nolan, 2012: The effect of vertical shear orientation on tropical cyclogenesis. *Q. J. R. Meteorol. Soc.*, **138**, 1035–1054.
- Raymond, D. J., and H. Jiang, 1990: A theory for long-lived mesoscale convective systems. *J. Atmos. Sci.*, **47**, 3067–3077.
- Raymond, D. J., C. López-Carrillo, and L. L. Cavazos, 1998: Case-studies of developing east Pacific easterly waves. *Q. J. R. Meteorol. Soc.*, **124**, 2005–2034.
- Raymond, D. J., and S. L. Sessions, 2007: Evolution of convection during tropical cyclogenesis. *Geophys. Res. Lett.*, **34**, L06811, doi:10.1029/2006GL028607.

- Raymond, D. J., S. L. Sessions, and Ž. Fuchs, 2007: A theory for the spinup of tropical depressions. *Q. J. R. Meteorol. Soc.*, **133**, 1743–1754.
- Raymond, D. J., and C. López Carrillo, 2011: The vorticity budget of developing Typhoon Nuri (2008). *Atmos. Chem. Phys.*, **11**, 147–163.
- Raymond, D. J., S. L. Sessions, and C. López Carrillo, 2011: Thermodynamics of tropical cyclogenesis in the northwest Pacific. *J. Geophys. Res.*, **116**, D18101, doi:10.1029/2011JD015624.
- Reasor, P. D., M. T. Montgomery, and L. F. Bosart, 2005: Mesoscale observations of the genesis of Hurricane Dolly (1996). *J. Atmos. Sci.*, **62**, 3151–3171.
- Reasor, P. D., M. D. Eastin, and J. F. Gamache, 2009: Rapidly intensifying Hurricane Guillermo (1997). Part I: Low-wavenumber structure and evolution. *Mon. Wea. Rev.*, **137**, 603–631.
- Riemer, M., M. T. Montgomery, and M. E. Nicholls, 2010: A new paradigm for intensity modification of tropical cyclones: Thermodynamic impact of vertical wind shear on the inflow layer. *Atmos. Chem. Phys.*, **9**, 10711–10775.
- Ritchie, E. A., and G. J. Holland, 1997: Scale interactions during the formation of Typhoon Irving. *Mon. Wea. Rev.*, **125**, 1377–1396.
- Ritchie, E. A., and G. J. Holland, 1999: Large-scale patterns associated with tropical cyclogenesis in the western Pacific. *Mon. Wea. Rev.*, **127**, 2027–2043.
- Rogers, R. F., and J. M. Fritsch, 2001: Surface cyclogenesis from convectively driven amplification of midlevel mesoscale convective vortices. *Mon. Wea. Rev.*, **129**, 605–637.
- Rogers, R. F., M. L. Black, S. S. Chen, and R. A. Black, 2007: An evaluation of microphysics fields from mesoscale model simulations of tropical cyclones. Part I: Comparisons with observations. *J. Atmos. Sci.*, **64**, 1811–1834.
- Rotunno, R., and K. A. Emanuel, 1987: An air-sea interaction theory for tropical cyclones. Part II: Evolutionary study using a nonhydrostatic axisymmetric numerical model. *J. Atmos. Sci.*, **44**, 542–561.
- Schubert, W. H., and J. J. Hack, 1982: Inertial stability and tropical cyclone development. *J. Atmos. Sci.*, **39**, 1687–1697.
- Shapiro, L. J., 1983: The asymmetric boundary layer flow under a translating hurricane. *J. Atmos. Sci.*, **40**, 1984–1998.
- Simpson, J., E. Ritchie, G. J. Holland, J. Halverson, and S. Stewart, 1997: Mesoscale interactions in tropical cyclone genesis. *Mon. Wea. Rev.*, **125**, 2643–2661.

- Simpson, J., J. B. Halverson, B. S. Ferrier, W. A. Petersen, R. H. Simpson, R. Blakeslee, and S. L. Durden, 1998: On the role of "hot towers" in tropical cyclone formation. *Meteorol. Atmos. Phys.*, **67**, 15–35.
- Sippel, J. A., J. W. Nielsen-Gammon, and S. E. Allen, 2006: The multiple-vortex nature of tropical cyclogenesis. *Mon. Wea. Rev.*, **134**, 1796–1814.
- Skamarock, W. C., et al., 2008: A description of the Advanced Research WRF version 3. Tech. Rep. NCAR Technical Note, NCAR/TN-475+STR, Mesoscale and Microscale Meteorology Division, National Center for Atmospheric Research, 125 pp.
- Smith, R. K., and M. T. Montgomery, 2012: Observations of the convective environment in developing and non-developing tropical disturbances. *Q. J. R. Meteorol. Soc.*, doi:10.1002/qj.1910.
- Stoelinga, M. T., 2009: A users' guide to RIP version 4.5: A program for visualizing mesoscale model output. [Available online at <http://www.mmm.ucar.edu/wrf/users/docs/ripug.htm>.]
- Tang, B., and K. Emanuel, 2012: A ventilation index for tropical cyclones. *Bull. Amer. Meteor. Soc.*, **93**, 1901–1912.
- Tory, K. J., M. T. Montgomery and N. E. Davidson, 2006: Prediction and diagnosis of tropical cyclone formation in an NWP system. Part I: The critical role of vortex enhancement in deep convection. *J. Atmos. Sci.*, **63**, 3077–3090.
- Tory, K. J., M. T. Montgomery, N. E. Davidson, and J. D. Kepert, 2006: Prediction and diagnosis of tropical cyclone formation in an NWP system. Part II: A diagnosis of tropical cyclone formation. *J. Atmos. Sci.*, **63**, 3091–3113.
- Tory, K. J., N. E. Davidson and M. T. Montgomery, 2007: Prediction and diagnosis of tropical cyclone formation in an NWP system. Part III: Diagnosis of developing and nondeveloping storms. *J. Atmos. Sci.*, **64**, 3195–3213.
- Trier, S. B., and C. A. Davis, 2002: Influence of balanced motions on heavy precipitation within a long-lived convectively generated vortex. *Mon. Wea. Rev.*, **130**, 877–899.
- Uhlhorn, E. W., P. G. Black, J. L. Franklin, M. Goodberlet, J. Carswell, and A. S. Goldstein, 2007: Hurricane surface wind measurements from an operational stepped frequency microwave radiometer. *Mon. Wea. Rev.*, **135**, 3070–3085.
- Vigh, J. L., and W. H. Schubert, 2009: Rapid development of the tropical cyclone warm core. *J. Atmos. Sci.*, **66**, 3335–3350.

- Wakimoto, R. M., W.-C. Lee, H. B. Bluestein, C.-H. Liu, and P. H. Hildebrand, 1996: ELDORA observations during VORTEX 95. *Bull. Amer. Meteor. Soc.*, **77**, 1465–1481.
- Wang, J., J. Bian, W. O. Brown, H. Cole, V. Grubišić, and K. Young, 2009: Vertical air motion from T-REX radiosonde and dropsonde data. *J. Atmos. Oceanic Technol.*, **26**, 928–942.
- Wang, Z., M. T. Montgomery, and T. J. Dunkerton, 2010: Genesis of pre-Hurricane Felix (2007). Part I: The role of the easterly wave critical layer. *J. Atmos. Sci.*, **67**, 1711–1729.
- Webster, P. J., 1972: Response of the tropical atmosphere to local, steady forcing. *Mon. Wea. Rev.*, **100**, 518–541.
- Yang, S., and E. A. Smith, 2006: Mechanisms for diurnal variability of global tropical rainfall observed from TRMM. *J. Climate*, **19**, 5190–5226.
- Young, K., J. Wang, and D. Lauritsen, 2009a: THORPEX Pacific Regional Campaign (TPARC) 2008 Quality Controlled Air Force C-130 Dropsonde Data Set. NCAR/Earth Observing Laboratory, 9 pp.
- Young, K., J. Wang, and D. Lauritsen, 2009b: THORPEX Pacific Regional Campaign (TPARC) 2008 Quality Controlled NRL-P3 Dropsonde Data Set. NCAR/Earth Observing Laboratory, 9 pp.



## **INITIAL DISTRIBUTION LIST**

1. Defense Technical Information Center  
Ft. Belvoir, Virginia
2. Dudley Knox Library  
Naval Postgraduate School  
Monterey, California